

UNIVERSITY OF SALERNO
DEPARTMENT OF CHEMISTRY AND BIOLOGY
"A.ZAMBELLI"



Ph.D. Course in Chemistry
XXXII Cycle

Dynamical control of engineered stimuli-responsive materials: synthesis and optimization of active micro-vesicles

Supervisor

Prof. Antonio Proto

Ph.D. Student

Ylenia Miele

Co-Supervisors

Prof. Federico Rossi

Prof. Lorella Izzo

External Supervisor

Dr. Annette Taylor

Ph.D Course Coordinator

Prof. Riccardo Zanasi

Academic year: 2018-2019

CONTENTS

1	Background and motivation	1
1.1	History of clock reactions: from Landolt clock to urea-urease	2
1.2	Stimuli-responsive materials	4
1.3	Coupling of clock reactions with pH-responsive materials: state of the art	8
1.4	Outline of the thesis	13
2	Urea-urease reaction in giant lipid vesicles	15
2.1	Introduction: properties and applications of Giant Lipid Vesicles	16
2.2	Experimental section	20
2.2.1	Modelling of the urea-urease reaction	20
2.2.2	Preparation and characterization of Giant Unilamellar Lipid Vesicles (GUVs)	21
2.3	Results	23
2.3.1	Preliminary results	23
2.3.2	pH calibration with ratiometric imaging	26
2.3.3	Number of vesicles	30
2.3.4	Clock reactions as a function of acetic acid concentration	31
2.3.5	Clock reactions as a function of the number of vesicles	36
2.4	Discussion	41
3	Urea-urease reaction in giant hybrid fatty acid/lipid vesicles	43
3.1	Fatty acid Vesicles: characteristics and methods of preparations	44
3.2	The importance of Fatty acid Vesicles in the Origins of Life studies	46
3.3	Materials and Methods	49
3.3.1	Preparation and characterization of Giant Hybrid Unilamellar Vesicles	49
3.4	Results and discussion	50
3.4.1	Clock reactions as a function of acetic acid concentration	50
3.4.2	Self division as an effect of the fast pH variation and osmotic pressure	54
4	Preparation of giant hybrid polymer/lipid vesicles	63
4.1	Living radical polymerization for the synthesis of block copolymers	64
4.2	Polymeric vesicles and hybrid polymer/lipid vesicles	66
4.3	Experimental section	70
4.3.1	Materials for polymers synthesis and purification	70
4.3.2	Polymer synthesis	70
4.3.3	Polymer characterization	73
4.3.4	Preparation and characterization of Giant Hybrid Unilamellar Vesicles	74
4.4	Results and discussion	76

4.4.1	Rational design of amphiphilic copolymers	76
4.4.2	Identification of the experimental conditions and relative reactivities of the monomers	77
4.4.3	Characterization of the copolymers selected for the vesicles preparation	85
4.4.4	Fluorescent labelling for the detection of polymeric phases in giant hybrid vesicles	87
4.4.5	Preparation of hybrid polymeric vesicles via electroformation	89
4.4.6	Preparation of hybrid polymeric vesicles by the droplet transfer method	92
5	Conclusions and future work	99
	Appendices	101
A	Models and Matlab codes for the analysis of pure POPC vesicles	101
A.1	Matlab code for the detection of vesicles	101
A.2	Matlab code for counting the number of vesicles	103
A.3	Matlab code for particle tracking	104
A.4	Fitting equation used in the ratiometric method	106
B	Kinetic model and pH calibration for POPC/HOA vesicles	108
B.1	pH calibration	108
B.2	Detailed model of urea-urease reaction in hybrid vesicles	109
C	Models, synthesis and characterization of polymers	112
C.1	Mayo-Lewis model and Meyer-Lowry equation	112
C.2	Preparation of the macroinitiator mPEG-Br	115
C.3	Synthesis and characterization of the fluorescent monomer	116
C.4	Synthesis and characterization of the copolymers PMMA- <i>ran</i> -PDMAEMA, mPEG- <i>b</i> -(PMMA- <i>grad</i> -PDMAEMA), fluorescent mPEG- <i>b</i> -(PMMA- <i>grad</i> -PDMAEMA)	122
C.5	Estimation of the hydrophobic mismatch	130
	Bibliography	131
	Papers	145
Paper I	Modelling Approach to Enzymatic pH Oscillators in Giant Lipid Vesicles	147
Paper II	The Relevance of Inorganic Nonlinear Chemical Reactions for the Origin of Life Studies	160
Paper III	Self-Division of Giant Vesicles Driven by an Internal Enzymatic Reaction.	174
Paper IV	On the Origin and Consequences of High DMAEMA Reactivity Ratio in ATRP Copolymerization with MMA: an Experimental and Theoretical Study	183

LIST OF ABBREVIATIONS

^{13}C NMR	Carbon nuclear magnetic resonance
16:0 PC (DPPC)	1,2-dipalmitoyl- <i>sn</i> -glycero-3-phosphocholine
16:0-18:1 PC (POPC)	1-palmitoyl-2-oleoyl- <i>sn</i> -glycero-3-phosphocholine
18:1 Liss Rhod PE	1,2-dioleoyl- <i>sn</i> -glycero-3-phosphoethanolamine-N-(lissamine rhodamine B sulfonyl) (ammonium salt)
^1H NMR	Proton nuclear magnetic resonance
ARGET ATRP	Activators regenerated by electron transfer ATRP
ATRP	Atom transfer radical polymerization
BMPB	2-bromoisobutyryl bromide
BODIPY-DMAEMA	2,6-diethyl-1,3,5,7-tetramethyl-8-[4-[4-(2-methacryloyl)ethyl-dimethylammoniumbromide]octaoxyphenyl]-4,4'-difluoroboradiaza indacene
bpy	2,2'-bipyridine
-co-	Copolymers with an unspecified arrangement of monomeric units
δ	Solubility parameter
D1	Relaxation delay
DMAEMA	2-(Dimethylamino)ethyl methacrylate
DMAP	4-(Dimethylamino)pyridine

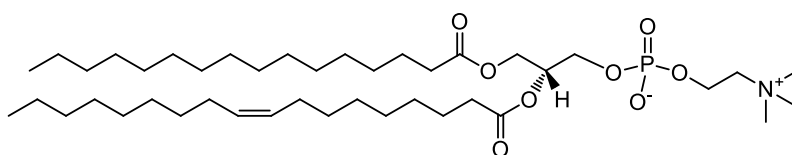
DMF	Dimethylformamide
DP	Degree of polymerization
DSC	Differential Scanning Calorimetry
$F_{\text{BODIPY-DMAEMA}}$	Molar fraction of BODIPY-DMAEMA in the final copolymer
f_{DMAEMA}	Molar fraction of 2-(Dimethylamino)ethyl methacrylate in the feed
F_{DMAEMA}	Molar fraction of 2-(Dimethylamino)ethyl methacrylate in the final copolymer
f_{MMA}	Molar fraction of Methyl methacrylate in the feed
F_{MMA}	Molar fraction of Methyl methacrylate in the final copolymer
F_{mPEG}	Molar fraction of Methoxy-poly(ethylene glycol) in the final copolymer
GPC	Gel Permeation Chromatography
GUV	Giant unilamellar vesicles
HOA	Oleic acid
HSQC	Heteronuclear Single Quantum Coherence
$I_{\text{BODIPY-DMAEMA}}$	Intensity of the NMR signal of BODIPY-DMAEMA in the final copolymer
I_{DMAEMA}	Intensity of the NMR signal of 2-(Dimethylamino)ethyl methacrylate in the final copolymer
I_{MMA}	Intensity of the NMR signal of Methyl methacrylate in the final copolymer

I_{mPEG}	Intensity of the NMR signal of Methoxy-poly(ethylene glycol) in the final copolymer
I-solution	Inner solution in the Droplet Transfer Method
ITO	Indium Tin Oxide
$M_{\text{BODIPY-DMAEMA}}$	Molar mass of BODIPY-DMAEMA
M_{DMAEMA}	Molar mass of 2-(Dimethylamino)ethyl methacrylate
MMA	Methyl methacrylate
M_{MMA}	Molar mass of Methyl methacrylate
MO	Mineral Oil
mPEG	Methoxy-poly(ethylene glycol) or Poly(ethylene glycol) monomethylether
mPEG-Br	Poly(ethylene glycol) methyl ether 2-bromoisobutyrate
mPEG- <i>b</i> -(PMMA- <i>grad</i> -PDMAEMA)	Methoxy-poly(ethylene glycol)- <i>block</i> -(Poly(methyl methacrylate)- <i>gradient</i> -poly[(2-dimethylamino)ethyl methacrylate])
MD	Molecular Dynamics
MD%	Copolymer made of MMA and DMAEMA, the subscript indicates the mole percent of DMAEMA
M_{EO}	Molar mass of ethylene glycol
M_{n}	Number average molecular weight
M_{w}	Weight average molecular weight

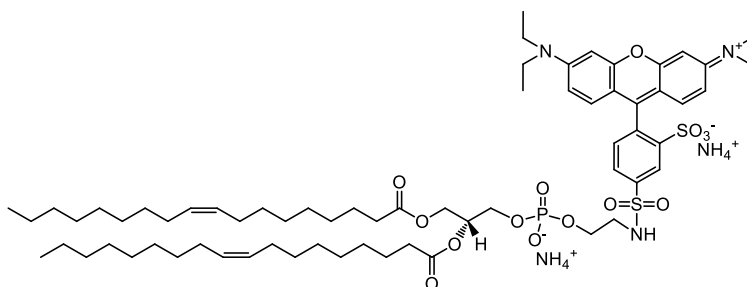
M_w/M_n	Polidispersity index
ODEs	Ordinary differential equations
O-solution	Outer solution in the Droplet Transfer Method
$P_{2k}MD\%$	Copolymer made of mPEG (2kDa), MMA and DMAEMA. The subscript % indicates the mole percent of DMAEMA
$P_{5k}MD\%$	Copolymer made of mPEG (5kDa), MMA and DMAEMA. The subscript % indicates the mole percent of DMAEMA
PDEs	Partial differential equations
PDMAEMA	Poly[(2-dimethylamino)ethyl methacrylate]
PDMS- <i>g</i> -PEO	Poly(dimethyl siloxane)- <i>grad</i> -poly(ethyleneoxide)
PEO-PBD	Poly(ethyleneoxide- <i>b</i> -butadiene)
PMMA	Poly(methyl methacrylate)
PMMA- <i>ran</i> -PDMAEMA	Poly(methyl methacrylate)- <i>random</i> -poly[(2-dimethylamino)ethyl methacrylate]
PMTs	Photomultiplier tubes
Pyr	Pyranine
r_{DMAEMA}	Reactivity ratio of DMAEMA
RI	Refractive index
r_{MMA}	Reactivity ratio of MMA
Sn(EH) ₂	tin (II) 2-ethylhexanoate
TEA	Triethylamine
T_g	Glass transition temperature
THF	Tetrahydrofuran

T_m	Melting temperature
w/o	Water-in-oil

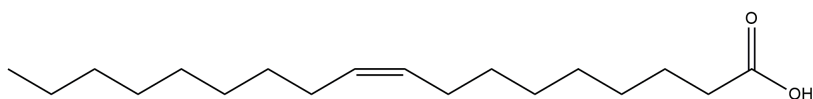
CHEMICAL STRUCTURES



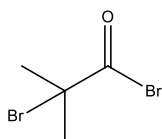
1-Palmitoyl-2-oleoyl-*sn*-glycero-3-phosphocholine (POPC)



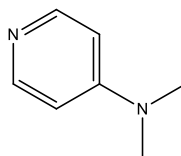
1,2-dioleoyl-*sn*-glycero-3-phosphoethanolamine-N-(lissamine rhodamine B sulfonyl) (ammonium salt)(18:1 Liss Rhod PE)



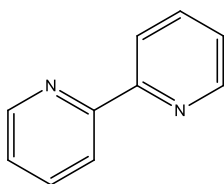
Oleic acid (HOA)



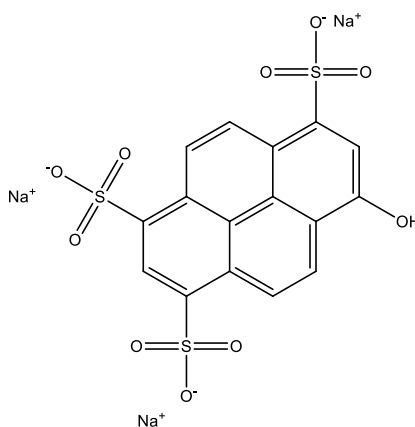
**2-bromoisobutyryl
bromide (BMPB)**



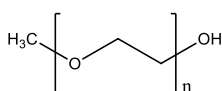
**4-(dimethylamino)pyridine
(DMAP)**



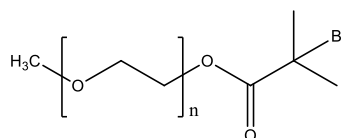
2,2'-bipyridine (bpy)



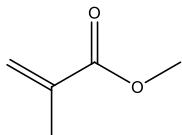
Pyranine (Pyr)



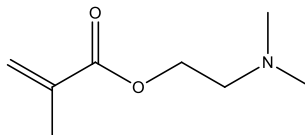
**Poly(ethylene glycol)
monomethylether
(mPEG)**



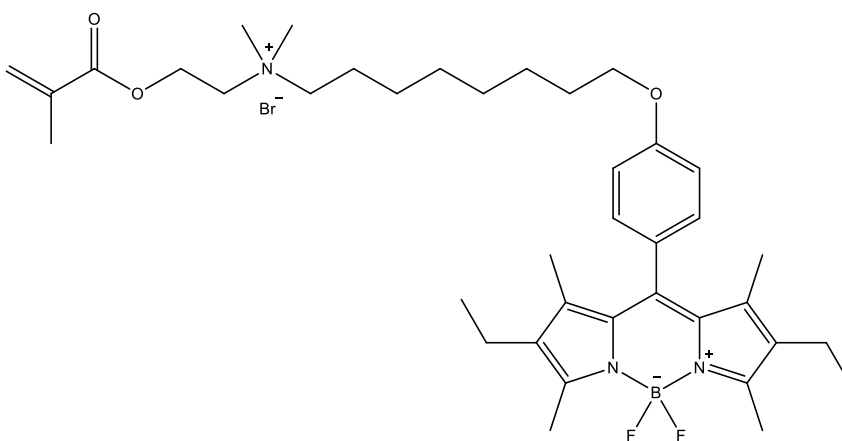
**Poly(ethylene glycol) methyl
ether 2-bromoisobutyrate
(mPEG-Br)**



**Methyl methacrylate
(MMA)**



**2-(Dimethylamino)ethyl
methacrylate (DMAEMA)**



**2,6-diethyl-1,3,5,7-tetramethyl-8-[4-[4-(2-
methacryloyl)ethyl-
dimethylammoniumbromide)]octaoxy) phenyl]-4,4'-
difluoroboradiaza indacene (BODIPY-DMAEMA)**

1

BACKGROUND AND MOTIVATION

This chapter introduces the most famous clock reactions and the most important stimuli-responsive materials. The paragraph 1.3 is a connection between the two topics, dealing with some successful examples of coupling of pH-responsive materials with pH-responsive reactions. Finally the outline of the thesis is presented.

Contents

1.1	History of clock reactions: from Landolt clock to urea-urease	2
1.2	Stimuli-responsive materials	4
1.3	Coupling of clock reactions with pH-responsive materials: state of the art	8
1.4	Outline of the thesis	13

1.1 History of clock reactions: from Landolt clock to urea-urease

Clock reactions are among the most dramatic and visually pleasing chemical demonstrations. After a clock reaction is initiated, there is a period during which no significant change takes place in the mixture, and then a change occurs suddenly. The time elapsed between the mixing of the reactants and the sudden change in the mixture is called **clock time** or **induction period** [1]. The term clock reaction ("clock" in a mechanical analogy with alarm clocks and stopwatches) was assigned for the first time to the Landolt reaction discovered in 1886 [2]. A solution of iodate ions is added to an acidified solution of sodium bisulfite and starch. First, the bisulfite ions (HSO_3^-) reduce some of the iodate ions (IO_3^-) to form iodide ions (I^-). Next, the iodide ions (I^-) are oxidized by the remaining iodate ions (IO_3^-) to form triiodide ions (I_3^-). In the third reaction, the triiodide ions (I_3^-) get reduced by the bisulfite ions (HSO_3^-) to become iodide ions (I^-). When all of the bisulfite has been consumed, the triiodide ions and starch combine to form a dark blue-black starch complex that looks like ink [3]. Thus, after two clear colorless solutions are mixed, the mixture remains colorless for a short time and then suddenly turns dark blue [1].

Other examples of clock reactions include the arsenic (III) sulfide clock reaction [4], the formaldehyde clock reaction [5], the hydration of carbon dioxide [6, 7]. Different phenomenological and kinetic aspects are involved in the clock reactions listed. In the Landolt reaction, the species responsible for the clock behaviour is the triiodide that increases its concentration after the consumption of the bisulfite. In the formaldehyde-sulfite the clock behavior is thought to result from the consumption of an internal sulfite-bisulfite buffer by formaldehyde to produce the formaldehyde-sulfite adduct. A possible mechanism of reaction is summarized in Figure 1.1. The rate-determining step is the dehydration of methylene glycol (reaction 1 in the scheme), SO_3^{2-} and H^+ are consumed through reactions 3 and 4, but are supplied through the dissociation of HSO_3^- in reaction 2, and the pH increases slowly. When HSO_3^- has been completely consumed, H^+ are no longer supplied from reaction 2 and the pH increases rapidly [8].

Mechanism for the Formaldehyde-Sulfite clock reaction

- (1) $\text{CH}_2(\text{OH})_2 \rightleftharpoons \text{CH}_2\text{O} + \text{H}_2\text{O}$
- (2) $\text{HSO}_3^- \rightleftharpoons \text{SO}_3^{2-} + \text{H}^+$
- (3) $\text{CH}_2\text{O} + \text{SO}_3^{2-} \rightarrow \text{CH}_2(\text{O}^-)\text{SO}_3^-$
- (4) $\text{CH}_2(\text{O}^-)\text{SO}_3^- + \text{H}^+ \rightleftharpoons \text{CH}_2(\text{OH})\text{SO}_3^-$
- (5) $\text{H}_2\text{O} \rightleftharpoons \text{H}^+ + \text{OH}^-$
- (6) $\text{CH}_2\text{O} + \text{HSO}_3^- \rightarrow \text{CH}_2(\text{OH})\text{SO}_3^-$
- (7) $\text{CH}_2(\text{OH})_2 + \text{SO}_3^{2-} \rightarrow \text{CH}_2(\text{O}^-)\text{SO}_3^- + \text{H}_2\text{O}$
- (8) $\text{CH}_2(\text{OH})_2 + \text{HSO}_3^- \rightarrow \text{CH}_2(\text{OH})\text{SO}_3^- + \text{H}_2\text{O}$

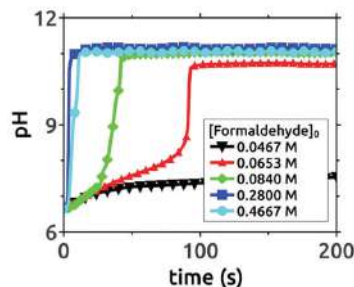


Figure 1.1: On the left: Mechanism for the Formaldehyde-Sulfite Clock reaction, reproduced with permission from [8]. Copyright ©, American Chemical Society. On the right: pH temporal evolution for constant sulfite concentration, reproduced from [9] by permission of The Royal Society of Chemistry.

The formaldehyde-sulfite is not the unique example of an “acid-to-alkali” clock. Few years ago, the group of A. Taylor started a thorough investigation on the urea-urease system. This well-known reaction consists in the hydrolysis of urea catalyzed by urease, a large nickel-based enzyme (typically > 500 kDa for jack-bean) [10, 11].



The maximum rate is at pH 7, and the base ammonia raises the solution pH:



If the initial pH is low ($\text{pH} \sim 4$), a slow increase in pH occurs followed by a rapid conversion to the high pH state ($\text{pH} \sim 9$) because the formation of ammonia and consequently of hydroxide ions leads to an increase of the reaction rate (figure 1.2) [11, 12]. The pH clock is due to the weak acid equilibria of the enzyme EH. At low pH, $\text{H}^+ > K_1$, the EH_2^+ form dominates, whereas at high pH the predominant form is E^- . The substrate can bind to the three enzyme forms, but the product derives only from the interaction with EH. Therefore, the rate will be maximum when EH is the main species, *i.e.* when the pH lies between $\text{p}K_1$ and $\text{p}K_2$ (Figure 1.2 a)[11].

A theoretical study on the urea-urease system, based on a linear stability analysis, allowed to find the conditions that lead to clock behaviour, sustained oscillations and bistability in flow reactors[13]. Experimentally, pH clocks are reported for certain concentrations of acid, enzyme and urea in batch and flow reactors [14], hydrogel beads [15], alginate beads [16]. More recently, the urea-urease system has been coupled with stimuli-responsive materials, but these results will be discussed in detail in Section 1.3 after a comprehensive introduction on stimuli-responsive materials in Section 1.2.

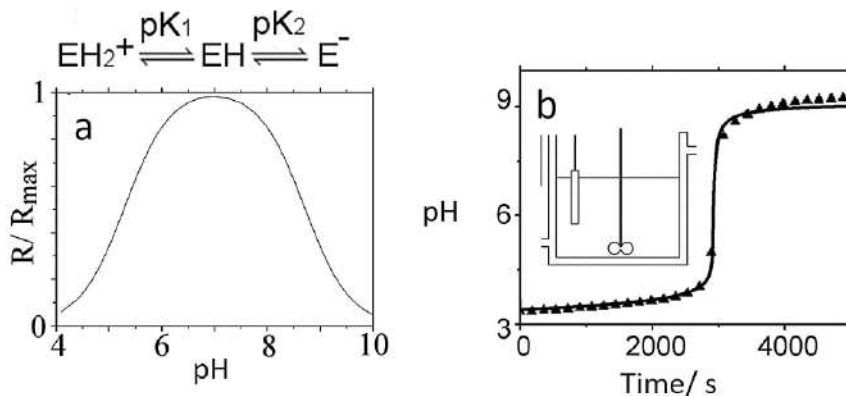


Figure 1.2: a) Bell-shaped rate-pH curve characteristic of urea-urease. b) Change in pH in a closed reactor for the urea-urease reaction. Reproduced with permission from [11]. Copyright ©2018, Wiley-VCH Verlag GmbH & Co. KGaA, Weinheim.

1.2 Stimuli-responsive materials

Stimuli-responsive polymer-based materials are capable of altering their chemical and/or physical properties upon exposure to external stimuli. Also named intelligent, smart, or environmentally-responsive polymers, they are responsive to several factors such as temperature, redox variations, pH, light and ionic strength [17, 18]. Because of their unique properties, stimuli-responsive materials are intensively studied for a diverse range of applications: on-demand drug delivery, tissue generation/repair, biosensing, chromatography and sample extraction, smart coatings and artificial muscles [18, 19].

Thermo-responsive polymers and hydrogels show a volume phase transition at a certain temperature, which causes a sudden change in the solvation state [20]. Based on their response to change in temperature, these polymers are divided in two classes: (i) polymers that become insoluble above a critical temperature called the lower critical solution temperature (LCST) and (ii) polymers that precipitate and undergo phase change below a critical temperature called as the upper critical solution temperature (UCST)[20]. Typical LCST polymers are based on *N*-isopropylacrylamide (NIPAM), *N,N*-diethylacrylamide (DEAM), methylvinylether (MVE) as monomers. The LCST in water of these three polymers is close to the physiological temperature, which makes them interesting for biomedical applications [20]. **Redox-responsive** polymers mainly incorporate disulfide or diselenide linkages and can be explored for their response to GSH and ROS in drug delivery systems [21].

Photo-responsive polymers contain light-sensitive chromophores such as azobenzene groups, spiropyran groups, nitrobenzyl groups that undergo conformational changes or modifications in their hydrophilicity transmitted to

the whole polymer [19, 22]. Figure 1.3 shows the conversion of light energy in mechanical work for a photosensitive film: the isomerization from *trans*-azobenzene to *cis*-azobenzene catalyzed by UV light causes a motion of bending in the polymeric film [23].

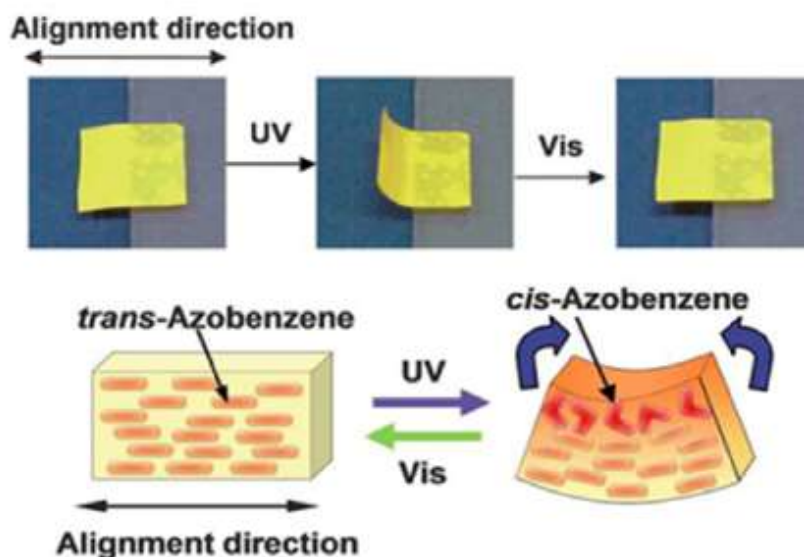


Figure 1.3: Liquid crystalline polymers film with in plane alignment, photographs and plausible mechanism of photoinduced bending behaviour. Reproduced with permission from [23]. Copyright ©, The Polymer Society of Korea and Springer Science+Business Media B.V. 2017

pH-responsive polymers are polyelectrolytes with weak acid (main groups in Figure 1.4) or basic groups (main groups in Figure 1.5) that can respond to solution pH by changing properties such as surface activity, chain conformation, solubility and configuration. [17]. pH-responsive polymers can have linear, branched or network structures; they can be synthetic or natural like dextran, hyaluronic acid, alginate, chitosan and gelatine [17]. The response to solution conditions can be different for the various polymers: a pH change can cause flocculation, precipitation, swelling-deswelling, self-assembly in micelles and vesicles [17] (polymeric vesicles will be discussed in Section 4.2). A large number of pH-responsive polymers can be designed using various ionisable groups, with pK_a values ranging from 1 to 14. Polymers with carboxylic groups at low pH are uncharged and loose protons at high pH. Poly(acrylic acid) and Poly(methacrylic acid) have been most frequently reported, the monomers can be easily polymerized and are inexpensive. Polymers containing sulfonic acid groups like poly(2-acrylamido-2-methylpropane sulfonic acid) (PAMPS) and poly(4-styrenesulfonic acid) (PSSA) are usually preferred in the preparation of

hydrogels because of the high degree of swelling. Polymers containing boronic acid groups are used in applications such as self-healing gels and glucose sensors. Weak polybases accept protons at low pH values by forming polyelectrolytes and release them becoming uncharged under basic conditions. These polymers usually contain tertiary amine, morpholino, pyrrolidine, imidazole, piperazine and pyridine groups. Poly[(2-dimethylamino)ethyl methacrylate] (PDMAEMA) is the most studied weak basic polymer having both pH-responsive nature and thermo-responsive nature useful in drug delivery applications. Poly-(2-vinyl pyridine) (P2VP) has been tested as a colorimetric sensor in photonic crystals (crystals with structural color due to light interaction with the periodic structure of the material)[24], in particular in ultrathin photonic polymer gel films. Changes of pH cause swelling or deswelling of the responsive polymer, consequently, the film thickness changes, the reflection peaks shift and the color of the film depends on the pH of the solution as illustrated in Figure 1.6.

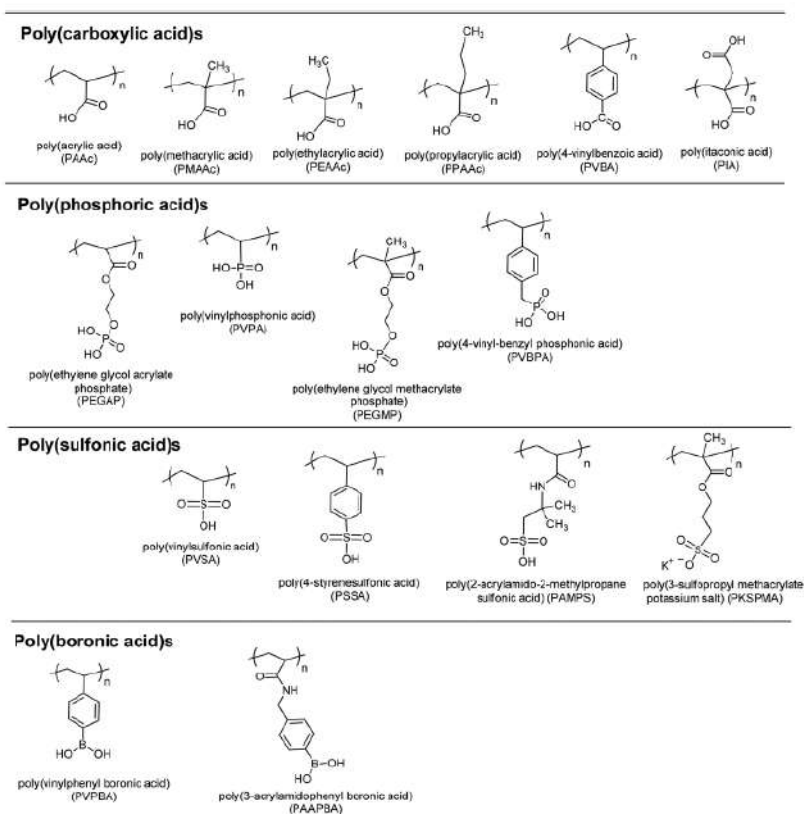


Figure 1.4: Chemical structures of pH-responsive acidic polymers. Reproduced from [17] by permission of The Royal Society of Chemistry.

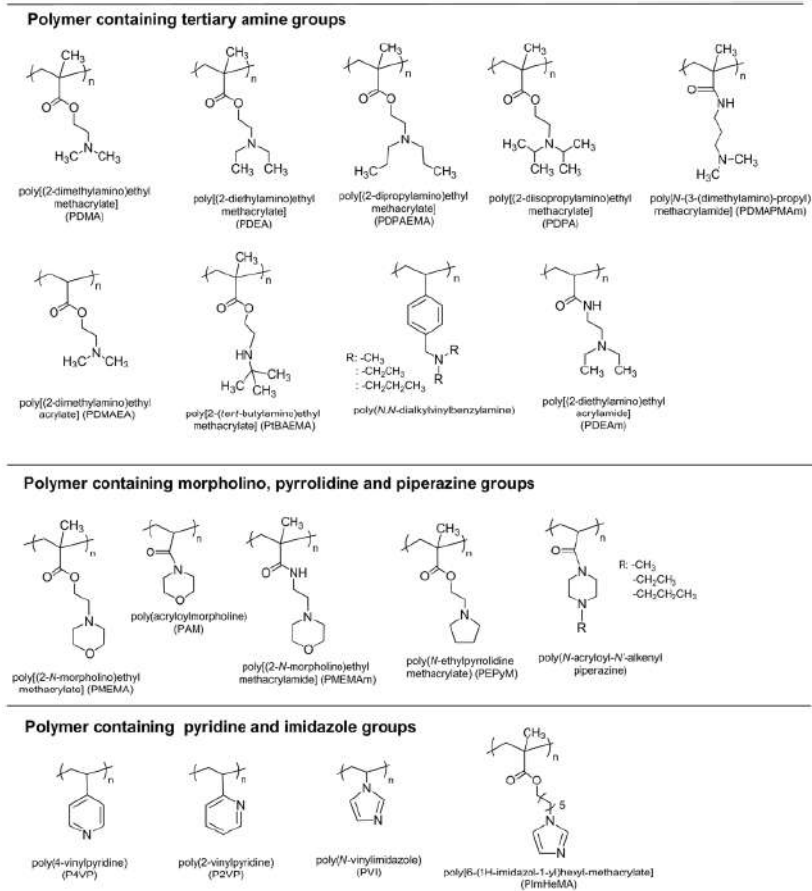


Figure 1.5: Chemical structures of pH-responsive basic polymers. Reproduced from [17] by permission of The Royal Society of Chemistry.

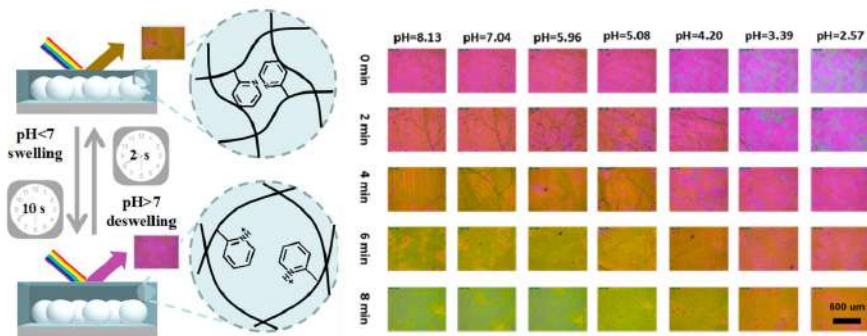


Figure 1.6: Mechanism of swelling-deswelling and optical micrographs showing the colorimetric response as a function of pH for the P2VP based photonic film. Reproduced from [24], licensed under Creative Commons Attribution (CC BY).

1.3 Coupling of clock reactions with pH-responsive materials: state of the art

In this paragraph, four examples of clock reactions coupled with stimuli-responsive materials will be presented: two systems involve the Formaldehyde-Sulfite (FS) reaction while the other two the more bio-compatible urea-urease. The Formaldehyde-Sulfite (FS) reaction can be studied alone or combined with the gluconolactone hydrolysis (FSG): the production of H^+ from the dormant deactivator lactone decreases the pH back to acidic. Thus, the system exhibits a sharp peak characterized by two parameters: the clock time and the transient pH state which is defined as the full width at half maximum of the pH-time curve (an example of the peak shape is shown in Figure 1.7 1b and 2c).

Escala *et al.* [9] coupled the FS and the FSG reactions with polyacrylic acid (PAA) to trigger temporal changes of viscosity (potential applications in chemical and petroleum engineering). PAA is capable to elongate its shape at high pH in aqueous solutions, which produces an increase in the solution viscosity. pH and viscosity evolve in a similar way for both systems FS-PAA (Figure 1.7 1a) and FSG-PAA (Figure 1.7 1b). The addition of the polymer modifies the FS chemical system by introducing longer induction times for clock behaviour and enhancing the viscosity gap between the initial and final states (Figure 1.7 2a and 2b). In the case of the FSG-PAA system, the increase of the gluconolactone initial concentration is the main responsible of the transition from a clock to peak shape in both the pH and dynamic viscosity temporal changes (Figure 1.7 2c).

Lagzi *et al.* [25] report the coupling of the FSG reaction with three kinds of pH-responsive materials: (i) oleic acid, (ii) gold nanoparticles functionalized with alkane-thiolates terminated with carboxylic groups, (iii) gel of poly(*N*-isopropylacrylamide)-*co*-poly(*N*-*tert*butylacrylamide). In the first example, the FSG reaction is responsible for the reverse transformation vesicles-micelles. At low pH the solution appears hazy (Tyndall effect) because the fatty acid molecules form unilamellar vesicles with an average diameter of ~ 100 nm. When the clock reaction reaches pH ~ 10 , the solution turns transparent because most of the OA molecules are deprotonated and form spherical micelles with an average diameter of ~ 5 nm. When the system returns back to the low-pH state due to the lactone hydrolysis, the micelles revert back to vesicles and an opaque phase appears again (Figure 1.8 a).

In the second system, when the pH is low the carboxylic ligands are uncharged and the electrostatic repulsion between the nanoparticles (NPs) is weak. At the beginning of the reaction, the color of the solution of NPs is blue, containing some NP precipitates. At high pH values, when most of carboxylic groups are negatively charged, the NPs are free and unaggregated, and the color becomes red due to surface plasmon resonance (SPR). When the pH returns back to the neutral/acidic range, the NPs lose their stability and they aggregate again, the

color of the solution changes from red back to blue with an intermediate purple colour (Figure 1.8 b). The third case differs from the others as the pH sensitive unit is not a carboxylic group, but a tertiary amine functional group (positively charged at acidic pH and neutral at high pH values). When charged, the gel is swollen because of the solvent uptake of the network. When uncharged, the solvation of the poly-NIPA-based polymer chains by water molecules is thermodynamically unfavourable, so the chains aggregate with each other and coil up. This rearrangement is accompanied by the expulsion of water and contraction of the gel filament. This step is reversible, the pH decrease due to the lactone hydrolysis leads to an expansion of the polymer chains that macroscopically is manifested as a reswelling.

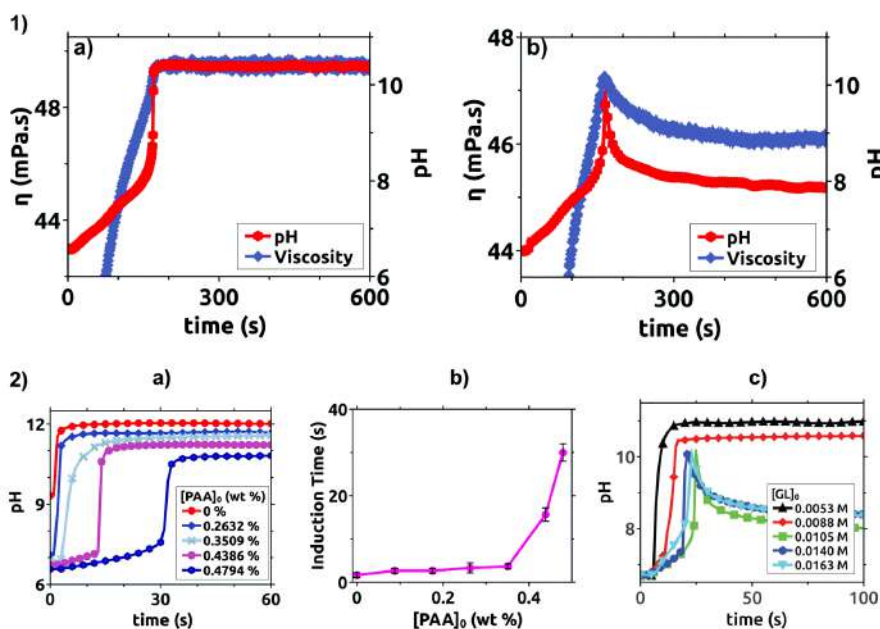


Figure 1.7: Row 1: Temporal evolution of pH and viscosity for a) FS-PAA and b) FSG-PAA systems. In both cases $[\text{SO}_3^{2-}]_0 = 0.0684$ M, $[\text{PAA}] = 0.4386\text{wt } \%$ and $[\text{formaldehyde}]_0 = 0.0653$ M. Row 2: PAA (a and b) and Gluconolactone (c) were varied for constant for constant concentrations of $[\text{SO}_3^{2-}]_0 = 0.0684$ and $[\text{formaldehyde}]_0 = 0.00933$ M. Reproduced from [9] by permission of The Royal Society of Chemistry.

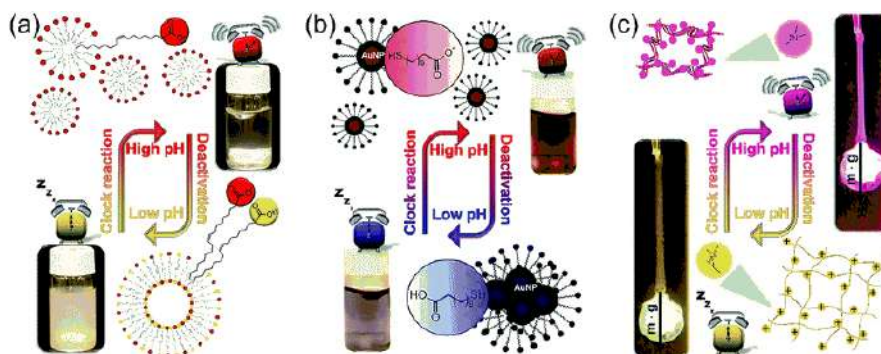


Figure 1.8: a) Reversible vesicle-micelle transformation of oleic acid molecules (low pH: vesicles-turbid solution, high pH: micelles-transparent solution) b) Reversible dissolution and aggregation of carboxyl terminated AuNPs (low pH: aggregated NPs-blue solution with microscopic aggregates, high pH: free NPs-transparent red solution), c) volume change (shrinking and swelling) of a hydrogel filament containing tertiary amine functional groups (low pH: swollen state; high pH: shrunken state). Reproduced from [25], published by The Royal Society of Chemistry.

The urea-urease system, known for years and mainly explored for analytical chemistry applications [26], just recently received attention for its pH-dependent properties. In 2017, this reaction has been used to programme a change in pH which in turn activated the disintegration of alginate fibers [27]. The mechanism of action is shown in Figure 1.9. Fibers are produced with a flow focusing device: oil droplets are formed in a flow of sodium alginate with different amounts of urease. This flow meets an aqueous solution of calcium chloride hexahydrate, upon which the solution is cross-linked by calcium ions. The hydrogel fibers are then immersed in an acidic solution containing urea and a colorimetric indicator. The sodium salt of ethylenediaminetetraacetic acid (EDTA) is added to the bulk aqueous solution as a chelating agent for calcium ions. The enzyme converts urea to ammonia generating a local increase in pH after a defined time period. At low pH, partially protonated EDTA can be found, at high pH EDTA is deprotonated locally and its affinity for calcium ions increases. The cation exchange from alginate to EDTA results in the loss of cross-linking and the release of oil droplets.

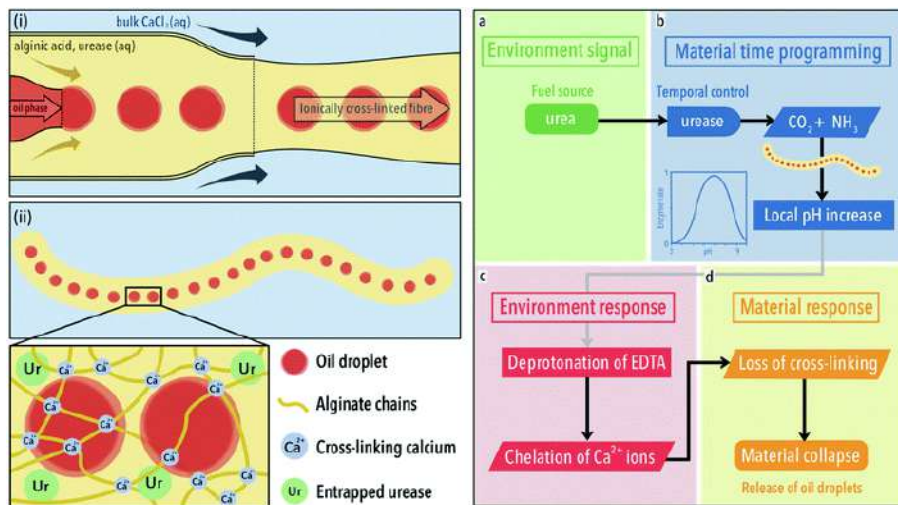


Figure 1.9: Synthesis and action of composite fibres. Left (i), Formation of calcium ion cross-linked alginate fibres using a microfluidic synthesis. (ii) The gel network entraps both the enzyme urease and the oil droplets. Right. a-b) the fibre converts urea in ammonia, after a defined time period, the fibre generates a local increase in pH. c-d) At high pH EDTA increases its binding affinity for calcium ions, this results in a loss of cross-linking and the release of oil droplets. Reproduced from [27], published by The Royal Society of Chemistry.

Another interesting coupling of urea-urease with a pH-responsive material was designed by Pojman's research group[12]: the base produced in the enzymatic reaction catalyzes the Michael addition of a trithiol to a diacrylate (Figure 1.10). The process is one pot and involves biofriendly and water soluble components (thiols are present in biological systems). The Michael addition leads to the formation of a hydrogel above pH 8: the reaction can be performed in a batch reactor where the time of gelation depends on the initial composition of the reaction or it can be initiated locally in unstirred reactors. In a Petri dish (2D system, thin layer with negligible convective motions), the reaction is able to produce gel fronts that propagate with constant velocity, curing the entire medium (Figure 1.11 a-c). The effect of convective motions has been analyzed in Eppendorf tubes where ascending and descending fronts have slightly different speeds (Figure 1.11 d-g). Independently of the orientation, the reaction can be initiated in a specific point and then the fronts propagate to cure the rest of the medium. The features of this systems are attractive for many materials-chemistry applications, such as adhesives, coatings and injectable biomedical formulations, where a slow reaction is followed by a rapid curing.

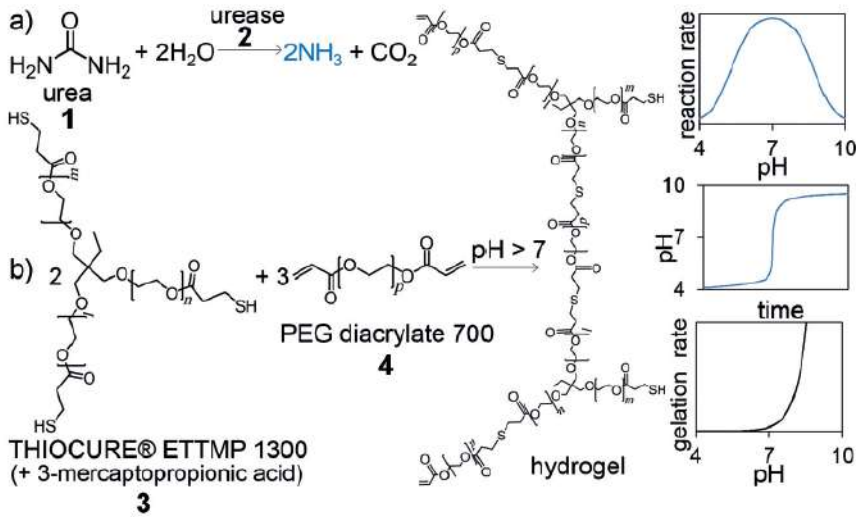


Figure 1.10: The reaction of urea and urease produces a base that catalyzes a thiol Michael addition. Sketched graphs show the dependence of the urea-urease reaction rate on the pH value, the resultant pH-time curve and the dependence of the gelation rate on the pH value. Reproduced from [12], licensed under Creative Commons Attribution (CC BY).

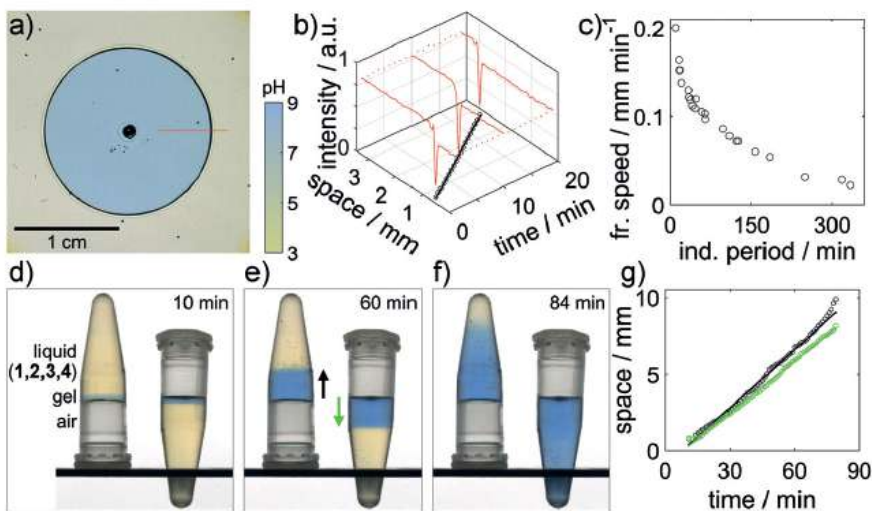


Figure 1.11: Experiments with a pH indicator bromothymol blue. a-c) Frontal polymerization in a Petri dish, d-g) Ascending and descending fronts in Eppendorf tubes. Reproduced from [12], licensed under Creative Commons Attribution (CC BY).

1.4 Outline of the thesis

The main goal of this thesis is the coupling of a pH sensitive clock reaction (the enzymatic urea-urease reaction) with pH-responsive giant hybrid vesicles (vesicles are self-assembled structures that mimic cell membrane properties) and study the mechanical answer (swelling or division) that can derive from this coupling. In Chapter 2, the urea-urease reaction is investigated in pure lipid vesicles. These experiments served as a starting point to choose the best conditions for the enzymatic reaction and a reference system for the hybrid vesicles. Part of the experiments with pure POPC vesicles were performed at the University of Sheffield during a six months stage funded by the Erasmus+ programme.

Two kinds of hybrid vesicles were synthesised in the context of the PhD work: lipid/oleate vesicles (the pH-sensitive unit is the COOH group, negatively charged at high pH) and lipid/polymeric vesicles (the pH-sensitive unit is the amine group, positively charged at low pH). Lipid/oleate vesicles are discussed in chapter 3, here we show that hybrid vesicles can spontaneously divide, thus mimicking cells' self-division processes, when coupled with pH changes induced by the urea-urease clock reaction. Chapter 4 is devoted to polymeric/lipid vesicles, in particular the synthesis of pH-sensitive polymers and the synthesis of giant hybrid vesicles by two methods (electroformation and *droplet transfer*) are discussed; part of these experiments were carried out during a stage at IMRCP (University of Toulouse Paul Sabatier) funded by the Erasmus+ programme. In chapter 5, the three systems are compared and new studies are suggested based on the results obtained.

2

UREA-UREASE REACTION IN GIANT LIPID VESICLES

This chapter starts with an introduction on giant lipid vesicles in which definitions, properties and applications are discussed. Theoretical and experimental results on the encapsulation of urea-urease system in lipid vesicles are then detailed, including the vesicles preparation method and the thorough investigation of the effect of reactants' concentration and dilution factors on the reaction dynamics.

Contents

2.1	Introduction: properties and applications of Giant Lipid Vesicles	16
2.2	Experimental section	20
2.2.1	Modelling of the urea-urease reaction	20
2.2.2	Preparation and characterization of Giant Unilamellar Lipid Vesicles (GUVs)	21
2.3	Results	23
2.3.1	Preliminary results	23
2.3.2	pH calibration with ratiometric imaging	26
2.3.3	Number of vesicles	30
2.3.4	Clock reactions as a function of acetic acid concentration	31
2.3.5	Clock reactions as a function of the number of vesicles	36
2.4	Discussion	41

2.1 Introduction: properties and applications of Giant Lipid Vesicles

Lipid vesicles (also called liposomes) are formed in aqueous solutions by the self-assembly of lipids in the form of bilayers, which close on themselves to form a hollow sphere, containing a portion of the aqueous phase [28]. The main characteristics of liposomes are the homogeneity of the membrane, the lamellarity and the size. Vesicles are homogeneous if the components are uniformly distributed in the membrane, they are heterogeneous if domains are present. For instance, the mixing of DPPC (1,2-dipalmitoyl-*sn*-glycero-3-phosphocholine) with DPhPC (1,2-diphytanoyl-*sn*-glycero-3-phosphocholine) at room temperature gives rise to the formation of domains within the membrane (Figure 2.1 A). In this case, the domain formation is caused by the different transition temperature of the two lipids. The transition temperature, T_m , is the temperature required to induce a change in the lipid physical state from the ordered gel phase, where the hydrocarbon chains are fully extended and closely packed, to the disordered liquid crystalline phase, where the hydrocarbon chains are randomly oriented and fluid. DPPC and DPhPC have a different T_m : at room temperature, DPPC is in the gel ordered state ($T_m = 41$ °C), DPhPC is in the liquid crystalline state (disordered phase from -120 to 120 °C).

The lamellarity is the number of bilayers surrounding the liposome. The most common architectures are (i) unilamellar, if vesicles have one single bilayer; (ii) multilamellar with a few or several (concentric) bilayers (MLV); (iii) multivesicular if vesicles contain other vesicles in non-concentric way (MVV) [28]. Depending on the size, vesicles can be small (SUV, diameter $d < 50$ nm), large (LUV, $d \approx 100$ to 200 nm) or giant (GUV, $d > 1 \mu\text{m}$) [28] (Figure 2.1 B for the lamellarity and the size). Giant vesicles can be easily monitored by optical microscopy, however the lamellarity can be confirmed only by bending elasticity measurements or fluorescence quenching assays [29].

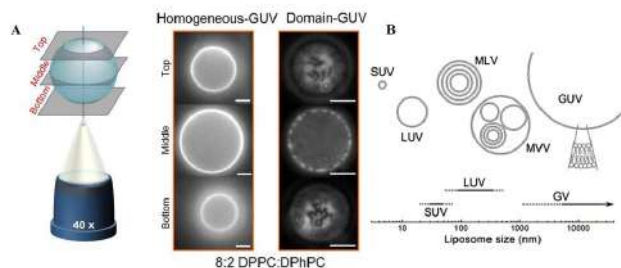


Figure 2.1: A) Homogeneous GUV and heterogenous GUV with domains for vesicles made of DPPC and DPhPC, reproduced from [30]. Copyright ©2018, Springer Nature, licensed under Creative Commons CC BY. B) Schematic drawing of vesicles with different morphologies and approximate size, reproduced from [28] with permission from The Royal Society of Chemistry.

The first bulk method described for the vesicles production is the controlled hydration of a lipid film [29, 31]. In this procedure, the lipids are first dissolved in an organic solvent, then the solvent is removed and the lipid film is dried passing nitrogen gas through the flask. After the addition of an aqueous solution the lipid film is allowed to swell and this leads to the formation of giant vesicles. A modified version of the film hydration is the electroformation [29, 32]. In this case, the hydration of lipids occurs on a conductive glass surface (ITO coated glass) or on platinum wires under the effect of externally applied electric fields. Giant vesicles can be also produced from w/o emulsions (Droplet Transfer method in section 2.2.2), w/o/w double emulsions, micellar lipid solutions, fusion of small vesicles (the most important bulk methods are summarized in Figure 2.2) [29]. GUVs and LUVs (Giant and Large Unilamellar Vesicles) are currently studied in different areas of biomimetic chemistry, biomembrane physics and in the field of artificial cell synthesis [29]. Giant lipid vesicles are simple model systems for studying physico-chemical properties of biological membranes such as lipid domain formation, lipid dynamics, membrane growth, budding, fission and membrane fusion [29, 33–36]. In synthetic biology, a very ambitious project is the synthesis of a minimal cell that has the minimal and sufficient number of components to be considered alive. Generally, the experimental approach consists in utilizing lipid vesicles as cell models, fill them with nucleic acids and enzymes and see if they can support the biochemistry of life [28, 37]. Complex biochemical reactions successfully encapsulated in GUVs are the synthesis of poly(A) from ADP catalysed by polynucleotide phosphorylase [38, 39], the polymerase chain reaction (PCR) [40], the DNA transcription by RNA polymerase [41]. In addition to the synthesis of proteins and nucleic acids that make giant vesicles more similar to living cells, a similar research line consists in inserting parts of the cytoskeleton and membrane proteins. The reconstitution of the sarcoplasmic reticulum Ca^{II} -ATPase and the H^+ -pump bacteriorhodopsin in giant vesicles is one of the first experiments reported [42]. More recently, Altamura *et al.* described the preparation of giant vesicles with photosynthetic reaction centers (RCs) extracted from *Rhodobacter sphaeroides* [43]. The RC embedded in the membrane of the GUVs with an high degree of orientation (orientation favoured by the method of preparation, Figure 2.3 A) is able to convert light into chemical energy, a significative step toward the implementation of photoautotrophic synthetic cells [43, 44]. The spatial distribution of RC was detected labelling the RC with a fluorophore (Figure 2.3 C). The photocycle (scheme in Figure 2.3 B) was monitored using pyranine as pH-sensitive probe (Figure 2.3 D). The kinetics of the proton uptake was followed experimentally and modelled with a deterministic kinetic model [43, 45].

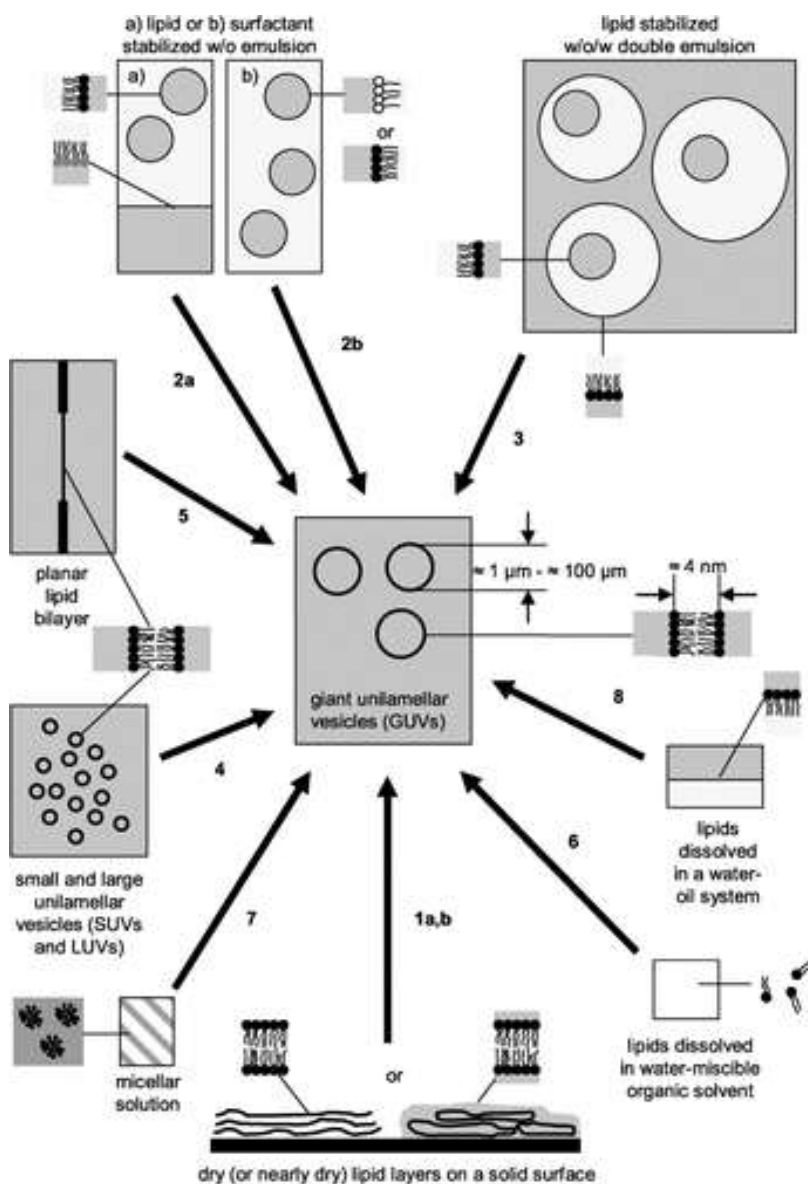


Figure 2.2: Schematic representation of the key concepts of the main methods for the formation of giant unilamellar vesicles (GUVs). Method 1a) Film hydration or spontaneous swelling. Method 1b) electroformation. Method 2a) Transformation of a lipid-stabilized w/o emulsion. Method 2b) Transformation of a surfactant-stabilized w/o emulsion. Method 3) Transformation of a lipid-stabilized w/o/w double emulsion into giant vesicles. Method 4) Giant vesicles formed by the fusion of small or large unilamellar vesicles (SUVs and LUVs). Method 5) Giant vesicles formed by jet-blowing onto an initially planar lipid bilayer kept between two aqueous solutions. Method 6) Giant vesicles formed from lipids dissolved in an organic solvent miscible with water. 7) Giant vesicles formed from micellized bilayer-forming lipids. Method 8) Giant vesicles formed from bilayer-forming lipids that are initially present in a w/o two-phase system. Reproduced with permission from [29]. Copyright ©2010 WILEY-VCH Verlag GmbH & Co. KGaA, Weinheim.

The experiments above-mentioned are just few examples of the achievements reached in the rich branch of synthetic biology, complete reviews on the topics are in refs [28, 29, 37]. From the first protocol for vesicles preparation, described in 1969 by Reeves and Dowben, many steps forward have been done to make the methods of preparation more reproducible and adapt them to the various applications. Currently, electroformation is mainly used for the study of the mechanical properties of the vesicle membrane especially when few vesicles need to be characterized. This method allows a reproducible formation of relatively monodispersed and unilamellar vesicles with a control over the population of vesicles. If one is interested in applying giant vesicles as bioreactors, a method which yields vesicles from an initial w/o emulsion is preferred.

In this chapter, we will build up a *blank* system by confining the urea-urease reaction in pure lipid vesicles with an emulsion transfer method (Section 2.2.2). This *blank* system will serve to understand the dynamical behaviour of the enzymatic reaction when encapsulated in micrometer-sized reactors. A theoretical model was developed to predict the nonlinear dynamics of the confined enzymatic reaction and evaluate the effect of the different transport rates of the chemicals through the semipermeable membrane (results discussed in subsection 2.3.1). Experimentally, several aspects have been investigated, namely: (i) the capability of the reaction precursors and products to cross the phospholipid membranes (subsection 2.3.1); (ii) the effective encapsulation of the enzyme inside the vesicles' lumen (subsection 2.3.1); the optimization of the image acquisition to convert the fluorescence in pH (subsection 2.3.2); (iii) the influence of the dilution factor on the total number of vesicles in the population (subsection 2.3.3); (iv) the dynamical parameters of the clock reaction for different experimental conditions (subsection 2.3.4); (v) The influence of the total number of vesicles on the dynamical behaviour of the population (subsection 2.3.5).

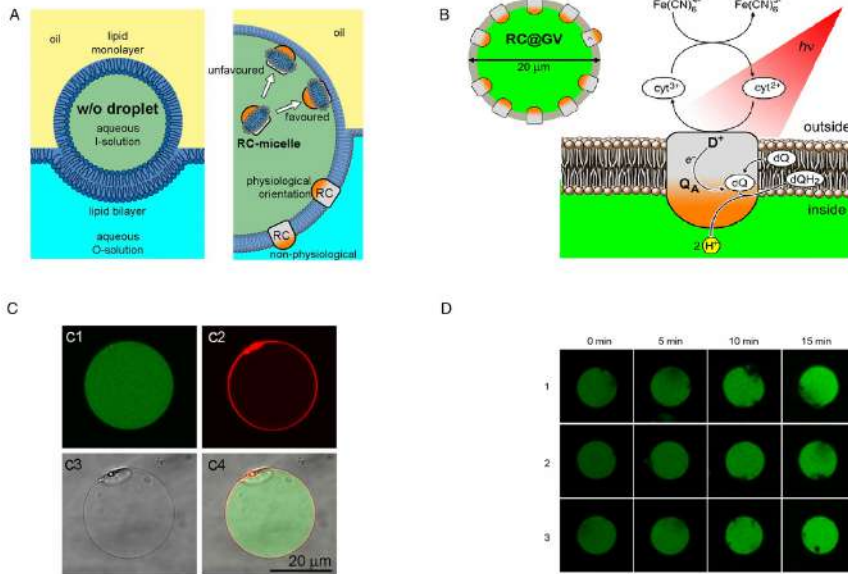


Figure 2.3: A) Water in oil droplets are transferred to an aqueous solution. A detergent-stabilized RC solution (RC micelles) is emulsified in oil, giving w/o droplets. Because RCs present asymmetric distribution of hydrophilic and hydrophobic regions, protein-containing micelles will have a preferential orientation while approaching, and interacting with, the lipid monolayer of the w/o droplet. B) Scheme of RC@GUVs. C1) Green fluorescence channel (calcein). C2) Red fluorescence channel (AE-RC). C3) Bright field. C4) Overlay of the C1, C2 and C3 channels. Reproduced with permission from [43].

2.2 Experimental section

2.2.1 Modelling of the urea-urease reaction

Simulations were carried out with XPPAUT [46] using CVODE as integration method. CVODE is an algorithm for solving ordinary differential equations suitable for stiff problems (an ordinary differential equation problem is stiff if the solution to be found is varying slowly, but there are nearby solutions that vary rapidly, so the numerical method must take small steps to obtain satisfactory results). The total time scale was fixed at 4000 s, while the integration timestep of 0.1 s. The phase diagrams for the two-variable models were built automatically using the routine AUTO of XPPAUT.

2.2.2 Preparation and characterization of Giant Unilamellar Lipid Vesicles (GUVs)

Materials. The following stock solutions were prepared for the urea-urease reaction: urea (Sigma) [urea] = 0.6 M, acetic acid (Sigma) [CH₃COOH] = 0.05 M, urease (type III Jack bean U1500-20KU, Sigma), [urease] = 800.6 U/mL. The urease solution was freshly prepared daily. The enzyme units (expressed as U/mL) were determined from the average urease activity (40318 U/g) provided on the packaging (1U is equivalent to the release of 1.0 μ mol of NH₃ from urea per minute at pH 7 at 25 °C). The chemicals necessary for the vesicles formation are 1-Palmitoyl-2-oleoyl-*sn*-glycero-3-phosphocholine (POPC), mineral oil (MO, a mixture of alkanes from C15 to C40), glucose and sucrose. A stock solution of POPC (Lipoid) [POPC] = 3mM was prepared in Mineral Oil (M5904, Sigma) at room temperature. Stock solutions of glucose and sucrose (Sigma) [glucose] = [sucrose] = 1M were used to adjust the density. Pyranine (Sigma) [pyr] = 0.1mM is the fluorescent probe chosen for monitoring the pH changes. All the reagents were of analytical grade and used without further purification.

Droplet transfer method. Figure 2.2.2 shows the mechanism of the "droplet transfer method". The procedure here described concerns vesicles without the enzymatic reaction. Anyway, the composition of the aqueous and the apolar phases can be changed to insert hydrophilic or hydrophobic fluorescent probes, pH buffers or chemicals to build micro-reactors. A solution of POPC (300 μ L of [POPC]=0.5mM in MO) is added to 500 μ L of an aqueous solution, the so-called outer solution (O-solution), which simply includes water and [glucose]=0.2 M. After few minutes, the interfacial region between the two phases will become saturated with lipids, and forms a monolayer in which the hydrophilic head groups of the lipids are in contact with the lower aqueous phase and the lipophilic chains are directed towards the apolar phase (Figure 2.4 step 1). Subsequently, an aqueous solution (20 μ L of inner solution, I-solution), is prepared containing [sucrose] = 0.2 M and pyranine (50 μ m). After the addition of 600 μ L of [POPC] = 0.5mM in MO, a lipid-stabilized water-in-oil emulsion (Figure 2.4 step 2) is prepared by pipetting for 20 times the solution with a P1000 micropipettor set at 500 μ L. The water in oil emulsion is poured above the oil water-interface prepared in the first step. I- and O-solutions are isotonic, but their densities are different, $\rho_{\text{sucrose}} \sim 1.24 \text{ g cm}^{-3}$, $\rho_{\text{glucose}} \sim 1.12 \text{ g cm}^{-3}$. Thus, the emulsion droplets, being denser than oil and denser than O-solution, spontaneously move across the interface, reaching the O-solution. While crossing the interface, a second POPC layer surrounds the droplets forming a bilayer. The transfer is very slow by gravity, it is facilitated by centrifuging the system for 10 minutes at 6000 rpm. About the 30% of the droplets are generally transformed in vesicles (Figure 2.4 step 3). After centrifuging, the supernatant is poured off and the pellet formed is washed with 200 μ L of O-solution to remove the excess solutes. Then, the pellet is recovered

with a micropipettor P1000 loaded at 30 μL and diluted with O-solution. A volume of 20 μL is taken, deposited in a chamber slide (microscope glass slide + 0.4 mm of rubber silicon layer + cover slip, Figure 2.5) and observed with an optical microscope. In the kinetic runs, the chamber slide was created after mixing the volume of 20 μL with 10 μL of a solution containing acetic acid, glucose and urea and the reaction was studied for a period of maximum two hours.

Instruments and softwares. The images reported in this chapter were acquired with an upright Leica TCS SP8 Confocal Microscope (SCARAB laboratory in Chemical and Biological Engineering, University of Sheffield) using a 20x objective and a photomultiplier tubes detector (PMT) for the fluorescence. For the pH calibration, the fluorescent probe, pyranine was excited at two different wavelengths: $\lambda_{x1} = 458$ nm with an Argon laser and $\lambda_{x2} = 405$ with an UV laser. A sequential scan between frames was performed with a scan speed of 400 Hz and a line average of 8. The images were collected keeping the same laser gain, the zoom and the pinhole in both channels. The settings used for the two excitation wavelengths were: 1024×1024 pixels ($406.47 \mu\text{m} \times 406.47 \mu\text{m}$), Smart gain = 860.2 V, Smart Offset = -0.8%, Zoom = 1.43 (objective zoom 20 \times), Pinhole = 1.00 Airy units. The laser power for the UV channel was 9%, the Argon laser had an initial main power of 27 %, while the power of the 458 nm line was 20.3%. The emission range analyzed was $\Delta\lambda_{e1} = \Delta\lambda_{e2} = 485 - 535$ nm.

The same settings were applied for the kinetic runs fixing a time sampling of 1 frame per 42 s for each channel. For the estimation of the number of vesicles, the format of the images was reduced from 1024×1024 pixels to 512×512 pixels ($581.25 \mu\text{m} \times 581.25 \mu\text{m}$) and the Zoom from 1.43 to 1.00.

The analysis of the images was performed with Matlab codes (Matlab R2017b) developed depending on the nature of the experiment [47].

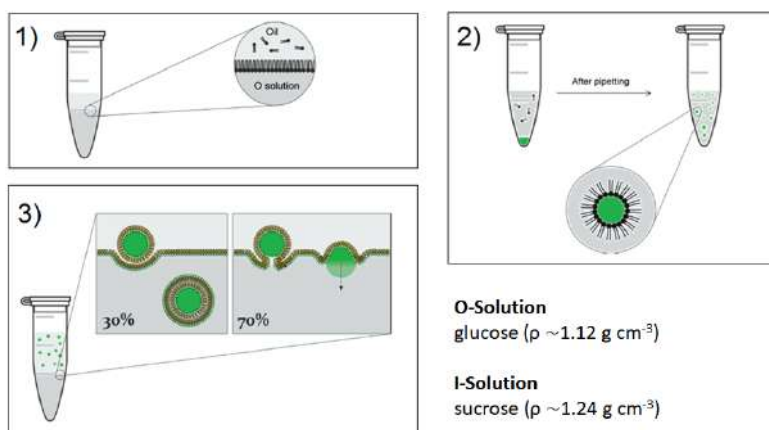


Figure 2.4: 1) Preparation of an oil over O-solution system with POPC at the interface. 2) Preparation of a water-in-oil emulsion with mineral oil, POPC and the I-solution. 3) The emulsion droplets are inserted in this system and sink down due to the density difference between the I- and O-solution. About 30 % of droplets become vesicles. Adapted from [48].

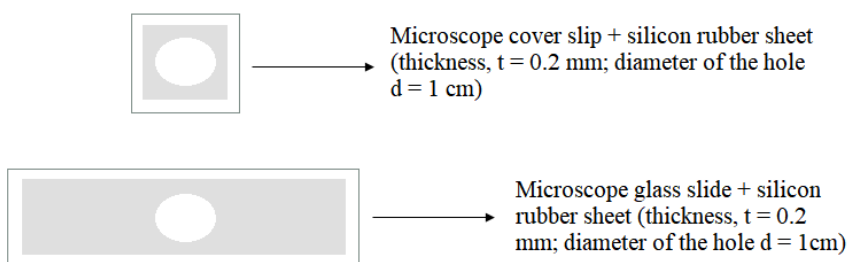


Figure 2.5: Chamber slide used for the experiment. A rubber silicon layer of 0.2 mm is cut and put over a glass slide. A hole is created in the center of the layer. Another rubber silicon layer of 0.2 mm is cut, holed and put over a cover slip. The chamber is created when the cover slip is put over the glass slide with a thickness of 0.4 mm suitable for the working distance of the upright microscope.

2.3 Results

2.3.1 Preliminary results

The experimental investigation of the confined urea-urease reaction was preceded by a theoretical study based on the development of a deterministic kinetic model. In a two-variable model, proposed by Taylor's group [13], the following behaviours were found in a single micro-compartment fed with urea and protons

at different transport rates k_H and k_S : low steady states (no reaction, low pH), high steady states (pH clock reactions), oscillations (the intermediate species display periodical variations of concentrations) and bistability (coexistence of two steady states for the same values of the parameters).

Here, starting from the two-variable model, a more complex model was built taking into account all the species involved in the reaction, including the pH probe, and the transport rates of proton (k_H), urea (k_S) and ammonia (k_N) were varied according to the permeability values for lipid vesicles reported in literature (equilibria in Figure 2.6a and b). Low steady states, high states and oscillations are still possible as expected from the two-variable model (Figure 2.6c and d), however the oscillations are damped (the amplitude decreases over time) rather than sustained and the ratio between ammonium and the ammonia permeability mostly affects the final pH (Figure 2.7 b) and d) and the total number of oscillations (Figure 2.7 a and c) [49].

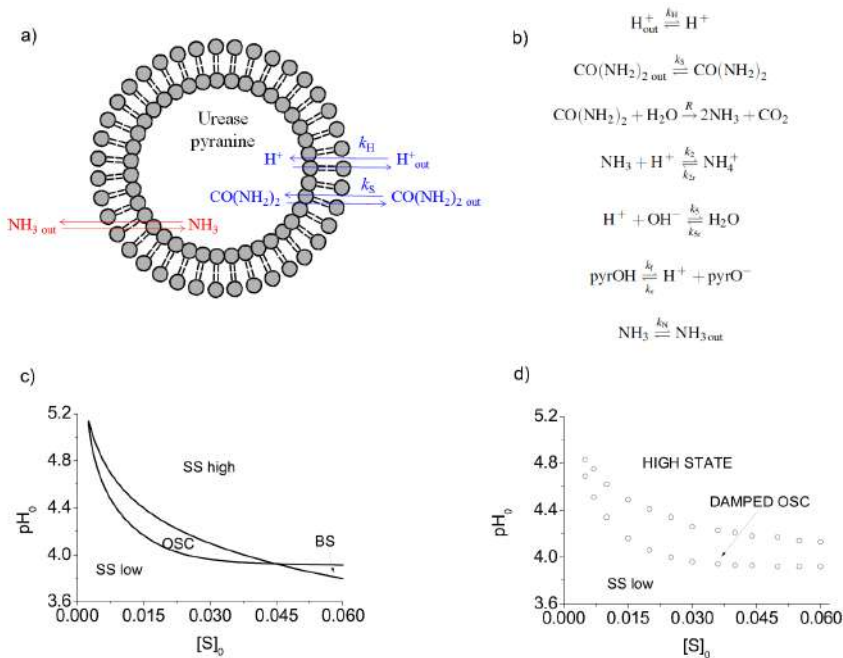


Figure 2.6: a) Lipid vesicle containing the urea-urease reaction and the fluorescent probe. k_H = exchange rate of the acid, k_S = exchange rate of the urea, k_N = exchange rate of the product ammonia with the external solution of concentrations $[H^+]_{out}$, $[S]_{out}$ and $[NH_3]_{out}$. b) Equilibria considered in the full model. c) Phase diagram derived from the two-variable model for $E=1300$ U/mL, $k_S = 0.0147$ s $^{-1}$, $k_H = 10.9$ s $^{-1}$. d) Phase diagram derived from the full model for $E=1300$ U/mL, $k_S = 0.0147$ s $^{-1}$, $k_H = 10.9$ s $^{-1}$, $k_N = 10.8$ s $^{-1}$. Reproduced from [49].

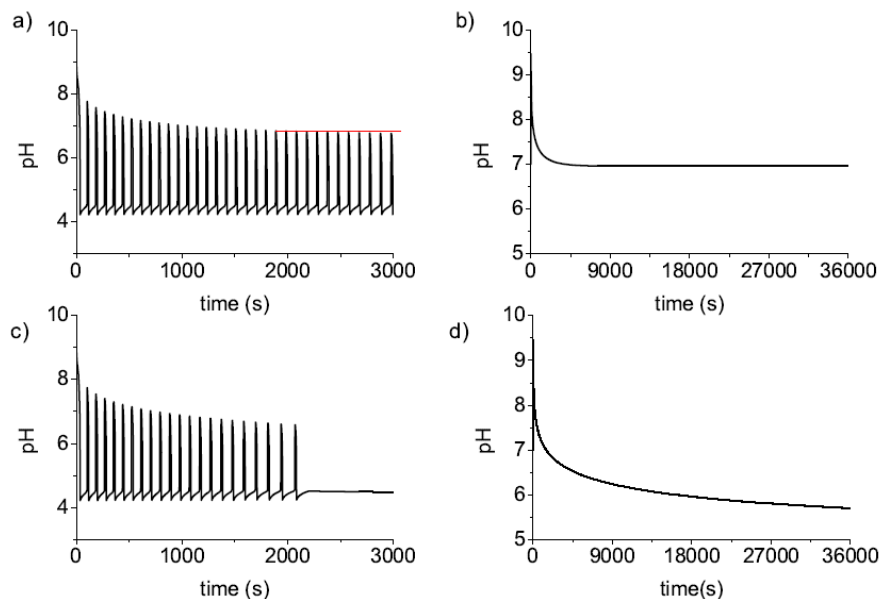


Figure 2.7: Addition of the equilibrium $\text{NH}_4^+ \xrightleftharpoons{k_{\text{NH}}} \text{NH}_{4\text{out}}^+$. Simulated time series for $[\text{S}]_0=0.024 \text{ M}$, $k_{\text{S}} = 0.0147 \text{ s}^{-1}$, $k_{\text{H}} = 10.9 \text{ s}^{-1}$, $k_{\text{N}} = 1.08 \text{ s}^{-1}$, a) $k_{\text{NH}} = 6 \times 10^{-4} \text{ s}^{-1}$, $\text{pH}_0=4.18$, $E=500 \text{ U/mL}$. b) $k_{\text{NH}} = 6 \times 10^{-4} \text{ s}^{-1}$, $\text{pH}_0=4.2$, $E=450 \text{ U/mL}$. c) $k_{\text{NH}} = 6 \times 10^{-8} \text{ s}^{-1}$, $\text{pH}_0=4.18$, $E=500 \text{ U/mL}$. d) $k_{\text{NH}} = 6 \times 10^{-8} \text{ s}^{-1}$, $\text{pH}_0=4.2$, $E=450 \text{ U/mL}$. Reproduced from [49].

Experimentally, we encapsulated the enzyme in giant lipid vesicles produced with the Droplet transfer method (Section 2.2.2), then we dispersed the vesicles in a solution containing urea and demonstrated the permeation of the substrate across the membrane from the increased intensity of the fluorescence over time (Figure 2.8)[50]. Moreover, we showed that the addition of a neutral aqueous solution to vesicles containing ammonia leads ammonia to cross the membrane to dissipate the concentration gradient. After these experiments designed to prove the flow of the substrate and of certain products across the vesicles' membrane, some clock experiments were performed using sulphuric acid to tune the pH of the solution. Successively, the sulphuric acid was replaced with the more biocompatible acetic acid. A systematic investigation of the clock behaviour has been carried out by varying the initial concentration of acetic acid, keeping urea and urease concentrations constant (section 2.3.4) and changing the number of vesicles by a different dilution of the solution (section 2.3.5).

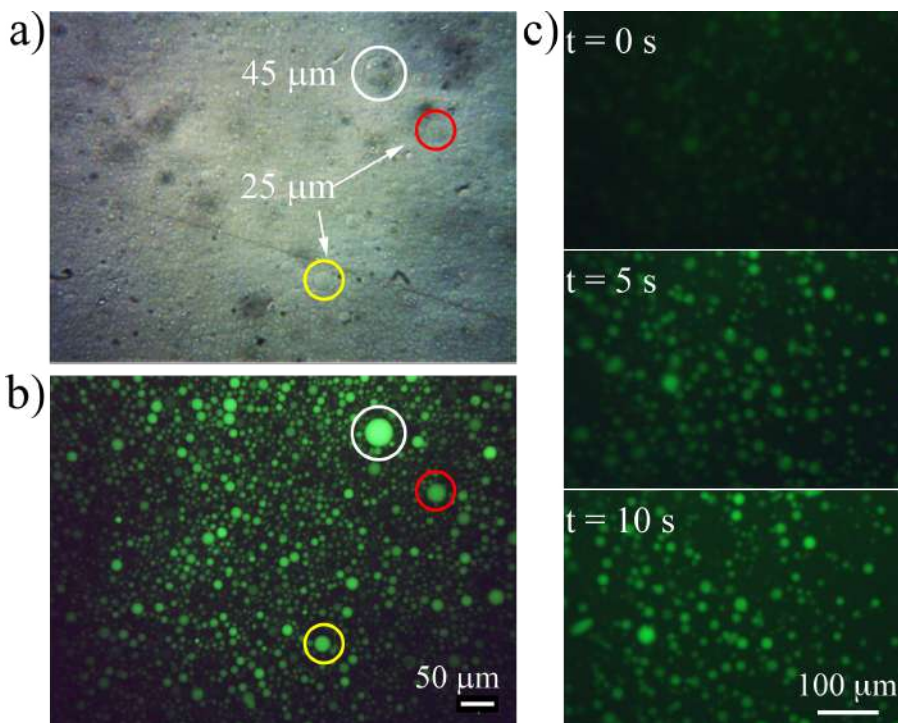


Figure 2.8: a) Bright field view of a sample of vesicles containing $[\text{urease}] = 10.3$ U/mL and $[\text{pyranine}] = 50 \mu\text{M}$. b) Fluorescence imaging of the sample of vesicles depicted in panel a). illumination at $\lambda = 488$ nm. c) Fluorescence intensity of the vesicles when immersed in a solution containing $[\text{urea}]_{\text{out}} = 3 \times 10^{-3}$ M. Reproduced from [50].

2.3.2 pH calibration with ratiometric imaging

A calibration procedure is necessary to relate the fluorescence intensity of pyranine with the pH of the solution[51]. The intensity of fluorescence was measured exciting the probe with two different excitation wavelengths (the equilibria of the probe are shown in Figure 2.9, the fluorescence emission spectra in Figure 2.10): $\lambda_{x1} = 458$ nm was used to excite the deprotonated form of the indicator (pyrO^-), while $\lambda_{x2} = 405$ nm excites mainly the protonated form of pyranine (pyrOH). The main advantage of the ratiometric imaging is the reduction of errors and artifacts: indeed, the ratio between the two intensities ($F(\lambda_{x1})/F(\lambda_{x2})$) is independent of the concentration of the probe, photobleaching, fluctuations of the source intensity and sensitivity of the instrument [52]. Lipid vesicles with different pH buffer solutions were prepared to obtain a pH calibration curve. The range of pH between 4.6 and 8.2 was covered with a citrate-phosphate buffer, pH 9.26 and 10.06 with an ammonia/ammonium buffer. The total concentration of the ions inside the vesicles was $[\text{HPO}_4^{2-}] + [\text{citric acid}] \sim 0.0015$ M and $[\text{NH}_4^+] + [\text{NH}_3] \sim 0.002$ M.

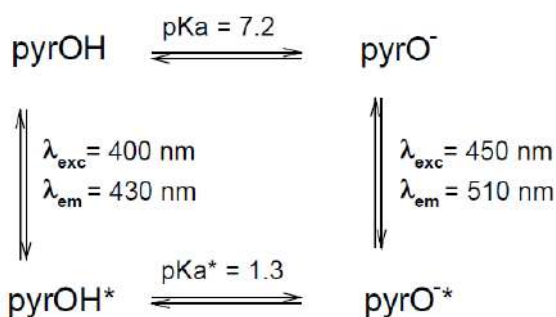


Figure 2.9: Scheme of the equilibria of pyranine in ground and excited states. Absorption and emission maxima wavelength are also indicated. Adapted from [53], licensed under Creative Commons Attribution.

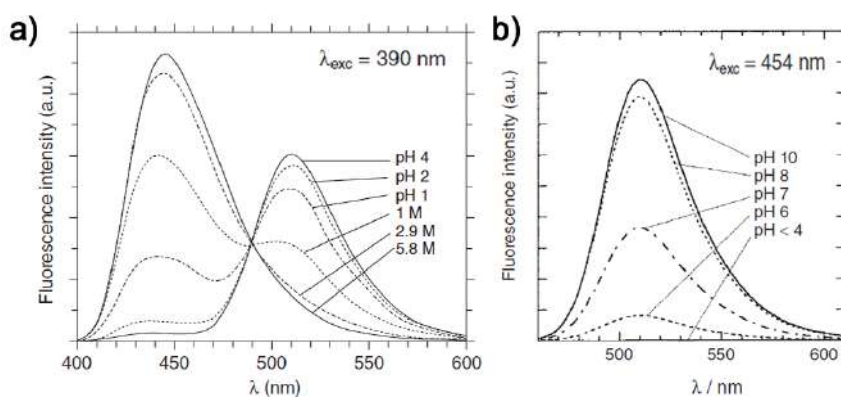


Figure 2.10: a) pH dependence of emission spectra of pyranine in very acidic media ($\lambda_{\text{x}1} = 390 \text{ nm}$). b) pH dependence of emission spectra of pyranine at $\lambda_{\text{x}1} = 454 \text{ nm}$. Reproduced from [52].

To extract data from images and correlate intensities with pH, a Matlab code (Appendix A.1) was used to detect the vesicles, measure the fluorescence as the mean gray value and generate a distribution in size. For each pH, an average ratio was calculated from the intensity ratios of all the vesicles detected in a frame. Here, it follows an example of the analysis performed at pH 7 (Figure 2.11 shows the vesicles detection and the size distribution, in Figure 2.12 the absolute intensities and the ratios are plotted for each vesicle).

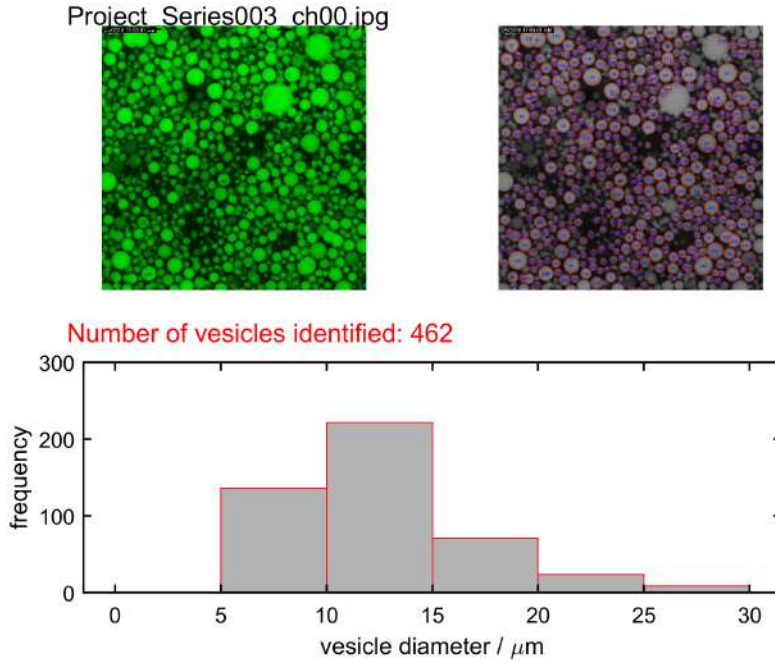


Figure 2.11: top) Original image with UV laser (left) and the grayscale image with the vesicles detected (right); bottom) Vesicles size distribution.

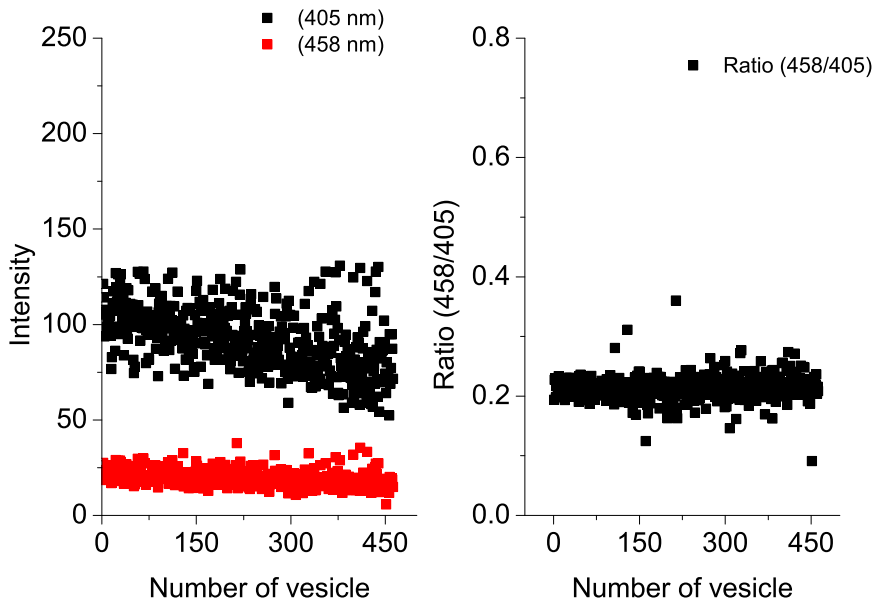


Figure 2.12: left) Fluorescence intensity for each vesicle detected at two different excitation wavelengths; right) Ratio $F(458\text{ nm})/F(405\text{ nm})$.

The intensity ratios at different pH values were fitted in Matlab with the equation [54, 55] (Appendix A.4 for the demonstration of the formula)

$$R [1 : 2] = R_0 [1 : 2] \times \left(\frac{R_f [1 : 2] + 10^{n(\text{p}K' - \text{pH})}}{1 + 10^{n(\text{p}K' - \text{pH})}} \right) \quad (2.1)$$

where

$$R [1 : 2] = \frac{F(\lambda_{x1}, \Delta\lambda_{e1})}{F(\lambda_{x2}, \Delta\lambda_{e2})}, \quad (2.2)$$

$$R_0 [1 : 2] = \frac{F_0(\lambda_{x1}, \Delta\lambda_{e1})}{F_0(\lambda_{x2}, \Delta\lambda_{e2})}, \quad (2.3)$$

$$R_f [1 : 2] = \frac{F_\infty(\lambda_{x1}, \Delta\lambda_{e1})}{F_0(\lambda_{x1}, \Delta\lambda_{e1})} \frac{F_0(\lambda_{x2}, \Delta\lambda_{e2})}{F_\infty(\lambda_{x2}, \Delta\lambda_{e2})} \quad (2.4)$$

and

$$\text{p}K' = \text{p}K - \log_{10} \frac{F_\infty(\lambda_{x2}, \Delta\lambda_{e2})}{F_0(\lambda_{x2}, \Delta\lambda_{e2})} \quad (2.5)$$

The parameters F_0 and F_∞ represent the intensities respectively at the lower asymptote (acidic pH) and at the higher asymptote (basic pH), $\text{p}K'$ is the apparent $\text{p}K$ that depends also on the instrumental settings, n is the Hill number that takes into account the degree of protonation, in the case of pyranine $n = 1$. Using the following initial guess values: $R_0 [1 : 2] = 0.002$, $R_f [1 : 2] = 1092$ and $\text{p}K' = 8$, the parameters estimated with the nonlinear regression model are: $R_0 [1 : 2] = 0.036$, $R_f [1 : 2] = 63.35$ and $\text{p}K' = 8.03$ with an Adjusted R-Squared of 0.957.

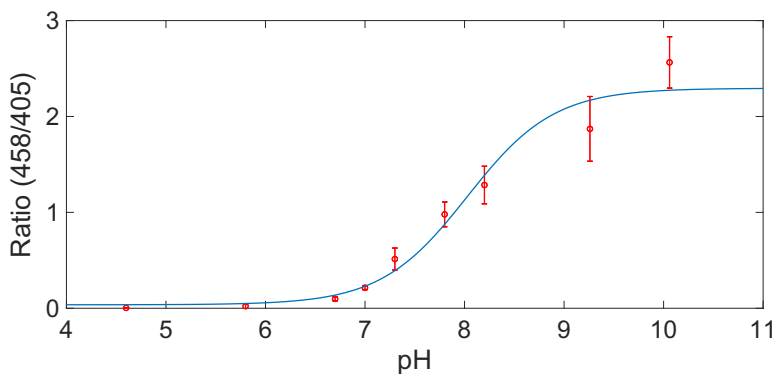


Figure 2.13: Dependence of the intensity ratio on pH for vesicles containing pyranine 50 μM .

2.3.3 Number of vesicles

The urea-urease hydrolysis products, especially NH_3 , are free to cross the phospholipid membrane, thus influencing the reaction dynamics of each single microreactor. Therefore, the total number of vesicles in the specimen is extremely important for tuning the communication among the population of single liposomes and, ultimately, to determine the global behaviour of the population itself.

The number of vesicles was estimated using the Tile scan acquisition mode of the confocal microscope: this option enables to scan multiple partial images from a specimen and stitch them together to form a complete image. The number of vesicles was evaluated for different dilutions of pellet, $30 \mu\text{L}$ of pellet + $x \mu\text{L}$ of outer solution where $x = 20, 70, 120, 170, 220$ and $270 \mu\text{L}$ corresponding respectively to the dilution factors ($\text{DF} = \text{Total volume} / \text{Volume of pellet}$) 1.7, 3.3, 5.0, 6.7, 8.3, 10 and different acetic acid concentrations ($[\text{CH}_3\text{COOH}] = 2.5 \times 10^{-3} \text{ M}$, $[\text{CH}_3\text{COOH}] = 1 \times 10^{-3} \text{ M}$, $[\text{CH}_3\text{COOH}] = 5 \times 10^{-3} \text{ M}$, $[\text{CH}_3\text{COOH}] = 7.5 \times 10^{-3} \text{ M}$, $[\text{urea}] = 0.08 \text{ M}$, $[\text{enzyme}] = 80.6 \text{ U/mL}$).

The single images for the different x and y positions were analyzed with a Matlab Code (Appendix A.2) and the total number of vesicles was calculated from the sum of the vesicles detected in each frame. The complete image obtained by merging the different frames shows the number and distribution of the vesicles in the microscope chamber. As an example, Figure 2.14 reports the vesicles captured in the presence of $[\text{CH}_3\text{COOH}] = 7.5 \times 10^{-3} \text{ M}$ and at a dilution factor $\text{DF} = 1.7$.

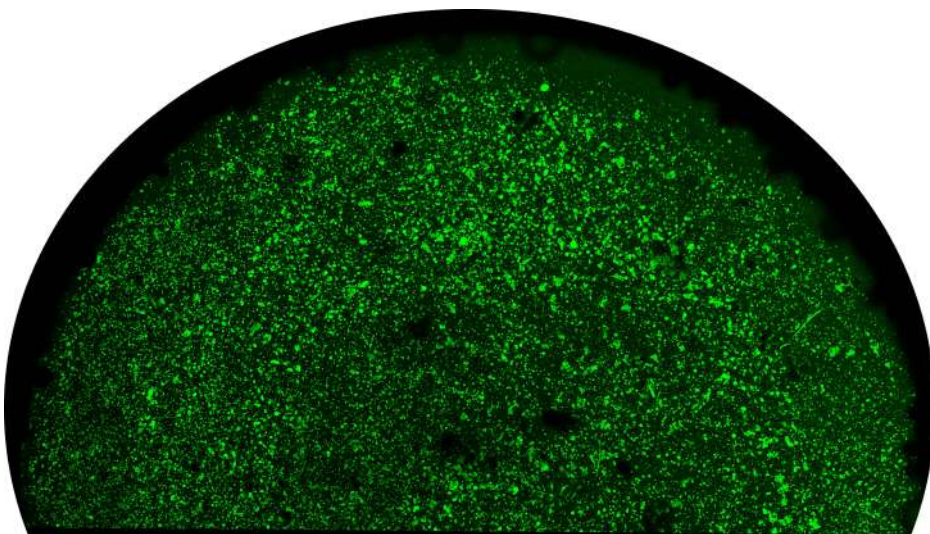


Figure 2.14: Vesicles at dilution factor $\text{DF} = 1.7$ and $[\text{CH}_3\text{COOH}] = 7.5 \times 10^{-3} \text{ M}$.

The number of vesicles was found to change with the dilution of pellet, as shown by the histogram in Figure 2.15, but it is not significantly influenced by the concentration of acetic acid, for $[\text{CH}_3\text{COOH}] = 1 \times 10^{-3}$ M the number of vesicles is ~ 22000 , for $[\text{CH}_3\text{COOH}] = 5 \times 10^{-3}$ M the number of vesicles is ~ 17000 , for $[\text{CH}_3\text{COOH}] = 7.5 \times 10^{-3}$ M the number of vesicles is ~ 19000 .

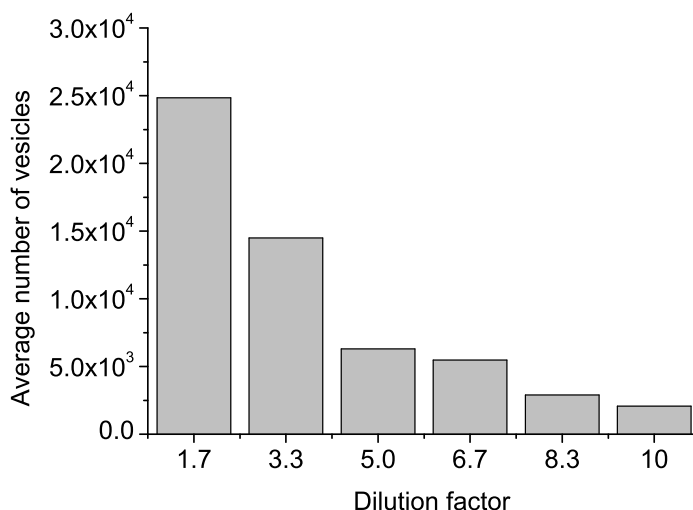


Figure 2.15: Number of vesicles in 20 μL of sample vs dilutions factors. $[\text{CH}_3\text{COOH}] = 2.5 \times 10^{-3}$ M, $[\text{urea}] = 0.08$ M, $[\text{enzyme}] = 80.6$ U/mL.

2.3.4 Clock reactions as a function of acetic acid concentration

In order to characterise the dynamical behaviour of the vesicles' population in different experimental conditions, the concentration of acetic acid was varied in the range $1 \times 10^{-3} - 7.5 \times 10^{-3}$ M, keeping constant the concentrations of urea and enzyme ($[\text{urea}] = 0.08$ M and $[\text{enzyme}] = 80.6$ U/mL) and the dilution factor 1.7. The fluorescence intensity ratio at the two excitation wavelengths ($R[1:2]$) was calculated for eight vesicles in each experimental run by using a particle tracking code that measures the intensity vs time taking into account slight variations of the spatial coordinates of the vesicles (see Appendix A.3 for the Matlab code). The induction period was calculated from the center of the sigmoid that corresponds to the half conversion ($\frac{y_{\max} + y_{\min}}{2}$), the pH reached at the end of each experiment was calculated using the equation 2.6, that is the inverse function of eq. 2.1:

$$\text{pH} = \text{p}K' - \log \left(\frac{R_0[1:2]R_f[1:2] - R[1:2]}{R[1:2] - R_0[1:2]} \right) \quad (2.6)$$

As an example of data treatment, the representative steps and results of

the analysis are reported for two experimental conditions: $[\text{CH}_3\text{COOH}] = 1 \times 10^{-3} \text{ M}$, $[\text{urea}] = 0.08 \text{ M}$, $[\text{enzyme}] = 80 \text{ U/mL}$ (Figure 2.16) and $[\text{CH}_3\text{COOH}] = 5 \times 10^{-3} \text{ M}$, $[\text{urea}] = 0.08 \text{ M}$ and $[\text{enzyme}] = 80 \text{ U/mL}$ (Figure 2.17). Figure 2.16 a) and Figure 2.17 a) show the results of the vesicles recognition and labelling procedure; Figure 2.16 b) and Figure 2.17 b) report the evolution of the fluorescence of eight single vesicles with respect to time, $t = 0$ is the time at which urea is delivered to the vesicles' population; Figure 2.16 c) and Figure 2.17 c) report the induction period of the eight vesicles, Figure 2.16 d) and Figure 2.17 d) the corresponding final pH.

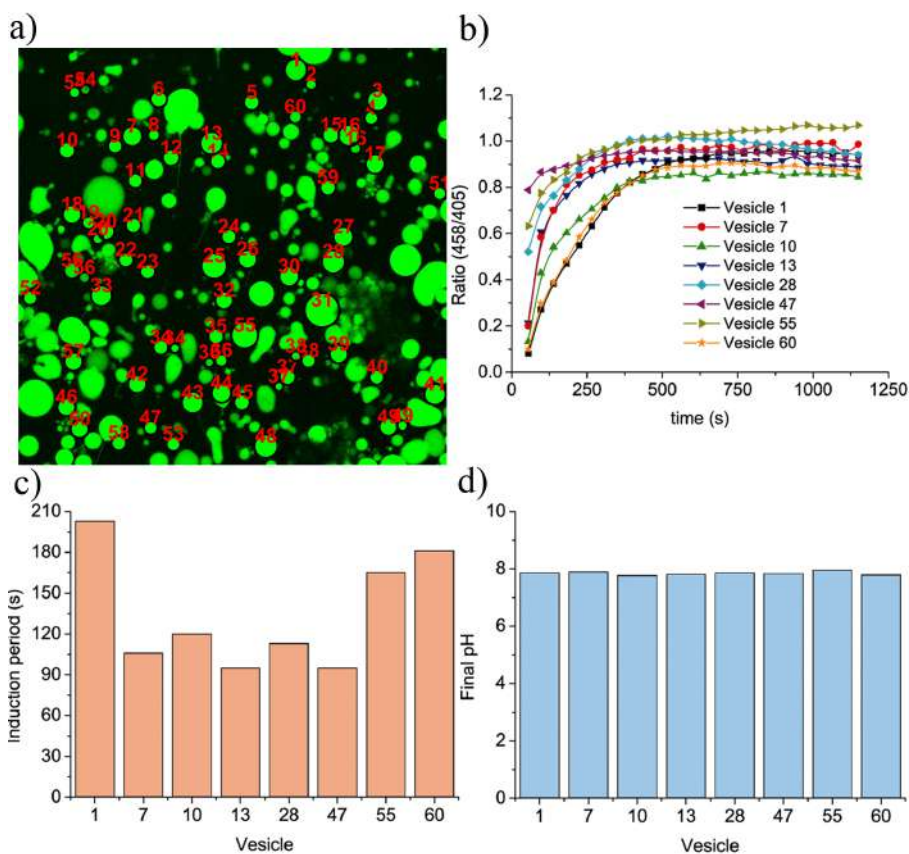


Figure 2.16: $[\text{CH}_3\text{COOH}] = 1 \times 10^{-3} \text{ M}$, $[\text{urea}] = 0.08 \text{ M}$, $[\text{enzyme}] = 80 \text{ U/mL}$. a) Vesicles detected with the particle tracking code. The red number indicates the number of the vesicle. Image in the UV channel. b) Time series for the vesicles 1, 7, 10, 13, 28, 47, 55, 60. c) Induction period for the vesicles 1, 7, 10, 13, 28, 47, 55, 60. d) Final pH for the vesicles 1, 7, 10, 13, 28, 47, 55, 60.

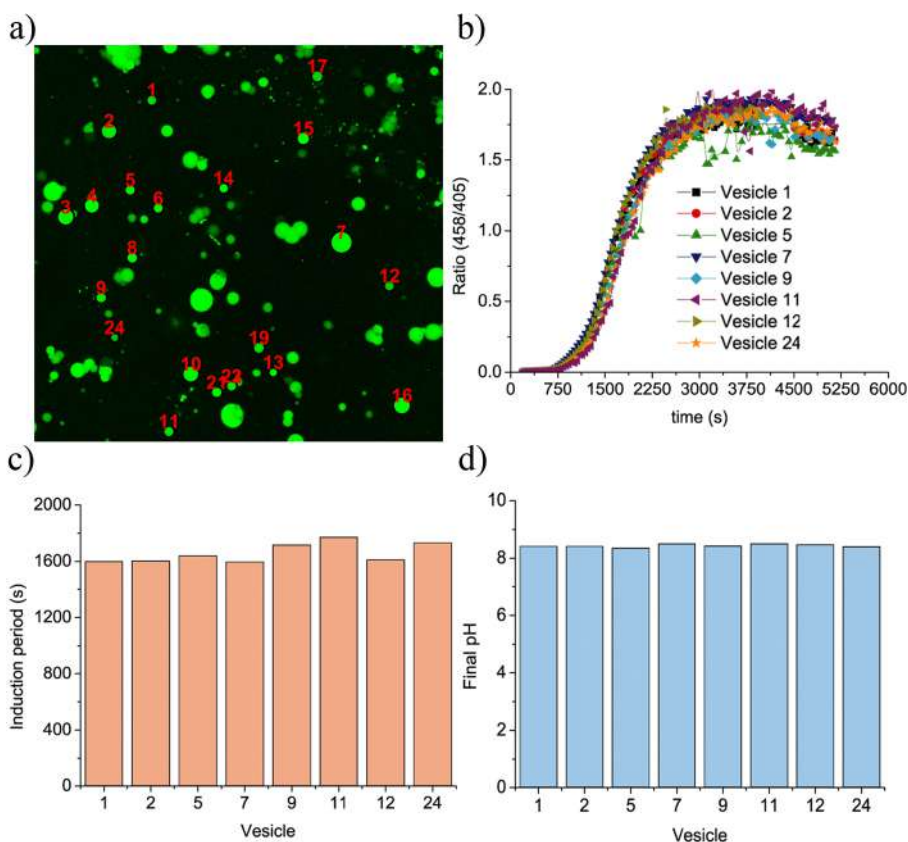


Figure 2.17: $[\text{CH}_3\text{COOH}] = 5 \times 10^{-3} \text{ M}$, $[\text{urea}] = 0.08 \text{ M}$, $[\text{enzyme}] = 80 \text{ U/mL}$. a) Vesicles detected with the particle tracking code. The red number indicates the number of the vesicle. Image in the UV channel. b) Time series for the vesicles 1, 2, 5, 7, 9, 11, 12, 24. c) Induction period for the vesicles 1, 2, 5, 7, 9, 11, 12, 24. d) Final pH for the vesicles 1, 2, 5, 7, 9, 11, 12, 24.

An average induction period was calculated from all the vesicles analyzed at the four different concentrations of acetic acid (each concentration was repeated at least three times). The induction period increases in an exponential fashion with the concentration of acetic acid that slows down the enzyme activity (Figure 2.18).

In the experiments with low concentrations of acetic acid (in particular $[\text{CH}_3\text{COOH}] = 1 \times 10^{-3} \text{ M}$, $[\text{CH}_3\text{COOH}] = 2.5 \times 10^{-3} \text{ M}$), a sort of "chemical wave" appears, the induction period depends on the position of the vesicles and on the presence of other vesicles nearby (see Figure 2.19). Chemical waves are spatial variations of chemical concentrations propagating in a medium [56]. This form of spatial organisation can occur when a chemical reaction, with an autocatalytic step in its reaction mechanism, is coupled with transport phenomena like molecular diffusion [57].

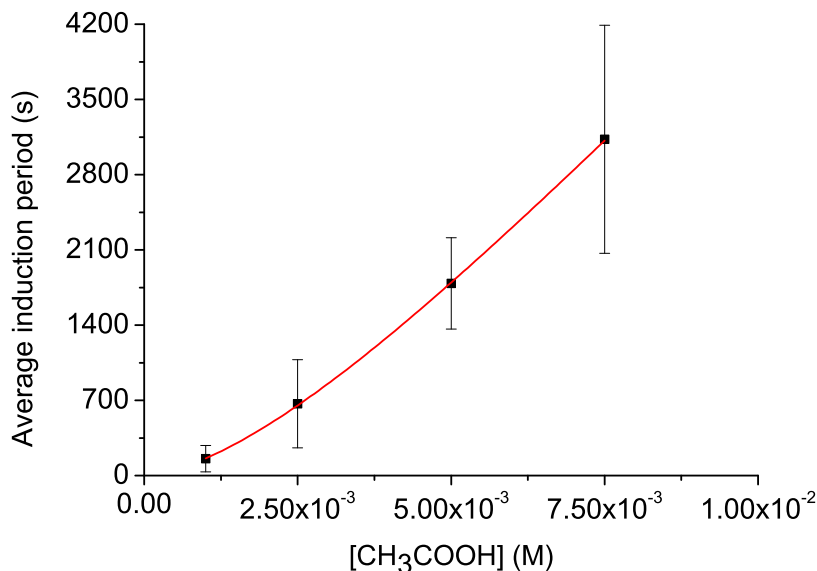


Figure 2.18: Average induction period for the concentrations: $[\text{CH}_3\text{COOH}] = 1 \times 10^{-3}$ M, $[\text{CH}_3\text{COOH}] = 2.5 \times 10^{-3}$ M, $[\text{CH}_3\text{COOH}] = 5 \times 10^{-3}$ M, $[\text{CH}_3\text{COOH}] = 7.5 \times 10^{-3}$ M. Red curve: exponential trend line.

The chemical waves start from an isolated point (called pacemaker) and propagate with constant speed and constant concentration profile [58]. The first example of chemical waves propagating inside or among different liposomes was found with the Belousov-Zhabotinsky (BZ) oscillating reaction [59]. BZ reaction has a scarce biomimetic character, due to the presence of sulfuric acid and the harsh redox chemistry, however, it is commonly studied even from biologists as a paradigmatic model for understanding phenomena like oscillations [58, 60], chemical waves [61, 62] and chaos [63, 64]. In liposomes loaded with the BZ reaction, the chemical waves were due to the diffusion of the autocatalytic species, HBrO_2 , that acts as a messenger for transmitting chemical information [59]. In the urea-urease reaction, the chemical waves are likely generated by the positive feedback of ammonia which is produced inside the lumen of the vesicles and it is free to spread in the reaction medium. The ammonia, generated in the early stage of the urea-urease reaction, quickly diffuses through the semipermeable membrane and increases the initial pH of the neighbouring vesicles. The chemical diffusion of ammonia is translated in an optical effect: the vesicles turn on (increase of brightness for the raise of pH) in different moments (the variability of the half conversion point is evident in the histogram of Figure 2.16 c). Usually the pacemaker points arise from local heterogeneities, for the vesicles the pacemaker points are generally located at the border of the chamber slide, where the zero-flux boundary condition and a lower vesicles'

density causes a different reactivity compared to the central vesicles, as it was also pointed out in the simulations of the urea-urease reaction in a group of hexagonally packed enzyme beads [65].

For higher concentrations of acetic acid $[\text{CH}_3\text{COOH}] = 5 \times 10^{-3} \text{ M}$, $[\text{CH}_3\text{COOH}] = 7.5 \times 10^{-3} \text{ M}$, the effect of "chemical wave" is negligible: the kinetic plots and the histograms of Figure 2.17 show how the induction period is roughly the same for the different vesicles. In this case, the pH of the vesicles depends mainly on the concentrations of urea and acetic acid and their permeabilities. High concentrations of acetic acid decrease the enzyme activity, ammonia is produced slowly and its diffusion in the surroundings does not influence the local kinetics inside single vesicles.

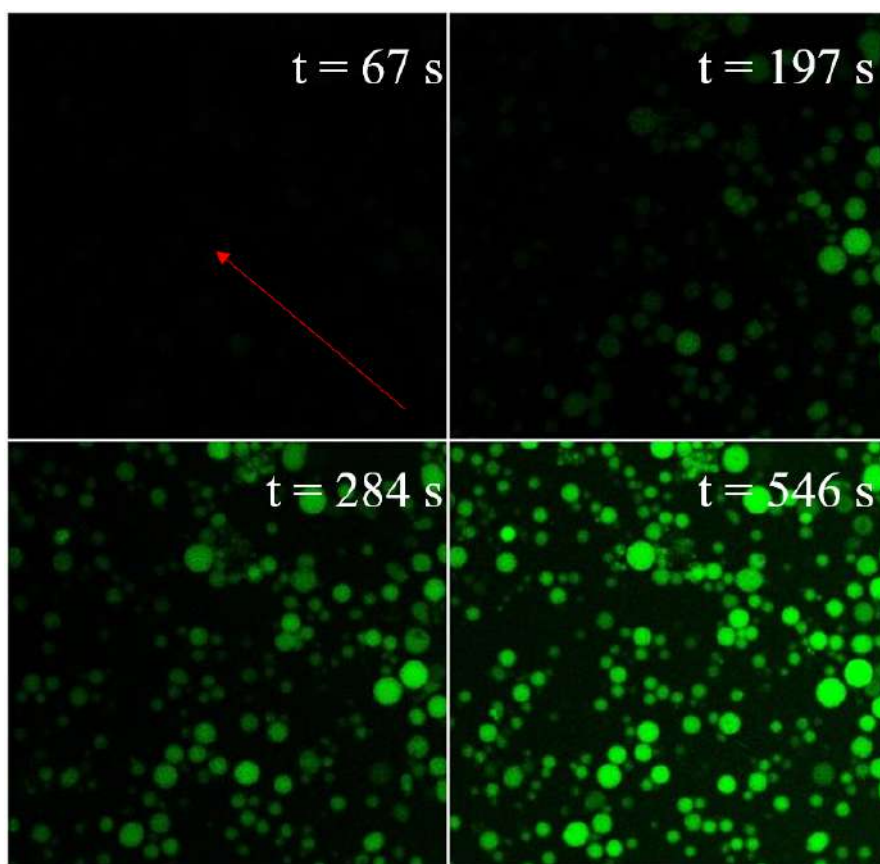


Figure 2.19: Confocal images at different time intervals at the excitation wavelength $\lambda_{x1} = 458 \text{ nm}$ ($[\text{CH}_3\text{COOH}] = 2.5 \times 10^{-3} \text{ M}$, $[\text{urea}] = 0.08 \text{ M}$, $[\text{enzyme}] = 60 \text{ U/mL}$), the red arrow shows the direction of the chemical wave.

While the induction period depends on the distribution of the vesicles and on the acetic acid concentration, the final pH is constant (above 8) for each vesicle detected in a frame and for the different concentrations of acetic acid tested as shown from Figure 2.20. The behaviours predicted from the model of the urea-urease reaction and here recalled are: low steady states, high steady states, oscillations and bistability (section 2.3.1). The four experimental conditions investigated fall in the region of high steady states and the change of the acetic acid concentration affects the clock time and the time to attain the high steady state, without changing the global dynamical behavior of the vesicles' population.

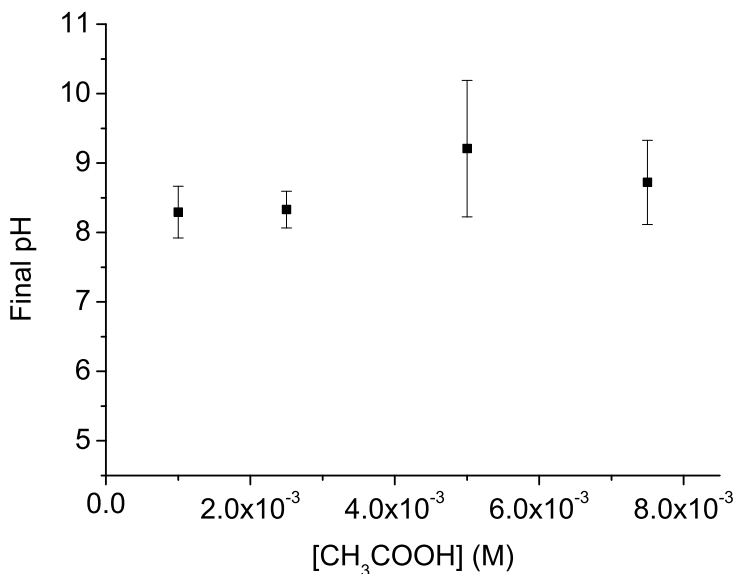


Figure 2.20: Average final pH for the concentrations: $[\text{CH}_3\text{COOH}] = 1 \times 10^{-3}$ M, $[\text{CH}_3\text{COOH}] = 2.5 \times 10^{-3}$ M, $[\text{CH}_3\text{COOH}] = 5 \times 10^{-3}$ M, $[\text{CH}_3\text{COOH}] = 7.5 \times 10^{-3}$ M.

2.3.5 Clock reactions as a function of the number of vesicles

The enzymatic reaction was studied for different dilutions of the pellet to verify the impact of the number of vesicles on the global dynamics. 30 μL of pellet were diluted with x μL of outer solution where $x = 20, 70, 120, 170, 220$ and 270 μL , corresponding respectively to the dilution factors 1.7, 3.3, 5.0, 6.7, 8.3, 10. For each dilution, 20 μL were mixed with 10 μL of a solution containing urea, acetic acid and glucose and studied for a period of maximum two hours as for the kinetics run of the previous section. The concentrations of the chemical species after mixing were $[\text{CH}_3\text{COOH}] = 2.5 \times 10^{-3}$ M, $[\text{urea}] = 0.08$ M and $[\text{enzyme}] = 80$ U/mL. As an example, the representative steps and results of the analysis are reported for two dilution factors: 5.0 (Figure 2.21) and 6.7

(Figure 2.22). Figure 2.21 a) and Figure 2.22 a) show the results of the vesicles recognition and labelling procedure; Figure 2.21 b) and Figure 2.22 b) report the evolution of the fluorescence of eight single vesicles with respect to time, $t = 0$ is the time at which urea is delivered to the vesicles' population; Figure 2.21 c) and Figure 2.22 c) report the induction period of the eight vesicles, Figure 2.21 d) and Figure 2.22 d) the corresponding final pH.

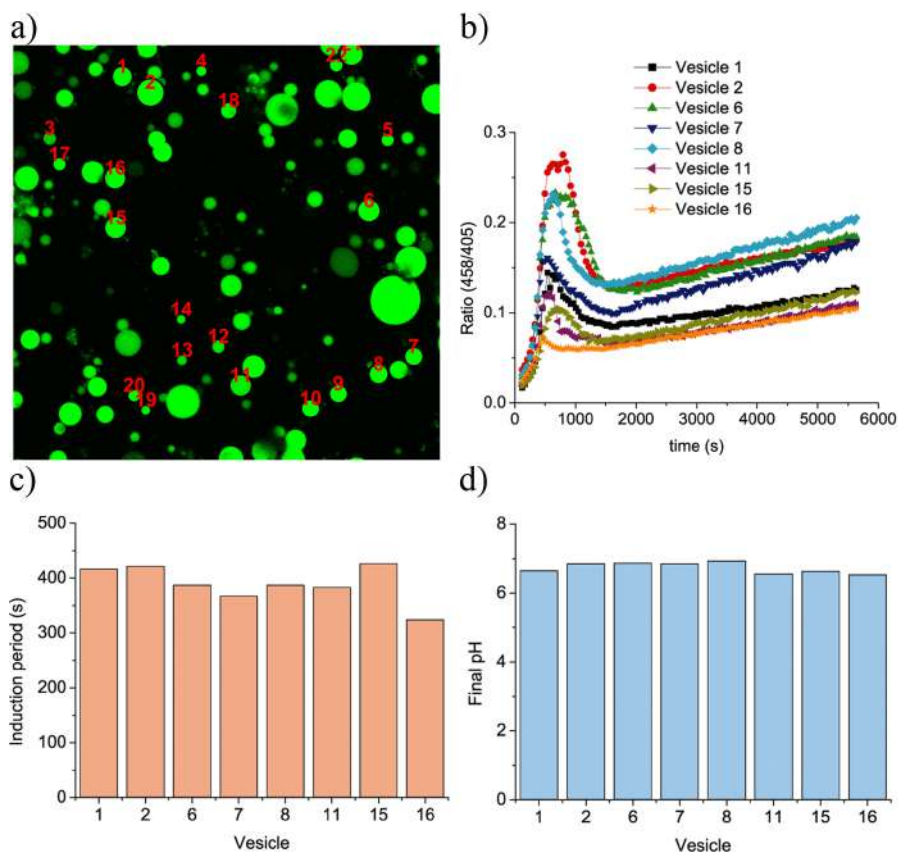


Figure 2.21: $[\text{CH}_3\text{COOH}] = 2.5 \times 10^{-3} \text{ M}$, $[\text{urea}] = 0.08 \text{ M}$, $[\text{enzyme}] = 80 \text{ U/mL}$, dilution factor 5.0. a) Vesicles detected with the particle tracking code. The red number indicates the number of the vesicle. Image in the UV channel. b) Time series for the vesicles 1, 2, 6, 7, 8, 11, 15, 16. c) Induction period for the vesicles 1, 2, 6, 7, 8, 11, 15, 16. d) Final pH for the vesicles 1, 2, 6, 7, 8, 11, 15, 16.

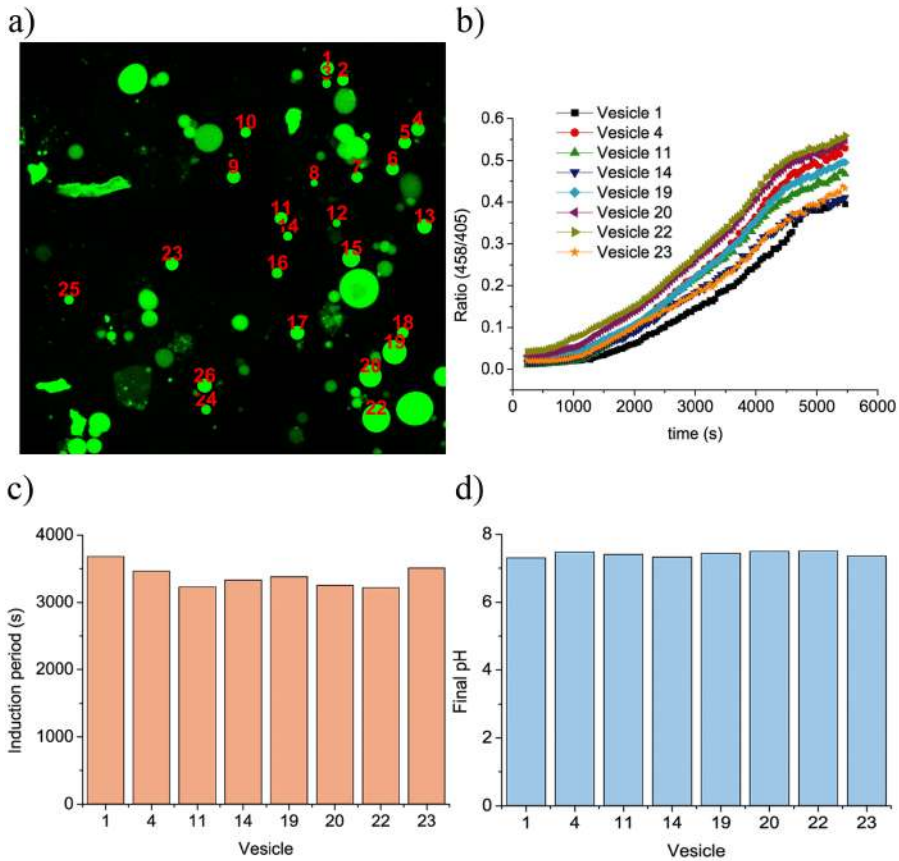


Figure 2.22: $[\text{CH}_3\text{COOH}] = 2.5 \times 10^{-3}$ M, $[\text{urea}] = 0.08$ M, $[\text{enzyme}] = 80$ U/mL, dilution factor 6.7. a) Vesicles detected with the particle tracking code. The red number indicates the number of the vesicle. Image in the UV channel. b) Time series for the vesicles 1, 4, 11, 14, 19, 20, 22, 23. c) Induction period for the vesicles 1, 4, 11, 14, 19, 20, 22, 23. d) Final pH for the vesicles 1, 4, 11, 14, 19, 20, 22, 23.

An average induction period was calculated from all the vesicles analyzed at the different dilutions of the pellet (Figure 2.23). The conversion of urea in ammonia slows down when the number of vesicles is reduced. In particular, the clock reactions have similar time scales for the dilution factors $DF = 1.7$ and $DF = 3.3$, there is an initial peak for the dilution factor $DF = 5.0$ (see Figure 2.21 b), the reaction gets slower with $DF = 6.7$ (Figure 2.22), 8.3 and 10.

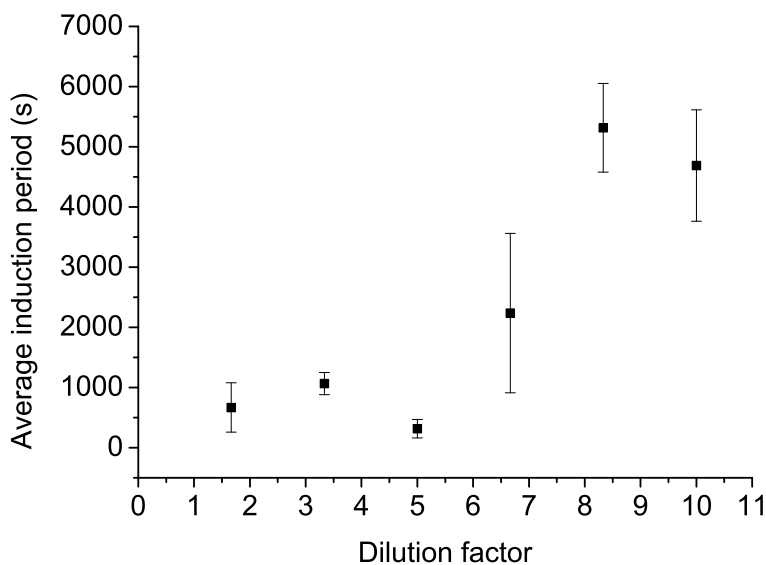


Figure 2.23: Average induction period for the dilution factors: 1.7, 3.3, 5.0, 6.7, 8.3, 10.

In contrast with the experiments at different concentrations of acetic acid (section 2.3.4), in these time series, the final pH is affected from the number of vesicles: in case of high dilutions ($DF = 8.3$ and $DF = 10$), it is impossible to overcome pH 7 within two hours (see Figure 2.24).

The number and the distribution of vesicles has an impact on the kinetics of the reaction: the dilution factors $DF = 1.7$ and $DF = 3.3$ correspond roughly to 2.5×10^4 and 1.5×10^4 vesicles (see section 2.3.3), the products, *e.g.* ammonia, can easily diffuse from one vesicle to another one resulting in a chemical wave. When the dilution factors are 5.0, 6.7, 8.3 and 10 that correspond respectively to $\sim 6 \times 10^3$, 5×10^3 , 3×10^3 and 2.0×10^3 vesicles, the vesicles are more isolated and the timescale of ammonia diffusion is too low to establish an effective communication pathway among the vesicles' population.

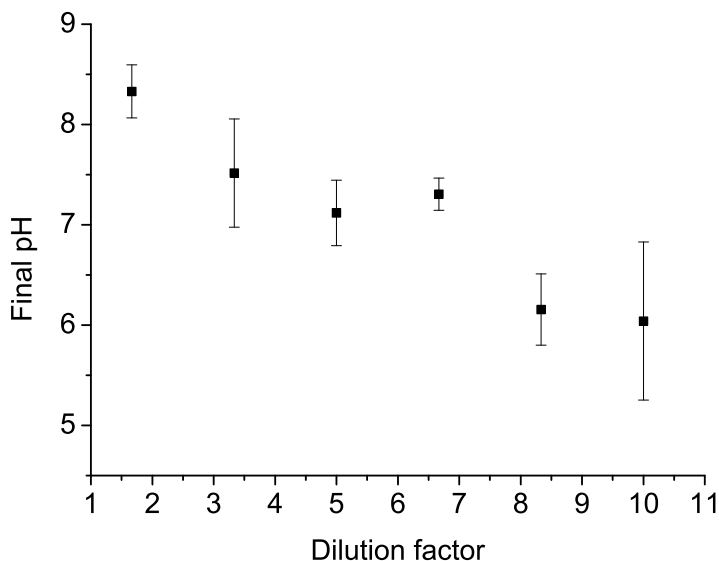


Figure 2.24: Average final pH for the the dilutions factors: 1.7, 3.3, 5.0, 6.7, 8.3, 10.

The dependence of the final pH from the number of vesicles could be explained through the phase diagrams mapped out with the kinetic model (section 2.3.1). The experiments at different concentrations of acetic acid may fall in the region of the high steady states: urea is converted in ammonia until basic pH is reached inside the vesicles. The conversion can be achieved in few seconds or in two hours depending on the initial concentration of acetic acid. The experiments with different populations of vesicles could not belong to a single region, but cross the boundary between the low steady states and the high steady states. In oscillating reactions, like the BZ, the low steady states and the high steady states are separated from regions of oscillations and bistability giving rise to a cross-shaped diagram as in Figure 2.6. The reactions with different number of vesicles can be rationalized as it follows: the dilution factors 10, 8.3, 6.7 may be located in the region of the low steady states (final pH < 7), the dilution factor 5.0 is characterized by the presence of one peak of oscillation, the dilutions 3.3 and 1.7 may be situated in the region of the high steady states (final pH > 7).

2.4 Discussion

The *blank* system POPC: urea-urease was characterized theoretically with a kinetic model and experimentally by changing the concentrations of acetic acid and the number of vesicles. The kinetic modelling of the urea-urease reaction helped us to interpret the results obtained. The induction period increases with the concentration of acetic acid: the conversion in ammonia is reached in few minutes for the concentrations $[\text{CH}_3\text{COOH}] = 1 \times 10^{-3}$ M and $[\text{CH}_3\text{COOH}] = 2.5 \times 10^{-3}$ M, whereas with $[\text{CH}_3\text{COOH}] = 5 \times 10^{-3}$ M and $[\text{CH}_3\text{COOH}] = 7.5 \times 10^{-3}$ the conversion is slower and the time series presents the typical sigmoidal shape of the clock reactions. In the range 1×10^{-3} M $< [\text{CH}_3\text{COOH}] < 7.5 \times 10^{-3}$ M and with the dilution factor $\text{DF} = 1.7$, the ammonia produced increases the pH of the aqueous lumen to basic values (high steady state). The effect of chemical wave in the fast reactions can be attributed to the diffusion of the positive feedback species, ammonia, that raises the initial pH of the surrounding vesicles increasing the reaction rate.

The number of vesicles affects the induction periods and the final pH values (pH > 7 for high population densities and pH < 7 for low population densities). Again, the diffusion of ammonia can justify the different reactivity: in sparse populations, the ammonia diffuses more slowly among the vesicles, in very dense populations the vesicles are closer to each other and the chemical communication is favoured. The dependence of the reactivity on the total number of vesicles resembles the collective behaviour of some bacteria known as *quorum sensing*, a phenomenon which allows bacteria populations to communicate and coordinate group behaviours such as regulating disease mechanisms, symbiotic processes and cell growth [66, 67]. Signal molecules, known as autoinducers, are secreted into the environment by bacteria and gradually increase in concentration as the bacteria population grows. After reaching a certain concentration threshold, the molecules become detectable to bacteria populations, triggering answers like changes in gene expression.

Transitions that recall the *quorum sensing* of bacteria were previously identified in populations of artificial microreactors. In cation exchange particles loaded with the BZ reaction, two kinds of transitions were observed depending on the stirring rate that controls the rate of diffusion of the autoinducer HBrO_2 in the reaction medium [68]. Gradual and sudden changes from stationary behaviour to synchronized oscillations were also found in the oscillatory Ni electrodissoolution-hydrogen ion reduction explored in a multi-electrode anode-single cathode system [69].

As for the microparticles and the multiple anodes systems, the POPC vesicles containing the urea-urease reaction represent a population of communicating elements where the chemical diffusion of the autoinducer (NH_3) allows to gradually tune the switch from low steady state (*reaction off* in low population densities) to high steady state (*reaction on* in high population densities). A

kinetic model with reaction-diffusion equations and a fine control of the number of vesicles could theoretically demonstrate the dependence of the enzymatic reactivity on the vesicles density.

3

UREA-UREASE REACTION IN GIANT HYBRID FATTY ACID/LIPID VESICLES

The experimental section is preceded by an introduction on the properties of fatty acid vesicles and their importance for the Origins of Life studies. The paragraph 3.2 is based on a minireview published during the PhD course (Paper II of the papers attached). The urea-urease reaction was studied in mixed vesicles at high concentrations of acetic acid (same conditions of chapter 2) and at a low concentration of acetic acid, giving phenomena of self-divisions. The self division was widely characterized in all its aspects and the results reported in Paper III (accepted paper).

Contents

3.1	Fatty acid Vesicles: characteristics and methods of preparations	44
3.2	The importance of Fatty acid Vesicles in the Origins of Life studies	46
3.3	Materials and Methods	49
3.3.1	Preparation and characterization of Giant Hybrid Unilamellar Vesicles	49
3.4	Results and discussion	50
3.4.1	Clock reactions as a function of acetic acid concentration	50
3.4.2	Self division as an effect of the fast pH variation and osmotic pressure	54

3.1 Fatty acid Vesicles: characteristics and methods of preparations

Fatty acid vesicles are colloidal suspensions of closed bilayers made of fatty acids and their ionized forms (soap). They are observed in a small region within the fatty acid-soap-water ternary phase diagram above the chain-melting temperature (T_m) of the corresponding fatty acid-soap mixture. Short chain (<14 C-atoms), long-chain (>14 C-atoms), saturated and unsaturated fatty acids can form vesicles if approximately equimolar amounts of the fatty acid and the soap are present [70, 71]. The difference in properties between fatty acid vesicles and diacyl phospholipid vesicles can be rationalized in terms of different physicochemical properties of the two molecules. While the monomer concentration of oleic acid in equilibrium with oleic acid vesicles is less than 1 mM, the monomer concentration in equilibrium with dipalmitoyl phosphatidylcholine bilayers is less than 10^{-10} M, so the monomer concentration is not negligible for fatty acid vesicles (a direct consequence is the difficulty in the separation of nontrapped molecules from the vesicles by size exclusion chromatography, dialysis or centrifugation) [70]. Both molecules have cylindrical geometry or shape, but the cross sectional area of one fatty acid molecule in the liquid-crystalline state is about half of that of a phospholipid molecule. The tighter packing of fatty acid molecules is associated with a significantly higher surface potential relative to phospholipid bilayers. This surface potential is also responsible for the marked shift of pK_a of 4.6 typical of a carboxylic group in aqueous solution to an apparent pK_a of 7 to 8.5 typical of a carboxylic group present at the fatty acid/soap bilayer interface [70]. The formation of vesicles is closely related to the pK_a of the fatty acid. Vesicles exist in a narrow pH range (ca. 7-9), where approximately half of the carboxylic groups are ionized (Figure 3.1 A for oleic acid/sodium oleate, HOA/OA⁻). Under these conditions, vesicles are stabilized due to the hydrogen bond networks formed between ionized RCOO⁻ and neutral acid RCOOH [70, 72]. At higher pH values, the transformation of vesicles into micelles occurs, at low pH values oil droplets are dominant. The pH stability can be increased by adding to the fatty acid/soap mixture a negatively charged surfactant with a high pK_b , *e.g.* sodium dodecylbenzenesulfonate (SDBS) [70, 73] (it increases the stability toward low pH) or by coaddition of an alcohol to increase the stability toward high pH [70, 74]. The increase of stability can be explained through the formation of mixed charged-uncharged dimers: soap (R¹-COO⁻)-alcohol (R²-OH) or fatty acid (R¹-COOH)-sulfonate (R³-SO₃⁻).

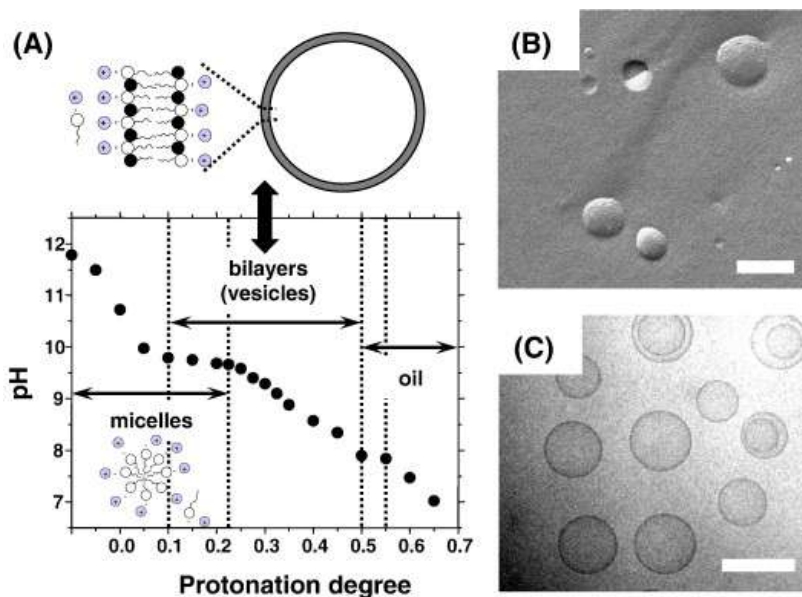


Figure 3.1: A) Titration curve for 80 mM oleic acid/sodium oleate. The region for the formation of micelles, vesicles and oil droplets are indicated. B) A freeze fracture electron microscopy image of vesicles produced by extrusion through 50 nm Nucleopore[®] membranes from 80 mM *rac*-2-methyldodecanoic acid in 40 mM Tris/HCl buffer at pH 8.0. Length of the bar: 100 nm. C) A cryo transmission electron microscopy image of vesicles prepared by extrusion through 100 nm Nucleopore[®] membranes from 100 mM decanoic acid in 100 mM sodium phosphate buffer at pH 7.0. Length of the bar: 100 nm. Reproduced with permission from [71]. Copyright ©2007 Elsevier Ltd.

A convenient method of fatty acid vesicles preparation is the addition of an alkalyne soap solution to a buffer solution of intermediate pH. For example, a concentrated solution of sodium oleate micelles is added to a buffered solution at pH 8.5, and oleic acid/sodium oleate vesicles form spontaneously after the drop of pH from 10.5 to 8.5. However the vesicles obtained are polydispersed in size and lamellarity. The polydispersity can be reduced by extruding the vesicles through polycarbonate membranes (electron microscopy images in Figure 3.1 B and C). Fatty acid vesicles can also be prepared by the common methods used for phospholipid vesicles: fatty acid vesicles produced from electroformation and film hydration are reported in literature [75, 76]. Pure fatty acid vesicles have not yet been synthesized with the droplet transfer method, however, hybrid vesicles have been successfully obtained with this technique. As shown in Figure 3.2 the presence of oleic acid enhances the formation of GUVs. The number of vesicles increases if oleic acid is used both in the emulsion and the interface (Figure 3.2 B vs Figure 3.2 A), better results are obtained when oleic acid is present just in the interface (Figure 3.2 C). A systematic variation of oleic acid percentage in the

interface allowed to find the concentrations of HOA that give the maximum number of vesicles (the maximum production lies in the range 20-50 % of HOA).

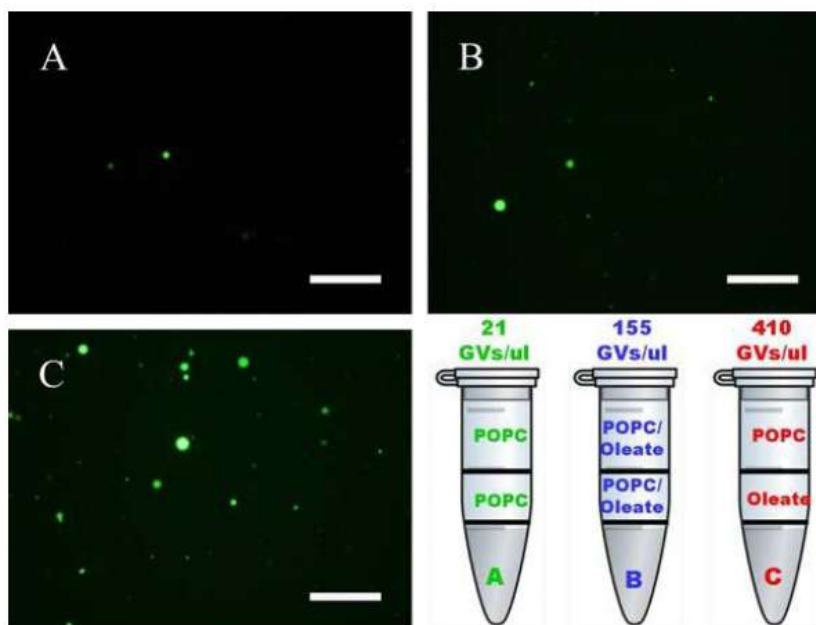


Figure 3.2: A) GUVs with POPC. B) GUVs with POPC and HOA. C) GUVs with POPC in the emulsion and HOA in the interfase. In the bottom right the number per μL of GUVs is reported for the three cases. Length of the bar: $250 \mu\text{m}$. Reproduced from the PhD thesis of Paolo Carrara.

3.2 The importance of Fatty acid Vesicles in the Origins of Life studies

Few studies examined the use of fatty acid vesicles as drug delivery systems. Oleic acid containing emulsion systems have been found in the past to increase the absorption efficiency of orally administered drugs [70, 77]. Vesicles composed of fatty acids like oleic acid and linoleic acid mimic the barrier properties of the upper-most layer of the skin that is mainly composed of fatty acids, cholesterol and ceramides rather than phospholipids encouraging their use for transdermal penetration and localization [78]. Actually, two factors limit the applications of fatty acid vesicles: the stability in a narrow range of pH and the sensitivity to ions, like Mg^{2+} . However, both these issues can be sorted out with mixed systems. The pH sensitivity has both benefits and drawbacks: it reduces the stability, but on the other hand, it enables the use of fatty acids

vesicles as drug carriers because the entrapped solutes can be released into the bulk medium by a simple change in pH (vesicles-micelles transformation) [70]. As mentioned previously, the pH range for vesicles formation can be widened with alcohols or sulfonate species to satisfy the pH values required in drug delivery systems. Divalent cations such as Mg^{2+} cause precipitation of vesicles even at low concentrations, prohibiting, for example the use of enzymes that depend on Mg^{2+} . The addition of phospholipids or fatty acid glycerol esters stabilize fatty acid vesicles in the presence of ionic solutes [71, 79, 80].

Whilst the possible applications of fatty acid vesicles in cosmetics, medicine and food technology are largely unexplored, the applications as protocell models in the Origins of Life studies are well documented [34, 81, 82]. Modern cell membranes contain different families of lipids in which transmembrane proteins with diverse functions are embedded. The structure of most of these lipids and proteins is quite complex and the probability that these molecules existed in the prebiotic era seems quite low. Simpler molecules like alkyl phosphates, alkyl sulfates, fatty acids have been proposed as possible constituents of early membranes [83]. Several studies showed that fatty acids can be formed under simulated primitive Earth conditions. It was postulated that small carbon-containing molecules such as methane could have formed hydrocarbons in the prebiotic era that gradually accumulated on the rocks. Subsequent carboxylation by atmospheric carbon oxides led to more complex structures. Normal fatty acids with C6 to C18 carbons can also be synthesized from CO and H_2 by Fischer-Tropsch-type reactions, using nickel-iron catalysts under conditions that may have occurred in the primitive Earth. Just in a later stage, fatty acids, glycerol and phosphate could have reacted to form phospholipids [72, 83]. For these reasons, fatty acid vesicles are convenient models of primitive cells, while mixed membranes of fatty acids and phospholipids have been proposed as intermediates in protocellular evolution. In fact, mixed membranes combine the stability typical of lipid bilayers (for example, they do not precipitate in the presence of divalent cations) with the plasticity and permeability of fatty acid structures.

In section 2.1, some liposomes-confined reactions that mimic the biochemistry of life (*e.g.* the synthesis of nucleic acids and proteins) were listed. Another challenge for the artificial cells is to make them accomplish some complex biological functions such as growth and division. Luisi *et al.* identified two ways to get growth and division [81]: (i) Addition of water-insoluble oleic anhydride to oleic acid/oleate vesicles; (ii) Addition of oleate micelles to POPC vesicles. In the first case, the hydrolysis of oleic anhydride produces extra amounts of oleic/oleate, in the second case phosphatidylcholine vesicles incorporate the added surfactant in their bilayer, giving rise to mixed POPC/oleic acid/oleate vesicles. Membrane growth and division can be found both in unilamellar and multilamellar vesicles. After feeding with fatty acid micelles, multilamellar fatty acid vesicles grow and transform into long thread-like vesicles. The process is driven by the transient imbalance between surface area and volume

growth, then the shear stress triggers the division of the deformed vesicles into multiple daughter vesicles. The mechanisms of vesicles growth and division are summarized in Figure 3.3 A) and B), while the confocal pictures of Figure 3.3 C) show the division of unilamellar (Figure 3.3 C4-C6) vesicles that elongate simmmetrically into tubular shapes and the division of multi-lamellar vesicles (Figure 3.3 C1-C3) that form tails during the growth [82].

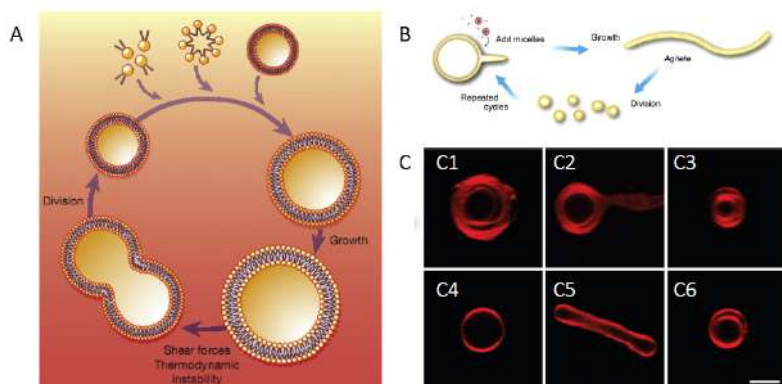


Figure 3.3: A) Modes of growth and division. Vesicle growth can occur by incorporation of fatty acid monomers, micelles or other vesicles. Reproduced from [72], licensed under Creative Commons Attribution-NonCommercial-No Derivatives License (CC BY NC ND). B) Schematic diagram of cyclic multilamellar vesicle growth and division. C1-C2) Confocal images of a multilamellar oleate vesicle labelled with Rh-DHPE before and after the addition of oleate micelles, respectively. C3) Confocal image of a multilamellar vesicle after division. C4-C5) Confocal images of a unilamellar oleate vesicle labelled with Rh-DHPE before and after the addition of oleate micelles, respectively. C6) Confocal image of a multilamellar vesicle formed after the agitation of elongated unilamellar vesicles. Scale bar for C) 2 μm . Reproduced from [82], licensed under American Chemical Society (ACS) AuthorChoice.

3.3 Materials and Methods

3.3.1 Preparation and characterization of Giant Hybrid Unilamellar Vesicles

Materials. Urea, acetic acid, urease, pyranine and fluorescein sodium salt were purchased from Sigma Aldrich. Stock solutions with the concentrations: $[\text{CH}_3\text{COOH}] = 0.05 \text{ M}$, $[\text{urea}] = 0.6 \text{ M}$ and $[\text{urease}] = 80 \text{ U/mL}$ were prepared for the slow clock reactions (results in section 3.4.1). Stock solutions with the following concentrations: $[\text{CH}_3\text{COOH}] = 1 \times 10^{-5} \text{ M}$, $[\text{urea}] = 0.6 \text{ M}$ and $[\text{urease}] = 5 \text{ U/mL}$ were prepared for the fast clock reaction (results in section 3.4.2). Pyranine and fluorescein sodium stock solutions were prepared in water with concentrations: $[\text{pyranine}] = [\text{fluorescein sodium}] = 0.1 \text{ mM}$. POPC (Lipoid) and oleic acid (HOA, Sigma) stock solutions were dissolved in Mineral oil (Sigma M5904), with concentrations : $[\text{POPC}] = 3 \text{ mM}$ and $[\text{HOA}] = 20 \text{ mM}$.

Droplet transfer method. The droplet transfer method was applied as in section 2.2.2, but adapted for fatty acid hybrid vesicles. Encouraged by the high yield in vesicles obtained with this method (section 3.1), the relative amounts of POPC and OA were changed both in the microemulsion and in the interface. Keeping the total concentration $[\text{POPC}] + [\text{HOA}] = 5 \text{ mM}$, several ratios of the two amphiphiles were explored. Similarly, keeping the ratio $[\text{POPC}]/[\text{HOA}] \sim 1.1$, the total concentration was varied between 0.025 and 10 mM. Urease, acetic acid and pyranine (fluorescein sodium for FRAP experiments) were introduced during the preparation of the vesicles. The reaction was started with the addition of urea. A schematic drawing of the procedure for the mixed vesicles is reported in Figure 3.4.

Instruments and softwares. The images reported in this chapter were acquired with an inverted epifluorescence microscope Eurotek Orma INV100TFL at University of Salerno using a 20x objective and a confocal laser scanning microscopy Leica SP8 X with HC PL APO CS2 40x/1.30 OIL objective (FRAP experiments). The epifluorescent microscope doesn't enable to follow kinetic runs at two different wavelengths. Thus, the ratiometric imaging was used to estimate the final pH of each experiment, whereas the time series are reported as absolute intensities vs time. Two fluorescent filters were used: a blue filter with an interval 460-490 nm for the excitation and 500-520 nm for the emission, and an UV filter. The images were analyzed with Matlab R2017b and ImageJ [47, 84]. In FRAP experiments, line 488 nm of an argon laser was used as excitation source while the fluorescence emission was recorded in the range 500-600 nm. The photobleaching was obtained zooming in the target vesicle and using the maximum laser power until the fluorescence disappeared. The images were recorded every 30 seconds with xyt scan mode.

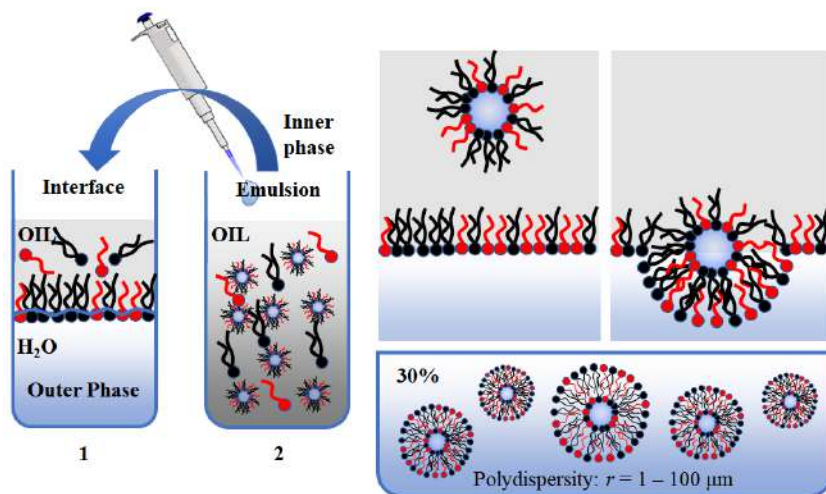


Figure 3.4: Schematic drawing of the preparation of mixed vesicles POPC/HOA through droplet transfer method. The red and black colours are used to emphasize the hybrid nature of the membrane.

3.4 Results and discussion

3.4.1 Clock reactions as a function of acetic acid concentration

The acetic acid concentration was varied in the range $1 \times 10^{-3} - 7.5 \times 10^{-3}$ M as already done for the pure POPC vesicles and the dilution factor kept at 1.7 V/V. This dilution factor was chosen to ensure the highest number of vesicles (results for pure POPC vesicles in section 2.3.3) and avoid a strong decrease of reactivity due to the presence of a second acidic species (oleic acid). For the sake of brevity, the data analysis are reported for just two concentrations: $[\text{CH}_3\text{COOH}] = 1 \times 10^{-3}$ M and $[\text{CH}_3\text{COOH}] = 2.5 \times 10^{-3}$ M. The vesicles recognition and labelling procedure are shown in Figures 3.5 a) and 3.6 a); the evolution of the fluorescence of eight single vesicles with respect to time, $t = 0$ is the time at which urea is delivered to the vesicles population is shown in Figures 3.5 b) and 3.6 b); the induction periods are reported in Figures 3.5 c) and 3.6 c); the corresponding final pH are in Figures 3.5 and 3.6.

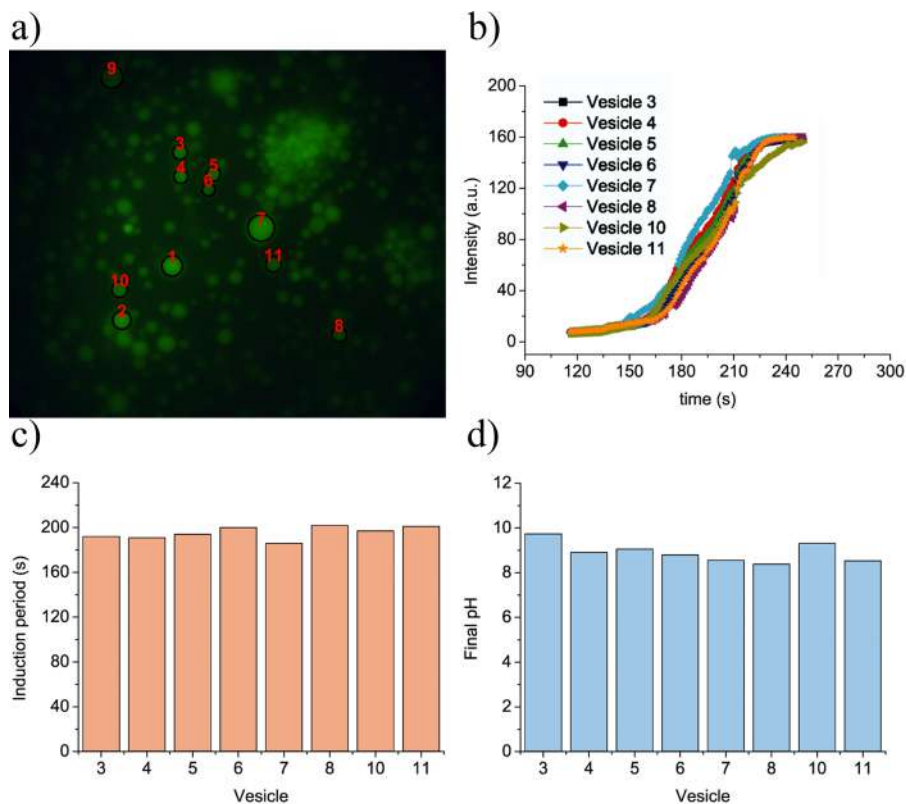


Figure 3.5: $[\text{CH}_3\text{COOH}] = 1 \times 10^{-3} \text{ M}$, $[\text{urea}] = 0.08 \text{ M}$, $[\text{enzyme}] = 80 \text{ U/mL}$, dilution factor 1.7 V/V, $[\text{POPC}]:[\text{HOA}] = 2.6 \text{ mM}: 2.4 \text{ mM}$. a) Vesicles detected with the particle tracking code. The red number indicates the number of the vesicle. Image in the UV channel. b) Time series for the vesicles 3, 4, 5, 6, 7, 8, 10, 11. c) Induction period for the vesicles 3, 4, 5, 6, 7, 8, 10, 11. d) Final pH for the vesicles 3, 4, 5, 6, 7, 8, 10, 11.

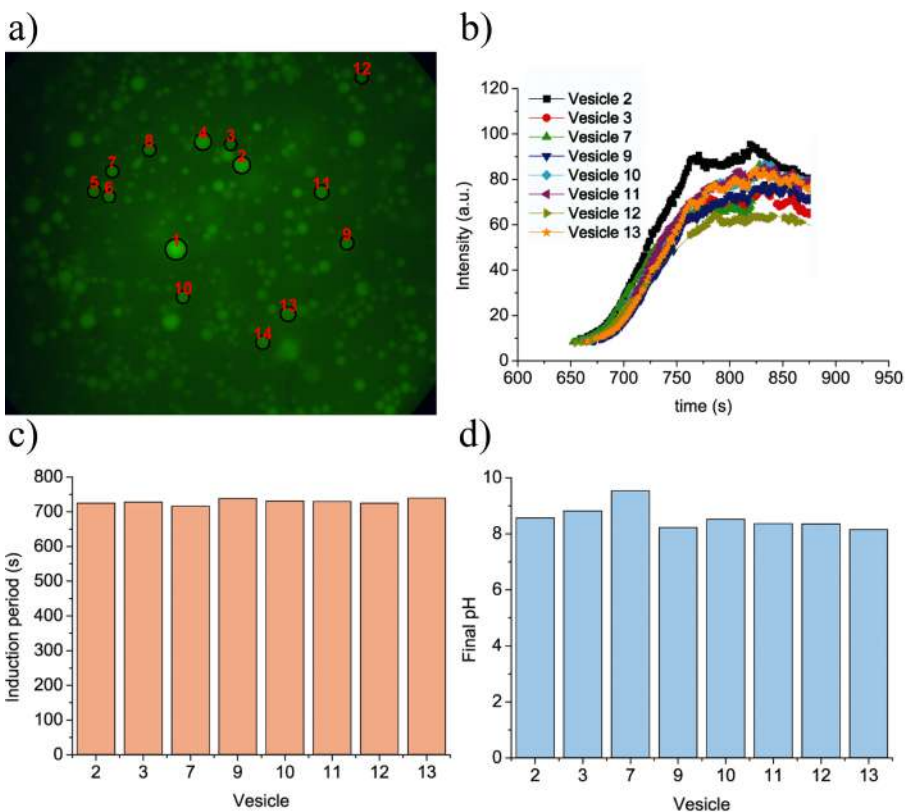


Figure 3.6: $[\text{CH}_3\text{COOH}] = 2.5 \times 10^{-3}$ M, $[\text{urea}] = 0.08$ M, $[\text{enzyme}] = 80$ U/mL, dilution factor 1.7 V/V, $[\text{POPC}]:[\text{HOA}] = 2.6$ mM: 2.4 mM. a) Vesicles detected with the particle tracking code. The red number indicates the number of the vesicle. Image in the UV channel. b) Time series for the vesicles 2, 3, 7, 9, 10, 11, 12, 13. c) Induction period for the vesicles 2, 3, 7, 9, 10, 11, 12, 13. d) Final pH for the vesicles 2, 3, 7, 9, 10, 11, 12, 13.

An average induction period was calculated from all the vesicles analyzed at the four different concentrations of acetic acid. The induction periods of Figure 3.7 are comparable with the ones obtained with pure POPC vesicles (Figure 2.18). Thus, the presence of oleic acid in the membrane at a concentration of 2.4 mM doesn't affect significantly the length of the induction period or the final pH (final pH values higher than 8 are shown both in Figure 2.20 and Figure 3.8, an indication that even in presence of oleic acid the concentrations tested cover the region of high steady states). However, the acid base equilibrium between oleic and oleate alters the shape of the curve. From the comparison of the time series for pure POPC (Figures 3.5 b) and mixed POPC/HOA (Figure 2.16 b) vesicles at the concentration of $[\text{CH}_3\text{COOH}] = 1 \times 10^{-3}$ M, the different length of the acidic plateau stands out: the oleic acid has a buffer effect, so that the initial increase of pH is not fast and the sigmoidal shape typical of the

clock reactions becomes more pronounced in mixed vesicles. In turn, this buffer effect reduces the chemical waves that appeared in pure POPC vesicles: the induction periods of several vesicles selected within a same frame are different in case of pure lipid membranes as evidenced in the histogram of Figure 2.16 c), but are uniform in the histograms of Figure 3.5 c) and 3.6 c) concerning the hybrid vesicles POPC/HOA. In hybrid vesicles POPC/HOA, ammonia still acts as a messenger molecule, but the increase of pH triggered from the diffusion of ammonia is balanced by the acid base equilibrium oleic acid/oleate.

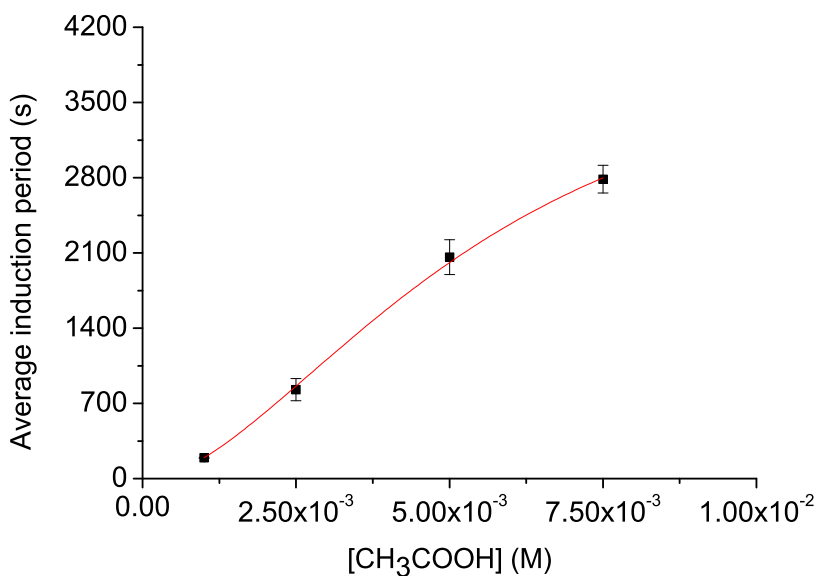


Figure 3.7: Average induction period for the concentrations: $[\text{CH}_3\text{COOH}] = 1 \times 10^{-3}$ M, $[\text{CH}_3\text{COOH}] = 2.5 \times 10^{-3}$ M, $[\text{CH}_3\text{COOH}] = 5 \times 10^{-3}$ M, $[\text{CH}_3\text{COOH}] = 7.5 \times 10^{-3}$ M.

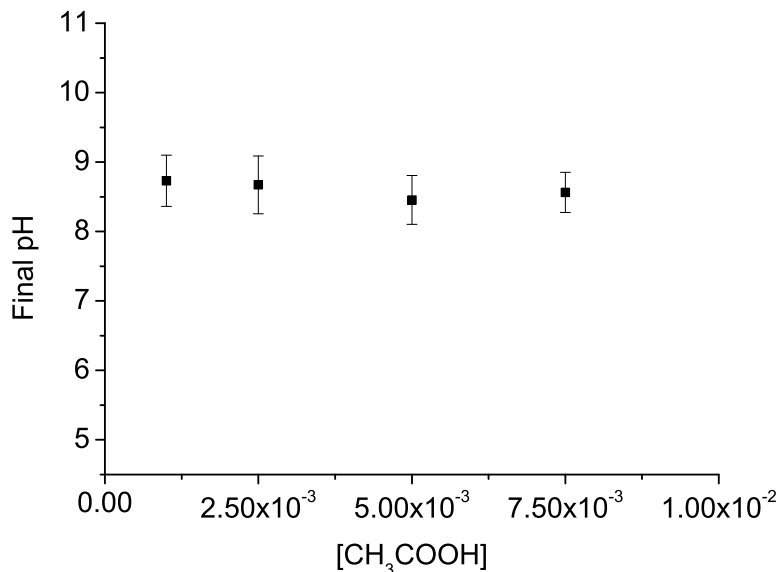


Figure 3.8: Average final pH for the concentrations: $[\text{CH}_3\text{COOH}] = 1 \times 10^{-3}$ M, $[\text{CH}_3\text{COOH}] = 2.5 \times 10^{-3}$ M, $[\text{CH}_3\text{COOH}] = 5 \times 10^{-3}$ M, $[\text{CH}_3\text{COOH}] = 7.5 \times 10^{-3}$ M.

3.4.2 Self division as an effect of the fast pH variation and osmotic pressure

The clock reactions studied in the previous section can be directly compared with the *blank* system of POPC, however no chemo-mechanical deformation was observed during the fluorescence acquisition, thus the experimental conditions were changed and a new set of experiments was built up starting from a fast enzymatic reaction. A fast enzymatic reaction was obtained in the following conditions: urease (0.5 U/mL), pyranine (50 μM) and acetic acid (1×10^{-6} M) were encapsulated in hybrid POPC/HOA vesicles with $[\text{POPC}] = 2.6$ mM and $[\text{HOA}] = 2.4$ mM, urea with a final concentration after mixing of 0.06 M was added to initiate the reaction. The low concentration of acetic acid and the high concentration of urea ensure the reaction is fast: indeed, in these conditions, in pure POPC vesicles pH 9 is reached within 3 minutes. In the presence of oleic acid, a division process takes place (example in Figure 3.9): starting from a spherical shape, the GUV elongates in a prolate form ($t \sim 12$ s), assumes a pear shape ($t \sim 16$ s) and eventually divides into two daughter vesicles ($t \sim 60$ s). In a typical experiment, the self-division process occurs with a probability of $\sim 25\%$ irrespective of the size (the histogram of the divided vesicles have the same shape of the histogram of the total vesicles, Figure 3.13 a).

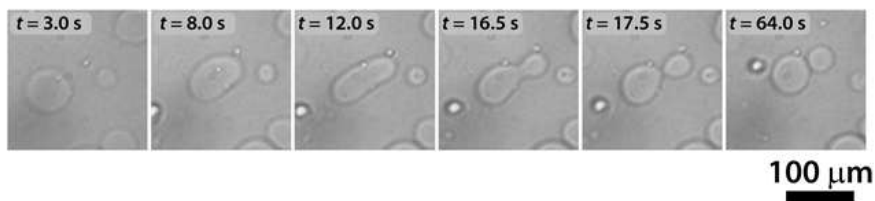


Figure 3.9: pH-triggered self division of a GUV. Continuous shape transformation of a GUV, triggered by urea-urease enzymatic reaction, starting from a spherical shape through prolate and pear shapes into two daughter vesicles.

A systematic variation of the total concentration $[\text{POPC}] + [\text{HOA}]$ (s) and the ratio $[\text{POPC}]/[\text{HOA}]$ (α) allowed to identify the composition $[\text{POPC}] = 2.6$ mM and $[\text{HOA}] = 2.4$ mM as the optimal one to get the highest proportion of divisions or elongations. Total concentrations higher than $s = 5$ mM do not improve the rate of division, the value of 5 mM lies on a plateau (the rate of division varies from $\sim 5\%$ to $\sim 20\%$ in the range $0.25 \text{ mM} < s < 10 \text{ mM}$, Figure 3.10 a). The presence of a plateau can be related to the yield in vesicles of the droplet transfer method. Giant vesicles with different initial POPC concentrations were analyzed through HPLC using a C18 column and a mobile phase composed of acetonitrile, methanol and formic acid at 0.1 % in the proportions 50:45:5 (the chromatogram is shown in the inset of Figure 3.10 b). As shown in Figure 3.10 b), the percentage of initial POPC that is converted in vesicles do not change for the interval $0.3 < [\text{POPC}] < 1 \text{ mM}$ (the percentage of POPC in the final vesicles is 2 - 4 %), therefore the increase of the initial total concentration could have no effects on the membrane composition. The ratio α was varied between 0.5 and 4 for a total amount of amphiphiles $[\text{POPC}] + [\text{HOA}] = 5 \text{ mM}$. The rate of elongation (deformation of the vesicles that elongate assuming a prolate shape, but don't divide into two daughter vesicles) and the rate of division were calculated for the different ratios (Figure 3.10 c and d). The ratio $\alpha = 2.6 \text{ mM}/2.4 \text{ mM}$ corresponds to the best rate, lower ratios or higher ratios are less effective: the composition $\alpha = 2.6 \text{ mM}/2.4 \text{ mM}$ can be a good compromise between the pH sensitivity given from the oleic acid and the stability guaranteed by POPC. A high content of POPC can make the vesicles more stable and less prone to get divisions, high amounts of oleic acid interfere with the vesicles preparation.

In all the experiments, complete separation of the daughter vesicles has never been observed. The vesicles stay in close proximity and, are most probably connected by a narrow neck. FRAP experiments (Fluorescence recovery after photobleaching) were performed to check whether the lumens of the two vesicles were contiguous. The fluorescence of one daughter vesicle was bleached after the division process with a laser beam: if the daughter vesicles are connected, the fluorescence should increase after bleaching because the fluorescent probe diffuses from one vesicle (not bleached) to the other one through the narrow

neck, in case of complete separation the bleached vesicle cannot recover the fluorescence. Fluorescein sodium was employed instead of pyranine because the former is more sensitive to photobleaching. The laser pulse led to a complete separation of the daughter vesicles, which then diffused away from each other, preventing the fluorescence recovery of the bleached vesicle (Figure 3.11). This effect recalls the behaviour observed from Zhu and Szostak in fatty acid vesicles [82]: the kinetic energy of mildly agitated liquid water triggered the division of vesicles and the breaking in thread-like aggregates. In our case, the energy of the laser beam induces the completion of the separation step. Therefore, based on FRAP experiments, it can be concluded that after the division, the daughter vesicles remain connected by a common membrane neck, which can be broken by additional environmental triggers.

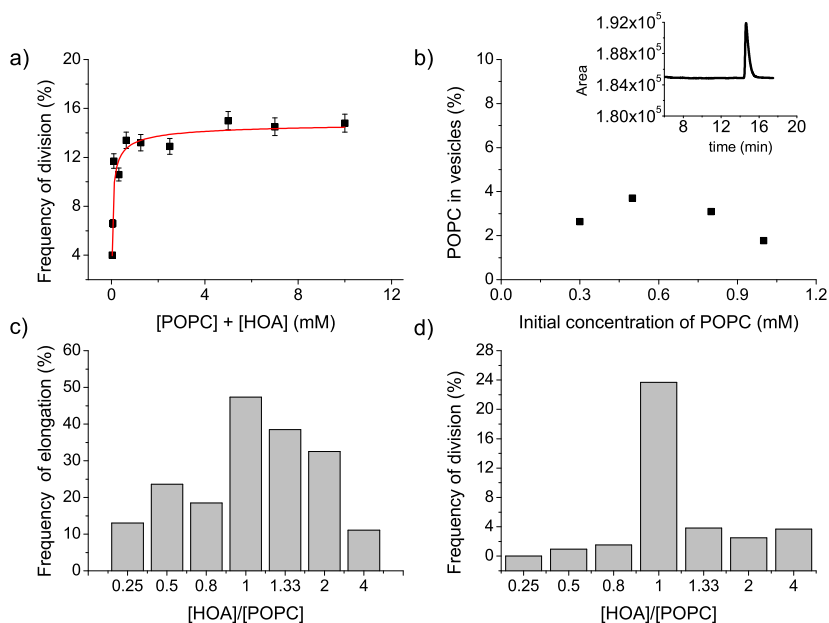


Figure 3.10: a) Frequency of division as a function of the sum [POPC] + [HOA]. b) Percentage of POPC in the final vesicles vs initial concentration of POPC in mineral oil. Data extrapolated from HPLC analysis (chromatogram in the inset). c) Frequency of elongation as a function of the ratio [HOA]/[POPC]. d) Frequency of division as a function of the ratio [HOA]/[POPC].

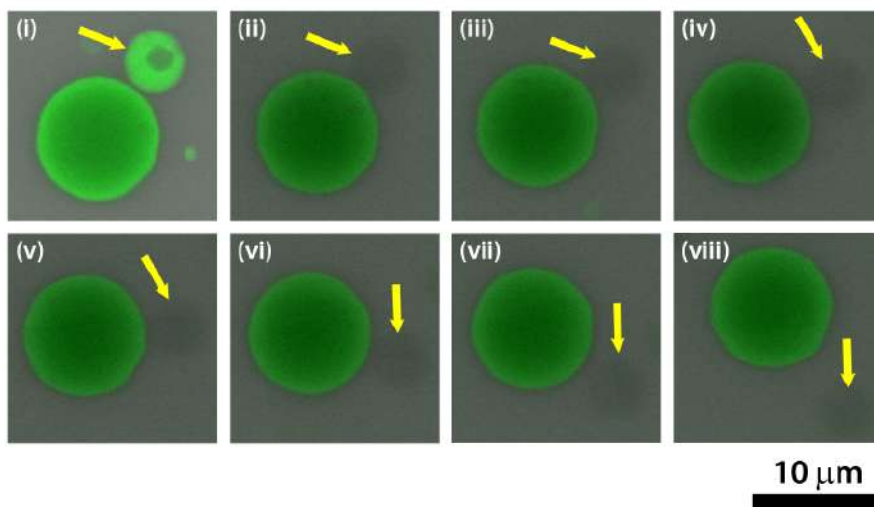


Figure 3.11: FRAP experiment using fluorescein as a fluorescent probe ($[\text{fluorescein sodium}] = 20 \mu\text{M}$). The fluorescence of one of the two daughter vesicles (indicated by a yellow arrow) was bleached after the division process. The lack of fluorescence recovery indicates an effective separation between the two daughter vesicles. The initially clumped vesicles clearly separated after the irradiation with the laser beam. The time between consecutive fluorescence micrographs is 30 s.

The images of divisions collected by optical microscopy for the amphiphiles ratio $[\text{POPC}]/[\text{HOA}] = 2.6 \text{ mM}/2.4 \text{ mM}$ (Figure 3.9) were repeated in presence of pyranine and monitored by epifluorescent microscopy to verify a possible correlation between the division and a pH change of the aqueous lumen. The epifluorescent imaging confirmed that the stages of the division process are correlated with the increase of pH inside vesicles (Figure 3.12 a). However, the pH increase is different compared to the pure POPC vesicles: herein, the pH doesn't reach the neutrality, but just a small change from $\text{pH} \sim 6$ to $\text{pH} \sim 6.5$ is observed (Figure 3.12 b and calibration in the Appendix B.1). This small change is enough to generate a change of up to 20 % (considering $\text{p}K_a$ of 7.2) in the protonation rate of HOA molecules. To explain this pH change and the osmotic concentration gradient inside and outside the GUVs driven by the enzymatic reaction, a simple kinetic model was constructed that qualitatively describes the behaviour observed in the experiments. The species considered are: urea, ammonia, urease, acetic acid, carbon dioxide, pyranine, protons and hydroxyls. The concentration of each chemical species inside a vesicle changes due to chemical reactions and transport by passive diffusion. The differential

equations for the species inside and outside the vesicles can be summarized as:

$$\frac{d[X]}{dt} = r([X]) + k_x ([X]_0 - [X]) \quad (3.1)$$

$$\frac{d[X]_0}{dt} = r([X]_0) + d_f k_x ([X] - [X]_0) \quad (3.2)$$

where $[X]$ is the concentration of the chemical species X , $r([X])$ represents the set of reaction rates involving X (kinetic constants of the acid base equilibria and the enzymatic reaction are in refs. [10, 14, 85, 86]), $[X]_0$ is the concentration of the chemical species in the outer phase. The transfer rate k_x (s^{-1}) is proportional to the surface-to-volume ratio of the vesicles and to the membrane permeability of the species: $k_x = 3P_x/R$ where P_x (dm/s) is the specific permeability (the permeability values used in the model are taken from literature [87–90]) and R (dm) is the vesicle’s radius. The dilution factor d_f that appears in the equation 3.2 is proportional to the total number of vesicles N and to the ratio between the inner volume of the vesicle V_i and the volume of the outer solution V_0 . The complete model is reported in Appendix B.2.

The osmotic pressures (Π) inside and outside the vesicles were calculated as the sums of the concentrations of the ionic species (taking into account the Van’t Hoff coefficients) and the concentrations of neutral species like urea and sugars. The results of the numerical simulations (Figure 3.12 c) are in accordance with the pH dynamics reconstructed from the fluorescence time series in Figure 3.12 b. The induction period, the pH change and the plateau time are consistent with the experiments (Figure 3.12 b and c). The osmotic concentration gradient is mostly due to the addition of urea ($\Delta\Pi \simeq 60$ mM). Two sets of experiments were carried out for a better comprehension of the role of the pH and the osmotic pressure. In the first set, the final solution added contained [urea]= 60 mM and [glucose] = 140 mM (inside the vesicles [sucrose] = 200 mM) to eliminate the initial osmotic concentration gradient and no division was observed. No division was observed in slow reactions (conditions of section 3.4.1) when the initial pH was reduced with higher concentrations of acetic acid. Thus osmotic pressure and pH change must act in synergy, approximately at the same time scale to observe self-division.

A further insight into the mechanism of self-division was provided from the analysis of the surface and the volume of the vesicles before and after the process of division (the changes of volume and surface area during the self-division were highlighted in the papers of Szostack and Svetina, section 3.2 and refs. [82, 91]). During the transition from a sphere to a prolate spheroid, both the surface area and the volume decreased after the addition of the substrate, the volume of the vesicles decreased of about 25 % on average (Fig 3.13 b), while the average total surface area remained within the 10 % of the mother vesicle (Fig 3.13 c). The volume decrease can be a consequence of the osmotic imbalance. The change of surface area can be due to the formation of protrusions and micro

aggregates inside the lumen of the mother vesicles (confocal images not shown in this section). Thus, the interpretation of the mechanism we put forward is the following: the added urea solution generates an osmotic shock, urea penetrates into GUVs, however, concurrently, some water leaves vesicles to equilibrate the osmotic difference. Since the permeability of water is greater than that of urea, the volume of the vesicles decreases. Parallel with this process, the enzymatic reaction starts in the GUVs and the pH increases due to the ammonia production and hence hydroxyls ions. The increase of pH leads to an increase of the deprotonated oleic acid molecules, introducing negative charges in the inner leaflets of the GUVs. This charge accumulation affects the membrane stability inducing formation of aggregates that reduce the surface area of the inner leaflet compared to the outer one. The volume loss and the surface area change drive the shape transformation of the GUVs causing the self-division.

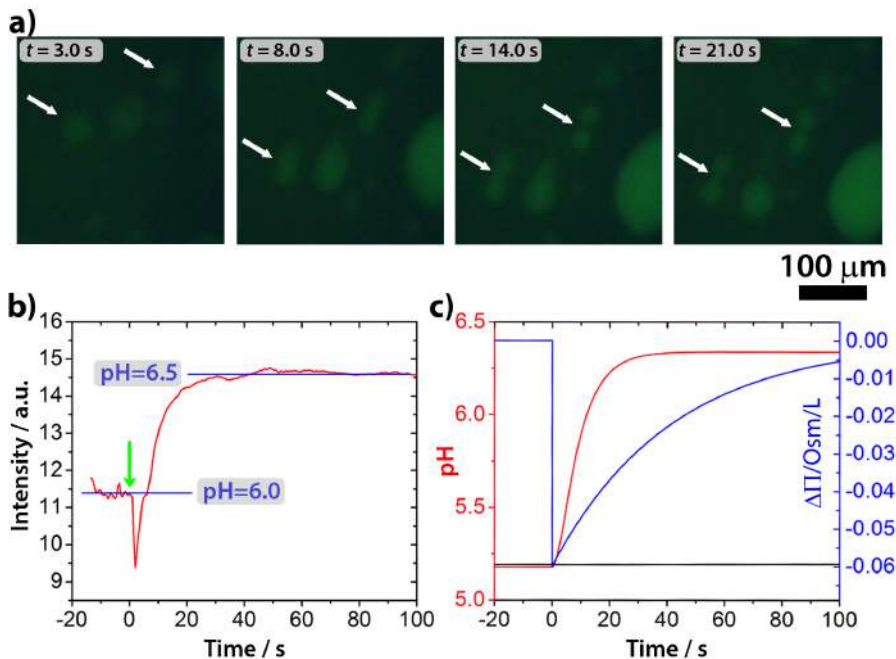


Figure 3.12: a) Fluorescence microscopy images of GUVs during the self-division process. An increase of the fluorescent signal of pyranine inside the GUVs indicates a pH change. b) Change of the fluorescent intensity in time inside the GUVs. c) Results of the numerical simulations of the osmotic concentration gradient (solid blue curve), pH change inside (solid red curve) and outside (solid black curve) of the vesicles. Urea is added in the model at $t = 0$

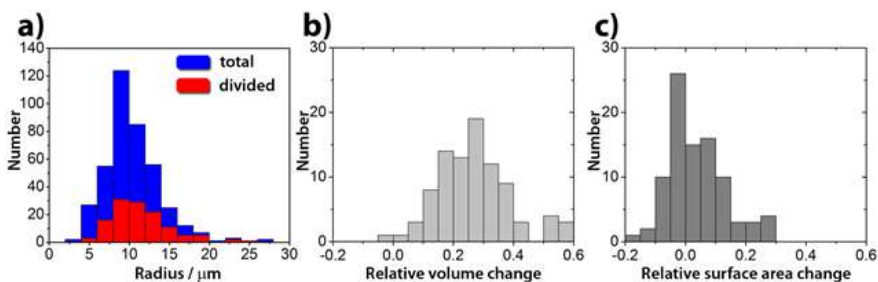


Figure 3.13: a) Size distribution of GUVs used in the experiments (blue) and the frequency histogram of the divisions (red). b) Relative volume change and c) relative surface area change in a population of GUVs. The relative change is defined as $(Y_{\text{mother}} - (Y_{\text{daughter1}} + Y_{\text{daughter2}}))/Y_{\text{mother}}$ where Y denotes either volume or surface area.

The change of surface area due to the pH increase in hybrid POPC/HOA membranes was also predicted with molecular dynamics (MD) simulations (results in 3.15 a and b). One of the two leaflets of the POPC/HOA bilayer was deprotonated step by step: in each step 10 % of the HOA molecules were deprotonated, then the system was equilibrated for 10 ns and the process repeated until all HOA molecules became deprotonated. Due to the electrostatic repulsion between the deprotonated head groups of the leaflet, the average molecular surface area of this leaflet increased monotonically with the deprotonation ratio, resulting in both an increase in the total surface area of the bilayer and a buckling of the membrane towards the deprotonated leaflet (Figure 3.15 a and b, Figure 3.14 c). The expansion of a POPC/HOA leaflet due to the electrostatic repulsion between the deprotonated HOA molecules was also confirmed by the Wilhelmy film balance experiments at different pHs in buffered media (Figure 3.14 b).

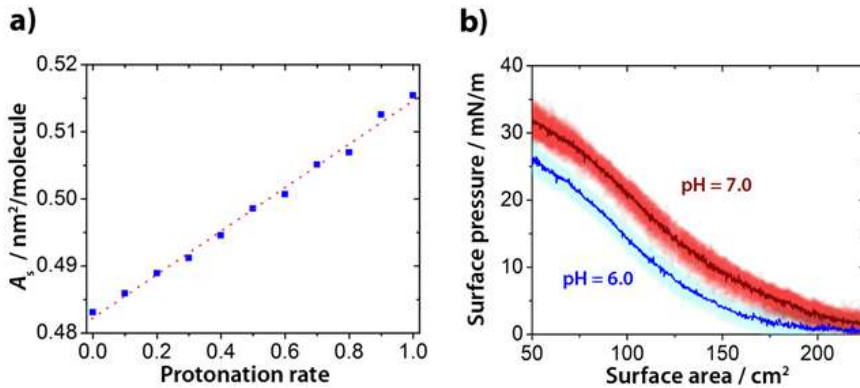


Figure 3.14: a) Results of the MD simulations. Effect of the protonation degree on the surface area of one leaflet of the mixed POPC/HOA bilayer in MD simulations. b) Surface pressure versus surface area isotherms of a monolayer of mixed POPC and HOA (2.6 mM:2.4 mM) using phosphate buffers at $\text{pH} = 6.0$ and 7.0 . The solid line and the shaded area represent the average and the standard deviation of five independent experiments. Analyzing the isotherms the characteristic surface area was $150 \pm 8 \text{ cm}^2$ and $174 \pm 14 \text{ cm}^2$ at $\text{pH} = 6.0$ and $\text{pH} = 7.0$, respectively. Simulations performed by Gábor Holló (University of Budapest), experiments performed by Borbála Tegze (University of Budapest).

Self division of hybrid giant unilamellar vesicles was generated through a chemical stimulus inside the lumen (the pH change caused by the enzymatic reaction) and influenced by cross-membrane transport. This approach is new compared to the systems previously explored in literature where external stimuli (addition of membrane precursors and temperature changes, see section 3.2) triggered the division process. The resemblance to living systems where the division is a process governed by the complex biochemical reaction network of the cell, often induced by environmental inputs sensed through cross-membrane transport, makes this system a plausible model for studying the self-division process of protocells under prebiotic conditions.

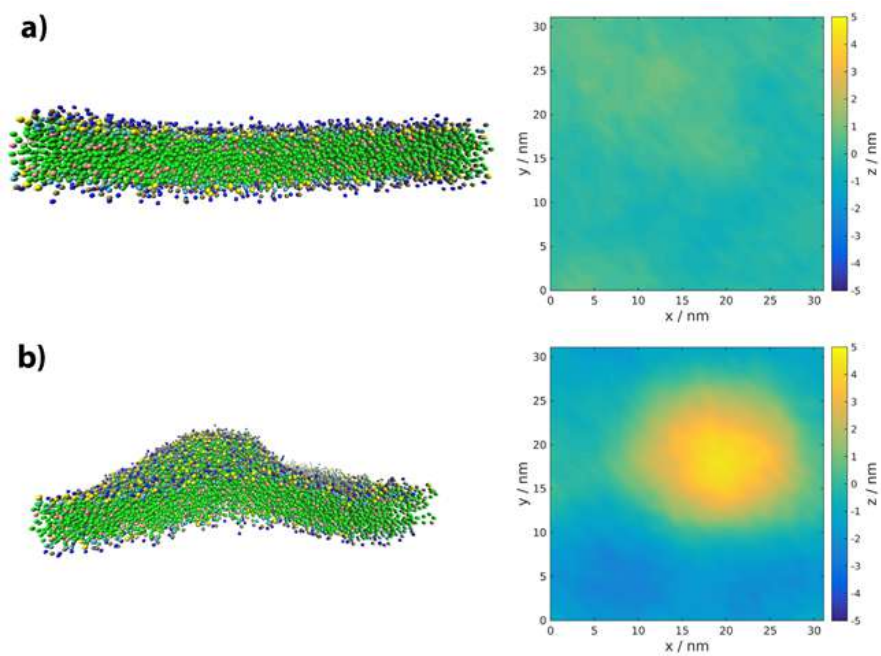


Figure 3.15: Results of the MD simulations. a) Structure of the mixed POPC/HOA bilayer, when all HOA molecules in the top leaflet are fully protonated (all HOA molecules have no charge). b) Structure of the mixed POPC/HOA bilayer, when all HOA molecules in the top leaflet are fully deprotonated (all HOA molecules have a negative charge). Simulations performed by Gábor Holló (University of Budapest).

4

PREPARATION OF GIANT HYBRID POLYMER/LIPID VESICLES

This chapter is focused on the synthesis of amphiphilic copolymers and their use in the preparation of giant hybrid polymeric vesicles. The experimental results on the polymers synthesis were accompanied by kinetic Monte Carlo simulations and DFT analysis performed by Prof. Mella at University of Insubria (details in Paper IV attached). The characterization of the hybrid vesicles was done in collaboration with the IDeAS team of University of Toulouse (Paper VIII of the list).

Contents

4.1	Living radical polymerization for the synthesis of block copolymers	64
4.2	Polymeric vesicles and hybrid polymer/lipid vesicles	66
4.3	Experimental section	70
4.3.1	Materials for polymers synthesis and purification . . .	70
4.3.2	Polymer synthesis	70
4.3.3	Polymer characterization	73
4.3.4	Preparation and characterization of Giant Hybrid Unilamellar Vesicles	74
4.4	Results and discussion	76
4.4.1	Rational design of amphiphilic copolymers	76
4.4.2	Identification of the experimental conditions and relative reactivities of the monomers	77
4.4.3	Characterization of the copolymers selected for the vesicles preparation	85
4.4.4	Fluorescent labelling for the detection of polymeric phases in giant hybrid vesicles	87
4.4.5	Preparation of hybrid polymeric vesicles via electroformation	89
4.4.6	Preparation of hybrid polymeric vesicles by the droplet transfer method	92

4.1 Living radical polymerization for the synthesis of block copolymers

The copolymers described in this chapter were synthesized by living radical polymerization, a new challenge compared to the traditional free radical polymerization. Free radical polymerization offers numerous advantages: relative insensitivity to impurities, tolerance to protic compounds such as water, high reaction rates, moderate reaction temperatures (generally higher than room temperature), multiple polymerization processes available [92, 93]. However, unlike ionic polymerizations where the growing intermediates repel each other, the growing radical species undergo bimolecular termination reactions such as recombination and disproportionations. Thus, free radical polymerization is unsuitable for precision polymer synthesis [92]. To overcome these limits new techniques were developed, called "living" or controlled radical polymerizations (CRPs) that are free from side reactions such as termination and chain transfer and can generate polymers of well-defined architectures and molecular weights: atom transfer radical polymerization (ATRP) [94], reversible addition-fragmentation chain transfer polymerization (RAFT) [95], and nitroxide-mediated polymerizations (NMP) [96] are the most known examples of CRPs [93]. The concept or the strategy behind the ATRP is the reduction of the (instantaneous) concentration of the growing radical species by introducing a covalent dormant species that exists predominantly over, and in fast equilibrium with, the growth-active radical species. The covalent bonds for dormant species include C-C, C-S, C-Se, C-O, C-halogen and C-metal, that can be reversibly and homolytically activated into the growing radical species by physical stimuli such as heat or light or by chemical stimuli such as a metal catalyst or another radical species [92]. In ATRP polymerizations, the reaction is initiated by the activation (homolytic cleavage) of the carbon-halogen bond of an organic halide (R-X) via one-electron oxidation of the metal center ($M^n X_n L_m$) to form an initiating radical species $R\cdot$ and an oxidized metal compound ($M^{n+1} X_{n+1} L_m$) (first reaction in Figure 4.1). The radical $R\cdot$ reacts with the halogen to regenerate R-X or adds to the monomer to generate a radical species $R-CH_2-C-(R^1)-(R^2)\cdot$. This radical is then transformed into the adduct $R-CH_2-C-(R^1)-(R^2)-X$ or reacts with other monomers. A repetitive set of additions makes the chain grow and the polymer end-functionalized with a carbon-halogen bond is subsequently activated by the metal complex in the same way of R-X (third equilibrium in Figure 4.1) [92]. The polymerization stops only when there is no more monomer, it restarts immediately if fresh monomer is added to the reaction mixture.

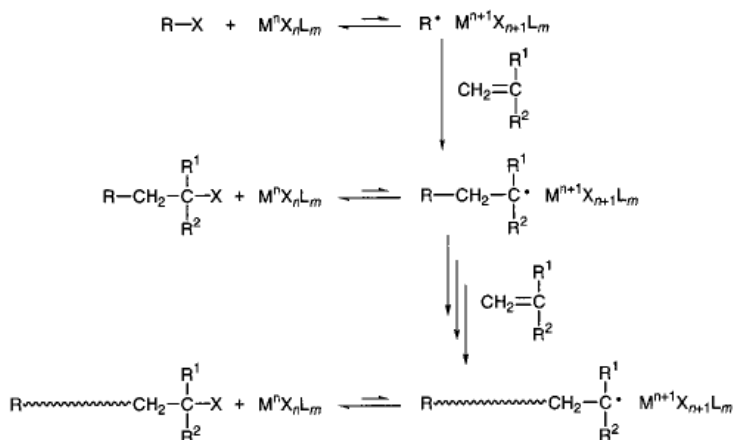


Figure 4.1: Metal catalyzed living radical polymerization. Generation of the initiating radical species through the one-electron oxidation of the metal center. Addition of monomers to the radical species and growth of the polymer. Reprinted with permission from [92]. Copyright ©2001, American Chemical Society.

Since 1995, when, for the first time, two ATRP reactions were reported independently by two research groups [97, 98], a myriad of polymerizations have been described with this procedure: a wise combination of metal catalysts, ligands and initiators allows to improve the rate and the control of the polymerization. The metal catalyst is usually a transition element that has: (i) two readily available oxidation states separated by one electron, (ii) reasonable affinity towards a halogen atom, (iii) an expandable coordination sphere to accommodate a (pseudo) halogen. Mostly used catalysts in ATRP are based on copper, nickel, iron and ruthenium. The ligands have two main functions: they solubilize the metal in the organic reaction media and secondly, they control the selectivity by steric and electronic effects. The initiator has the function of forming an initiating radical species via homolytic cleavage of the C-X bond. Most of the initiators are organic halides with proper substituents that through electric and steric effects stabilize the radical species formed. So organic halides usually possess surplus halogens, or conjugated substituents such as allyl, aryl, carbonyl and cyano groups. Haloalkanes, allyl halides, halonitriles, halo ketones and haloesters have been widely employed [92]. The initiator can be also a polymer. Macroinitiators can be designed by attaching a functional group to a halogen compound such as a haloester, (haloalkyl)benzene, haloalkane, or sulfonyl halide [92]. For instance, random, gradient and block copolymers of 2-(Dimethylamino)ethyl methacrylate (DMAEMA) and *n*-butyl methacrylate (BMA) were synthesized using CuBr as metal catalyst, 2,2'-bipyridine (bpy) as ligand and a methoxy-poly(ethylene glycol) macroinitiator (mPEG-Br) [99]. This system was taken as a benchmark and properly modified to prepare am-

phiphilic copolymers suitable for giant hybrid vesicles, the synthetic procedure will be described in section 4.3.2 and commented in section 4.4.2.

4.2 Polymeric vesicles and hybrid polymer/lipid vesicles

Introduction. Polymeric vesicles or polymersomes are self-assembled structures of amphiphilic block copolymers made of hydrophilic and hydrophobic covalently linked blocks [100]. Compared to liposomes, polymersomes have a longer stability and a greater tunability. The stability is due to the major membrane thickness that affects the mechanical properties of the membrane (for example, polymeric vesicles are less permeable to solutes compared to liposomes). The tunability is accomplished by varying the chemical composition of the copolymers. Although polymersomes have an increased stability, the biocompatible nature typical of lipids is difficult to achieve: the dilution of block copolymers in composite membranes with lipids can reduce health risks and make these systems suitable for in vivo applications. Therefore, hybrid lipid-diblock copolymer giant unilamellar vesicles or "lipopolymersomes" incorporate the advantages of phospholipids and copolymers in the same vesicle membrane [100].

Formation of polymersomes. The main block copolymers able to form vesicles are poly(ethyleneoxide-*b*-ethylethylene) (PEO-PEE) [101], poly(styrene-*b*-acrylic acid) (PS-PAA) [102], poly(ethyleneoxide-*b*-butadiene) (PEO-PBD) [103], poly(ethyleneoxide-*b*-isobutylene) (PEO-PIB) [104], poly(ethyleneoxide-*b*-butadiene) (PEO-PBD) [103], poly(ϵ -caprolactone)-*b*-poly(ethylene glycol) (PCL-PEG) [105] and poly(dimethyl siloxane)-*b*-poly(2-methyloxazoline) (PDMS-PMOXA) [106]. Pure and hybrid polymeric vesicles can be synthesized with the same methods used for liposomes: the most popular procedures are (i) the film hydration and its modified version, the electroformation (method 1a and 1b of Figure 2.2), (ii) the cosolvent addition (adapted from method 6 reported in Figure 2.2 for liposomes) in which the dissolution of a block copolymer in a water-miscible solvent is followed by the slow addition of water and subsequently the organic solvent is removed through evaporation or dialysis [107]. The formation of polymersomes is controlled by several factors: the glass transition temperature (T_g) that is responsible for the chain mobility, the molecular weight, the weight fraction of hydrophilic block (f_{phil}) and the parameter of interaction with water of the hydrophobic blocks (χ). For block copolymers with high χ , vesicles are favoured when $f_{\text{phil}} = 20\text{-}40\%$, at $f_{\text{phil}} = 45\text{-}55\%$ cylindrical micelles tend to form, at $f_{\text{phil}} = 55\text{-}70\%$ spherical micelles are predominantly formed [108]. However these parameters are not universal: sometimes the morphology cannot be predicted exclusively from the weight fraction of the hydrophilic block (f_{phil}), but even the experimental conditions (methods of preparation, use of co-solvent,...)

influence the thermodynamics and the kinetics of polymersomes formation [107]. In mixed systems lipid/polymer, the membrane structure (homogeneous membrane or phase separation with domains formation) is controlled by: (i) the discrepancy of chemical composition, (ii) the size of hydrophobic segments between polymers and lipids and (iii) the physical state of the components [109]. The discrepancy of chemical composition can be evaluated with the Hildebrand solubility parameter (δ): it is directly proportional to the cohesive energy density (the amount of energy needed to completely remove unit volume of molecules from their neighbours to infinite separation) and provides a numerical estimate of the degree of interaction between materials. The solubility parameter (δ) of hydrocarbon moieties in phospholipids is $\delta = 9.1 \text{ cal}^{1/2}/\text{cm}^{3/2}$, the solubility parameters of two polymer blocks, commonly used for the polymersomes formation, PDMS and PIB are respectively $\delta = 7.3 \text{ cal}^{1/2}/\text{cm}^{3/2}$, and $\delta = 7.7 \text{ cal}^{1/2}/\text{cm}^{3/2}$ [109]. These similar values suggest a good chemical compatibility between the components. The difference in size between the polymeric and lipid membranes is also called hydrophobic mismatch. The usual bilayer thickness of liposomes is 3-5 nm, it varies from 5 to 50 nm for polymersomes according to the molecular weight and the hydrophilic weight fraction. The physical state of lipids (gel state at $T < T_m$, fluid state at $T > T_m$) and the glass transition temperature of the polymers (T_g) control the flexibility of the carbon chains. The combined effect of the size gap and the chain flexibility on the formation of domains is depicted in Figure 4.2. The formation of a lipid domain implies a high line tension at the lipid/polymer boundaries. To reduce the energetic cost, the polymer chains can deform elastically to adapt to the lipid chains (scenario described in Figure 4.2 a). If the adaptation cannot be achieved (high T_g or high hydrophobic mismatch), the formation of domains is unlikely and a homogeneous mixture of the components is expected (scenario described in Figure 4.2 b) [109]. The main behaviours experimentally observed for poly(dimethyl siloxane)-*g*-poly(ethyleneoxide) (PDMS-*g*-PEO) hybrid vesicles are illustrated in Figure 4.3. The block copolymer chosen has a membrane thickness close to that of liposomes ($\sim 5 \text{ nm}$). In presence of DPPC ($T_m = 41 \text{ }^\circ\text{C}$, gel state) micrometric lipid domains are observed in a large composition range. When associated with POPC (fluid state, $T > T_m$), PDMS-*g*-PEO spontaneously forms vesicles with micrometric lipid domains that evolve into separated liposomes and polymersomes through a process of budding and fission [109, 110]. The sketches of Figure 4.3 illustrate the cases obtained by the study of confocal microscopy images: fluorescent molecules that selectively interact with the lipids or polymers are used as membrane probes. Even if the overview of these hybrid structures refers to PDMS-*g*-PEO copolymers, it can be used as a guideline for vesicles made of different block copolymers.

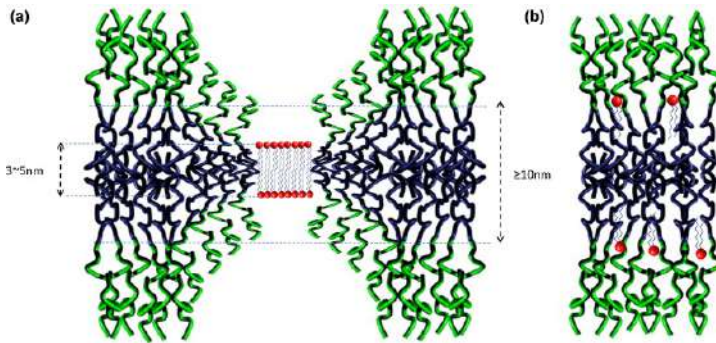


Figure 4.2: a) Elastic deformation of polymer chains at the boundary lipid/polymer. b) Homogeneous mixture of the components when the adaptation cannot be achieved. Reproduced from [109], licensed under Creative Commons Attribution (CC BY-NC-ND 3.0).

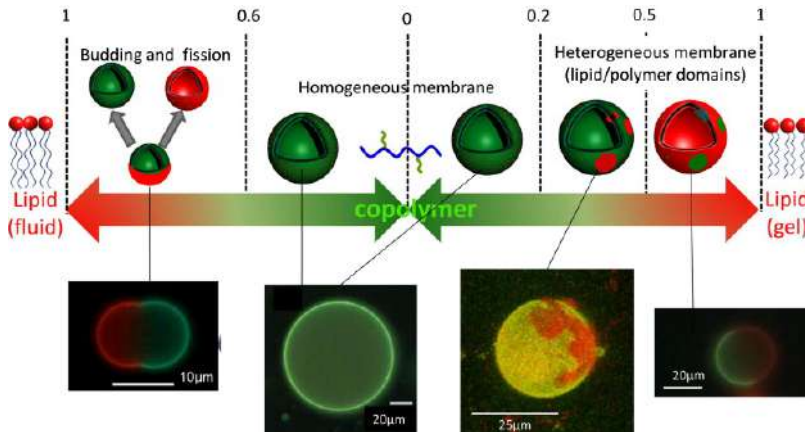


Figure 4.3: Overview of the different hybrid vesicular structures that can be obtained varying the molar composition and thermodynamic phase of the phospholipid. Sketches on the top lines illustrate the different cases obtained by study of confocal fluorescence microscopy images. All these hybrid vesicles were formulated with polydimethylsiloxane-graft-poly(ethylene oxide) and dipalmitoylphosphatidylcholine (DPPC) in the gel state or 1-palmitoyl-2-oleoyl-sn-glycero-3-phosphocholine (POPC) in the fluid state at room temperature. Reproduced from [109], licensed under Creative Commons Attribution (CC BY-NC-ND 3.0).

pH-responsive polymersomes. As stated before, a peculiarity of polymersomes is the chemical tunability: in fact, the addition of functional groups allows the synthesis of stimuli-responsive polymersomes that respond to changes in environment such as temperature, pH and light (common stimuli responsive polymers are described in section 1.2) [100]. pH-sensitive polymersomes can be constructed from polypeptides or block copolymers. Vesicles based on poly(ethylene glycol)-*b*-poly((2-(diethylamino) ethyl

methacrylate)-*s*-(3-(trimethoxysilyl) propyl methacrylate)) (PEG-*b*-P(DEA)-*s*-TMSPMA) where TMSPMA, after the hydrolysis of the $-\text{Si}(\text{OCH}_3)_3$ groups react to give siloxane cross-links have been synthesized in 2005 by Armes *et al.* The pH-sensitivity of such vesicles increases for higher DEA contents and the hydrodynamic diameter increases at low pH (at low pH, more amine units are protonated increasing the electrostatic repulsions) [111]. A similar behaviour was observed for another pH-sensitive copolymer, mPEG-*b*-(PMMA-*co*-PDMAEMA), intensively studied in our research group in its linear and branched form. Nano vesicles produced with this copolymer release hydrophilic and hydrophobic drugs like paclitaxel (PTX), ampicillin sodium salt and curcumin in a pH-dependent fashion, and the low cytotoxicity assessed through MTT assays makes these vesicles suitable for drug delivery applications [112, 113]. Moreover, these polymeric vesicles modify the size with the pH of the solution. The histograms extrapolated from Dynamic Light Scattering (DLS) analysis of Figure 4.4 show how the molecular weights and the percentage of DMAEMA allow to control the degree of swelling, while polymeric vesicles without DMAEMA have the same dimensions with the pH (no swelling for copolymers AB and $(\text{AB})_2$ of Figure 4.4) [112].

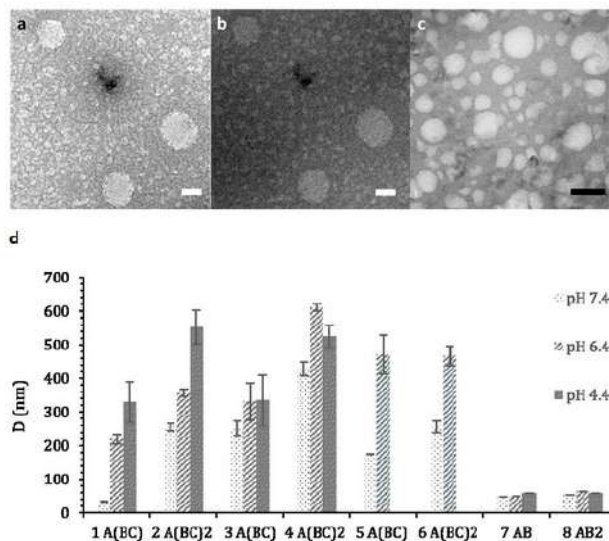


Figure 4.4: a) and b) TEM images of vesicles from A(BC) with a molecular weight of 19 kDa and 22 % of DMAEMA. c) TEM images of vesicles from A(BC) with a molecular weight of 11 kDa and 28 % of DMAEMA. The scale bar is 100 nm. d) Diameter of vesicles measured in buffer solutions at pH 7.4, 6.4 and 4.4 using DLS. AB and AB_2 do not contain DMAEMA, A(BC) copolymers have mPEG unit of 5 kDa and DMAEMA that varies from 20 to 60 %. Reprinted with permission from [112].

4.3 Experimental section

4.3.1 Materials for polymers synthesis and purification

Copper bromide (CuBr_2), 2,2'-bipyridine (bpy), ascorbic acid, tin (II) 2-ethylhexanoate ($\text{Sn}(\text{EH})_2$), 2-bromoisobutyryl bromide (BMPB), 4-(dimethylamino)pyridine (DMAP), triethylamine (TEA), basic alumina, Sephadex LH-20 and the solvents: chloroform, toluene, acetonitrile, dimethylformamide (DMF) and methanol were purchased by Aldrich and used without any further purification. Poly(ethylene glycol) monomethylether (m-PEG) with two different molecular weights ($M_n = 5000$ Da with $M_w/M_n = 1.02$ and $M_n = 2000$ Da with $M_w/M_n = 1.16$) was purchased from Aldrich and functionalized to create a macroinitiator mPEG-Br suitable for the ARGET ATRP (Synthesis in Appendix C.2). A fluorescent monomer that incorporates a BODIPY moiety (BODIPY-DMAEMA) was synthesized and characterized at the University of Insubria by Prof. Banfi's research group (Synthetic procedure and reaction scheme in Appendix C.3). MMA and DMAEMA were passed through a column filled with basic alumina prior to use to remove the inhibitors. All manipulations involving air-sensitive compounds were carried out under nitrogen atmosphere using Schlenk techniques.

4.3.2 Polymer synthesis

Linear copolymers comprising MMA and DMAEMA were synthesized in DMF at $T = 60$ °C (chemical scheme in Figure 4.7). Stock solutions of ascorbic acid, Cu (II) and bpy were prepared separately dissolving respectively 20 mg, 2.2 mg and 17.1 mg in 10 mL of DMF. The concentrations of the prepared solutions are: $[\text{CuBr}_2] = 1 \times 10^{-3}$ M, $[\text{bpy}] = 1 \times 10^{-2}$ M and $[\text{ascorbic acid}] = 1 \times 10^{-2}$ M. In a typical run, 100 μL of CuBr_2 stock solution, 100 μL of bpy stock solution, 0.5-4.5 mL of MMA and DMAEMA (Table 4.1 for the volumes used), 1.2 μL of 2-bromoisobutyryl bromide (BMPB), 100 μL of ascorbic acid stock solution were added in a 50 mL glass flask, under nitrogen atmosphere. The final molar ratios are CuBr_2 : bpy: ascorbic acid: BMPB = 1:10:10:0.1. After the addition of the last reactant (ascorbic acid), the mixture was thermostated at 60 °C and magnetically stirred. The reaction was stopped after 8 hours with n-hexane that favours the precipitation of the copolymer. The solid was then filtered and dried in vacuum at 40 °C.

$^1\text{H-NMR}$: δ 0.88-1.04 (CH_3 main chain), 1.82-1.91 (CH_2 main chain), 2.30 ($-\text{N}(\text{CH}_3)_2$), 2.56 ($-\text{O}-\text{CH}_2-\text{CH}_2-\text{N}(\text{CH}_3)_2$), 3.59 (OCH_3), 4.06 ($\text{O}-\text{CH}_2-\text{CH}_2-\text{N}(\text{CH}_3)_2$). $^{13}\text{C-NMR}$: δ 16.9-19.1 (CH_3 main chain), 44.9-45.3 (quaternary carbon in the main chain), 46.2 ($\text{N}(\text{CH}_3)_2$), 52.2 (OCH_3 , MMA), 54.6 (CH_2 main chain), 57.6 ($-\text{O}-\text{CH}_2-\text{CH}_2-\text{N}(\text{CH}_3)_2$), 63.5 ($-\text{O}-\text{CH}_2-\text{CH}_2-\text{N}(\text{CH}_3)_2$), 176.3-178.2 ($-\text{C}=\text{O}$).

The molar fractions of MMA (F_{MMA}) and DMAEMA (F_{DMAEMA}) in the final

copolymer were evaluated from ^1H NMR (^1H NMR spectrum and assignment of the signals in Appendix C.4) with the equations

$$F_{\text{MMA}} = \frac{2I_{\text{MMA}}}{2I_{\text{MMA}} + 3I_{\text{DMAEMA}}} \quad (4.1)$$

$$F_{\text{DMAEMA}} = \frac{3I_{\text{DMAEMA}}}{2I_{\text{MMA}} + 3I_{\text{DMAEMA}}} \quad (4.2)$$

where I_{MMA} is the signal corresponding to the units $-\text{OCH}_3$ of MMA and I_{DMAEMA} integrates the protons of DMAEMA ($-\text{O}-\text{CH}_2-\text{CH}_2-\text{N}(\text{CH}_3)_2$). Block copolymers made of hydrophilic mPEG segments and hydrophobic chains of MMA and DMAEMA were synthesized using the same stock solutions prepared for the synthesis of poly(MMA-*co*-DMAEMA), but 2-bromoisobutyryl bromide was replaced with the macroinitiator mPEG-Br. In a typical run, 100 μL of CuBr_2 stock solution (1×10^{-2} M), 100 μL of bpy stock solution (1×10^{-2} M), different volumes of MMA and DMAEMA (depending on the initial feed ratio), 100 mg of the macroinitiator, 100 μL of ascorbic acid stock solution (1×10^{-2} M) and 2 mL of solvent were added in a 50 mL glass flask, under nitrogen atmosphere. After the addition of the last reactant (reducing agent), the mixture was thermostated at 60 $^\circ\text{C}$ and magnetically stirred. The reaction was stopped with n-hexane. The solid was then filtered, washed with cold methanol and dried in vacuum at 40 $^\circ\text{C}$.

^1H -NMR: δ 0.87-1.03 (CH_3 main chain), 1.83-1.91 (CH_2 main chain), 2.30 ($-\text{N}(\text{CH}_3)_2$), 2.58 ($-\text{O}-\text{CH}_2-\text{CH}_2-\text{N}(\text{CH}_3)_2$), 3.61 (OCH_3), 3.66 (OCH_2CH_2-), 4.08 ($\text{O}-\text{CH}_2-\text{CH}_2-\text{N}(\text{CH}_3)_2$). ^{13}C -NMR: δ 16.9-19.1 (CH_3 main chain), 44.9-45.3 (quaternary carbon in the main chain), 46.2 ($\text{N}(\text{CH}_3)_2$), 52.2 (OCH_3 , MMA), 54.6 (CH_2 main chain), 57.6 ($\text{O}-\text{CH}_2-\text{CH}_2-\text{N}(\text{CH}_3)_2$), 63.5 ($\text{O}-\text{CH}_2-\text{CH}_2-\text{N}(\text{CH}_3)_2$), 70.9 ($\text{O}-\text{CH}_2-\text{CH}_2-$), 176.3-178.2 ($-\text{C}=\text{O}$).

The molar fractions of mPEG (F_{mPEG}), MMA (F_{MMA}) and DMAEMA (F_{DMAEMA}) in the final copolymer were evaluated from ^{13}C NMR (^{13}C NMR is preferable to ^1H NMR because of the partial overlap between the ^1H NMR signals of the methoxyl group in MMA and the methylenic group in mPEG, ^1H NMR and ^{13}C NMR spectra are reported in Appendix C.4) using the following equations:

$$F_{\text{mPEG}} = \frac{I_{\text{mPEG}}}{I_{\text{mPEG}} + 2I_{\text{MMA}} + I_{\text{DMAEMA}}} \quad (4.3)$$

$$F_{\text{MMA}} = \frac{2I_{\text{MMA}}}{I_{\text{mPEG}} + 2I_{\text{MMA}} + I_{\text{DMAEMA}}} \quad (4.4)$$

$$F_{\text{DMAEMA}} = \frac{I_{\text{DMAEMA}}}{I_{\text{mPEG}} + 2I_{\text{MMA}} + I_{\text{DMAEMA}}} \quad (4.5)$$

where I_{mPEG} is the integration of the signal relative to mPEG units: $-\text{OCH}_2\text{CH}_2-$, I_{MMA} is the signal corresponding to the units $-\text{OCH}_3$ of MMA

and I_{DMAEMA} integrates the six protons of the amine group of DMAEMA ($-\text{N}(\text{CH}_3)_2$). The molar mass of the copolymers was determined by the degree of polymerization (DP), by the molecular weights of the monomers (M) and the signal intensities I :

$$M_n = \text{DP}_{\text{mPEG}} (M_{\text{EO}}) + \text{DP}_{\text{MMA}} (M_{\text{MMA}}) + \text{DP}_{\text{DMAEMA}} (M_{\text{DMAEMA}}) \quad (4.6)$$

where:

$$\text{DP}_{\text{mPEG}} = (M_{\text{EO}}) / 44; \quad (4.7)$$

$$\text{DP}_{\text{MMA}} = \text{DP}_{\text{mPEG}} (2I_{\text{MMA}}/I_{\text{mPEG}}); \quad (4.8)$$

$$\text{DP}_{\text{DMAEMA}} = \text{DP}_{\text{mPEG}} (I_{\text{DMAEMA}}/I_{\text{mPEG}}) \quad (4.9)$$

The fluorescent labelling was done adding 5 mg of the fluorescent monomer BODIPY-DMAEMA (BODIPY-DMAEMA: MMA \simeq 1:1000) to the reaction mixture containing 100 μL of Cu (II) stock solution (1×10^{-2} M), 100 μL of bpy (1×10^{-2} M), 100 mg mPEG-Br, different volumes of MMA and DMAEMA, 100 μL of reducing agent (ascorbic acid or $\text{Sn}(\text{EH})_2$, 1×10^{-2} M) and 2 mL of solvent (DMF or toluene). The reaction was performed under nitrogen atmosphere, magnetically stirred and thermostated at a temperature of 60 $^\circ\text{C}$. The reaction was stopped with n-hexane. The solid was then filtered, dried in vacuum at 40 $^\circ\text{C}$ and purified through a column chromatography loaded with lipophilic Sephadex.

$^1\text{H-NMR}$: δ 0.87-1.04 (CH_3 main chain), 1.27 ppm (4 CH_2 of the alkylic chain of the BODIPY-DMAEMA), 1.83-1.91 (CH_2 main chain), 2.30 ($-\text{N}(\text{CH}_3)_2$), 2.59 ($-\text{O}-\text{CH}_2-\text{CH}_2-\text{N}(\text{CH}_3)_2$), 3.61 (OCH_3), 3.65 (OCH_2CH_2-), 4.08 ($\text{O}-\text{CH}_2-\text{CH}_2-\text{N}(\text{CH}_3)_2$). $^{13}\text{C-NMR}$: δ 16.5-18.7 (CH_3 main chain), 29.7 ppm (4 CH_2 of the alkylic chain of the BODIPY-DMAEMA), 44.6-44.9 (quaternary carbon in the main chain), 45.8 ($\text{N}(\text{CH}_3)_2$), 51.8 (OCH_3 , MMA), 54.4 (CH_2 main chain), 57.2 ($\text{O}-\text{CH}_2-\text{CH}_2-\text{N}(\text{CH}_3)_2$), 63.1 ($\text{O}-\text{CH}_2-\text{CH}_2-\text{N}(\text{CH}_3)_2$), 70.6 ($\text{O}-\text{CH}_2-\text{CH}_2-$), 176.3-178.2 ($-\text{C}=\text{O}$).

The ^{13}C NMR, ^1H NMR and HSQC spectra for the purified copolymer are shown in Appendix C.4 together with a chemical scheme indicating the assignment of each signal. The molar fractions of mPEG (F_{mPEG}), MMA (F_{MMA}), DMAEMA (F_{DMAEMA}) and BODIPY-DMAEMA ($F_{\text{BODIPY-DMAEMA}}$) in the final copolymer were evaluated from ^{13}C NMR using the following equations:

$$F_{\text{mPEG}} = \frac{I_{\text{mPEG}}}{I_{\text{mPEG}} + 2I_{\text{MMA}} + I_{\text{DMAEMA}} + I_{\text{BODIPY-DMAEMA}}/2} \quad (4.10)$$

$$F_{\text{MMA}} = \frac{2I_{\text{MMA}}}{I_{\text{mPEG}} + 2I_{\text{MMA}} + I_{\text{DMAEMA}} + I_{\text{BODIPY-DMAEMA}}/2} \quad (4.11)$$

$$F_{\text{DMAEMA}} = \frac{I_{\text{DMAEMA}}}{I_{\text{mPEG}} + 2I_{\text{MMA}} + I_{\text{DMAEMA}} + I_{\text{BODIPY-DMAEMA}}/2} \quad (4.12)$$

$$F_{\text{fluor}} = \frac{I_{\text{fluor}}/2}{I_{\text{mPEG}} + 2I_{\text{MMA}} + I_{\text{DMAEMA}} + I_{\text{BODIPY-DMAEMA}}/2} \quad (4.13)$$

The molar mass of the copolymers was determined by the degree of polymerization (DP), by the molecular weights of the monomers (M) and the signal intensities I :

$$M_n = \text{DP}_{\text{mPEG}} (M_{\text{EO}}) + \text{DP}_{\text{MMA}} (M_{\text{MMA}}) + \text{DP}_{\text{DMAEMA}} (M_{\text{DMAEMA}}) + \text{DP}_{\text{BODIPY-DMAEMA}} (M_{\text{BODIPY-DMAEMA}}) \quad (4.14)$$

where:

$$\text{DP}_{\text{mPEG}} = (M_{\text{EO}}) / 44; \quad (4.15)$$

$$\text{DP}_{\text{MMA}} = \text{DP}_{\text{mPEG}} (2I_{\text{MMA}}/I_{\text{mPEG}}); \quad (4.16)$$

$$\text{DP}_{\text{DMAEMA}} = \text{DP}_{\text{mPEG}} (I_{\text{DMAEMA}}/I_{\text{mPEG}}); \quad (4.17)$$

$$\text{DP}_{\text{BODIPY-DMAEMA}} = \text{DP}_{\text{mPEG}} (I_{\text{BODIPY-DMAEMA}}/2I_{\text{mPEG}}) \quad (4.18)$$

4.3.3 Polymer characterization

The polymers were characterized by NMR for the composition and by Gel Permeation Chromatography (GPC) for the polydispersity index ($\text{PDI} = M_w/M_n$). ^1H NMR spectra and ^{13}C NMR were recorded in CDCl_3 as a solvent using a Bruker 400 MHz spectrometer ($D_1 = 5$ s for ^{13}C NMR). Chemical shifts (δ) are listed as parts per million. ^1H NMR spectra are referenced using the residual solvent peak at $\delta = 7.26$ ppm for CDCl_3 , in ^{13}C NMR spectra the residual solvent peak is at $\delta = 77.2$ ppm for CDCl_3 . The GPC was conducted with a Waters 1525 binary system equipped with a Waters 2414 RI detector using four Styragel columns (range 1000-1,000,000 Å) in tetrahydrofuran (THF) as eluent at a flow rate of 1.0 mL/min at 25 °C. Linear polystyrene standards were used for calibration. Differential Scanning Calorimetry (DSC, Q2000, TA Instruments) was used to measure the glass transition temperature (T_g) of the copolymers (two runs of heating and one run of cooling with a scan rate of 20 K/min). Measurements of contact angle (Ossila Contact Angle Goniometer) were performed at different pH values on the copolymer selected

for the hybrid vesicles preparation. A solution of the copolymer dissolved in CHCl_3 at a concentration of 5 mg/mL was spread over a microscope glass slide (area covered 25 mm \times 75 mm) and left at room temperature to let the chloroform evaporate. Four kind of buffer solutions were prepared to construct a titration curve: phosphate/citrate (pH 3-8), ammonia/ammonium (pH 8.5-9.5), sodium carbonate/sodium bicarbonate (pH 10-11), di-sodium hydrogen phosphate/sodium hydroxide (pH 11.5-12). The procedure applied for the contact angle measurements is adapted from refs. [114, 115].

4.3.4 Preparation and characterization of Giant Hybrid Unilamellar Vesicles

Materials. In the electroformation method, POPC (Sigma) and mPEG-*b*-(PMMA-*co*-PDMAEMA) were dissolved in chloroform to prepare stock solutions at 1 mg/mL. A stock solution of sucrose, [sucrose] = 240 mM was prepared for the hydration step and filtered before use.

In the droplet transfer method, POPC (Sigma) and mPEG-*b*-(PMMA-*co*-PDMAEMA) stock solutions were dissolved in Mineral oil ([POPC] = 3 mM and [Copolymer] = 5 mg/mL). 1,2-dioleoyl-*sn*-glycero-3-phosphoethanolamine-N-(lissamine rhodamine B sulfonyl) (18:1 Liss Rhod PE) provided from Avanti Polar Lipids was dissolved in chloroform ([18:1 Liss Rhod PE] = 1 mg/mL), the fluorescent block copolymers were dissolved in chloroform at the concentration of 10 mg/mL.

Electroformation method. The electroformation is a modification of the film hydration method described in section 2.1. The application of an AC field leads to a higher GUV yield compared to the film hydration because of a periodic redistribution of the charges [116]. Vesicles were prepared following the steps below:

- 1) ITO conductive glass slides were washed first with water, secondly with ethanol and finally with chloroform and dried for 30 minutes in a vacuum desiccator.
- 2) 5 μL of the lipid and/or polymer solution were spread on the conductive side of the ITO glass slide. The chloroform was evaporated in a vacuum desiccator for three hours.
- 3) A Teflon ring was applied around the film and 255 μL of sucrose 240 mM were slowly added to the lipid/polymer layer. The second ITO slide was positioned on top of the ring (scheme in Figure 4.5 a). The prepared slide was positioned in the device for the electroformation (Vesicle Prep Pro, Nanion technologies Figure 4.5 b). The vesicles formed were observed with a phase contrast microscope (Figure 4.5 c).

Droplet transfer method. The droplet transfer method was applied as in section 2.2.2, but adapted for polymeric hybrid vesicles. POPC and mPEG-*b*-(PMMA-*co*-PDMAEMA) were introduced both in the microemulsion and in the interface. The fluorescent probes (18:1 Liss Rhod PE and fluorescent

copolymers) were added in small amounts (maximum 5 μL) to the amphiphiles dissolved in mineral oil and the microemulsion was prepared only after evaporation of chloroform.

Instruments and softwares. The mixed membranes were characterized with a confocal microscope (TIRF OLYMPUS FV1000 Confocal Microscope) at University of Toulouse. The fluorescent polymer and the fluorescent lipid were excited respectively at 488 nm, with an Ar laser, and 561 nm, with DPSS 561 laser and the fluorescence was collected with photomultiplier tubes PMTs in the wavelength ranges 498-530 nm and 571-630 nm.

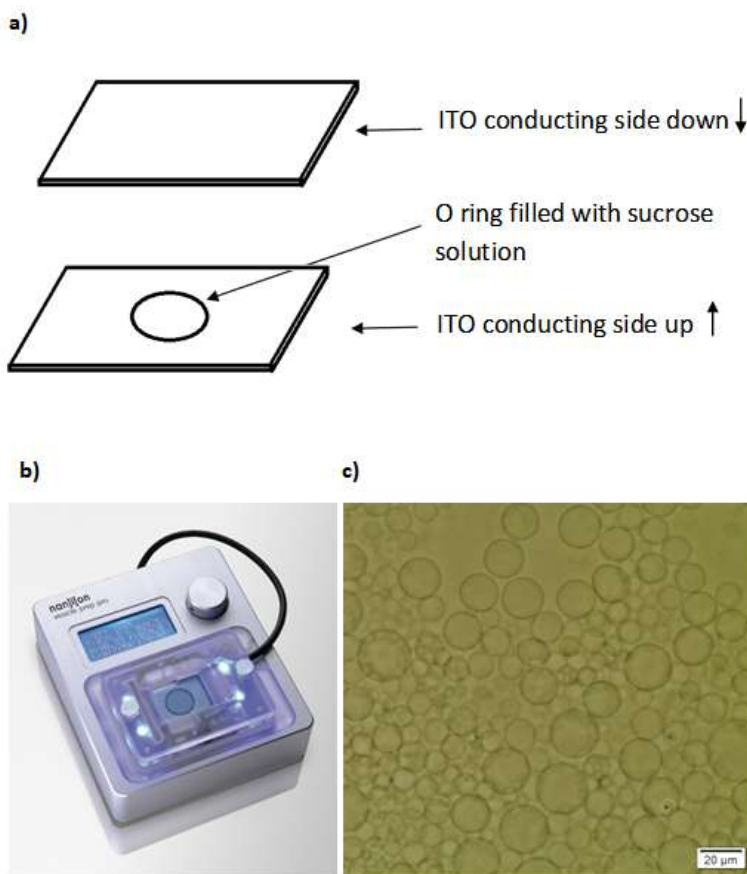


Figure 4.5: a) Scheme of the assembling procedure of the ITO slides. b) Vesicle Prep Pro setup including the slide with film and sucrose solution. c) Giant unilamellar vesicles obtained with pure POPC.

4.4 Results and discussion

4.4.1 Rational design of amphiphilic copolymers

As stated in the synopsis (section 1.4), the main goal of the thesis is the coupling of a pH-dependent clock reaction with pH-sensitive giant hybrid vesicles. In chapter 3, the coupling was achieved blending the pH-stable phospholipid POPC with the pH-sensitive oleic acid inducing a division of one vesicle into two daughter vesicles under certain conditions. In this chapter, hybrid vesicles of POPC and pH-sensitive copolymers were prepared and characterized to accomplish another kind of chemomechanical answer: a pH-sensitive swelling-deswelling. While the division of POPC: oleic acid vesicles can find its main application in the Origin of Life studies, the swelling-deswelling deformation could be exploited for the engineering of programmed drug delivery systems. To this end, a rational design in terms of molecular weight, composition and hydrophilic/hydrophobic ratio of amphiphilic copolymers is necessary to control the stability and the chemomechanical deformation of the vesicles. The pH-sensitive copolymers synthesized for tuning the swelling behaviour are linear, three components A(BC) copolymers where A is a hydrophilic block of methoxy-poly(ethylene glycol) (mPEG), while BC is a copolymer containing methyl methacrylate (MMA) and 2-(Dimethylamino)ethyl methacrylate (DMAEMA) (Figure 4.6). The methoxy-poly(ethylene glycol) (mPEG) is neutral, highly hydrophilic and biocompatible [117], thus suitable for future biomedical applications, moreover the methoxy group is inert in the reaction conditions used during the copolymers synthesis. The chain based on methyl methacrylate (MMA) is biocompatible and highly hydrophobic, 2-(Dimethylamino)ethyl methacrylate (DMAEMA) has a carbon backbone similar to MMA, but includes the pH-sensitive moiety $-N(CH_3)_2$. The pK_a of the monomer DMAEMA is ~ 8.4 [118], it reduces to ~ 7 in the homopolymer [119, 120], and it can be modulated varying the percentage of the non-responsive monomer MMA in the random copolymer [121]. To induce a pH-sensitive swelling-deswelling behaviour the DMAEMA units must be distributed in the hydrophobic portion of the copolymer: this part will constitute the double layer of the vesicles and the expected behaviour is a swelling at acidic pH and a deswelling at neutral/basic pH. The swelling motion is caused by the increased electrostatic repulsions since at low pH the number of the protonated DMAEMA units increases (Figure 4.6).

In the introductory section (section 4.2), the weight fraction of the hydrophilic portion was introduced as a key parameter for the control of the polymeric vesicles: generally, vesicles are favoured when $f_{\text{phil}} = 20\text{-}40\%$, while cylindrical micelles are common for $f_{\text{phil}} = 45\text{-}55\%$, and spherical micelles are predominant for $f_{\text{phil}} = 55\text{-}70\%$. In block copolymers mPEG-*b*-(PMMA-*co*-PDMAEMA) the weight fraction of the hydrophilic portion varies according to the pH: the chains of DMAEMA are considered hydrophobic when the pH is largely above the pK_a

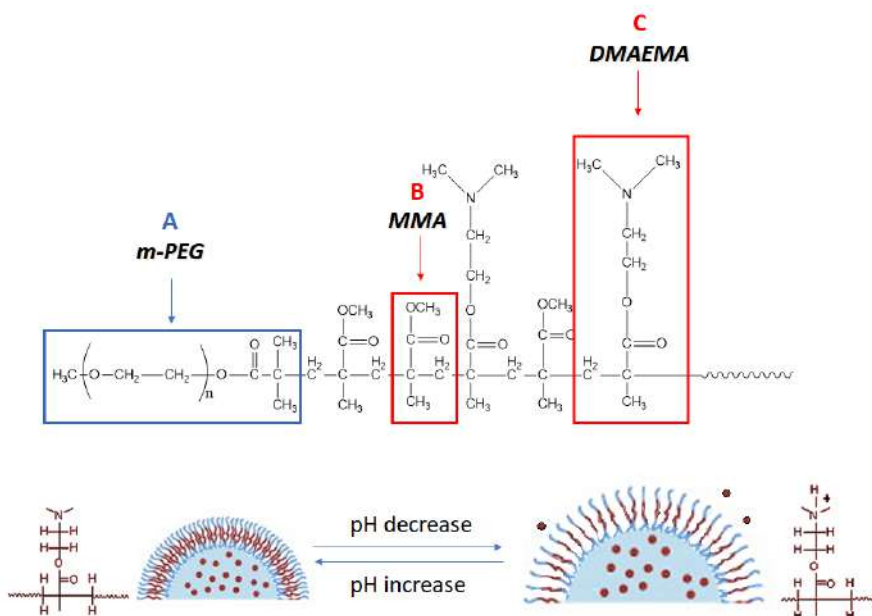


Figure 4.6: Structure of the copolymer mPEG-*b*-(PMMA-*co*-PDMAEMA) and mechanism of swelling.

and hydrophilic at low pH with the increase of the protonated amine groups. In this case, it is impossible to calculate a unique value of f_{phil} and thus to predict the formation of polymersomes or micelles, however the studies mentioned in the introduction (section 4.2) showed that these block copolymers are able to form nanovesicles for a wide range of compositions (TEM in Figure 4.4 a-c) [112] and, interestingly for our purposes, they present a pH-dependent swelling behaviour (DLS in Figure 4.4 d). The strong increase in size (up to 10 times passing from pH 7.4 to pH 4.4) encouraged us to synthesize and characterize polymeric giant hybrid vesicles (POPC: mPEG-*b*-(PMMA-*co*-PDMAEMA)).

4.4.2 Identification of the experimental conditions and relative reactivities of the monomers

The copolymers mPEG-*b*-(PMMA-*co*-PDMAEMA) were synthesized using a modified version of the ATRP method (section 4.1), the activators regenerated by electron transfer ATRP (ARGET ATRP) [122, 123]. In this version, the amount of the metal catalyst is significantly reduced to few ppm: the metal is used in its highest oxidation state and the active species is continuously regenerated by appropriate reducing agents such as tin (II) 2-ethylhexanoate ($\text{Sn}(\text{EH})_2$), glucose, ascorbic acid, hydrazine and phenyl hydrazine [123, 124]. ARGET ATRP offers numerous advantages compared to a conventional ATRP: it can be performed in the presence of limited amount of air, the

reaction times are reduced, furthermore the purification steps are simplified: the low amounts of catalyst do not have to be removed from the final polymer and the two monomers MMA and DMAEMA are not dried and distilled before use. So far, ARGET ATRP enabled the synthesis of well defined homopolymers like poly(2-(dimethylamino)ethyl methacrylate) (PDMAEMA), poly(methyl methacrylate) (PMMA), poly(buthyl methacrylate) (PBMA), polystyrene (PS), polyacrylonitrile (PAN) and related block copolymers like PBMA-*b*-PS and PS-*b*-PAN [122–128]. The use of ARGET ATRP for the synthesis of copolymers made of MMA and DMAEMA has not yet been reported in literature, thus the first step was to estimate the reactivities of the two monomers in the modified ATRP. The copolymers were prepared using 2-bromoisobutyryl bromide (BMPB) as initiator (reaction scheme in Figure 4.7) and the feed composition (indicated through the molar fractions f_{MMA} and f_{DMAEMA}) was systematically varied to evaluate its impact on the final composition (indicated through the molar fractions F_{MMA} and F_{DMAEMA}).

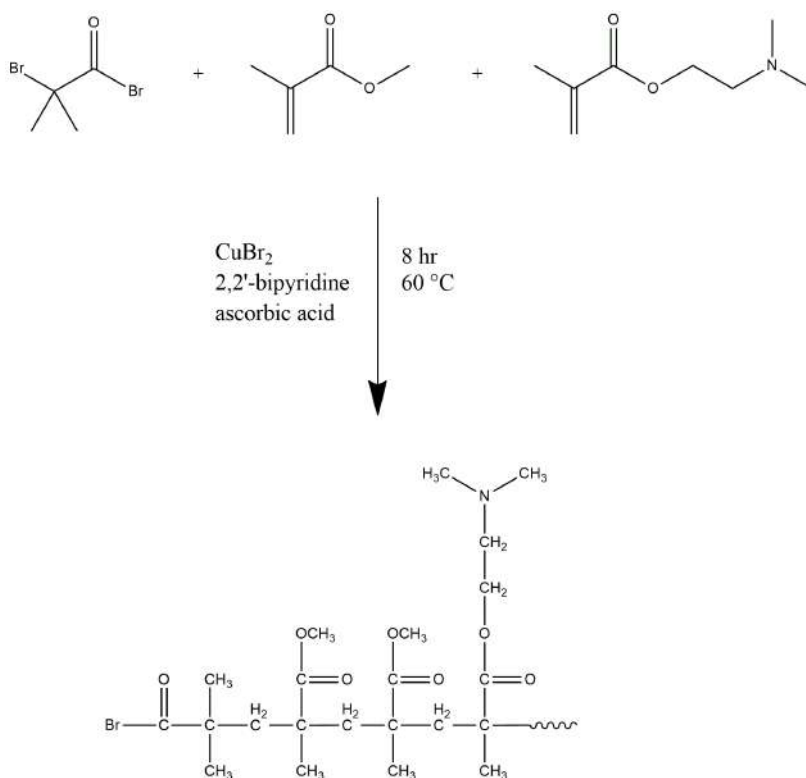


Figure 4.7: Reaction scheme for the synthesis of PMMA-*ran*-PDMAEMA.

The reactivity ratios for the two monomers are defined as $r_{\text{MMA}} = k_{\text{MMA,MMA}}/k_{\text{MMA,DMAEMA}}$ and $r_{\text{DMAEMA}} = k_{\text{DMAEMA,DMAEMA}}/k_{\text{DMAEMA,MMA}}$, where k_i, j are kinetic rate constants for the reaction between two possible radical sites. As shown in Table 4.1, the molar fractions in the copolymer F_{MMA} and F_{DMAEMA} reflect the feed composition f_{MMA} and f_{DMAEMA} . In this case, $r_{\text{MMA}} \simeq r_{\text{DMAEMA}} \sim 1$ and the copolymers are expected to present a random comonomer distribution. The reactivities of the two monomers in ARGET ATRP are in accordance with previously published results on MMA/DMAEMA copolymers produced with other radical polymerizations (*e.g.* the reactivity ratios calculated in ref. [129] are: $r_{\text{MMA}} = 0.71(\pm 7\%)$ and $r_{\text{DMAEMA}} = 1.25(\pm 12\%)$).

Table 4.1: Volumes, molar fractions in the feed (f) and molar fractions in the copolymer (F). The copolymers are indicated as MD _{$x\%$} where the abbreviation M stands for MMA, D is DMAEMA, the subscript is the final molar fraction of DMAEMA

Polymer	V_{MMA} (mL)	V_{DMAEMA} (mL)	f_{MMA}	f_{DMAEMA}	F_{MMA}	F_{DMAEMA}
MD _{88%}	0.5	4.5	0.15	0.85	0.12	0.88
MD _{74%}	1	4	0.29	0.71	0.26	0.74
MD _{53%}	2	3	0.52	0.48	0.47	0.53
MD _{48%}	2.5	2.5	0.61	0.39	0.52	0.48
MD _{34%}	3	2	0.71	0.29	0.66	0.34
MD _{18%}	4	1	0.86	0.14	0.82	0.18

Once evaluated the reactivities of the two monomers in ARGET ATRP, the initiator 2-bromoisobutryl bromide (BMPB) was replaced with the macroinitiator m-PEG-Br (the reaction scheme is in Figure 4.8) to produce amphiphilic block copolymers appropriate for the formation of giant hybrid vesicles.

Surprisingly, the distribution of the two comonomers in the final polymer is different when mPEG-Br is used in lieu of 2-bromoisobutryl bromide. The compositions of the copolymers prepared without solvent (rows 1 and 2 of Table 4.2) suggest a higher reactivity of DMAEMA compared to MMA. The addition of DMF (rows 3 and 4 of Table 4.2), intended to dilute the reaction mixture, confirms the higher reactivity of DMAEMA ($\frac{F_{\text{MMA}}}{F_{\text{DMAEMA}}}$ is still minor than $\frac{[\text{MMA}]_0}{[\text{DMAEMA}]_0} = q_0$).

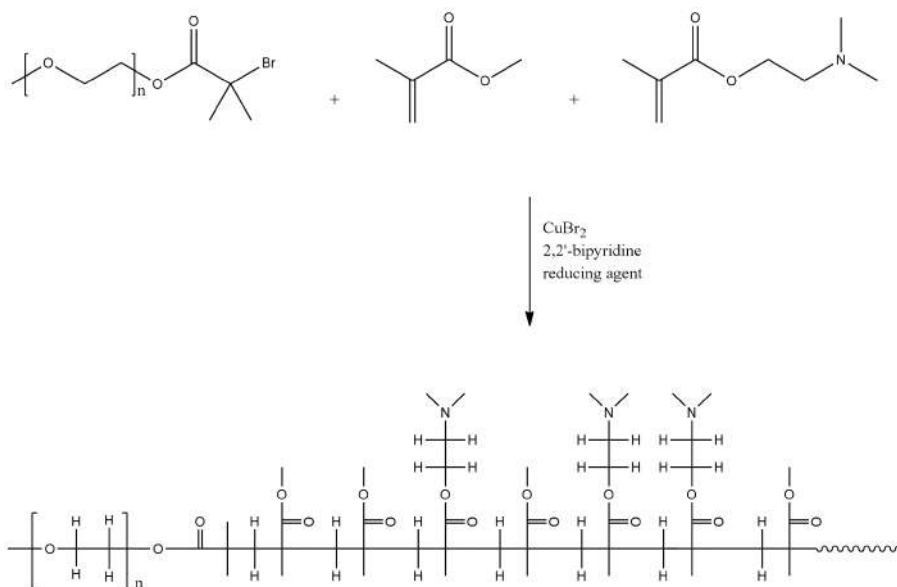


Figure 4.8: Reaction scheme for the synthesis of the copolymers mPEG-*b*-(PMMA-*co*-PDMAEMA).

Table 4.2: Results for mPEG-*b*-(PMMA-*co*-PDMAEMA) obtained by ARGET ATRP conducted at $T = 60\text{ }^\circ\text{C}$ and $q_0 = 1.59$.

Polymer	Polymerization time (h)	DMF (mL)	$\frac{F_{\text{MMA}}}{F_{\text{DMAEMA}}}$	Conversion (MMA, %)	$M_n/10^3$ (Da)	M_w/M_n
P _{5k} MD _{61%}	24	0	0.56	29	260	2.12
P _{5k} MD _{55%}	16	0	0.71	24	224	2.65
P _{5k} MD _{53%}	24	2.5	0.76	37	208	1.88
P _{5k} MD _{53%}	24	10	0.95	37	197	1.57

The marked reactivity of DMAEMA in these preliminary polymerizations was also noticed in conventional ATRP polymerizations of MMA and DMAEMA with mPEG-Br as initiator (unpublished experiments previously performed in our research group). The similarity between the two cases motivated us to investigate more deeply the polymerization kinetics from a theoretical and experimental standpoint. Taking advantage of the wide variety of copolymers synthesized through conventional ATRP, the data of Table 4.3 were used to calculate the reactivity ratios of the two comonomers in the presence of mPEG-

Br. The data of Table 4.3 demonstrate that the copolymers architecture (linear or branched) has no influence on the relative monomer reactivities, however to test if the reaction conditions influence the final composition, mPEG-*b*-(PMMA-*co*-PDMAEMA) copolymers prepared in three different solvents DMF, acetonitrile and toluene are compared in Table 4.4. The copolymers synthesized with the three different solvents (Table 4.4) have all a ratio $\frac{F_{\text{MMA}}}{F_{\text{DMAEMA}}} < q_0$, indicative of the higher reactivity of DMAEMA with respect to MMA, however the ratio $\frac{F_{\text{MMA}}}{F_{\text{DMAEMA}}}$ is much lower in toluene than in the other two solvents, suggesting that the polarity of the solvent may play a role in defining the effective relative reactivities of the comonomers.

Table 4.3: Results for mPEG-*b*-(PMMA-*co*-PDMAEMA) obtained by ATRP conducted in toluene (T = 90 °C). The abbreviation P_x stands for mPEG 5000 or 2000 Da).

Polymer	q_0	$\frac{F_{\text{MMA}}}{F_{\text{DMAEMA}}}$	Conversion (MMA, %)	$M_n/10^3$ (Da)	M_w/M_n
P _{2k} MD _{17%}	7.9	4.2	42	38	1.40
P _{2k} MD _{31%}	3.8	2.0	30	70	1.28
P _{2k} MD _{37%}	3.1	1.4	26	48	1.32
P _{2k} MD _{42%}	2.3	1.2	34	76	1.50
(P _{2k} MD _{8%}) ₂	17	11	57	61	1.52
(P _{2k} MD _{20%}) ₂	7.7	3.6	54	58	1.51
(P _{2k} MD _{34%}) ₂	3.1	1.7	34	62	1.44
(P _{2k} MD _{42%}) ₂	2.6	1.2	42	87	1.61
(P _{2k} MD _{19%}) ₄	7.7	3.8	55	75	1.48
(P _{2k} MD _{23%}) ₄	5.3	3.1	45	80	1.51
(P _{2k} MD _{29%}) ₄	3.8	2.2	47	90	1.51
(P _{2k} MD _{34%}) ₄	3.1	1.7	45	93	1.60

Table 4.4: Results for mPEG-*b*-(PMMA-*co*-PDMAEMA) obtained by ATRP conducted in different solvents at T = 60 °C and $q_0 = 2.66$.

Polymer	Solvent	Yield (g)	$\frac{F_{\text{MMA}}}{F_{\text{DMAEMA}}}$	M_n (Da)	M_w/M_n
P _{5k} MD _{38%}	CH ₃ CN	0.1441	1.4	169979	2.29
P _{5k} MD _{36%}	DMF	0.1968	1.4	98663	1.70
P _{5k} MD _{41%}	Toluene	0.5682	0.85	51689	1.80

The reactivity ratios were estimated from the composition data of Table 4.3, optimizing the parameters r_1 and r_2 of equation 4.19 in order to fit the model to the experimental data (the model takes into account the variation of the feed during the copolymerization, the fitting was carried out with the nonlinear least-squares Marquardt-Levenberg algorithm)

$$1 - \frac{M}{M_0} = 1 - \left[\frac{f_1}{(f_1)_0} \right]^{\frac{r_2}{(1-r_2)}} \left[\frac{f_2}{(f_2)_0} \right]^{\frac{r_1}{1-r_1}} \left[\frac{(f_1)_0 - \frac{(1-r_2)}{(2-r_2-r_1)}}{f_1 - \frac{(1-r_2)}{(2-r_2-r_1)}} \right]^{\frac{(1-r_1)r_2}{(1-r_1)(1-r_2)}} \quad (4.19)$$

where $f_1 = f_{\text{MMA}}$, $f_2 = f_{\text{DMAEMA}}$, $r_1 = r_{\text{MMA}}$ and $r_2 = r_{\text{DMAEMA}}$ for the sake of notation simplicity.

The parameters calculated are $r_{\text{MMA}} = 0.36(\pm 10\%)$ and $r_{\text{DMAEMA}} = 2.76(\pm 15\%)$. These reactivity ratios were inserted in Kinetic Monte Carlo simulations to provide additional insights on the micro-structure of the MMA-DMAEMA copolymers. In Figure 4.9 the simulated probability of finding all possible triads are plotted as a function of the position n of the first monomer in each triad for two different feed ratios $q_0 = 1$ and $q_0 = 9$. The DMAEMA-richest triad DDD monotonically decreases along the chain because of the consumption of this monomer with the progress of the reaction. The other two DMAEMA-rich triads (DDM and DMD) do not follow the monotonic behaviour and slightly increase at the beginning of the polymerization and later decrease due to the consumption of DMAEMA. In parallel to the decrease of DMAEMA-rich triads, the probability to find MMA-rich triads (MMM, DMM and MDM) increases along the chain.

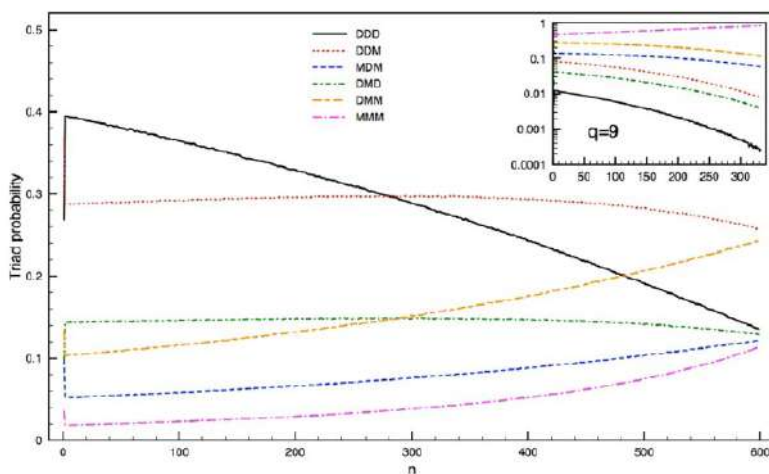


Figure 4.9: Probability of finding a specific triad with its first monomer sitting at position n along the chain when $q=1$ and 9 (in the inset). D indicates DMAEMA, while M indicates MMA. Simulations were conducted with $r_{\text{MMA}} = 0.36(\pm 10\%)$ and $r_{\text{DMAEMA}} = 2.76(\pm 15\%)$ and 60 % monomer conversion. Simulations performed by Massimo Mella (University of Insubria).

The higher reactivity of DMAEMA vs MMA that emerges from the simulations and the experiments, was rationalized supposing an interaction of DMAEMA with CuBr/bpy complex, that induces a preferential partitioning of DMAEMA closer to the just formed radical disregarding its nature compared to MMA. A DFT analysis suggested the likely formation of a DMAEMA: CuBr:bpy complex (for details, see the paper IV attached) that has the effect to locally increase DMAEMA concentration favouring its addition to the growing chains. This hypothesis was tested experimentally carrying out ^1H NMR experiments on various mixtures of CuBr, bpy and DMAEMA species at the same temperature used for the polymerizations. The results are shown in Figure 4.10: the proton chemical shifts of bpy change shape due to the interaction with, first, CuBr, and successively DMAEMA. Similar shifts are also apparent for the hydrogen atoms on the sp^2 carbon of DMAEMA, suggesting that the complexation is indeed possible. Future theoretical and experimental investigations can involve the macroinitiator mPEG-Br: a stabilization of the interaction between the metal, bpy and DMAEMA from the macroinitiator could explain the different reactivity ratios obtained in the synthesis of the copolymers mPEG-*b*-(PMMA-*co*-PDMAEMA).

To resume, the large difference in the reactivity ratios extracted from the numerical analysis on the "feed versus polymer composition" data suggests

that the copolymers obtained in the indicated conditions present gradient-like compositions with the initial part of the chains being richer in the ionisable monomer (gradient copolymers exhibit a gradual change in monomer composition from predominantly one species to predominantly the other). The finding of the gradient like microstructure could have direct consequences in the swelling behaviour of the polymeric vesicles. The rich content of DMAEMA in proximity of the hydrophilic block can be beneficial for the swelling: the protonation of DMAEMA is related to the penetration of water in the hydrophobic portion, if DMAEMA is closer to the hydrophilic part, the contact with water is facilitated thus increasing the pH-sensitivity of the double layer.

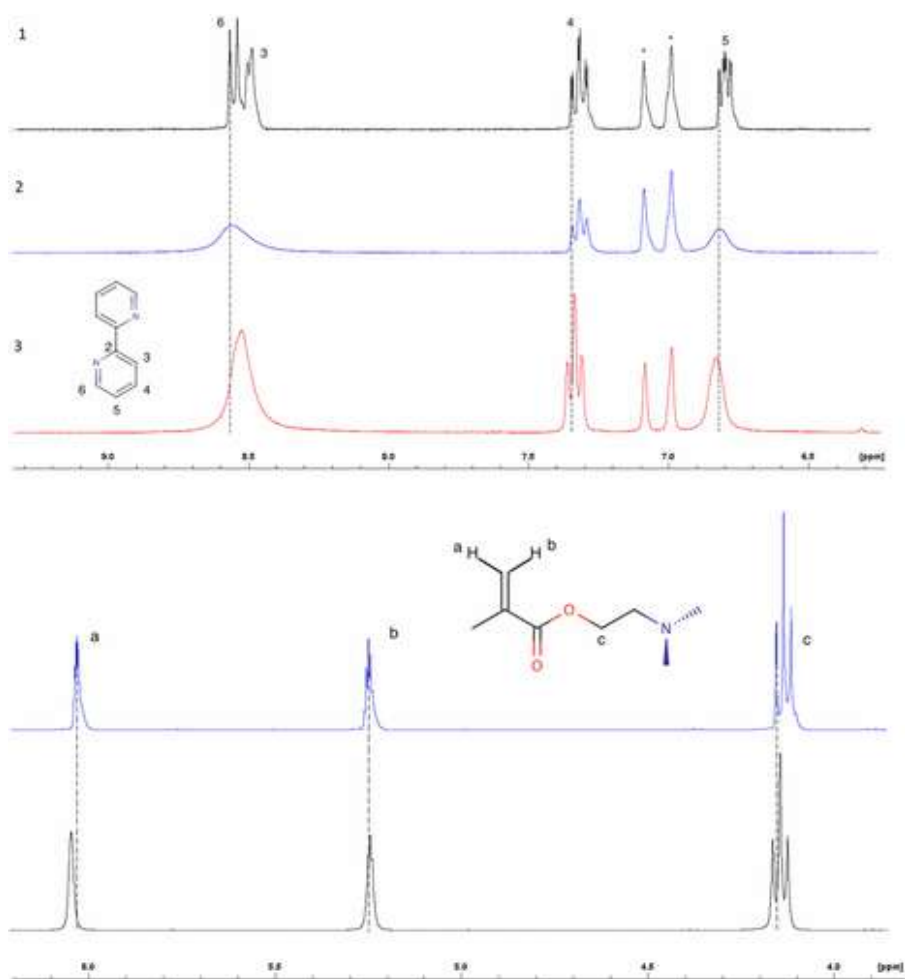


Figure 4.10: Top panel: ^1H NMR in toluene of bpy (1), CuBr/bpy 1:2 (2), and CuBr/bpy/DMAEMA 1:2:10 (3). Bottom panel: ^1H NMR in toluene of DMAEMA (top) and CuBr/bpy/DMAEMA 1:2:10 (bottom).

4.4.3 Characterization of the copolymers selected for the vesicles preparation

As discussed in the introductory section 4.2, the formation, the stability and the characteristics of hybrid polymer/lipid vesicles are controlled by the chemical compatibility (solubility parameter δ), the chain flexibility and the hydrophobic mismatch. The solubility parameter of PMMA ($\delta = 18.7 \text{ MPa}^{1/2}$) [130] is comparable with the solubility parameter of the fatty acid chains ($\delta = 18.2 \text{ MPa}^{1/2}$), suggesting a good compatibility between POPC and the copolymers containing PMMA. A series of mPEG-*b*-(PMMA-*grad*-PDMAEMA) copolymers synthesized through ARGET ATRP (Table 4.5) were characterized in terms of composition, molecular weight and glass transition temperature (T_g) to verify if the flexibility of the chains and the hydrophobic mismatch were suitable for the vesicles formation.

Table 4.5: Chemical composition, molar masses, T_g of the copolymers synthesized.

Sample	M_n mPEG	F_{mPEG}	F_{MMA}	F_{DMAEMA}	$M_n/10^3$	T_g ($^\circ\text{C}$)
P _{2k} MD _{0%}	2000	0.24	0.76	/	16.3	97
P _{5k} MD _{35%}	5000	0.14	0.51	0.35	91.8	85
P _{5k} MD _{21%}	5000	0.44	0.35	0.21	22.7	50
P _{5k} MD _{23%}	5000	0.50	0.27	0.23	19.4	55
P _{2k} MD _{40%}	2000	0.34	0.26	0.40	13.8	44

Considering that the T_g of homopolymers is $\sim -65^\circ\text{C}$ for PEG, $\sim 105^\circ\text{C}$ for PMMA and $\sim 20^\circ\text{C}$ for PDMAEMA, data reported in Table 4.5 show that the lower is the content of MMA and the value of molecular weight (*e.g.* entries 3-5 of the Table), the lower is the T_g of the corresponding copolymer. The copolymer with a molar composition 34% – 26% – 40% appears the most suitable for the preparation of hybrid vesicles: it is reasonable that its low molecular weight ($M_n = 13.8 \text{ kDa}$) and the lowest T_g ensure a minor hydrophobic mismatch. To check whether this copolymer was effectively pH dependent, measurements of contact angles were performed at different pH values.

The traditional definition of a contact angle is the angle that a liquid creates with the solid or liquid when it is deposited on it. This angle is determined by the balance between the cohesive forces of similar molecules such as between the liquid molecules (*i.e.* hydrogen bonds and Van der Waals forces) and the adhesive forces between dissimilar molecules such as between the liquid and solid molecules (*i.e.* mechanical and electrostatic forces). A small contact angle is formed when cohesive forces are weaker than adhesive forces and

the molecules of the liquid tend to interact more with the solid molecules, in this case the solid surface is considered hydrophilic. Large contact angles are observed when the cohesive forces are stronger than the adhesive forces, this behaviour is typical of hydrophobic solid surfaces.

Thus, the determination of the contact angle at different pH values can give an idea of the hydrophobicity of the polymer $P_{2k}MD_{40\%}$. Buffer solutions droplets (approximate volume $2 \mu\text{L}$) were deposited carefully onto the polymeric film and the contact angles were measured after two minutes at different points of the surface (each measurement represents an average of four positions to check the uniformity of the surface). The images were acquired with a high-resolution camera and analyzed with the software provided by the goniometer to measure the left and the right angle of the droplet. Figures 4.11 a) and b) show respectively the shape of the droplet at pH 10.5 and at pH 5. The contact angle of the copolymer $P_{2k}MD_{40\%}$ increases in a sigmoidal fashion with the pH as shown in Figure 4.12, from which a $pK_a \sim 7$ could be estimated. The reduction of the contact angle with pH is consistent with the increased ionization of the DMAEMA amine groups. At high pH, most of the DMAEMA units are neutral and the polymer is more hydrophobic, at pH 5 the number of amine groups protonated increase, the polymer is more hydrophilic, the surface is more wettable (small contact angle).

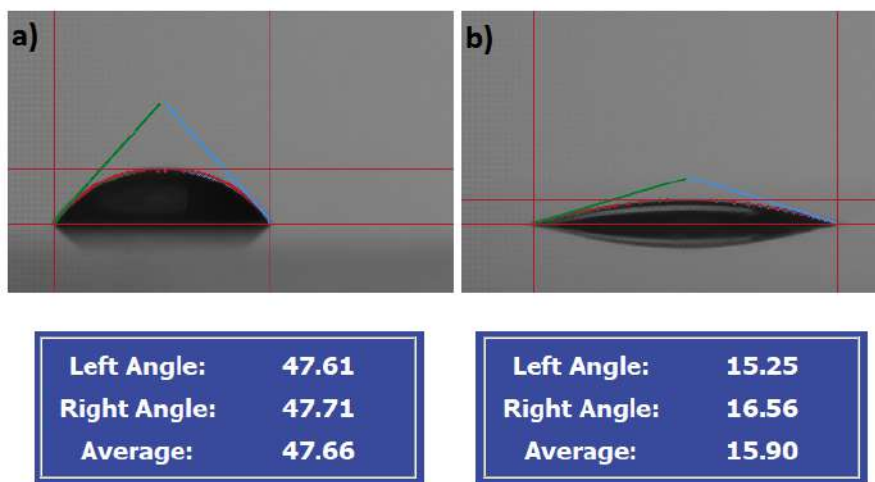


Figure 4.11: a) Contact angle of a droplet at pH 10.5. b) Contact angle of a droplet at pH 5.

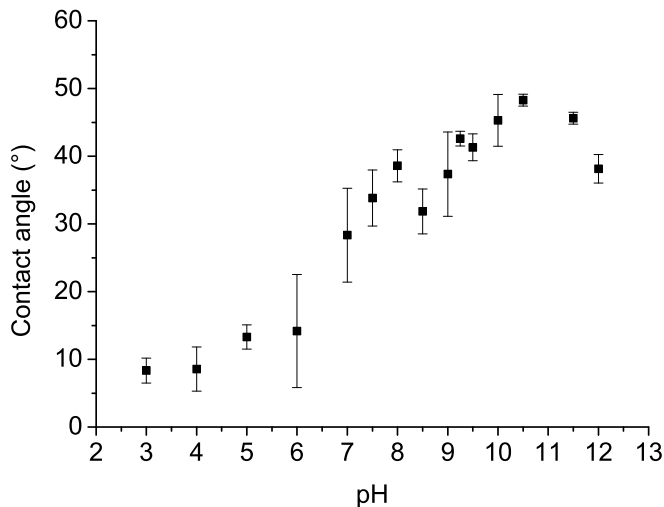


Figure 4.12: Variation of contact angle of buffer aqueous solutions vs pH.

4.4.4 Fluorescent labelling for the detection of polymeric phases in giant hybrid vesicles

A BODIPY-based fluorescent dye, abbreviated as BODIPY-DMAEMA for the sake of simplicity (complete name in section Chemical Structures), was used to label the mPEG-*b*-(PMMA-*grad*-PDMAEMA) copolymers to detect polymeric phases in the hybrid vesicles. The minimal amount (4 mg) used in the synthetic procedure is enough to label the block copolymer and prevents significant changes in the microstructure (another fluorescent monomer, fluorescein *O*-methacrylate was screened, but the final copolymer didn't give a fluorescent signal because of a lower quantum yield).

A particular attention was paid to the purification of the fluorescent copolymers: traces of unreacted fluorescent monomer can interfere with the fluorescence signal of the polymer producing misleading results. The procedure of purification developed (adapted from ref. [131]) is based on the use of lipophilic sephadex LH-20 to separate molecules with different molecular weights. A mini column (Pasteur pipette) was loaded with the lipophilic stationary phase (~ 1.5 g of Sephadex previously swollen for one hour in 10 mL of methanol) and filled with methanol to elute the samples (scheme in Figure 4.13). The fractions collected were analyzed with a spectrophotometer to identify the monomer and the polymer. An example of chromatogram is given in Figure 4.14. The black curve is obtained after the elution of the original sample (copolymer + unreacted monomer), the red curve is constructed when the purified copolymer is passed through the column (the absence of the monomer peak denotes a complete purification).



Figure 4.13: On the left: fluorescent copolymer unpurified. On the right: schematic drawing of the copolymer purification through a Sephadex LH-20 column.

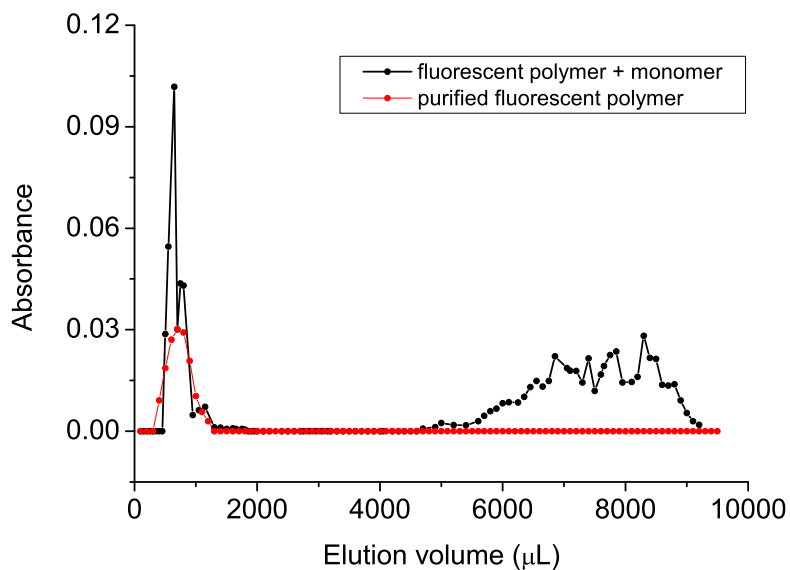


Figure 4.14: Elution of the fluorescent copolymer through a Sephadex LH-20 column with methanol as mobile phase. The first peak corresponds to the polymer, the second one to the free monomer.

The fluorescent copolymers were prepared with different chain length and hydrophilic/hydrophobic ratio. Two copolymers were selected as membrane probes: P_{5k}MD_{53%} is highly hydrophobic for the low content of mPEG and the abundance of MMA, P_{2k}MD_{20%} represents the opposite case, the high content of mPEG guarantees a high hydrophilicity. The characteristics of the nonfluorescent P_{2k}MD_{40%} and the fluorescent copolymers P_{5k}MD_{53%} and P_{2k}MD_{20%} are indicated in Table 4.6. The polymer with the highest molecular weight is also characterized by the highest polydispersity index, an indication that the polymer growth occurred in a less controlled manner. The increase of MMA percentage has the effect to increase the glass transition temperature as seen also for the unlabeled copolymers. The copolymer P_{2k}MD_{20%} has a thermal behaviour similar to the macroinitiator mPEG-Br, no glass transition temperature was observed in the range of temperatures scanned, but a peak corresponding to the melting point (DSC in Appendix C.4). The use of these copolymers in giant hybrid vesicles will be described in section 4.4.6.

Table 4.6: Characterization of the copolymers. Average molar masses for the copolymer, polydispersity index, molar composition and glass transition temperature.

Polymer	M_n (kDa)	M_w/M_n	T_g (°C)	F_{mPEG}	F_{MMA}	F_{DMAEMA}	F_{fluor}
P _{2k} MD _{40%}	13	1.25	50.6	0.34	0.26	0.40	/
P _{5k} MD _{53%}	371	1.97	83.0	0.045	0.53	0.39	0.042
P _{2k} MD _{20%}	4.4	1.04	48.3*	0.72	0.08	0.195	0.05

* Melting point

4.4.5 Preparation of hybrid polymeric vesicles via electroformation

The electroformation was the first choice because is one of the most popular techniques for the preparation of polymeric vesicles. The stock solutions of POPC and P_{2k}MD_{40%} were mixed to get the final molar ratios POPC: P_{2k}MD_{40%} = 92 %: 8% with [POPC] + [P_{2k}MD_{40%}] = 0.25 mg/mL (the total deposited amount was fixed in order to avoid the formation of a thick film). The electroformation plate was set at a frequency of 10 Hz, a voltage of 3 V and a temperature of 55 °C, the vesicles formed are shown in Figure 4.15 b) while a) is the *blank* system with pure POPC. The pure POPC vesicles could be easily obtained within 30 minutes at room temperature, while with a small amount of copolymer the temperature had to be increased till 55 °C to obtain few vesicles after 2 hours. In order to enhance the vesicles formation, mineral oil (2% on the total weight), was included in the stock solutions

with the purpose to increase the fluidity of the polymeric and lipid chains.

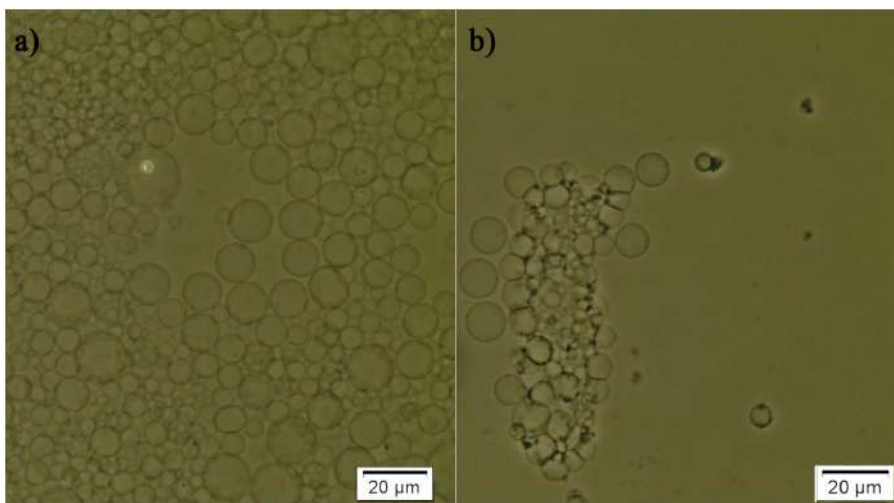


Figure 4.15: a) Pure POPC vesicles. b) POPC: P_{2k}MD_{40%} = 92 %: 8% at $T = 55$ °C.

In the presence of mineral oil, the molar ratios were changed from POPC: P_{2k}MD_{40%} = 85 %: 15% to POPC: P_{2k}MD_{40%} = 60 %: 40% (Figure 4.16), the increase of polymer content changes the morphology of the vesicles: while few electroformed vesicles aggregated in conglomerates were formed with the molar ratios POPC:P_{2k}MD_{40%} = 92 %: 8% (the vesicles often contained solid residues of presumably precipitated polymers and/or lipids, Figure 4.15 b), at intermediate concentrations only scant irregular objects could be detected (Figure 4.16), higher concentrations of polymer interfered in the vesicles formation. The effect of mineral oil on the mixture POPC:P_{2k}MD_{40%} was also studied by means of DSC. A film of POPC and P_{2k}MD_{40%} in the molar ratios 92 %: 8% was thermally characterized with and without mineral oil (Figure 4.17). The mineral oil has the effect to slightly shift the two transition temperatures of POPC (pre-melting and melting) towards lower temperatures, unfortunately the glass transition of P_{2k}MD_{40%} is not visible (it can be hidden under the transitions of POPC).

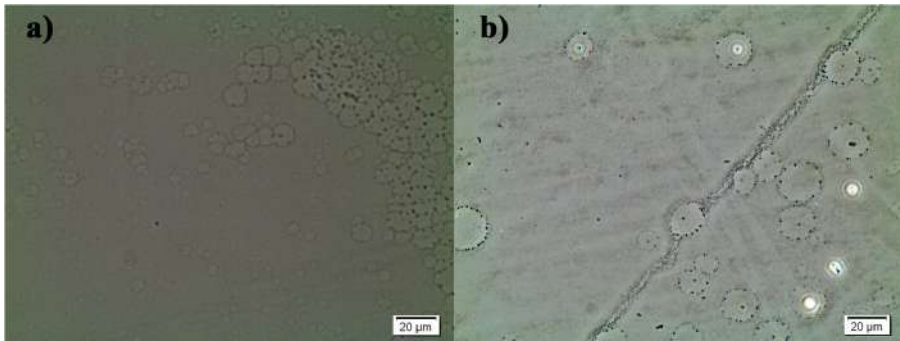


Figure 4.16: Vesicles formed at $T = 55\text{ }^{\circ}\text{C}$ and with mineral oil 2% w/w. a) POPC: P_{2k}MD_{40%} = 85 %: 15%. b) POPC: P_{2k}MD_{40%} = 59 %: 41%. The scale bar is 20 μm .

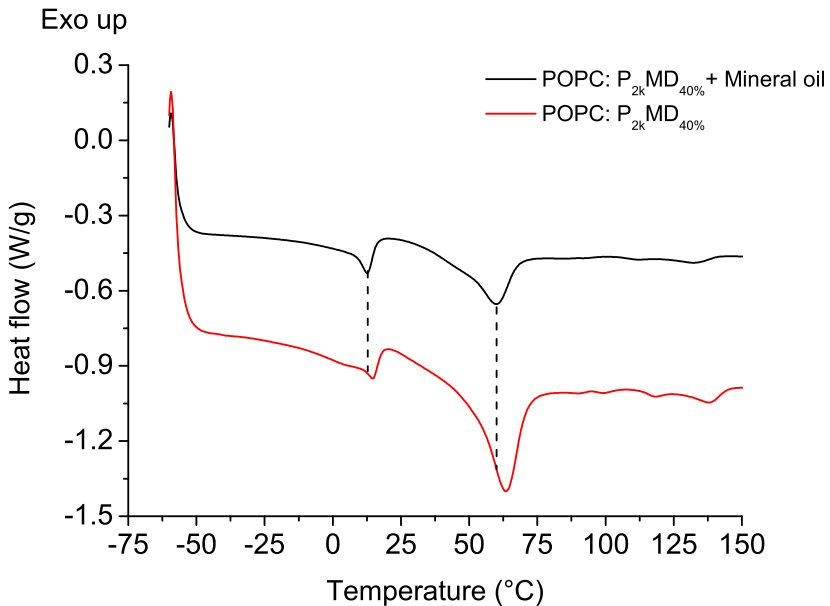


Figure 4.17: DSC thermogram of a film composed of POPC: P_{2k}MD_{40%} = 92 %: 8%. The black curve was registered with mineral oil (2% on the total weight), the red curve without mineral oil.

The electroformed vesicles were difficult to detach from the plate, possibly because of electrostatic interactions between the charged copolymer and the conductive glass slide (this effect was also noticed in mixed vesicles PEO:PBD where the detachment was favoured with the addition of PBD:PEO-COOH [103]). The selected experimental conditions made demanding the further characterization of the produced vesicles (the main obstacles were the difficult detachment of the vesicles from the plate and the necessity to adopt microfluidic

channels to load the enzymatic reaction in the sealed chamber slide), therefore the electroformation method was dismissed and the droplet transfer method chosen for the vesicles preparation and characterization.

4.4.6 Preparation of hybrid polymeric vesicles by the droplet transfer method

Vesicles made of POPC: P_{2k}MD_{40%} were marked with a fluorescent lipid (18:1 Liss Rhod PE) and fluorescent polymeric markers (P_{5k}MD_{53%} and P_{2k}MD_{20%}) to identify the presence of lipid and polymeric regions. Firstly, experiments of control (images in Figure 4.18) with just the lipid marker or just the polymeric marker were devised to set the conditions for the confocal acquisition. A very low amount of the fluorescent polymer is homogeneously dispersed into the POPC phospholipid membranes and confirms that the solubility parameter of the synthesized polymer is close to that of pure PMMA.

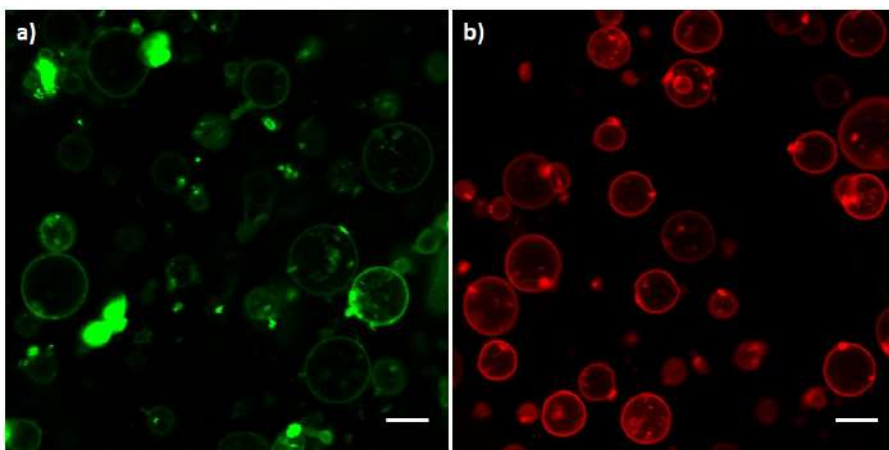


Figure 4.18: Pure POPC vesicles labelled with fluorescent probes. a) POPC and P_{5k}MD_{53%} 99.98 %: 0.02 %. b) POPC and 18:1 Liss Rhod PE 99.2 %: 0.8%. The scale bar represents 10 μ m.

Mixed vesicles were prepared by increasing P_{2k}MD_{40%} mole percentage from 7 % to 40 %. Vesicles with the compositions POPC - P_{2k}MD_{40%}: 92% - 8%, 85% - 15%, 60% - 40% labelled with 18:1 Liss Rhod PE and P_{5k}MD_{53%} (long chain fluorescent polymer) are shown respectively in Figures 4.19, 4.20 and 4.21. In each figure, the green channel represents the fluorescence of the polymer P_{5k}MD_{53%}, the red channel corresponds to the fluorescence of 18:1 Liss Rhod PE, the third image is constructed from the superposition of the two channels. From the merged frame it is possible to distinguish regions with a higher content of lipids (the membrane is red), regions richer in polymer (the membrane is green) and vesicles with similar amounts of lipid and polymer (the membrane is yellow from the overlay of the two colours). The increase of

$P_{2k}MD_{40\%}$ leads to a decrease of the number of vesicles, indeed concentrations of $P_{2k}MD_{40\%}$ higher than 40 % were unsuccessful. Another effect is the change of the distribution of the fluorescent polymer, when the concentration of $P_{2k}MD_{40\%}$ increases the membrane incorporates more fluorescent polymer: in Figure 4.19 c) vesicles of the pure components are predominant over hybrid vesicles, in Figure 4.20 c) the membrane has red and yellow regions, in Figure 4.21 c) the membrane is totally yellow. The concentration dependence of both the lipid/polymer distribution in the membrane and the successful formation of vesicles might depend on the complex attractive interactions taking place between the two molecules, as observed for a DPPC/PIB₃₇-*b*-PEO₄₈ system [132].

A novel feature compared to the systems explored in the previous chapters is the formation of colonies (most noticeable in the case 92% - 8%): the fusion of vesicles can derive from the use of a fluorescent polycation, indeed, similar aggregates due to electrostatic interactions were evidenced in mixed vesicles like POPC: HOA with poly-L-arginine [133] and POPC:HOA with Mg²⁺ [80]. Vesicles POPC: $P_{2k}MD_{40\%}$ were also labelled with the short chain fluorescent polymer $P_{2k}MD_{20\%}$. The image of Figure 4.22 a) shows how this fluorescent polymer is distributed inside the mixed vesicles. $P_{2k}MD_{20\%}$ has a high percentage of mPEG ($F_{mPEG} \sim 70\%$), the higher hydrophilic/hydrophobic ratio can be invoked to explain the different localization on the surface of the vesicles between $P_{5k}MD_{53\%}$ and $P_{2k}MD_{20\%}$.

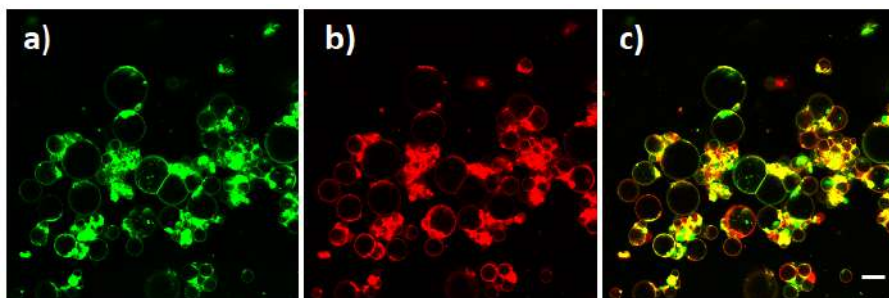


Figure 4.19: Vesicles made of POPC, $P_{2k}MD_{40\%}$, $P_{5k}MD_{53\%}$ and 18:1 Liss Rhod PE (POPC: $P_{2k}MD_{40\%}$: $P_{5k}MD_{53\%}$: 18:1 Liss Rhod PE = 92 %: 7 %: 0.02 %: 0.6 %). a) Channel with the fluorescence of the polymer, b) channel with the fluorescence of the lipid, c) Overlay of the two channels. The scale bar represents 20 μ m.

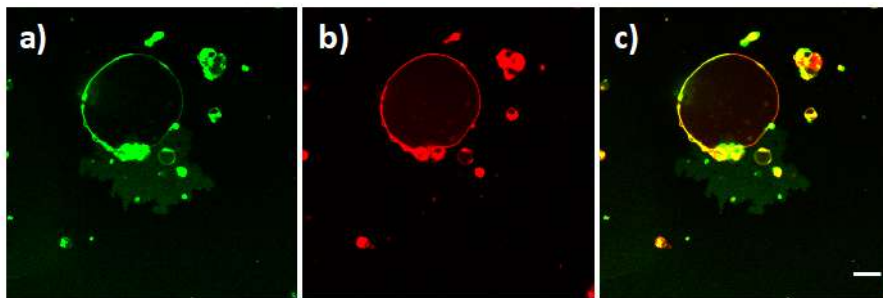


Figure 4.20: Vesicles made of POPC, P_{2k}MD_{40%}, P_{5k}MD_{53%} and 18:1 Liss Rhod PE (POPC: P_{2k}MD_{40%}: P_{5k}MD_{53%}: 18:1 Liss Rhod PE = 85 %: 14 %: 0.02 %: 0.6 %). a) Channel with the fluorescence of the polymer, b) channel with the fluorescence of the lipid, c) Overlay of the two channels. The scale bar represents 20 μm .

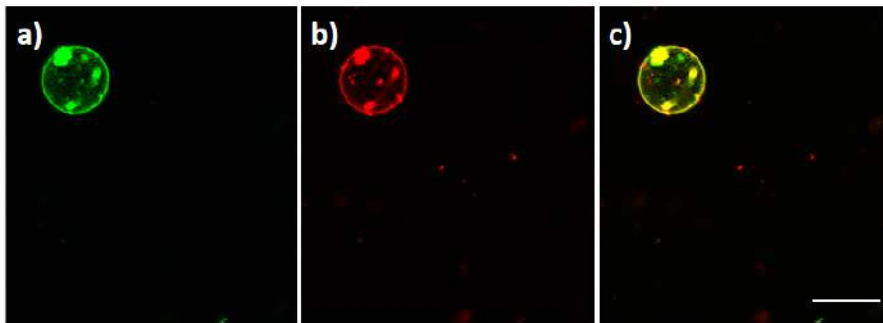


Figure 4.21: Vesicles made of POPC, P_{2k}MD_{40%}, P_{5k}MD_{53%} and 18:1 Liss Rhod PE (POPC: P_{2k}MD_{40%}: P_{5k}MD_{53%}: 18:1 Liss Rhod PE = 59 %: 40 %: 0.01 %: 0.4 %). a) Channel with the fluorescence of the polymer, b) channel with the fluorescence of the lipid, c) Overlay of the two channels. The scale bar represents 20 μm .

It is interesting to compare these results with those previously reported in literature concerning POPC-based giant vesicles blended with PBD or PDMS. In the case of PBD, homogeneous giant vesicles were formed in a restricted range of composition (region of low and high mole polymer content) [132]. In the case of PDMS triblock copolymers [134], hybrid GUVs were formed in all the weight concentration ranges and were homogeneous in the polymer-rich region (till 85wt % polymer content for 1.5k copolymers, 50 weight % for 3k copolymers), below which domain formation was observed. Mixtures of 5k PDMS copolymers with POPC led to different results: at lipid fractions as high as 50 % and 75% (wt/wt), no phase coexistence was observed. With the 5k triblock copolymer chains, three populations of vesicles were systematically present: liposomes, polymersomes and a number of homogeneous structures. The copolymers presented in this work recall the behaviour of the 5k PDMS

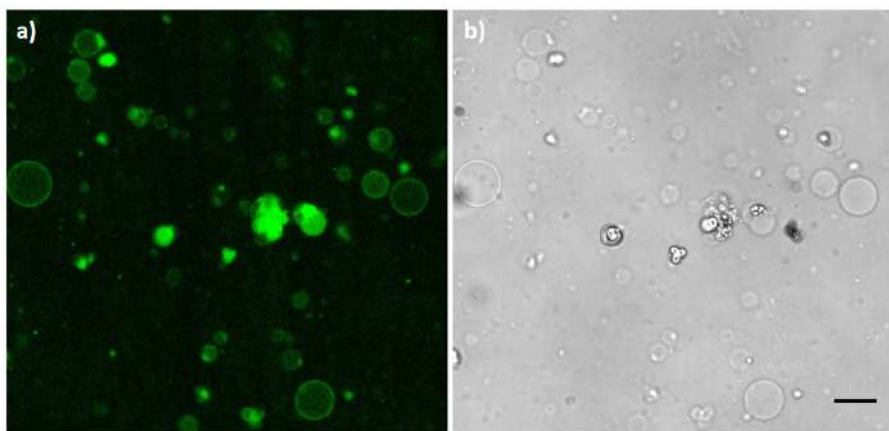


Figure 4.22: Vesicles made of POPC, P_{2k}MD_{40%} and P_{2k}MD_{20%}. POPC: P_{2k}MD_{40%}: P_{2k}MD_{20%} = 88 %:7 %:5 % a) Confocal image, b) Optical microscopy image. The scale bar represents 20 μm .

copolymers: pure liposomes, pure polymersomes and mixed systems are present depending on the copolymer and lipid concentrations without observing budding and fission phenomena.

In a different set of experiments, the influence of the polymer on the distribution of the water-soluble fluorescent probe pyranine was investigated. In pure POPC vesicles and in POPC: oleate vesicles (chapters 2 and 3) the pyranine is totally confined inside the aqueous lumen, in the presence of P_{2k}MD_{40%} the pyranine accumulates on the membrane (the comparison between the localization of the pyranine in pure POPC and in hybrid polymeric vesicles is shown in Figure 4.23 a and b). An interaction between pyranine and the polymer P_{2k}MD_{40%} could explain the different distribution of the probe (possibly the -OH moiety or the sulfonate groups $-\text{SO}_3^-$ of the pyranine bind to the amine group of the polymer $-\text{N}(\text{CH}_3)_2$ in the deprotonated or protonated form). The control of pH in the above-mentioned vesicles, achieved with a phosphate/citrate buffer at pH 4.6, corroborates the hypothesis of an interaction between the probe and the polymer. As can be seen from Figure 4.24 some vesicles look empty, but the fluorescent lipid dye (red channel) is embedded into the membrane, other vesicles have a green fluorescence, some of the vesicles are not visible in the green channel because of the partition of the pyranine (a high signal of background is detected compared to the pure POPC vesicles), but are clearly recognized in the red channel.

Hybrid vesicles of POPC and P_{2k}MD_{40%} were also prepared at three different pH values (pH = 4.6, pH = 7.3 and pH = 10) without pyranine and observed by optical microscopy (Figures 4.25 a, 4.26 a and 4.27 a). The size of the vesicles is similar for the three different pH: the histograms of Figures 4.25 b, 4.26 b and 4.27 b show how the diameter spans from 4 to 28 μm for all the

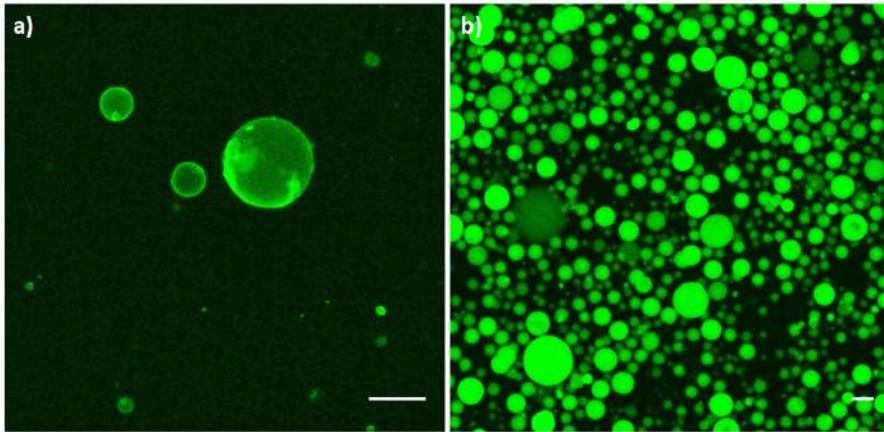


Figure 4.23: a) Vesicles made of POPC-P14 (92 % - 7 %) and pyranine 50 μM . b) Pure POPC vesicles with pyranine. Both the images were acquired in the UV channel. The scale bar represents 20 μm .

three pH values, no size difference is noticeable possibly for the micrometric size and the small polymer percentage in each vesicle. However, in the image at pH 10 (Figure 4.27a) some microcrystals are clearly visible and sometimes overlap with the vesicles. These microcrystals (absent at acidic and neutral pHs) could belong to the polymer. As seen in the contact angle measurements (Figures 4.11 and 4.12), at pH 10 the polymer is more hydrophobic than pH 4.6 or 7.3 where the surface is instead more wettable. The polymer unable to go inside the membrane precipitates and is recovered with the pellet together with the vesicles.

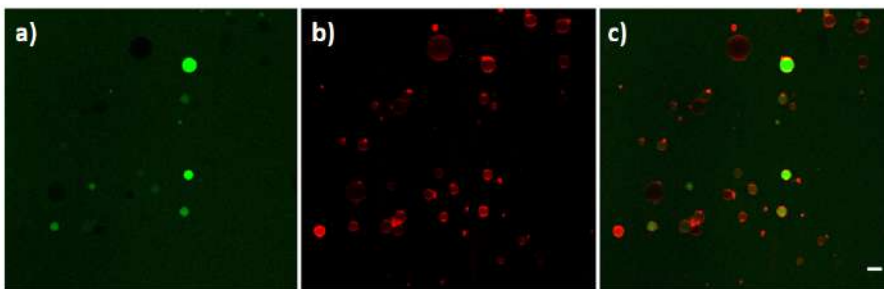


Figure 4.24: Vesicles made of POPC-P_{2k}MD_{40%} (91.8 %-7 %), pyranine 50 μM , 18:1 Liss Rhod PE (1.2 %). a) Channel with the fluorescence of the polymer, b) channel with the fluorescence of the lipid, c) Overlay of the two channels. The scale bar represents 20 μm .

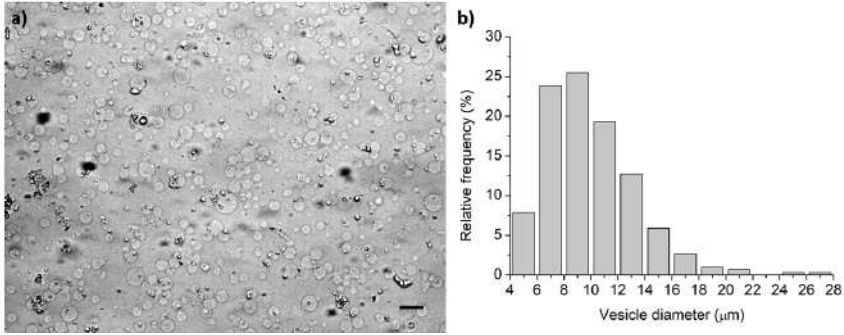


Figure 4.25: a) Optical microscopy image of mixed vesicles (POPC: P_{2k}MD_{40%} = 85 %-15 %) at pH 4.7, b) size distribution. The scale bar represents 30 μm.

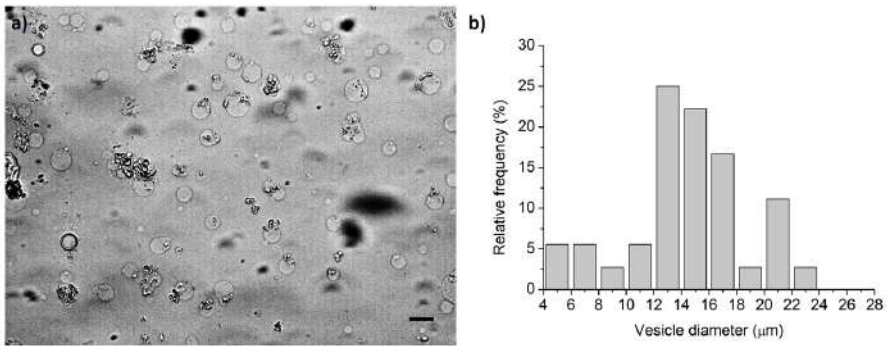


Figure 4.26: a) Optical microscopy image of mixed vesicles (POPC: P_{2k}MD_{40%} = 85 %-15 %) at pH 7.3, b) size distribution. The scale bar represents 30 μm.

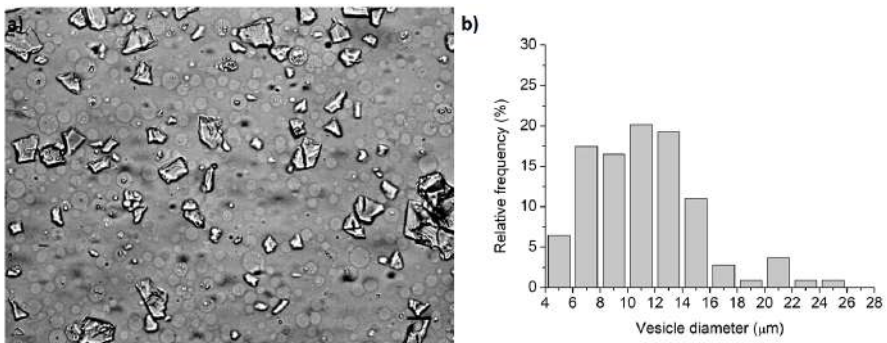


Figure 4.27: a) Optical microscopy image of mixed vesicles (POPC: P_{2k}MD_{40%} = 85 %-15 %) at pH 10, b) size distribution. The scale bar represents 30 μm.

5

CONCLUSIONS AND FUTURE WORK

The objective of the PhD project was the use of a nonlinear reaction coupled with micro-sized vesicles to produce a chemo-mechanical coupling. The nonlinear urea-urease reaction generates a sudden change in pH due to the typical bell-shaped form of the reaction rate. This reaction was confined in pure POPC vesicles and the induction period varied according to the concentration of acetic acid and the number of vesicles. As expected, the induction period increases with the concentration of acetic acid used as proton source. The number of vesicles, modified through different dilutions of the pellet, has an impact on the induction period and on the final pH. A critical number of vesicles ($\sim 10^4$) is necessary to promote the urea-urease reaction in all the micro-compartments for the concentrations adopted. This effect recalls the phenomenon of quorum sensing that is the ability of bacteria and other single-celled organisms to change behaviour above a critical density or number of cells, driven by the production and release of small diffusible molecules into the environment. The number of vesicles calculated could be introduced in simple kinetic models (composed of ordinary differential equations, ODEs, as described in Appendix B.2 or in ref. [49]) or more complex models that describe the kinetics of single vesicles taking into account the number, the position and the size by means of partial differential equations (PDEs) [65].

The same reaction conditions used for the pure lipid vesicles were applied in mixed systems with oleic acid (POPC: HOA). Parameters like induction period and final pH are similar to those calculated in pure POPC vesicles, but the shape of the curve slightly changes because of the buffer effect of oleic acid. Clock reactions with an induction period of several minutes don't generate noticeable deformations in the morphology of the mixed vesicles. On the contrary, a fast clock reaction, that gives a small change of pH from 6 to 6.5 in few seconds is able to give phenomena of self-division, explained through the synergic action between the osmotic change and the fast pH increase. Thus, the aim of a chemo-mechanical answer which derives from the coupling of negatively charged pH-sensitive membranes with the pH-dependent urea-urease reaction was fully accomplished. The use of an internally confined reaction as a stimulus for the self division represents a new approach in the Origins of Life

research field and make these vesicles more similar to the simple cells typical of the prebiotic era.

Polymeric hybrid vesicles with POPC and a block copolymer mPEG-*b*-(PMMA-*grad*-PDMAEMA) were prepared and characterized as possible hosts for the urea-urease system. The confinement of the enzymatic reaction is the natural next step: as done for the POPC: HOA system, fast and slow clock reactions can be tested to generate phenomena of swelling or deswelling according to the pH of the solution. Possibly, another pH sensitive hydrophilic dye should be used instead of pyranine: the probe-polymer interaction, confirmed from the confocal imaging, can interfere in the evaluation of pH. The estimation of the effective concentration of HOA/OA⁻ or PDMAEMA/PDMAEMA⁺ into the mixed membranes could add further informations in the kinetic models above-cited to simulate the dynamical behaviour of an ensemble of pH-sensitive microreactors.

APPENDICES

A Models and Matlab codes for the analysis of pure POPC vesicles

A.1 Matlab code for the detection of vesicles

```
tic
dir = 'C:\Users\user\Desktop\Erasmus_2018_Sheffield\Confocal_data_analysis\';
FileName1 = 'Project_Series013_ch00.jpg'; % bright for pH <7.6
FileName2 = 'Project_Series013_ch01.jpg'; % dark at low pH
Pixel2MicroMeterRatio = 1024/406.47; % pixel size/pixel um
HistBinEdges = (0:5:30);
rm = 1; % radius for intensity readout (0 < rm <=1)
mask_height = 20; % in pixels; band on top disregarded

vi = 0.05; % vertical increase in subplot size (normalized)
hi = 0.08; % horizontal increase in subplot size (normalized)
i1 = imread(FileName1);
i2 = imread(FileName2);
i12 = rgb2gray(i1); %rgb2gray, mean grey value = 0.299 Red + 0.587 Green + 0.114 Blue
i22 = rgb2gray(i2);
ims = size(i12);
i12m = medfilt2(i12,[10 10]); %performs median filtering (it removes the noise)
i12a = imadjust(i12m); % it increases the contrast
[CircCenter, CircRadii] = imfindcircles(i12a(mask_height:end,:),[10 50],
'ObjectPolarity','bright');
CircCenter(:,2) = CircCenter(:,2)+mask_height;

sp(1) = subplot(2,2,1);
imshow(i1)

NumOfCells = length(CircRadii);
cnt = 0;
for q = 1:NumOfCells
if (((CircCenter(q,1)-CircRadii(q,1))< 1)||((CircCenter(q,1)+CircRadii(q,1)>ims(2))
||((CircCenter(q,2)-CircRadii(q,1))<1)||((CircCenter(q,2)+CircRadii(q,1)>ims(1))))
cnt = cnt+1;
del(cnt) = q;
end
end

CircCenter(del,:) = [ ];
CircRadii(del) = [ ];
NumOfCells = length(CircRadii);

for q = 1:NumOfCells
r2 = (CircRadii(q,1)*rm)^2;
inty1 = 0.0;
inty2 = 0.0;
pix_count = 0;
for hc = CircCenter(q,1)-CircRadii(q,1):CircCenter(q,1)+CircRadii(q,1)
for vc = CircCenter(q,2)-CircRadii(q,1):CircCenter(q,2)+CircRadii(q,1)
```

```

    if (((hc-CircCenter(q,1))^2 + (vc-CircCenter(q,2))^2) < r2)
        inty1 = inty1 + double(i12(round(vc),round(hc)));
        inty2 = inty2 + double(i22(round(vc),round(hc)));
        pix_count = pix_count + 1;
    end
end
end
inty1(q,1)=inty1; % vector of intensity 1
inty2(q,1)=inty2; % vector of intensity 2
pix_countv(q,1)=pix_count;
intensity1(q,1) = inty1/pix_count;
intensity2(q,1) = inty2/pix_count;
end
int_ratio = intensity2./intensity1;
sp(2) = subplot(2,2,2);
imshow(i12)
hold on
c=viscircles(CircCenter, CircRadii,'EdgeColor','r','linewidth',0.4,'linestyle',':');
c.Children(2).Visible = 'off';

for i=1:NumOfCells
    text(CircCenter(i,1),CircCenter(i,2),num2str(i),'fontsize',2,'color','b',
'HorizontalAlignment','center','VerticalAlignment','middle')
end

sp(3) = subplot(2,2,[3 4]);
RealCircDiameter = 2*CircRadii/Pixel2MicroMeterRatio;
h = histogram(RealCircDiameter);
h.BinEdges = HistBinEdges;
h.FaceColor = [0.5 0.5 0.5];
h.EdgeColor = 'r';
h.Parent.LineWidth = 1;
set(gca,'XTick',HistBinEdges,'XColor','k','YColor','k')
xlabel('vesicle diameter / \mum')
ylabel('frequency')

annotation('textbox',[0.1 0.95 0.9 0.05],'String',strrep(FileName1,'_','\_' ),
'fontsize',12,'color','k','HorizontalAlignment','left','linestyle','none')
annotation('textbox',[0.1 0.48 0.9 0.05],'String',['Number of vesicles identified:
',num2str(NumOfCells)],'fontsize',12,'color','r',
'HorizontalAlignment','left','linestyle','none')

for spi = 1:2
    p = get(sp(spi),'Position');
    p = [p(1)-hi/2 p(2)-vi/2 p(3)+hi p(4)+vi];
    set(sp(spi),'Position',[p(1) p(2) p(3) p(4)]);
end
set(gcf,'color','w')
xlsoutput1(:,1) = vertcat(RealCircDiameter,NaN,NaN,HistBinEdges(1:end-1)');
xlsoutput1(1:NumOfCells+2,2:4) = NaN;
xlsoutput1(1:NumOfCells,2) = intensity1';
xlsoutput1(1:NumOfCells,3) = intensity2';
xlsoutput1(1:NumOfCells,4) = int_ratio';
xlsoutput1(NumOfCells+3:end,2) = HistBinEdges(2:1:end)';
xlsoutput1(NumOfCells+3:end,3) = h.Values';

```

```

xlsoutput2=[{'diameter', 'int brt', 'int drk', 'int ratio'}];
arrayfun(@(x) num2str(x), xlsoutput1, 'UniformOutput', 0)];
xlsoutput2(NumOfCells+3,:) = {'[Bin Low' 'Bin High)' 'Frequency' ''}];
xlsoutput2(cellfun(@(x) strcmp(x,'NaN'),xlsoutput2))={'}');
FileName1Root = FileName1(1:end-4);
FileName2Root = FileName2(1:end-4);
xlswrite([dir,FileName1Root,'_',FileName2Root],xlsoutput2);
print([dir,FileName1Root,'_',FileName1Root,'_eval'],'-dpng','-r400')
figure
subplot(1,2,1)
plot(intensity1,'o')
hold on;
plot(intensity2,'s')
legend('bright','dark')
grid on
subplot(1,2,2)
plot(int_ratio,'^')
legend('intensity ratio')
toc

```

A.2 Matlab code for counting the number of vesicles

```

Pixel2MicroMeterRatio = 512/581.25; % pixel size/um size
rm = 1; % radius for intensity readout (0 < rm <=1)
vi = 0.05; % vertical increase in subplot size (normalized)
hi = 0.08; % horizontal increase in subplot size (normalized)
mask_height = 15; % in pixels; band on top disregarded
d = 'C:\Users\user\Desktop\Erasmus_2018_Sheffield\Matlab\';
d1= 'C:\Users\user\Desktop\Erasmus_2018_Sheffield\Confocal_data_analysis\';
filelist=dir(fullfile(d,'TileScan_001_s*.jpg'));
numImages=length(filelist);
for k=1:numImages
myfilename=filelist(k).name;
i1 = imread(myfilename);
i12 = rgb2gray(i1);
ims = size(i12);
i12m = medfilt2(i12,[10 10]); %it performs median filtering
i12a = imadjust(i12m); % contrast verified on ImageJ
[CircCenter, CircRadii] = imfindcircles(i12a(mask_height:end,:),[5 40],
'ObjectPolarity','bright');
CircCenter(:,2) = CircCenter(:,2)+mask_height;
[~, index] =sort(CircCenter(:,2)); % 1 instead of 2 would sort by x coord
CircCenter= CircCenter(index, :);
CircRadii = CircRadii(index, :);
figure(k);
set(figure(k),'Visible', 'off');
sp(1) = subplot(2,2,1); % subplot (m,n,p)= divides the current figure
into an m-by-n grid and creates axes in the position specified by p.
imshow(i1)
NumOfCells = length(CircRadii);
Num(k,:)=NumOfCells;
total=sum(Num);
% Start: creation of the figure with the circles
sp(2) = subplot(2,2,2);

```

```

imshow(i12)
hold on
c=viscircles(CircCenter, CircRadii,'EdgeColor','r','linewidth',0.4,
'linestyle',':');
c.Children(2).Visible = 'off';
for i=1:NumOfCells
text(CircCenter(i,1),CircCenter(i,2),num2str(i),'fontsize',2,'color','b',
'HorizontalAlignment','center','VerticalAlignment','middle')
end
% Start: Histogram
sp(3) = subplot(2,2,[3 4]);
RealCircDiameter = 2*CircRadii/Pixel2MicroMeterRatio;
h = histogram(RealCircDiameter);
HistBinEdges = (0:5:30);
h.BinEdges = HistBinEdges;
h.FaceColor = [0.5 0.5 0.5];
h.EdgeColor = 'r';
h.Parent.LineWidth = 1;
set(gca,'XTick',HistBinEdges,'XColor','k','YColor','k')
xlabel('vesicle diameter / \mum')
ylabel('frequency')
annotation('textbox',[0.1 0.95 0.9 0.05],'String',strrep(myfilename,'_','\_' ),
'fontsize',12,'color','k','HorizontalAlignment','left','linestyle','none')
annotation('textbox',[0.1 0.48 0.9 0.05],'String',
['Number of vesicles identified: ',num2str(NumOfCells)],'fontsize',12,'color',
'r','HorizontalAlignment','left','linestyle','none')
for spi = 1:2
p = get(sp(spi),'Position');
p = [p(1)-hi/2 p(2)-vi/2 p(3)+hi p(4)+vi];
set(sp(spi),'Position',[p(1) p(2) p(3) p(4)]);
end
set(gcf,'color','w')
myfilenameRoot = myfilename(1:end-4);
print([d1,myfilenameRoot,'_eval'],'-dpng','-r800')
end
col_header = {'Sequence','Number of vesicles in each frame',
'Total number of vesicles' };
files = struct2cell(filelist);
files_name=files(1,:);
xlswrite([[d1,myfilenameRoot,'_s','_data'],'_'],col_header,1,'A1:C1');
xlswrite([[d1,myfilenameRoot,'_s','_data'],'_'],files_name,1,'A2');
xlswrite([[d1,myfilenameRoot,'_s','_data'],'_'],Num,1,'B2');
xlswrite([[d1,myfilenameRoot,'_s','_data'],'_'],total,1,'C2');

```

A.3 Matlab code for particle tracking

```

dir = 'C:\Users\user\Desktop\Erasmus_2018_Sheffield\Matlab\';
dir1='C:\Users\user\Desktop\Erasmus_2018_Sheffield\Confocal_data_analysis\';
fnr = 'Project_Series004'; % file mane root
nov =19; % number of vesicles to track
fi = 0; % first image
li = 59; % last image
% if the time series is long divide the pictures in two parts:
% from 0 to 99 add 0 at every '_t'

```

```

ch = {'00' '01'};
fmt = 'jpg'; % image format
thd = 35; % displacement threshold for vesicles movement between frames
tr = '0';
Pixel2MicroMeterRatio = 1024/406.47;
if fi < 10
    st = [tr,num2str(fi)];
else
    st = num2str(fi);
end
i0 = imread([dir,fnr,'_t',st,'_ch',ch{1},'.',fmt]);
imshow(i0);
p = ginput(nov);
close
for q = fi:li
    if q < 10
        st = [tr,num2str(q)];
    else
        st = num2str(q);
    end
    i1 = imread([dir,fnr,'_t',st,'_ch',ch{1},'.',fmt]);
    i2 = imread([dir,fnr,'_t',st,'_ch',ch{2},'.',fmt]);
    imshow(i1);
    i12 = rgb2gray(i1);
    i22 = rgb2gray(i2);
    i12a1 = medfilt2(i12,[7 7]);
    i12a2 = imadjust(i12a1);
    [CircCenter CircRadii] = imfindcircles(i12a2,[11 60],'ObjectPolarity',
    'bright','Sensitivity',0.7);
    NumOfCells = length(CircRadii);
    for v = 1:NumOfCells
        for vt = 1:nov
            if sqrt((p(vt,1)-CircCenter(v,1))^2+(p(vt,2)-CircCenter(v,2))^2) < thd
                hold on
                viscircles(CircCenter(v,:), CircRadii(v,1),'EdgeColor','r','linewidth',0.5);
                hold on
                text(CircCenter(v,1),CircCenter(v,2)+2,num2str(vt),'fontsize',8,
                'horizontalalignment','center','verticalalignment','bottom','color','red');
                hold on
                text(CircCenter(v,1),CircCenter(v,2)-2,num2str(q),'fontsize',8,
                'horizontalalignment','center','verticalalignment','top','color','red');
                r2 = CircRadii(v,1)^2;
                inty1 = 0.0;
                inty2 = 0.0;
                pix_count = 0;
                for hc = CircCenter(v,1)-CircRadii(v,1):CircCenter(v,1)+CircRadii(v,1)
                    for vc = CircCenter(v,2)-CircRadii(v,1):CircCenter(v,2)+CircRadii(v,1)
                        if (((hc-CircCenter(v,1))^2 + (vc-CircCenter(v,2))^2) < r2)
                            inty1 = inty1 + double(i12(round(vc),round(hc)));
                            inty2 = inty2 + double(i22(round(vc),round(hc)));
                        end
                    end
                end
                pix_count = pix_count + 1;
            end
        end
    end
end
end

```

```

end
intensity1(q-fi+1,vt) = inty1/pix_count;
intensity2(q-fi+1,vt) = inty2/pix_count;
int_ratio(q-fi+1,vt) = intensity2(q-fi+1,vt)/intensity1(q-fi+1,vt);
p(vt,:) = CircCenter(v,:);
RealCircDiameter(vt)=2*CircRadii(vt)/Pixel2MicroMeterRatio;

end
end

drawnow
end
vesicles_tracked=[1:1:nov]';

print([dir1,fnr,'_t',st,'_ch',ch{1},'_eval'],'-dpng','-r800')
end
xlswrite([[dir1,fnr,'_t',st,'_ch',ch{1},'_data'],'_'],RealCircDiameter,'RealCircDiameter');
xlswrite([[dir1,fnr,'_t',st,'_ch',ch{1},'_data'],'_'],intensity1,'intensity1');
xlswrite([[dir1,fnr,'_t',st,'_ch',ch{1},'_data'],'_'],intensity2,'intensity2');
xlswrite([[dir1,fnr,'_t',st,'_ch',ch{1},'_data'],'_'],int_ratio,'int_ratio');

close

```

A.4 Fitting equation used in the ratiometric method

This method is taken from the references [54, 55]. Let's define A the acidic form of the probe, B the deprotonated form and C_0 the analytic concentration.



$$K = \frac{[B][H^+]}{[A]} \quad (\text{A.2})$$

$$[A] + [B] = C_0 \quad (\text{A.3})$$

$$[A] = \frac{(C_0 - [A])[H^+]}{K} \quad (\text{A.4})$$

$$[A] = \frac{(C_0 10^{-\text{pH}})}{10^{-\text{p}K} + 10^{-\text{pH}}} \quad (\text{A.5})$$

$$[B] = \frac{C_0 10^{-\text{p}K}}{10^{-\text{p}K} + 10^{-\text{pH}}} \quad (\text{A.6})$$

Multiplying and dividing A and B for $10^{\text{p}K}$, equations A.5 and A.6 can be rewritten as:

$$[A] = \frac{C_0 10^{\text{p}K - \text{pH}}}{1 + 10^{\text{p}K - \text{pH}}} \quad (\text{A.7})$$

$$[B] = \frac{C_0}{1 + 10^{\text{p}K - \text{pH}}} \quad (\text{A.8})$$

The fluorescence will depend on the pH as

$$F(\lambda_x, \lambda_e) = C_0 \left(\frac{F_B(\lambda_x, \lambda_e) + F_A(\lambda_x, \lambda_e) 10^{pK-pH}}{1 + 10^{pK-pH}} \right) \quad (\text{A.9})$$

where F_A and F_B are the molar fluorescence emissions of the A and B states, respectively. The ratio between two different wavelengths gives:

$$\frac{F(\lambda_{x1}, \lambda_{e1})}{F(\lambda_{x2}, \lambda_{e2})} = \left(\frac{F_B(\lambda_{x1}, \lambda_{e1}) + F_A(\lambda_{x1}, \lambda_{e1}) 10^{pK-pH}}{F_B(\lambda_{x2}, \lambda_{e2}) + F_A(\lambda_{x2}, \lambda_{e2}) 10^{pK-pH}} \right) \quad (\text{A.10})$$

Replacing F_B with F_∞ and F_A with F_0 and introducing the equations:

$$R [1 : 2] = \frac{F(\lambda_{x1}, \lambda_{e1})}{F(\lambda_{x2}, \lambda_{e2})}, \quad (\text{A.11})$$

$$R_0 [1 : 2] = \frac{F_0(\lambda_{x1}, \lambda_{e1})}{F_0(\lambda_{x2}, \lambda_{e2})}, \quad (\text{A.12})$$

$$R_f [1 : 2] = \frac{F_\infty(\lambda_{x1}, \lambda_{e1}) F_0(\lambda_{x2}, \lambda_{e2})}{F_0(\lambda_{x1}, \lambda_{e1}) F_\infty(\lambda_{x2}, \lambda_{e2})} \quad (\text{A.13})$$

$$\frac{F_0(\lambda_{x2}, \lambda_{e2})}{F_\infty(\lambda_{x2}, \lambda_{e2})} = \frac{K}{K'} \quad (\text{A.14})$$

the equation A.10 can be rewritten as

$$R [1 : 2] = R_0 [1 : 2] \times \left(\frac{R_f [1 : 2] + 10^{n(pK'-pH)}}{1 + 10^{n(pK'-pH)}} \right) \quad (\text{A.15})$$

B Kinetic model and pH calibration for POPC/HOA vesicles

B.1 pH calibration

The intensity ratios at different pH values were fitted in Matlab with the equation [54, 55] (Appendix A.4 for the demonstration of the formula)

$$R [1 : 2] = R_0 [1 : 2] \times \left(\frac{R_f [1 : 2] + 10^{n(pK' - pH)}}{1 + 10^{n(pK' - pH)}} \right) \quad (\text{B.1})$$

Using the initial guess values: $R_0 [1 : 2] = 0.002$, $R_f [1 : 2] = 1092$ and $pK' = 8$, the parameters estimated with the nonlinear regression model are: $R_0 [1 : 2] = 0.088$, $R_f [1 : 2] = 31.42$ and $pK' = 8.37$ with an Adjusted R-Squared of 0.99.

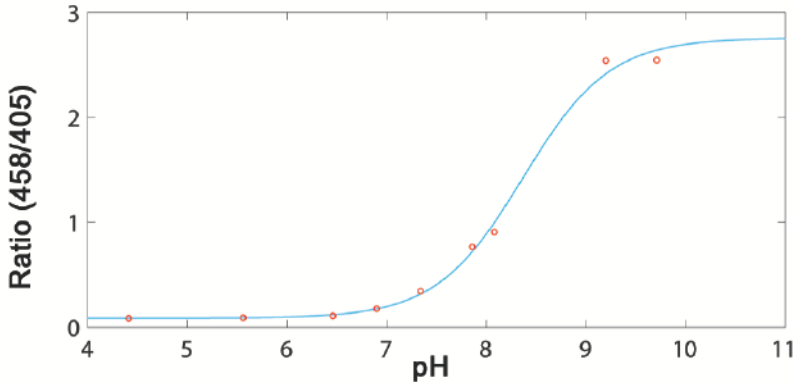


Figure 1: Dependence of the intensity ratio on pH for vesicles containing pyranine $50\mu\text{m}$

B.2 Detailed model of urea-urease reaction in hybrid vesicles

The chemical model is based on seven main chemical species, namely urea (S, substrate), urease (E, enzyme), pyranine (fluorescent dye, pyrOH), oleic acid (HOA), acetic acid (HA), ammonia (NH₃) and carbon dioxide (CO₂). Some of these chemical species can be located outside of the vesicles having cross membrane properties. The transfer rates k_x (s⁻¹) are proportional to the vesicle surface/volume ratio and to the specific membrane permeability of each species:

$$k_x = \frac{3P_x}{R} \quad (\text{B.2})$$

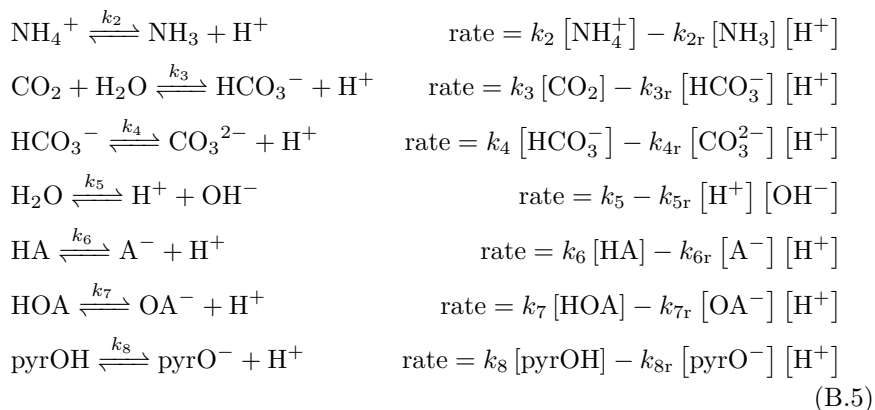
where P_x is the permeability and R (dm) is the vesicle radius, respectively. The rate of the enzyme-catalyzed reaction



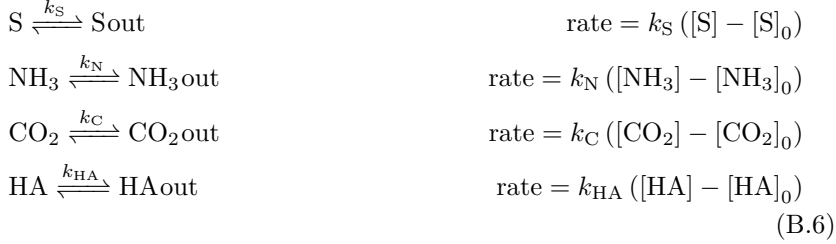
is given by a modified Michaelis-Menten rate law, which accounts for the pH dependence and the product inhibition

$$R = \frac{v_{\max} [\text{S}]}{\left(K_{\text{M}} + [\text{S}] \left(1 + \frac{[\text{S}]}{K_{\text{S}}} \right) \left(1 + \frac{[\text{P}]}{K_{\text{P}}} \right) \left(1 + \frac{K_{\text{es2}}}{[\text{H}^+]} + \frac{[\text{H}^+]}{K_{\text{es1}}} \right) \right)} \quad (\text{B.4})$$

where $v_{\max} = k_1 [\text{E}]$, being $[\text{E}]$ expressed as enzyme activity (units/mL), K_{M} is the Michaelis constant, K_{es1} and K_{es2} are protonation equilibrium constants of the substrate-enzyme complex, $[\text{P}]$ is the concentration of the protonated form of ammonia (NH₄⁺), $[\text{S}]$ is the concentration of urea, K_{S} and K_{P} are the equilibrium constants for uncompetitive substrate and product inhibition, respectively. The pH inside and outside the vesicles is governed by the following equilibria



Finally, the transfer of the chemical species across the membranes can be considered as a first order process described by the following reactions



where $[\text{X}]_0$ is the concentration of the chemical species of X outside the vesicles in the water phase. The set of ordinary differential equations derived from the reaction rates B.4-B.6 was numerically integrated by using the software XPPAUT with the initial conditions and parameters listed in Table 1 and Table 2.

Table 1: Initial concentrations and parameters used for the kinetic simulations. $[\text{CO}_2]$ and $[\text{CO}_2]_0$ are calculated by considering the solution at the equilibrium with the atmosphere at 25 °C; $[\text{HOA}] + [\text{HOA}]_0 = 2\text{mM}$ is the analytical concentration of oleic acid used for the vesicles preparation in experiments. N is the number of vesicles, R the radius, N and R appear in the ODEs that describe the kinetics of the outer species $[\text{X}]_0$

[X] (M)		Parameters	
[E] (U/mL)	1.1	N	10^4
[S]	0	R (dm)	5×10^{-5}
[S] ₀	6×10^{-2}	V_i (dm ³)	5.24×10^{-13}
[pyrOH]	5×10^{-5}	V_0 (dm ³)	3×10^{-5}
[HA]	1×10^{-6}	P_S (dm/s) [87]	4×10^{-7}
[HA] ₀	1×10^{-6}	P_N (dm/s) [88]	1×10^{-3}
[HOA]	1×10^{-3}	P_{HA} (dm/s) [89]	6.5×10^{-4}
[HOA] ₀	1×10^{-3}	P_C (dm/s) [90]	1.2
[CO ₂]	1.2×10^{-5}		
[CO ₂] ₀	1.2×10^{-5}		

Table 2: Kinetic constants used in the model. k_x were calculated from the permeabilities P_x and the radius R reported in Table 1. Enzymatic constants were taken from refs. [10, 14, 85]. Equilibrium rate constants were derived from the pK_a according to refs. [14, 135, 136].

Enzymatic		pH equilibria		
k_1 ($\text{U}^{-1} \text{mL M s}^{-1}$)	3.7×10^{-6}		forward (s^{-1})	reverse ($\text{M}^{-1} \text{s}^{-1}$)
K_m (M)	3×10^{-3}	k_2	24	4.3×10^{10}
K_{es1} (M)	5×10^{-6}	k_3	3.7×10^{-2}	7.9×10^4
K_{es2} (M)	2×10^{-9}	k_4	2.8	5×10^{10}
K_S (M)	3	k_5	$1 \times 10^{-3} (\text{M}^{-1} \text{s}^{-1})$	1×10^{11}
K_P (M)	2×10^{-3}	k_6	7.8×10^5	4.5×10^{10}
		k_7	3.2×10^2	1×10^{10}
		k_8	1	2.5×10^7

C Models, synthesis and characterization of polymers

C.1 Mayo-Lewis model and Meyer-Lowry equation

The Mayo-Lewis equation or copolymer equation describes the distribution of monomers in a copolymer [137]. The equation considers a monomer mix of two components M_1 and M_2 and the four different reactions that can take place at the reactive chain ends M_1^* and M_2^* with their reaction rate constants k :



The reactivity ratios are defined as

$$r_1 = \frac{k_{11}}{k_{12}} \quad (\text{C.5})$$

$$r_2 = \frac{k_{22}}{k_{21}} \quad (\text{C.6})$$

$$(\text{C.7})$$

Monomer 1 is consumed with the reaction rate

$$-\frac{d[M_1]}{dt} = k_{11} [M_1] \sum [M_1^*] + k_{21} [M_1] \sum [M_2^*] \quad (\text{C.8})$$

with $\sum [M_1^*]$ the concentration of all the active chains terminating in monomer 1, summed over chain lengths and $\sum [M_2^*]$ is defined similarly for monomer 2. The rate of consumption for monomer 2 is

$$-\frac{d[M_2]}{dt} = k_{12} [M_2] \sum [M_1^*] + k_{22} [M_2] \sum [M_2^*] \quad (\text{C.9})$$

The ratio between eq. C.8 and C.9 and the following division by $\sum [M_2^*]$ yields

$$\frac{d[M_1]}{d[M_2]} = \frac{k_{11} [M_1] \sum \frac{[M_1^*]}{[M_2^*]} + k_{21} [M_1]}{k_{12} [M_2] \sum \frac{[M_1^*]}{[M_2^*]} + k_{22} [M_2]} \quad (\text{C.10})$$

The steady state approximation gives

$$\frac{d \sum [M_1^*]}{dt} = \frac{d \sum [M_2^*]}{dt} \approx 0 \quad (\text{C.11})$$

The rate of formation of active centers of monomer 1 ($M_2^* + M_1 \xrightarrow{k_{21}} M_2M_1^*$) is equal to the rate of their destruction ($M_1^* + M_2 \xrightarrow{k_{12}} M_1M_2^*$) so that

$$k_{21} [M_1] \sum [M_2^*] = k_{12} [M_2] \sum [M_1^*] \quad (\text{C.12})$$

or

$$\frac{\sum [M_1^*]}{\sum [M_2^*]} = \frac{k_{21} [M_1]}{k_{12} [M_2]} \quad (\text{C.13})$$

Substitution of eq. C.13 into eq. C.10 and following rearrangement yield the Mayo-Lewis equation

$$\frac{d [M_1]}{d [M_2]} = \frac{[M_1]}{[M_2]} \left(\frac{k_{11} \frac{k_{21} [M_1]}{k_{12} [M_2]} + k_{21}}{k_{12} \frac{k_{21} [M_1]}{k_{12} [M_2]} + k_{22}} \right) = \left(\frac{\frac{k_{11} [M_1]}{k_{12} [M_2]} + 1}{\frac{[M_1]}{[M_2]} + \frac{k_{22}}{k_{21}}} \right) = \frac{[M_1]}{[M_2]} \left(\frac{r_1 [M_1] + [M_2]}{[M_1] + r_2 [M_2]} \right) \quad (\text{C.14})$$

The Mayo-Lewis equation is often expressed in terms of mole fractions. Mole fractions of monomers $[M_1^*]$ and $[M_2^*]$ in the feed are defined as f_1 and f_2 where

$$f_1 = 1 - f_2 = \frac{M_1}{M_1 + M_2} \quad (\text{C.15})$$

F represents the mole fraction of each monomer in the copolymer:

$$F_1 = 1 - F_2 = \frac{dM_1}{d(M_1 + M_2)} \quad (\text{C.16})$$

These equations can be combined with the Mayo-Lewis equation to give:

$$F_1 = 1 - F_2 = \frac{r_1 f_1^2 + f_1 f_2}{r_1 f_1^2 + 2 f_1 f_2 + r_2 f_2^2} \quad (\text{C.17})$$

This equation gives the composition of copolymer formed at each instant.

Fineman and Ross [138] rearranged the copolymer equation into a linear form:

$$G = H r_1 - r_2 \quad (\text{C.18})$$

where

$$G = \frac{f_1(2F_1 - 1)}{(1 - f_1)F_1} \quad (\text{C.19})$$

$$H = \frac{f_1^2(1 - F_1)}{(1 - f_1)^2 F_1} \quad (\text{C.20})$$

or

$$G = x \left(1 - \frac{1}{y} \right) \quad (\text{C.21})$$

$$H = \frac{x^2}{y} \quad (\text{C.22})$$

with $x = f_1/f_2$ and $y = F_1/F_2$. Thus, a plot of H vs G yields a straight line with slope r_1 and intercept $-r_2$.

The Fineman-Ross equation doesn't consider the variation of the copolymer and monomer mixture composition that occurs during the course of a batch-type copolymerization. The Meyer-Lowry equation allows to remove the low conversion assumption and to use samples with high conversions. First of all, the Mayo-Lewis equation is rearranged in the form

$$F_1 = \frac{(r_1 - 1)f_1^2 + f_1}{(r_1 + r_2 - 2)f_1^2 + 2(1 - r_2)f_1 + r_2} \quad (\text{C.23})$$

Skeist [139] derived an equation that can be used to calculate the expected change in the monomer mixture and copolymer composition corresponding to the total mole conversion $1 - (M/M_0)$

$$\ln M/M^0 = \int_{f_1^0}^{f_1} [1/(F_1 - f_1)] df_1 \quad (\text{C.24})$$

The equation C.23 is substituted in the Skeist equation C.24 to give:

$$\ln \frac{M}{M^0} = \frac{1}{(2 - r_1 - r_2)} \int_{f_1^0}^{f_1} \frac{(r_1 + r_2 - 2)f_1^2 + 2(1 - r_2)f_1 + r_2}{f_1(f_1 - 1) \left(f_1 - \frac{1 - r_2}{2 - r_1 - r_2} \right)} df_1 \quad (\text{C.25})$$

The equation C.25 can be split into three terms:

$$-\int_{f_1^0}^{f_1} \frac{f_1}{(f_1-1)(f_1-\delta)} df_1 = -\left(\int_{f_1^0}^{f_1} \frac{f_1-1}{(f_1-1)(f_1-\delta)} df_1 + \int_{f_1^0}^{f_1} \frac{1}{(f_1-1)(f_1-\delta)} df_1\right) = \quad (C.26)$$

$$\ln \left[\left(\frac{f_1-1}{f_1^0-1}\right)^{(2-r_1-r_2)/(r_1-1)} \left(\frac{f_1-\delta}{f_1^0-\delta}\right)^{(r_2-1)/(r_1-1)} \right] \quad (C.27)$$

$$\frac{2(1-r_2)}{2-r_1-r_2} \int_{f_1^0}^{f_1} \frac{1}{(f_1-1)(f_1-\delta)} df_1 = \ln \left[\left(\frac{f_1-1}{f_1^0-1}\right)^{2(r_2-1)/(r_1-1)} \left(\frac{f_1-\delta}{f_1^0-\delta}\right)^{2(1-r_2)/(r_1-1)} \right] \quad (C.28)$$

and

$$\frac{r_2}{2-r_1-r_2} \int_{f_1^0}^{f_1} \frac{1}{f_1(f_1-1)(f_1-\delta)} df_1 = \quad (C.29)$$

$$\ln \left[\left(\frac{f_1}{f_1^0}\right)^{\frac{r_2}{1-r_2}} \left(\frac{f_1-1}{f_1^0-1}\right)^{\frac{r_2}{2(r_2-1)} + \frac{r_2(3-2r_2-r_1)}{2(1-r_2)(1-r_1)}} \left(\frac{f_1-\delta}{f_1^0-\delta}\right)^{\frac{r_2}{2(r_2-1)} + \frac{r_2(3-2r_2-r_1)}{2(1-r_2)(r_1-1)}} \right] \quad (C.30)$$

with the restriction $r_1 \neq 1$, $r_2 \neq 1$. After collecting terms and rearranging, one obtains:

$$\frac{M}{M_0} = \left(\frac{f_1}{f_1^0}\right)^\alpha \left(\frac{f_2}{f_2^0}\right)^\beta \left(\frac{f_1^0-\delta}{f_1-\delta}\right)^\gamma \quad (C.31)$$

where the constants α , β , γ , and δ have the values: $\alpha = r_2/(1-r_2)$; $\beta = r_1/(1-r_1)$; $\gamma = (1-r_1r_2)/(1-r_1)(1-r_2)$ and $\delta = (1-r_2)/(2-r_1-r_2)$.

C.2 Preparation of the macroinitiator mPEG-Br

mPEG-Br linear macroinitiator was synthesized from mPEG (reaction scheme in Figure 3) following the procedure reported in ref. [140]. mPEG (1 mmol) was dissolved under nitrogen atmosphere, in 15 mL of dry CH_2Cl_2 into a 100 mL three neck round-bottom flask equipped with condenser (to avoid evaporation of dichloromethane), dropping funnel, gas inlet/outlet and a magnetic stirrer. Then 0.37 g di DMAP (3 mmol) and 280 μL of TEA (2 mmol) were added and the reactor was thermostated at 0 °C. After cooling, 310 μL of BMPB (2.5 mmol) in 5 mL of dry CH_2Cl_2 were added dropwise during 1hr. Subsequently, the temperature was allowed to raise to room temperature and the reaction was continued under stirring for further 24 hr. The filtered solution was concentrated, dissolved in dichloromethane, washed with aqueous HCl (0.3

mol/L) and water for three times, and then dried by anhydrous magnesium sulfate for 30 min. The solvents were evaporated, and the raw product was precipitated in a large volume of diethyl ether. The purified mPEG-Br was obtained by recrystallization from methanol and dried in vacuum (purification procedure according to ref [141]).

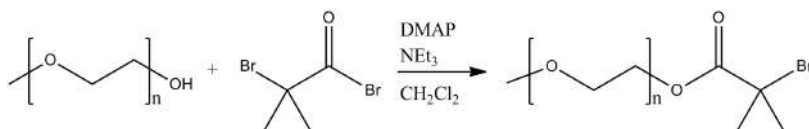


Figure 2: Reaction scheme for the synthesis of the macroinitiator mPEG-Br.

The chemical structure of the resulting mPEG-Br macroinitiator was characterized through ^1H NMR spectroscopy (Figure 3). The complete substitution of the hydroxyl group of mPEG is confirmed by the disappearance of the chemical shift at $\delta = 2.45$ ppm and the appearance of two new signals at 4.33 and 1.94 ppm due to the substituted mPEG. The peak area ratio of a, b and d is roughly 6:2:3, which also confirmed the complete esterification.

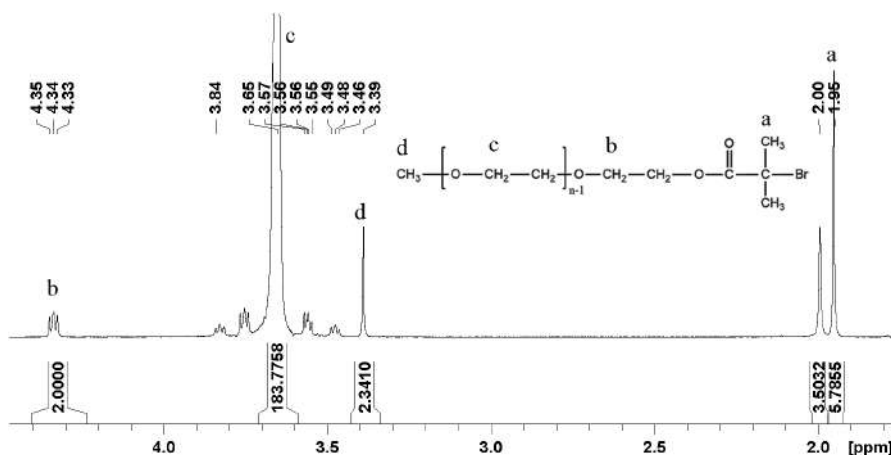


Figure 3: ^1H NMR of the macroinitiator mPEG-Br.

C.3 Synthesis and characterization of the fluorescent monomer

The fluorescent-labeled monomer BODIPY-DMAEMA was prepared with the following procedure: 10 mg (0.045 mmol) of 2,6-diterbutyl-4-methylphenol (BHT) were added to a mixture of 236 mg of 2,6-diethyl-1,3,5,7-tetramethyl-8-[4-(8-bromooctaoxy)phenyl]-4,4'-difluoroboradiaza indacene (compound **1**, 0.402 mmol) in 3 mL of DMAEMA (17.75 mmol), reaction scheme and chemical

structures are reported in Figure 4. The mixture was kept at 70 °C for 24 h. During the reaction time, a solid product was formed. After filtration, the product was washed 4 times with 20 mL of diethyl ether affording 214 mg (71.4 %) of compound product. $C_{39}H_{57}BBrF_2N_3O_3$, MM = 744.60 g/mol (ESI-MS spectrum is reported in Figure 5). 1H NMR ($CDCl_3$) δ : 0.97 (t, 6H, $2 \times CH_3$); 1.33 (s, 6H, $2 \times CH_3$); 1.40 (m, 8H, $4 \times CH_2$); 1.80 (m, 4H, $2 \times CH_2$); 1.95 (s, 3H, CH_3), 2.25-2.33 (q, 4H, $2 \times CH_2$); 2.51 (s, 6H, $2 \times CH_3$); 3.56 (s, 6H, $2 \times CH_3$); 3.61-3.65 (t, 2H, CH_2); 3.97-4.02 (t, 2H, CH_2); 4.15 (t, 2H, CH_2); 4.65 (t, 2H, CH_2); 5.68 (s, 1H, CH); 6.15 (s, 1H, CH); 6.96-6.99 (d, 2H, $2 \times CH$); 7.13-7.15 (d, 2H, $2 \times CH$). The 1H NMR and HSQC-NMR spectra are reported in Figures 6 - 8. The peak assignment of BODIPY-DMAEMA is based on comparison with 1H NMR chemical shifts of (4-((8-Bromooctyl)oxy)benzaldehyde) [142] and 2,6-diethyl-1,3,5,7-tetramethyl-8-(3-hydroxyphenyl)-4,4'-difluoroboradiazaindacene (chemical structure similar to compound **1**) [143].

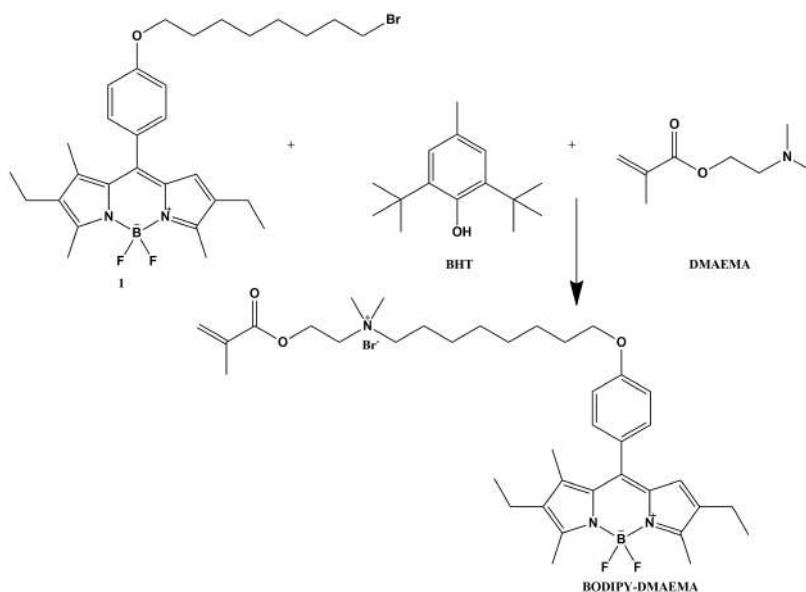


Figure 4: Reaction scheme for the synthesis of 2,6-diethyl-1,3,5,7-tetramethyl-8-[4-[4-(2-methacryloyl)ethyl-dimethylammoniumbromide]octaoxyphenyl]-4,4'-difluoroboradiaza indacene (BODIPY-DMAEMA).

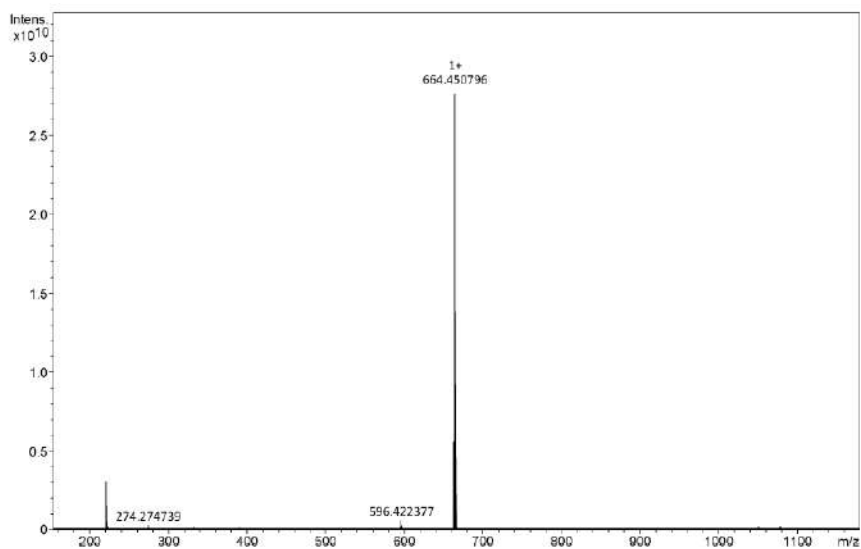


Figure 5: ESI MS (electrospray ionization-mass spectrometry) spectrum of the fluorescent monomer. The spectrum is in positive mode. The peak corresponding to $m/z = 664.450796$ is the peak of the fluorescent probe without bromide ($C_{39}H_{57}BF_2N_3O_3^+$).

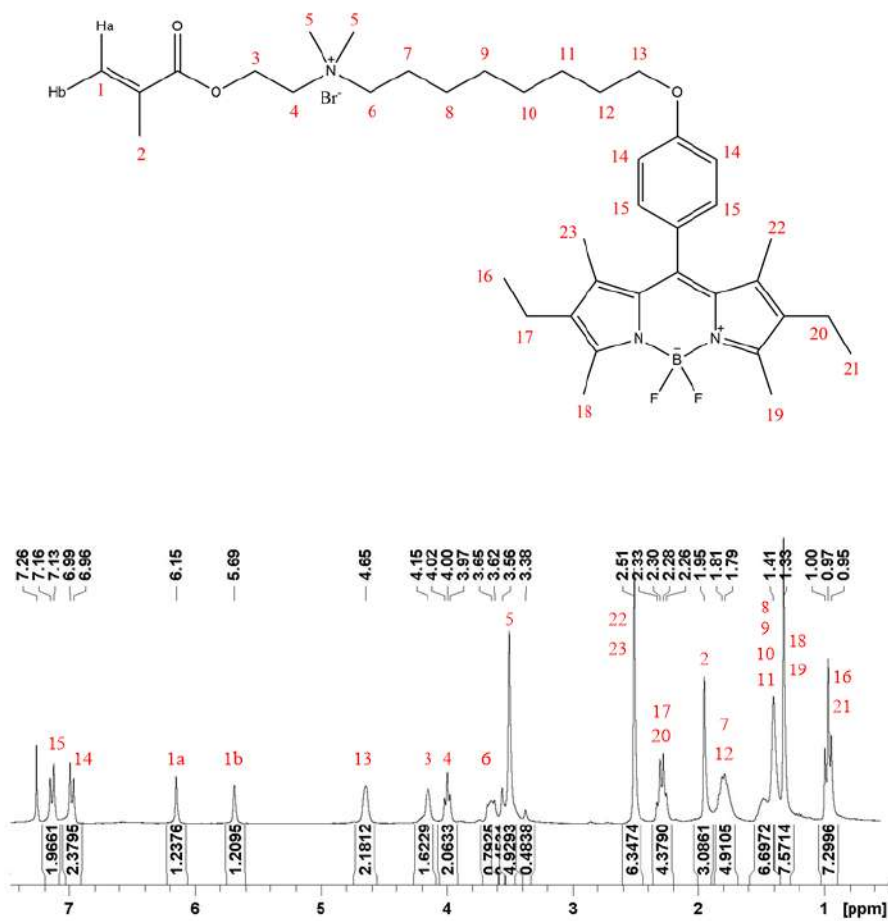


Figure 6: Peak assignments for ^1H spectrum of the fluorescent monomer.

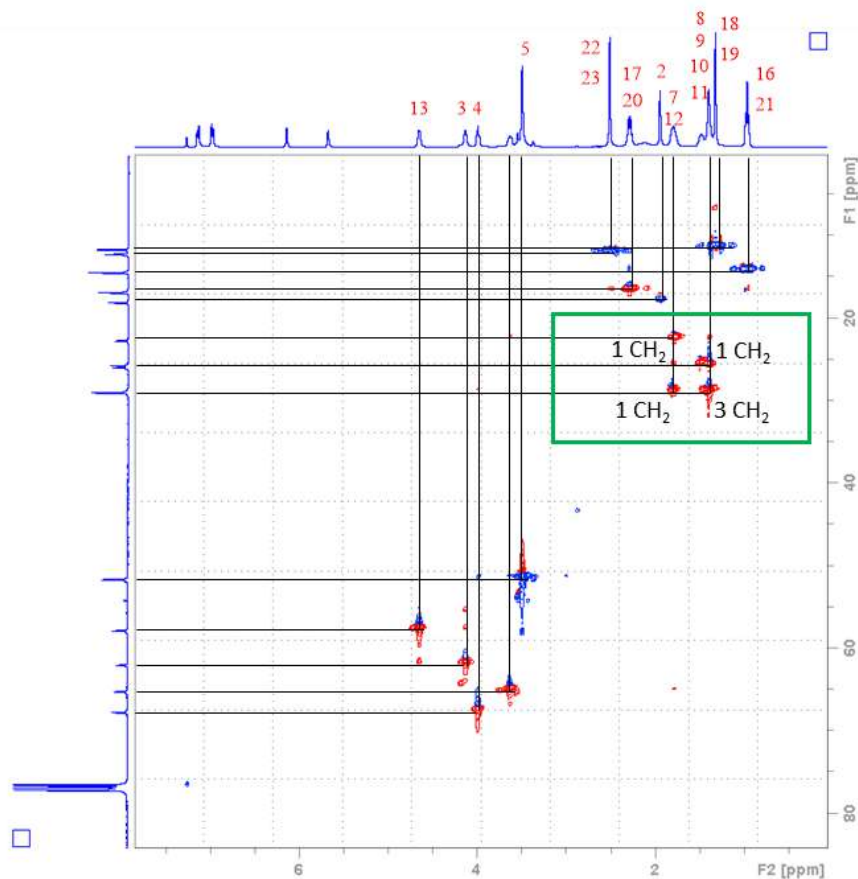


Figure 7: HSQC-NMR spectrum of the fluorescent monomer in the region of ^1H NMR 0 – 5 ppm. The green box highlights the aliphatic CH₂ corresponding to the protons labeled as 7, 8, 9, 10, 11 and 12.

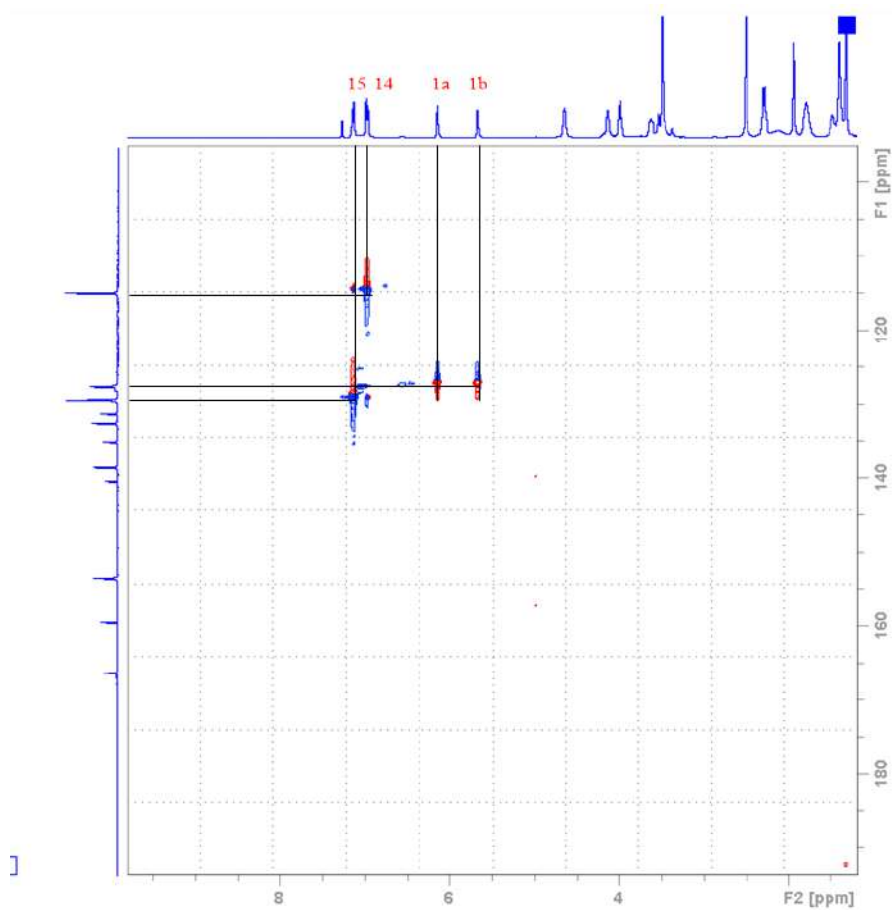


Figure 8: HSQC-NMR spectrum of the fluorescent monomer in the region of ^1H NMR 5-9 ppm.

C.4 Synthesis and characterization of the copolymers PMMA-*ran*-PDMAEMA, mPEG-*b*-(PMMA-*grad*-PDMAEMA), fluorescent mPEG-*b*-(PMMA-*grad*-PDMAEMA)

The ^1H NMR spectrum and the chemical assignment for the copolymer PMMA-*ran*-PDMAEMA is reported in Figure 9.

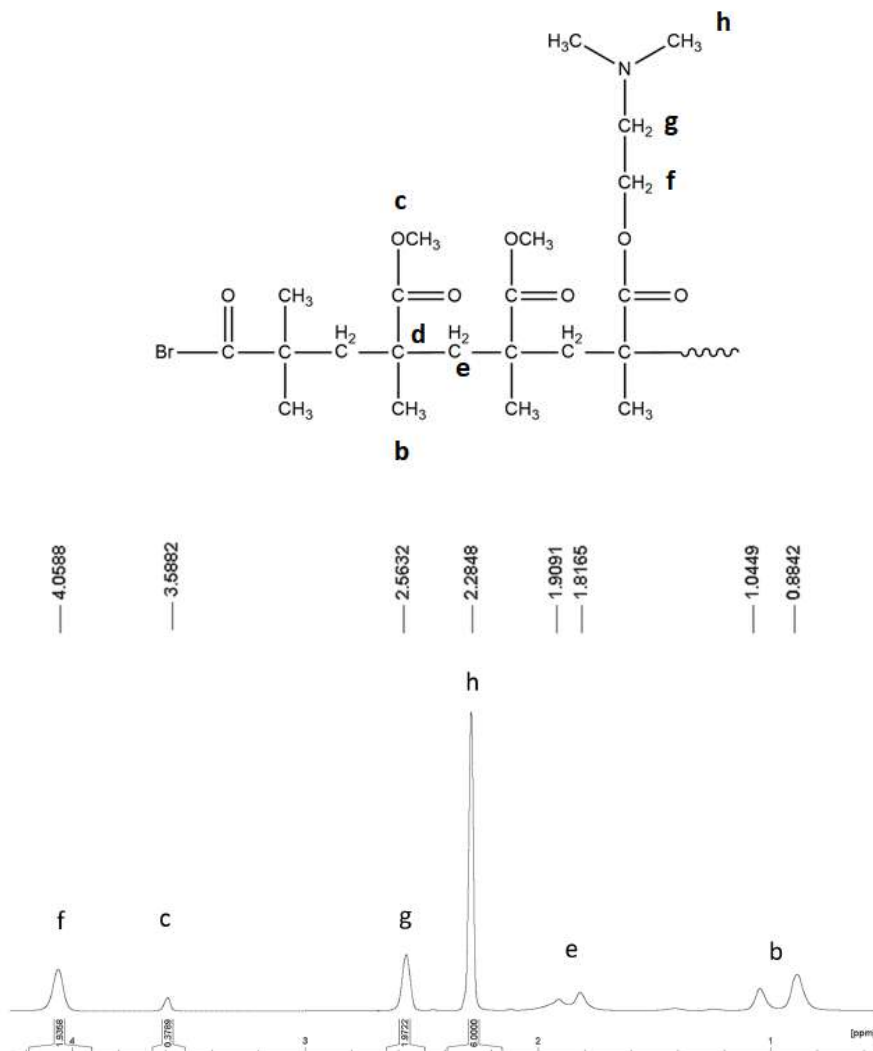


Figure 9: ^1H NMR of a copolymer PMMA-*ran*-PDMAEMA.

The DSC of the copolymer selected for the vesicles preparation P_{2k}MD_{40%} is shown in Figure 10.

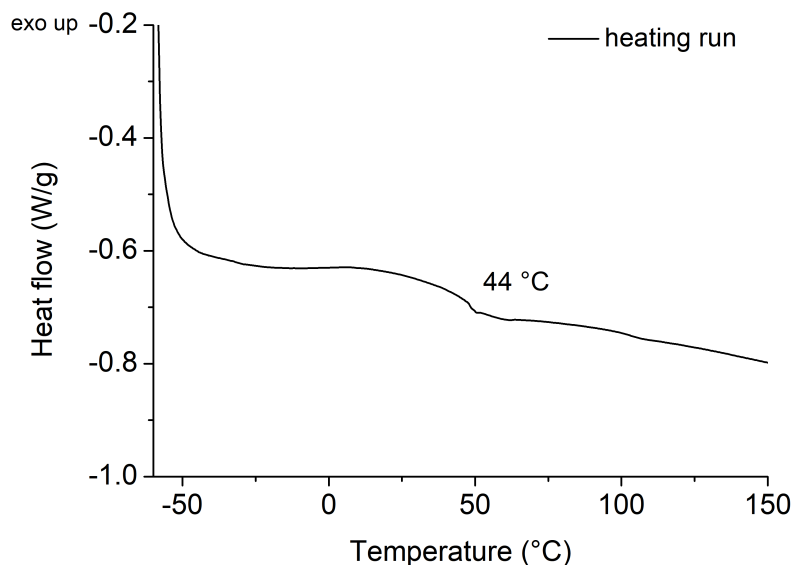
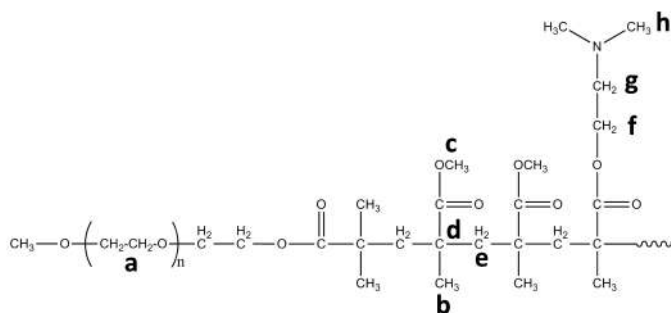


Figure 10: DSC of copolymer P_{2k}MD_{40%}. The curve indicates the second heating run with the corresponding glass transition temperature.

Typical ¹H NMR and ¹³C NMR spectra for the amphiphilic copolymer mPEG-*b*-(PMMA-*grad*-PDMAEMA) are shown in Figure 11 together with a chemical scheme indicating the assignment of each signal.



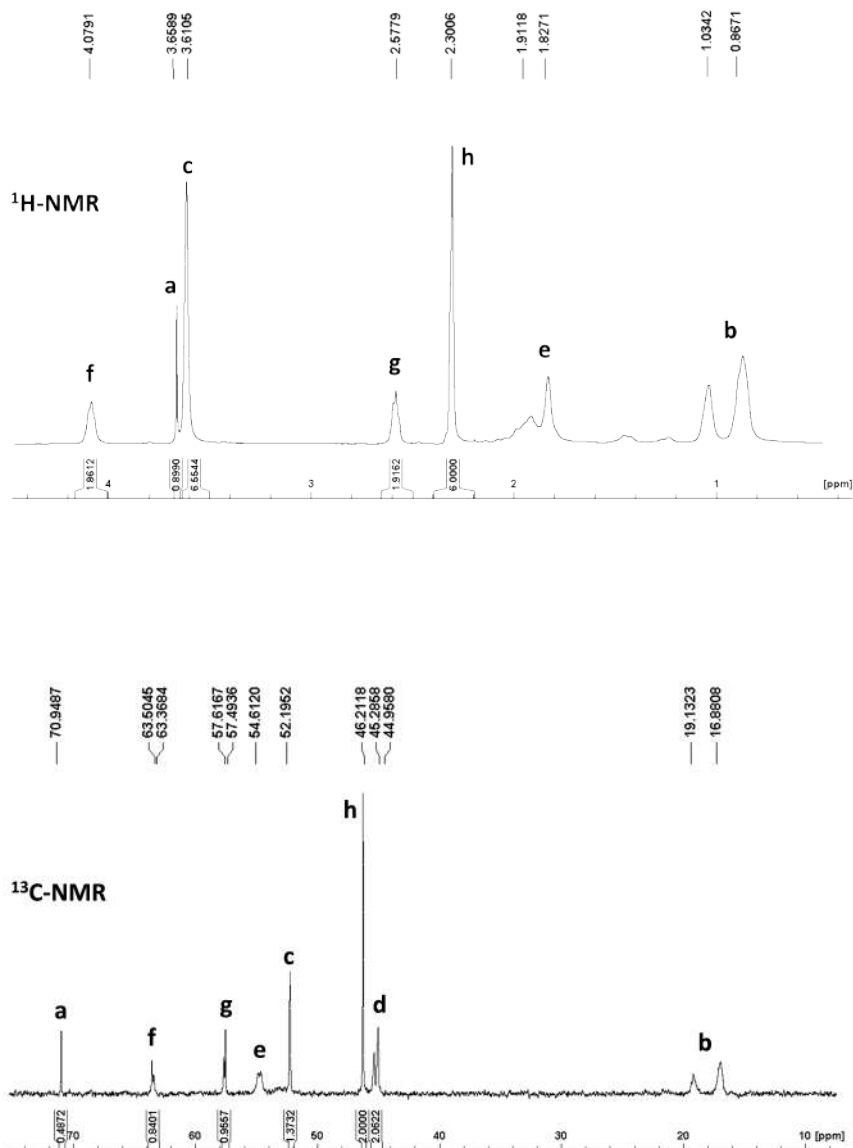


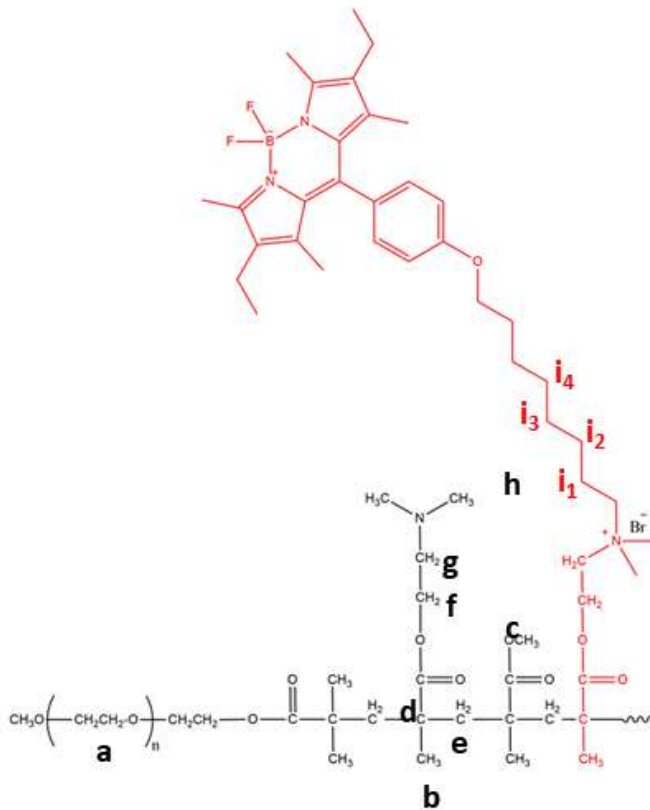
Figure 11: $^1\text{H-NMR}$ and $^{13}\text{C-NMR}$ spectra of a copolymer mPEG-*b*-PMMA-*grad*-PDMAEMA.

The $^1\text{H-NMR}$, $^{13}\text{C-NMR}$ and HSQC spectra of the fluorescent labeled mPEG-*b*-(PMMA-*grad*-PDMAEMA) copolymer are shown in Figures 12 and 14. The signal ($^1\text{H-NMR}$: $\delta = 1.27$ ppm and $^{13}\text{C-NMR}$: $\delta = 29.7$ ppm), indicated with \mathbf{i}_{1-4} , has been assigned to the four carbons $-\text{CH}_2$ of the fluorescent

monomer (supposed to be signals 7, 8, 9 and 10 of the fluorescent monomer, figures 6 and 7). The molar fractions in the final copolymer (F_x) where the subscript x is referred to one of the components (mPEG, MMA, DMAEMA, BODIPY-DMAEMA) are calculated from the intensities of the NMR signal as

$$F_x = \frac{\frac{I_x}{N_x}}{\frac{I_{\text{mPEG}}}{N_{\text{mPEG}}} + \frac{I_{\text{MMA}}}{N_{\text{MMA}}} + \frac{I_{\text{DMAEMA}}}{N_{\text{DMAEMA}}} + \frac{I_{\text{BODIPY-DMAEMA}}}{N_{\text{BODIPY-DMAEMA}}}} \quad (\text{C.32})$$

where I_x is the NMR intensity and N_x is the number of carbon atoms integrated for the component x . In equations 4.10 - 4.18 of chapter 4, the compositions and the degrees of polymerization are calculated considering the signal **a** of mPEG (it corresponds to 2 carbon atoms, O-CH₂-CH₂), the signal **h** of DMAEMA (it corresponds to 2 carbon atoms, N-(CH₃)₂), the signal **c** of MMA (one carbon atom, -OCH₃) and the signal **i**₁₋₄ of the fluorescent BODIPY-DMAEMA that accounts for four carbon atoms (-(CH₂)₄).



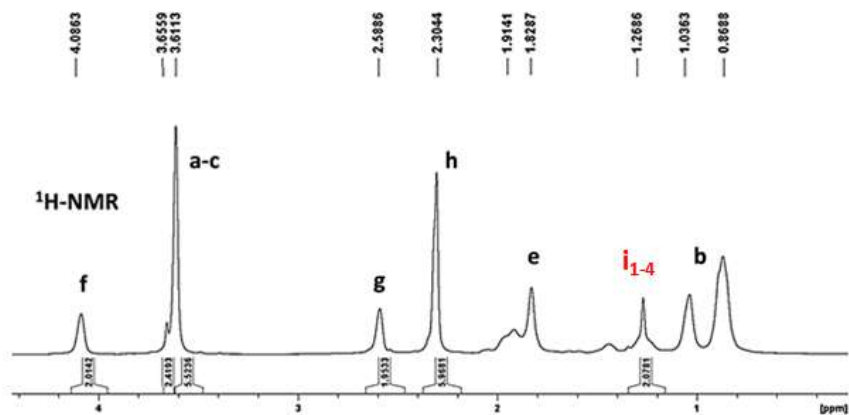


Figure 12: ¹H NMR spectrum of a fluorescent copolymer mPEG-*b*-(PMMA-*grad*-PDMAEMA).

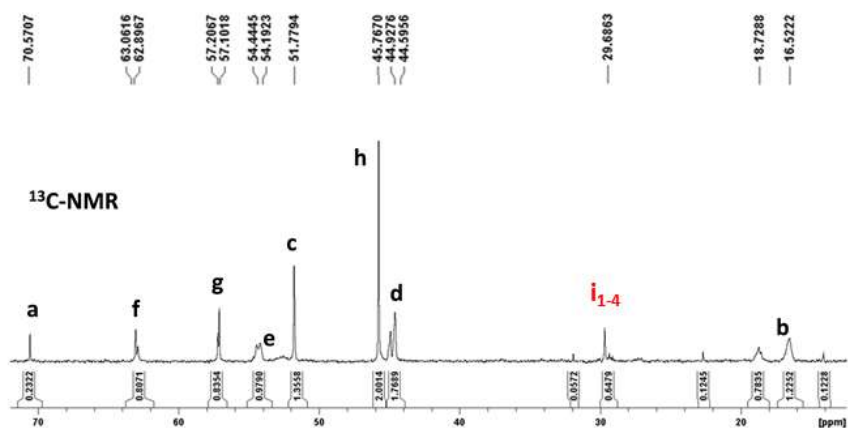


Figure 13: ¹³C NMR spectrum of a fluorescent copolymer mPEG-*b*-(PMMA-*grad*-PDMAEMA).

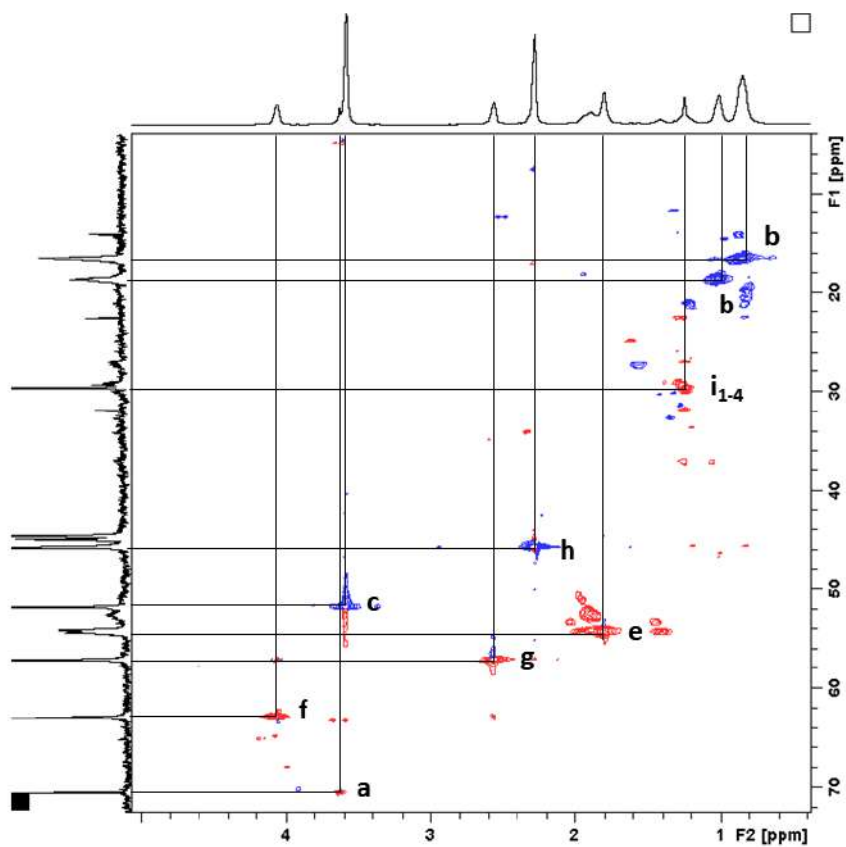


Figure 14: HSQC spectrum of a fluorescent copolymer mPEG-*b*-(PMMA-*grad*-PDMAEMA).

The DSC and the GPC results of the fluorescent copolymers P_{5k}MD_{53%} and P_{2k}MD_{20%} are shown in Figures 15 and 16.

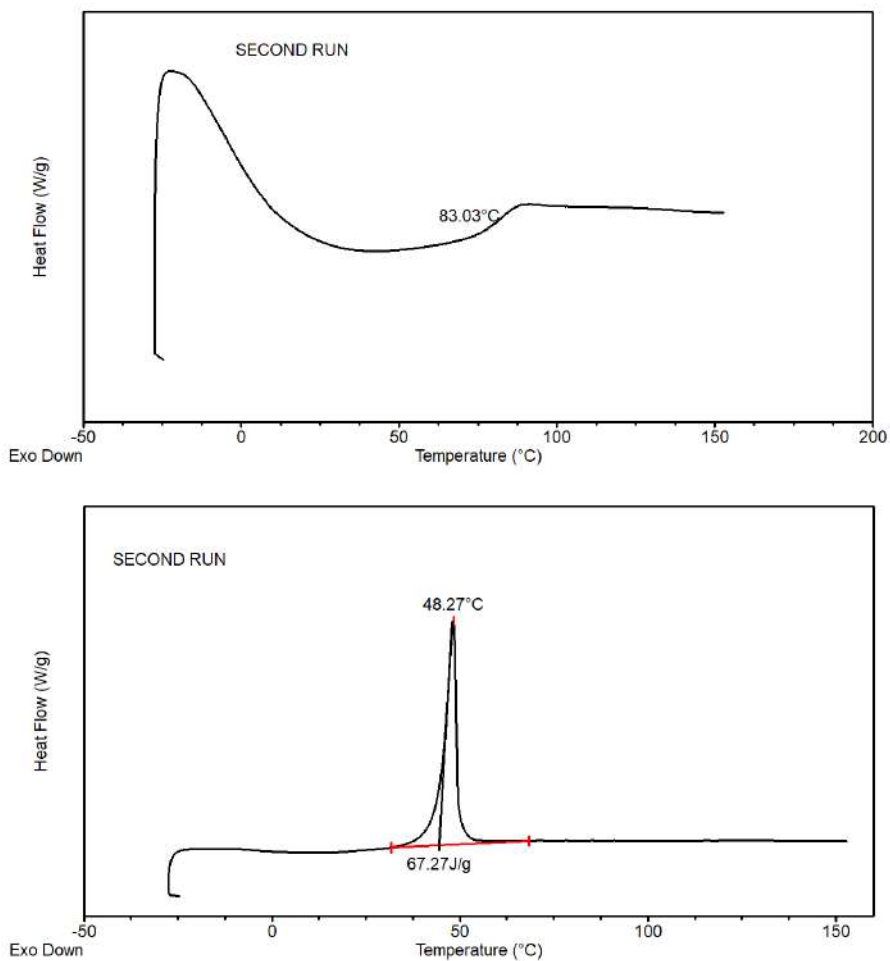
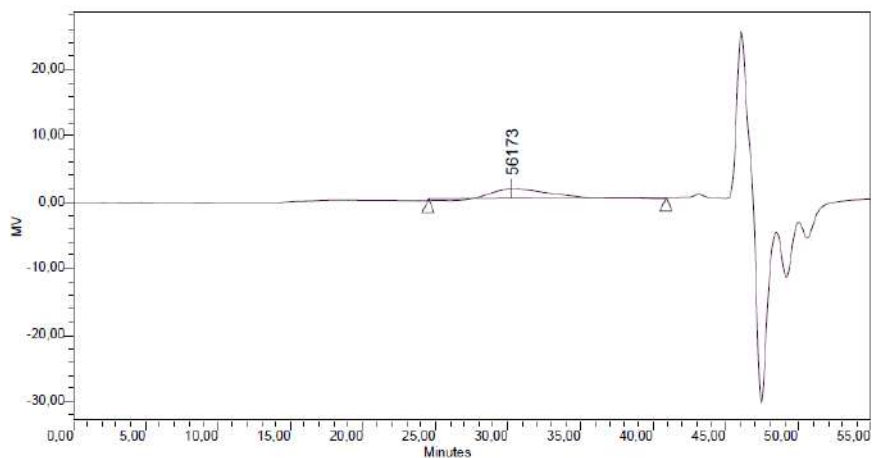
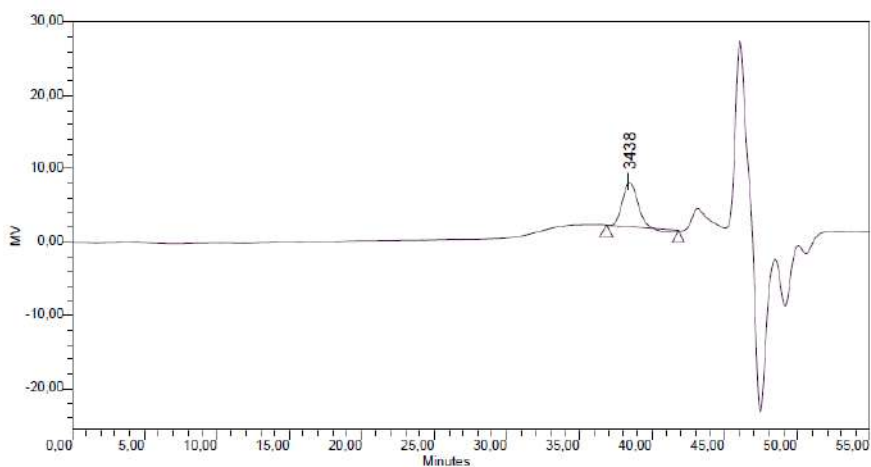


Figure 15: On the top, DSC of the copolymer P_{5k}MD_{53%}. The curve indicates the second heating run with the corresponding glass transition temperature. At the bottom, DSC of the copolymer P_{2k}MD_{20%}. The curve indicates the second heating run with the corresponding melting temperature.



Broad Unknown Relative Peak Table

Distribution Name	Mn (Daltons)	Mw (Daltons)	MP (Daltons)	Mz (Daltons)	Mz+1 (Daltons)	Polydispersity	Mz/Mw	Mz+1/Mw
1	25890	50893	56173	77251	102080	1,965749	1,517911	2,005779



Broad Unknown Relative Peak Table

Distribution Name	Mn (Daltons)	Mw (Daltons)	MP (Daltons)	Mz (Daltons)	Mz+1 (Daltons)	Polydispersity	Mz/Mw	Mz+1/Mw
1	3272	3387	3438	3498	3606	1,035192	1,032922	1,064634

Figure 16: On the top, GPC of the copolymer P_{5k}MD_{53%}. At the bottom, GPC of the copolymer P_{2k}MD_{20%}.

C.5 Estimation of the hydrophobic mismatch

The thickness of a hydrated POPC bilayer is 4 nm (estimated from cryo-electron microscope combined with image simulation examination of the bilayer thickness [29, 144]). The thickness of the copolymers bilayer was estimated calculating the mean-square end-to-end distance approximated for long chains [145]

$$\langle R^2 \rangle \cong C_\infty n l^2 \quad (\text{C.33})$$

where C_∞ is the Flory's characteristic ratio that can be seen as a measure of the stiffness of the polymer in a given ideal chain model, n is the number of backbone bonds (degree of polymerization), l is the average monomer length. l was calculated from the density (ρ), the Avogadro's number (N_{Av}) and the molar mass of the monomer (M_0) through the equation

$$l = \left(V^{1/3} \right) = (M_0 / (\rho N_{\text{Av}}))^{1/3} \quad (\text{C.34})$$

The size of the double layer for the copolymer P_{2k}MD_{40%} is ~ 18.7 nm if the DMAEMA is considered hydrophilic and ~ 50.3 nm if the DMAEMA is considered hydrophobic (Table 3).

Table 3: Estimation of the hydrophobic mismatch for the copolymer P_{2k}MD_{40%}

Polymer	C_∞	l (cm)	n	Double layer $2 \times R$ (nm)
PMMA	7.9 ^a	5.6×10^{-8}	35	18.7
PDMAEMA	11 ^b	6.5×10^{-8}	53	31.6

^a ref.[146]

^b ref. [147]

BIBLIOGRAPHY

- [1] Shakhshiri, B.Z.: *Chemical Demonstrations: A Handbook for Teachers of Chemistry*. Volume 3. Univ of Wisconsin Press (1989)
- [2] Landolt, H.: Ueber die Zeitdauer der Reaction zwischen Jodsäure und schwefliger Säure. *Berichte der deutschen chemischen Gesellschaft* **19**(1) (1886) 1317–1365
- [3] Lyle, K.: TEACHING KINETICS WITH THE LANDOLT IODINE CLOCK RXN. 6
- [4] Watkins, K.W.: The arsenic (iii) sulfide clock reaction. *Journal of Chemical Education* **64**(3) (1987) 255
- [5] Jones, P., Oldham, K.B.: The theory of the formaldehyde clock reaction. *Journal of Chemical Education* **40**(7) (1963) 366
- [6] Jones, P., Haggett, M.L., Longridge, J.L.: The hydration of carbon dioxide: A double clock experiment. *Journal of Chemical Education* **41**(11) (1964) 610
- [7] Preece, S.J., Billingham, J., King, A.C.: Chemical clock reactions: The effect of precursor consumption. *Journal of Mathematical Chemistry* **26**(1-3) (1999) 47
- [8] Kovacs, K., McIlwaine, R., Gannon, K., Taylor, A.F., Scott, S.K.: Complex Behavior in the Formaldehyde- Sulfite Reaction. *The Journal of Physical Chemistry A* **109**(1) (2005) 283–288
- [9] Escala, D.M., Muñuzuri, A.P., De Wit, A., Carballido-Landeira, J.: Temporal viscosity modulations driven by a pH sensitive polymer coupled to a pH-changing chemical reaction. *Physical Chemistry Chemical Physics* **19**(19) (2017) 11914–11919
- [10] Krajewska, B., Ciurli, S.: Jack bean (*Canavalia ensiformis*) urease. Probing acid–base groups of the active site by pH variation. *Plant Physiology and Biochemistry* **43**(7) (2005) 651–658
- [11] Bánsági Jr, T., Taylor, A.F.: Exploitation of Feedback in Enzyme-catalysed Reactions. *Israel Journal of Chemistry* **58**(6-7) (2018) 706–713
- [12] Jee, E., Bánsági, T., Taylor, A.F., Pojman, J.A.: Temporal control of gelation and polymerization fronts driven by an autocatalytic enzyme reaction. *Angewandte Chemie International Edition* **55**(6) (2016) 2127–2131

- [13] Bánsági Jr, T., Taylor, A.F.: Role of differential transport in an oscillatory enzyme reaction. *The Journal of Physical Chemistry B* **118**(23) (2014) 6092–6097
- [14] Hu, G., Pojman, J.A., Scott, S.K., Wrobel, M.M., Taylor, A.F.: Base-Catalyzed Feedback in the Urea- Urease Reaction. *The Journal of Physical Chemistry B* **114**(44) (2010) 14059–14063
- [15] Bubanja, I.N., Bánsági, T., Taylor, A.F.: Kinetics of the urea–urease clock reaction with urease immobilized in hydrogel beads. *Reaction Kinetics, Mechanisms and Catalysis* **123**(1) (2018) 177–185
- [16] Muzika, F., Bansagi, T., Schreiber, I., Schreiberova, L., Taylor, A.F.: A bistable switch in pH in urease-loaded alginate beads. *Chemical Communications* **50**(76) (2014) 11107–11109
- [17] Kocak, G., Tuncer, C., Bütün, V.: pH-Responsive polymers. *Polymer Chemistry* **8**(1) (2017) 144–176
- [18] Wei, M., Gao, Y., Li, X., Serpe, M.J.: Stimuli-responsive polymers and their applications. *Polymer Chemistry* **8**(1) (2017) 127–143
- [19] Lorenzo, R.A., Carro, A.M., Concheiro, A., Alvarez-Lorenzo, C.: Stimuli-responsive materials in analytical separation. *Analytical and bioanalytical chemistry* **407**(17) (2015) 4927–4948
- [20] Schmaljohann, D.: Thermo-and pH-responsive polymers in drug delivery. *Advanced drug delivery reviews* **58**(15) (2006) 1655–1670
- [21] Huo, M., Yuan, J., Tao, L., Wei, Y.: Redox-responsive polymers for drug delivery: from molecular design to applications. *Polymer Chemistry* **5**(5) (2014) 1519–1528
- [22] Cabane, E., Zhang, X., Langowska, K., Palivan, C.G., Meier, W.: Stimuli-responsive polymers and their applications in nanomedicine. *Biointerphases* **7**(1) (2012) 9
- [23] Gao, Y., Wei, M., Li, X., Xu, W., Ahiabu, A., Perdiz, J., Liu, Z., Serpe, M.J.: Stimuli-responsive polymers: Fundamental considerations and applications. *Macromolecular Research* **25**(6) (2017) 513–527
- [24] Yu, S., Dong, S., Jiao, X., Li, C., Chen, D.: Ultrathin Photonic Polymer Gel Films Templated by Non-Close-Packed Monolayer Colloidal Crystals to Enhance Colorimetric Sensing. *Polymers* **11**(3) (2019) 534
- [25] Tóth-Szeles, E., Horváth, J., Holló, G., Sz\Hucs, R., Nakanishi, H., Lagzi, I.: Chemically coded time-programmed self-assembly. *Molecular Systems Design & Engineering* **2**(3) (2017) 274–282

- [26] Qin, Y., Cabral, J.M.: Review properties and applications of urease. *Biocatalysis and biotransformation* **20**(1) (2002) 1–14
- [27] Jagers, R.W., Bon, S.A.: Independent responsive behaviour and communication in hydrogel objects. *Materials Horizons* **4**(3) (2017) 402–407
- [28] Stano, P., Carrara, P., Kuruma, Y., de Souza, T.P., Luisi, P.L.: Compartmentalized reactions as a case of soft-matter biotechnology: synthesis of proteins and nucleic acids inside lipid vesicles. *Journal of Materials Chemistry* **21**(47) (2011) 18887–18902
- [29] Walde, P., Cosentino, K., Engel, H., Stano, P.: Giant vesicles: preparations and applications. *ChemBioChem* **11**(7) (2010) 848–865
- [30] Perrier, D.L., Rems, L., Kreutzer, M.T., Boukany, P.E.: The role of gel-phase domains in electroporation of vesicles. *Scientific reports* **8**(1) (2018) 4758
- [31] Reeves, J.P., Dowben, R.M.: Formation and properties of thin-walled phospholipid vesicles. *Journal of cellular physiology* **73**(1) (1969) 49–60
- [32] Angelova, M.I., Dimitrov, D.S.: Liposome electroformation. *Faraday discussions of the Chemical Society* **81** (1986) 303–311
- [33] Wick, R., Walde, P., Luisi, P.L.: Light microscopic investigations of the autocatalytic self-reproduction of giant vesicles. *Journal of the American Chemical Society* **117**(4) (1995) 1435–1436
- [34] Peterlin, P., Arrigler, V., Kogej, K., Svetina, S., Walde, P.: Growth and shape transformations of giant phospholipid vesicles upon interaction with an aqueous oleic acid suspension. *Chemistry and physics of lipids* **159**(2) (2009) 67–76
- [35] Döbereiner, H.G., Käs, J., Noppl, D., Sprenger, I., Sackmann, E.: Budding and fission of vesicles. *Biophysical journal* **65**(4) (1993) 1396–1403
- [36] Pantazatos, D.P., MacDonald, R.C.: Directly observed membrane fusion between oppositely charged phospholipid bilayers. *The Journal of membrane biology* **170**(1) (1999) 27–38
- [37] Luisi, P.L., Ferri, F., Stano, P.: Approaches to semi-synthetic minimal cells: a review. *Naturwissenschaften* **93**(1) (2006) 1–13
- [38] Treyer, M., Walde, P., Oberholzer, T.: Permeability enhancement of lipid vesicles to nucleotides by use of sodium cholate: basic studies and application to an enzyme-catalyzed reaction occurring inside the vesicles. *Langmuir* **18**(4) (2002) 1043–1050

- [39] Yoshimoto, M., Wang, S., Fukunaga, K., Treyer, M., Walde, P., Kuboi, R., Nakao, K.: Enhancement of apparent substrate selectivity of proteinase K encapsulated in liposomes through a cholate-induced alteration of the bilayer permeability. *Biotechnology and bioengineering* **85**(2) (2004) 222–233
- [40] Shohda, K.i., Tamura, M., Kageyama, Y., Suzuki, K., Suyama, A., Sugawara, T.: Compartment size dependence of performance of polymerase chain reaction inside giant vesicles. *Soft Matter* **7**(8) (2011) 3750–3753
- [41] Tsumoto, K., Nomura, S.i.M., Nakatani, Y., Yoshikawa, K.: Giant liposome as a biochemical reactor: transcription of DNA and transportation by laser tweezers. *Langmuir* **17**(23) (2001) 7225–7228
- [42] Girard, P., Pecreaux, J., Lenoir, G., Falson, P., Rigaud, J.L., Bassereau, P.: A new method for the reconstitution of membrane proteins into giant unilamellar vesicles. *Biophys. J.* **87**: 419–429. The first affiliation should read: Laboratoire Physico-Chimie Curie. *Biophysical Journal* **87** (2004) 2098
- [43] Altamura, E., Milano, F., Tangorra, R.R., Trotta, M., Omar, O.H., Stano, P., Mavelli, F.: Highly oriented photosynthetic reaction centers generate a proton gradient in synthetic protocells. *Proceedings of the National Academy of Sciences* **114**(15) (2017) 3837–3842
- [44] Stano, P., Altamura, E., Mavelli, F.: Novel directions in molecular systems design: The case of light-transducing synthetic cells. *Communicative & integrative biology* **10**(5-6) (2017) 3837–3842
- [45] Altamura, E., Milano, F., Trotta, M., Stano, P., Mavelli, F.: Modelling Giant Lipid Vesicles Designed for Light Energy Transduction. In: *Advances in Bionanomaterials*. Springer (2018) 97–109
- [46] Ermentrout, B.: Simulating, analyzing, and animating dynamical systems: a guide to XPPAUT for researchers and students. Volume 14. Siam (2002)
- [47] MATLAB: Matlab & Simulink - Version R2017b - MathWorks Italia
- [48] Stano, P., Wodlei, F., Carrara, P., Ristori, S., Marchettini, N., Rossi, F.: Approaches to Molecular Communication Between Synthetic Compartments Based on Encapsulated Chemical Oscillators. In: *Advances in Artificial Life and Evolutionary Computation*. Springer (2014) 58–74
- [49] Miele, Y., Bansagi, Tamas Jr., Taylor, A.F., Rossi, F.: Modelling Approach to Enzymatic pH Oscillators in Giant Lipid Vesicles. Lecture notes in Bioengineering

- [50] Miele, Y., Bánsági Jr, T., Taylor, A.F., Stano, P., Rossi, F.: Engineering Enzyme-Driven Dynamic Behaviour in Lipid Vesicles. In: Italian Workshop on Artificial Life and Evolutionary Computation, Springer (2015) 197–208
- [51] Clement, N.R., Gould, J.M.: Pyranine (8-hydroxy-1, 3, 6-pyrenetrisulfonate) as a probe of internal aqueous hydrogen ion concentration in phospholipid vesicles. *Biochemistry* **20**(6) (1981) 1534–1538
- [52] Valeur, B., Berberan-Santos, M.N.: *Molecular Fluorescence: Principles and Applications*. Wiley (March 2013)
- [53] Sandoval, C., Ortega, A., Sanchez, S.A., Morales, J., Gunther, G.: Structuration in the interface of direct and reversed micelles of sucrose esters, studied by fluorescent techniques. *PloS one* **10**(4) (2015) e0123669
- [54] Diaspro, A.: *Nanoscopy and Multidimensional Optical Fluorescence Microscopy*. CRC Press (April 2010)
- [55] Bizzarri, R., Arcangeli, C., Arosio, D., Ricci, F., Faraci, P., Cardarelli, F., Beltram, F.: Development of a novel GFP-based ratiometric excitation and emission pH indicator for intracellular studies. *Biophysical journal* **90**(9) (2006) 3300–3314
- [56] Zaikin, A.N., Zhabotinsky, A.M.: Concentration wave propagation in two-dimensional liquid-phase self-oscillating system. *Nature* **225**(5232) (1970) 535
- [57] Biosa, G., Bastianoni, S., Rustici, M.: Chemical waves. *Chemistry–A European Journal* **12**(13) (2006) 3430–3437
- [58] Taylor, A.F.: Mechanism and phenomenology of an oscillating chemical reaction. *Progress in Reaction Kinetics and Mechanism* **27**(4) (2002) 247–325
- [59] Tomasi, R., Noël, J.M., Zenati, A., Ristori, S., Rossi, F., Cabuil, V., Kanoufi, F., Abou-Hassan, A.: Chemical communication between liposomes encapsulating a chemical oscillatory reaction. *Chemical Science* **5**(5) (2014) 1854–1859
- [60] Rossi, F., Rustici, M., Rossi, C., Tiezzi, E.: Isotopic effect on the kinetics of the Belousov-Zhabotinsky reaction. *International journal of molecular sciences* **8**(9) (2007) 943–949
- [61] Winfree, A.T.: Spiral waves of chemical activity. *Science* **175**(4022) (1972) 634–636

- [62] Rossi, F., Lombardo, R., Sciascia, L., Sbriziolo, C., Liveri, M.L.T.: Spatio-Temporal Perturbation of the Dynamics of the Ferroin Catalyzed Belousov-Zhabotinsky Reaction in a Batch Reactor Caused by Sodium Dodecyl Sulfate Micelles. *The Journal of Physical Chemistry B* **112**(24) (2008) 7244–7250
- [63] Petrov, V., Gaspar, V., Masere, J., Showalter, K.: Controlling chaos in the Belousov–Zhabotinsky reaction. *Nature* **361**(6409) (1993) 240–243
- [64] Budroni, M.A., Calabrese, I., Miele, Y., Rustici, M., Marchettini, N., Rossi, F.: Control of chemical chaos through medium viscosity in a batch ferroin-catalysed Belousov–Zhabotinsky reaction. *Physical Chemistry Chemical Physics* **19**(48) (2017) 32235–32241
- [65] Bánsági Jr, T., Taylor, A.F.: Switches induced by quorum sensing in a model of enzyme-loaded microparticles. *Journal of The Royal Society Interface* **15**(140) (2018) 20170945
- [66] Abisado, R.G., Benomar, S., Klaus, J.R., Dandekar, A.A., Chandler, J.R.: Bacterial quorum sensing and microbial community interactions. *MBio* **9**(3) (2018) e02331–17
- [67] Mukherjee, S., Bassler, B.L.: Bacterial quorum sensing in complex and dynamically changing environments. *Nature Reviews Microbiology* (2019) 1
- [68] Taylor, A.F., Tinsley, M.R., Wang, F., Huang, Z., Showalter, K.: Dynamical quorum sensing and synchronization in large populations of chemical oscillators. *Science* **323**(5914) (2009) 614–617
- [69] Hankins, M.J., Gáspár, V., Kiss, I.Z.: Abrupt and gradual onset of synchronized oscillations due to dynamical quorum sensing in the single-cathode multi-anode nickel electrodisolution system. *Chaos: An Interdisciplinary Journal of Nonlinear Science* **29**(3) (2019) 033114
- [70] Walde, P., Namani, T., Morigaki, K., Hauser, H.: Formation and properties of fatty acid vesicles (liposomes). In: *Liposome technology*. CRC Press (2018) 23–42
- [71] Morigaki, K., Walde, P.: Fatty acid vesicles. *Current Opinion in Colloid & Interface Science* **12**(2) (2007) 75–80
- [72] Xu, C., Hu, S., Chen, X.: Artificial cells: from basic science to applications. *Materials Today* **19**(9) (2016) 516–532
- [73] Namani, T., Walde, P.: From decanoate micelles to decanoic acid/dodecylbenzenesulfonate vesicles. *Langmuir* **21**(14) (2005) 6210–6219

- [74] Apel, C.L., Deamer, D.W., Mautner, M.N.: Self-assembled vesicles of monocarboxylic acids and alcohols: conditions for stability and for the encapsulation of biopolymers. *Biochimica et Biophysica Acta (BBA)-Biomembranes* **1559**(1) (2002) 1–9
- [75] Walde, P., Wick, R., Fresta, M., Mangone, A., Luisi, P.L.: Autopoietic self-reproduction of fatty acid vesicles. *Journal of the American Chemical Society* **116**(26) (1994) 11649–11654
- [76] Rendón, A., Carton, D.G., Sot, J., García-Pacios, M., Montes, L.R., Valle, M., Arrondo, J.L.R., Goñi, F.M., Ruiz-Mirazo, K.: Model systems of precursor cellular membranes: long-chain alcohols stabilize spontaneously formed oleic acid vesicles. *Biophysical journal* **102**(2) (2012) 278–286
- [77] Murakami, M., Yoshikawa, H., Takada, K., Muranishi, S.: Effect of oleic acid vesicles on intestinal absorption of carboxyfluorescein in rats. *Pharmaceutical research* **3**(1) (1986) 35–40
- [78] Kumar, L., Verma, S., Kumar, S., Prasad, D.N., Jain, A.K.: Fatty acid vesicles acting as expanding horizon for transdermal delivery. *Artificial cells, nanomedicine, and biotechnology* **45**(2) (2017) 251–260
- [79] Chen, I.A., Salehi-Ashtiani, K., Szostak, J.W.: RNA catalysis in model protocell vesicles. *Journal of the American Chemical Society* **127**(38) (2005) 13213–13219
- [80] Jin, L., Kamat, N.P., Jena, S., Szostak, J.W.: Fatty acid/phospholipid blended membranes: a potential intermediate state in protocellular evolution. *Small* **14**(15) (2018) 1704077
- [81] Berclaz, N., Müller, M., Walde, P., Luisi, P.L.: Growth and transformation of vesicles studied by ferritin labeling and cryotransmission electron microscopy. *The Journal of Physical Chemistry B* **105**(5) (2001) 1056–1064
- [82] Zhu, T.F., Szostak, J.W.: Coupled growth and division of model protocell membranes. *Journal of the American Chemical Society* **131**(15) (2009) 5705–5713
- [83] Ruiz-Mirazo, K., Briones, C., de la Escosura, A.: Prebiotic systems chemistry: new perspectives for the origins of life. *Chemical reviews* **114**(1) (2013) 285–366
- [84] Rasband, W.S.: ImageJ. Bethesda, MD, <https://imagej.nih.gov/ij/> (1997)
- [85] Fidaleo, M., Lavecchia, R.: Kinetic study of enzymatic urea hydrolysis in the pH range 4–9. *Chemical and biochemical engineering quarterly* **17**(4) (2003) 311–318

- [86] Krajewska, B.: Ureasas I. Functional, catalytic and kinetic properties: A review. *Journal of Molecular Catalysis B: Enzymatic* **59**(1-3) (2009) 9–21
- [87] Walter, A., Gutknecht, J.: Permeability of small nonelectrolytes through lipid bilayer membranes. *The Journal of membrane biology* **90**(3) (1986) 207–217
- [88] Lande, M.B., Donovan, J.M., Zeidel, M.L.: The relationship between membrane fluidity and permeabilities to water, solutes, ammonia, and protons. *The Journal of general physiology* **106**(1) (1995) 67–84
- [89] Xiang, T.X., Anderson, B.D.: Permeability of acetic acid across gel and liquid-crystalline lipid bilayers conforms to free-surface-area theory. *Biophysical journal* **72**(1) (1997) 223–237
- [90] Missner, A., Kügler, P., Saparov, S.M., Sommer, K., Mathai, J.C., Zeidel, M.L., Pohl, P.: Carbon dioxide transport through membranes. *Journal of Biological Chemistry* **283**(37) (2008) 25340–25347
- [91] Svetina, S., Žekš, B.: Shape behavior of lipid vesicles as the basis of some cellular processes. *The Anatomical Record: An Official Publication of the American Association of Anatomists* **268**(3) (2002) 215–225
- [92] Kamigaito, M., Ando, T., Sawamoto, M.: Metal-catalyzed living radical polymerization. *Chemical Reviews* **101**(12) (2001) 3689–3746
- [93] Mishra, V., Kumar, R.: Living radical polymerization: A review. *J. Sci. Res* **56** (2012) 141–176
- [94] Patten, T.E., Xia, J., Abernathy, T., Matyjaszewski, K.: Polymers with very low polydispersities from atom transfer radical polymerization. *Science* **272**(5263) (1996) 866–868
- [95] Chong, .Y., Le, T.P., Moad, G., Rizzardo, E., Thang, S.H.: A more versatile route to block copolymers and other polymers of complex architecture by living radical polymerization: the RAFT process. *Macromolecules* **32**(6) (1999) 2071–2074
- [96] Puts, R.D., Sogah, D.Y.: Control of living free-radical polymerization by a new chiral nitroxide and implications for the polymerization mechanism. *Macromolecules* **29**(9) (1996) 3323–3325
- [97] Wang, J.S., Matyjaszewski, K.: Controlled/" living" radical polymerization. atom transfer radical polymerization in the presence of transition-metal complexes. *Journal of the American Chemical Society* **117**(20) (1995) 5614–5615

- [98] Kato, M., Kamigaito, M., Sawamoto, M., Higashimura, T.: Polymerization of methyl methacrylate with the carbon tetrachloride/dichlorotris-(triphenylphosphine) ruthenium (II)/methylaluminum bis (2, 6-di-tert-butylphenoxide) initiating system: possibility of living radical polymerization. *Macromolecules* **28**(5) (1995) 1721–1723
- [99] Lee, S.B., Russell, A.J., Matyjaszewski, K.: ATRP synthesis of amphiphilic random, gradient, and block copolymers of 2-(dimethylamino) ethyl methacrylate and n-butyl methacrylate in aqueous media. *Biomacromolecules* **4**(5) (2003) 1386–1393
- [100] Nam, J., Beales, P.A., Vanderlick, T.K.: Giant phospholipid/block copolymer hybrid vesicles: mixing behavior and domain formation. *Langmuir* **27**(1) (2010) 1–6
- [101] Discher, B.M., Won, Y.Y., Ege, D.S., Lee, J.C., Bates, F.S., Discher, D.E., Hammer, D.A.: Polymersomes: tough vesicles made from diblock copolymers. *Science* **284**(5417) (1999) 1143–1146
- [102] Wu, J., Eisenberg, A.: Proton diffusion across membranes of vesicles of poly (styrene-*b*-acrylic acid) diblock copolymers. *Journal of the American Chemical Society* **128**(9) (2006) 2880–2884
- [103] Magnani, C., Montis, C., Mangiapia, G., Mingotaud, A.F., Mingotaud, C., Roux, C., Joseph, P., Berti, D., Lonetti, B.: Hybrid vesicles from lipids and block copolymers: phase behavior from the micro-to the nano-scale. *Colloids and Surfaces B: Biointerfaces* **168** (2018) 18–28
- [104] Schulz, M., Werner, S., Bacia, K., Binder, W.H.: Controlling molecular recognition with lipid/polymer domains in vesicle membranes. *Angewandte Chemie International Edition* **52**(6) (2013) 1829–1833
- [105] Ghoroghchian, P.P., Li, G., Levine, D.H., Davis, K.P., Bates, F.S., Hammer, D.A., Therien, M.J.: Bioresorbable vesicles formed through spontaneous self-assembly of amphiphilic poly (ethylene oxide)-block-polycaprolactone. *Macromolecules* **39**(5) (2006) 1673–1675
- [106] Ruyschaert, T., Sonnen, A.F., Haefele, T., Meier, W., Winterhalter, M., Fournier, D.: Hybrid nanocapsules: Interactions of ABA block copolymers with liposomes. *Journal of the American Chemical Society* **127**(17) (2005) 6242–6247
- [107] Dionzou, M., Morère, A., Roux, C., Lonetti, B., Marty, J.D., Mingotaud, C., Joseph, P., Goudouneche, D., Payré, B., Léonetti, M.: Comparison of methods for the fabrication and the characterization of polymer self-assemblies: what are the important parameters? *Soft Matter* **12**(7) (2016) 2166–2176

- [108] Meng, F., Zhong, Z., Feijen, J.: Stimuli-responsive polymersomes for programmed drug delivery. *Biomacromolecules* **10**(2) (2009) 197–209
- [109] Le Meins, J.F., Schatz, C., Lecommandoux, S., Sandre, O.: Hybrid polymer/lipid vesicles: state of the art and future perspectives. *Materials today* **16**(10) (2013) 397–402
- [110] Chemin, M., Brun, P.M., Lecommandoux, S., Sandre, O., Le Meins, J.F.: Hybrid polymer/lipid vesicles: fine control of the lipid and polymer distribution in the binary membrane. *Soft Matter* **8**(10) (2012) 2867–2874
- [111] Du, J., Armes, S.P.: pH-responsive vesicles based on a hydrolytically self-cross-linkable copolymer. *Journal of the American Chemical Society* **127**(37) (2005) 12800–12801
- [112] Villani, S., Adami, R., Reverchon, E., Ferretti, A.M., Ponti, A., Lepretti, M., Caputo, I., Izzo, L.: pH-sensitive polymersomes: controlling swelling via copolymer structure and chemical composition. *Journal of drug targeting* **25**(9-10) (2017) 899–909
- [113] Barrella, M.C., Di Capua, A., Adami, R., Reverchon, E., Mella, M., Izzo, L.: Impact of intermolecular drug-copolymer interactions on size and drug release kinetics from pH-responsive polymersomes. *Supramolecular Chemistry* **29**(11) (2017) 796–807
- [114] Yadav, V., Harkin, A.V., Robertson, M.L., Conrad, J.C.: Hysteretic memory in pH-response of water contact angle on poly (acrylic acid) brushes. *Soft matter* **12**(15) (2016) 3589–3599
- [115] Badre, C., Mayaffre, A., Letellier, P., Turmine, M.: Modification of the wettability of a polymeric substrate by pH effect. Determination of the surface acid dissociation constant by contact angle measurements. *Langmuir* **22**(20) (2006) 8424–8430
- [116] Stein, H., Spindler, S., Bonakdar, N., Wang, C., Sandoghdar, V.: Production of isolated giant unilamellar vesicles under high salt concentrations. *Frontiers in physiology* **8** (2017) 63
- [117] Larson, N., Ghandehari, H.: Polymeric conjugates for drug delivery. *Chemistry of Materials* **24**(5) (2012) 840–853
- [118] Çavuş, S., Gürdağ, G.: Synthesis and swelling behavior of pH-and temperature-sensitive poly [2-(dimethylamino) ethyl methacrylate-co-2-acrylamido-2-methylpropane-1-sulfonic acid] hydrogels. *Polymer Bulletin* **58**(1) (2007) 235–242
- [119] Huang, Y., Yong, P., Chen, Y., Gao, Y., Xu, W., Lv, Y., Yang, L., Reis, R.L., Pirraco, R.P., Chen, J.: Micellization and gelatinization in

- aqueous media of pH-and thermo-responsive amphiphilic ABC (PMMA 82-b-PDMAEMA 150-b-PNIPAM 65) triblock copolymer synthesized by consecutive RAFT polymerization. *RSC advances* **7**(46) (2017) 28711–28722
- [120] Tapeinos, C., Efthimiadou, E.K., Boukos, N., Kordas, G.: Sustained release profile of quatro stimuli nanocontainers as a multi sensitive vehicle exploiting cancer characteristics. *Colloids and Surfaces B: Biointerfaces* **148** (2016) 95–103
- [121] Cotanda, P., Wright, D.B., Tyler, M., O'Reilly, R.K.: A comparative study of the stimuli-responsive properties of DMAEA and DMAEMA containing polymers. *Journal of Polymer Science Part A: Polymer Chemistry* **51**(16) (2013) 3333–3338
- [122] Min, K., Gao, H., Matyjaszewski, K.: Use of ascorbic acid as reducing agent for synthesis of well-defined polymers by ARGET ATRP. *Macromolecules* **40**(6) (2007) 1789–1791
- [123] Dong, H., Matyjaszewski, K.: ARGET ATRP of 2-(dimethylamino) ethyl methacrylate as an intrinsic reducing agent. *Macromolecules* **41**(19) (2008) 6868–6870
- [124] Jakubowski, W., Min, K., Matyjaszewski, K.: Activators regenerated by electron transfer for atom transfer radical polymerization of styrene. *Macromolecules* **39**(1) (2006) 39–45
- [125] Kwak, Y., Magenau, A.J., Matyjaszewski, K.: ARGET ATRP of methyl acrylate with inexpensive ligands and ppm concentrations of catalyst. *Macromolecules* **44**(4) (2011) 811–819
- [126] Jakubowski, W., Matyjaszewski, K.: Activators regenerated by electron transfer for atom-transfer radical polymerization of (meth) acrylates and related block copolymers. *Angewandte Chemie International Edition* **45**(27) (2006) 4482–4486
- [127] Wang, G., Lu, M.: ARGET ATRP of copolymerization of styrene and acrylonitrile with environmentally friendly catalyst and ligand. *e-Polymers* **12**(1) (2012)
- [128] Zong, G., Chen, H., Wang, C., Liu, D., Hao, Z.: Synthesis of polyacrylonitrile via ARGET ATRP using CCl₄ as initiator. *Journal of applied polymer science* **118**(6) (2010) 3673–3677
- [129] Camail, M., Essaoudi, H., Margailan, A., Vernet, J.L.: Copolymérisation radicalaire de méthacrylates de 2-aminoéthyle avec le méthacrylate de méthyle. *European polymer journal* **31**(11) (1995) 1119–1125

- [130] Gilbert, M.: Chapter 5 - Relation of Structure to Chemical Properties. In Gilbert, M., ed.: *Brydson's Plastics Materials (Eighth Edition)*. Butterworth-Heinemann (January 2017) 75–102
- [131] Berna, M., Dalzoppo, D., Pasut, G., Manunta, M., Izzo, L., Jones, A.T., Duncan, R., Veronese, F.M.: Novel monodisperse PEG- dendrons as new tools for targeted drug delivery: synthesis, characterization and cellular uptake. *Biomacromolecules* **7**(1) (2006) 146–153
- [132] Schulz, M., Glatte, D., Meister, A., Scholtysek, P., Kerth, A., Blume, A., Bacia, K., H. Binder, W.: Hybrid lipid / polymer giant unilamellar vesicles: effects of incorporated biocompatible PIB-PEO block copolymers on vesicle properties. *Soft Matter* **7**(18) (2011) 8100–8110
- [133] Carrara, P., Stano, P., Luisi, P.L.: Giant vesicles “colonies”: a model for primitive cell communities. *ChemBioChem* **13**(10) (2012) 1497–1502
- [134] Dao, T.P.T., Fernandes, F., Ibarboure, E., Ferji, K., Prieto, M., Sandre, O., Meins, J.F.L.: Modulation of phase separation at the micron scale and nanoscale in giant polymer/lipid hybrid unilamellar vesicles (GHUVs). *Soft Matter* **13**(3) (January 2017) 627–637
- [135] Eigen, M.: Proton transfer, acid-base catalysis, and enzymatic hydrolysis. Part I: elementary processes. *Angewandte Chemie International Edition in English* **3**(1) (1964) 1–19
- [136] Wang, X., Conway, W., Burns, R., McCann, N., Maeder, M.: Comprehensive study of the hydration and dehydration reactions of carbon dioxide in aqueous solution. *The journal of physical chemistry A* **114**(4) (2009) 1734–1740
- [137] Mayo, F.R., Lewis, F.M.: Copolymerization. I. A basis for comparing the behavior of monomers in copolymerization; the copolymerization of styrene and methyl methacrylate. *Journal of the American Chemical Society* **66**(9) (1944) 1594–1601
- [138] Fineman, M., Ross, S.D.: Linear method for determining monomer reactivity ratios in copolymerization. *Journal of Polymer Science* **5**(2) (1950) 259–262
- [139] Skeist, I.: Copolymerization: the composition distribution curve. *Journal of the American Chemical Society* **68**(9) (1946) 1781–1784
- [140] Sun, X., Zhang, H., Huang, X., Wang, X., Zhou, Q.F.: Synthesis of poly (ethylene oxide)-block-poly (methyl methacrylate)-block-polystyrene triblock copolymers by two-step atom transfer radical polymerization. *Polymer* **46**(14) (2005) 5251–5257

- [141] Zhou, F., Gu, K.H., Zhang, Z.Y., Zhang, M.Y., Zhou, S., Shen, Z., Fan, X.H.: Exploiting Host–Guest Interactions for the Synthesis of a Rod–Rod Block Copolymer with Crystalline and Liquid-Crystalline Blocks. *Angewandte Chemie* **128**(48) (2016) 15231–15235
- [142] Jiang, X., Gou, F., Chen, F., Jing, H.: Cycloaddition of epoxides and CO₂ catalyzed by bisimidazole-functionalized porphyrin cobalt(III) complexes. *Green Chemistry* **18** (2016) 3567–3576
- [143] Banfi, S., Caruso, E., Zaza, S., Mancini, M., Gariboldi, M.B., Monti, E.: Synthesis and photodynamic activity of a panel of BODIPY dyes. *Journal of Photochemistry and Photobiology B: Biology* **114** (September 2012) 52–60
- [144] Tahara, Y., Fujiyoshi, Y.: A new method to measure bilayer thickness: cryo-electron microscopy of frozen hydrated liposomes and image simulation. *Micron* **25**(2) (1994) 141–149
- [145] Mark, J.E.: *Physical Properties of Polymers Handbook*. Springer Science & Business Media (March 2007) Google-Books-ID: fZl7q7UgEXkC.
- [146] Wu, S.: Control of intrinsic brittleness and toughness of polymers and blends by chemical structure: a review. *Polymer International* **29**(3) (1992) 229–247
- [147] Linton, D., Driva, P., Sumpter, B., Ivanov, I., Geohegan, D., Feigerle, C., Dadmun, M.D.: The importance of chain connectivity in the formation of non-covalent interactions between polymers and single-walled carbon nanotubes and its impact on dispersion. *Soft Matter* **6**(12) (2010) 2801

PAPERS

LIST OF PAPERS

- I Miele, Y., Bánsági, T. Jr., Taylor, A.F., and Rossi, F.
Modelling Approach to Enzymatic pH Oscillators in Giant Lipid Vesicles
Lecture notes in Bioengineering (**2018**), 63-74
- II Miele, Y., Medveczky, Z., Lagzi, I., Budroni, M. A., and Rossi, F.
The Relevance of Inorganic Nonlinear Chemical Reactions for the Origin of Life Studies
Communications in Computer and Information Science (**2019**), 900, 138-150
- III Miele, Y., Medveczky, Z., Holló, G., Tegze, B., Derényi, I., Hórvölgyi, Z., Altamura, E., Lagzi, I., and Rossi, F.
Self-Division of Giant Vesicles Driven by an Internal Enzymatic Reaction
Accepted. Chemical Science (**2020**)
- IV Mella, M., La Rocca, M. V., Miele, Y., and Izzo, L.
On the Origin and Consequences of High DMAEMA Reactivity Ratio in ATRP Copolymerization with MMA: an Experimental and Theoretical Study
J. Polym. Sci., Part A: Polym. Chem. (**2018**), 56, 1366-1382

CONTRIBUTION REPORT

In Paper I, Miele Y. modified and applied a kinetic model developed from Bánsági T. Jr. and Taylor A.F.; Rossi F. provided the initial ideas. All authors discussed the results and contributed to the final manuscript.

Miele Y. wrote the first draft of Paper II, and all authors contributed substantially to revisions; Rossi F. conceived the study.

In Paper III, Miele Y. and Medveczky Z. prepared the vesicles and analysed the data; Altamura E. carried out the FRAP experiments; the MD simulations and the Wilhelmy film balance experiments were done at University of Budapest (Holló G., Derényi I., Tegze B., Hórvölgyi Z.); Rossi F. and Miele Y. planned and carried out the kinetic simulations; Lagzi I. and Rossi F. supervised the project and wrote the manuscript with input from all authors.

The contributions of the different authors of Paper IV are the following: Mella

M. and Izzo L. conceived and designed the experiments and modelling approach; Miele Y. and Izzo L. performed the copolymers synthesis and the NMR experiments; Mella M. and La Rocca M.V. carried out the kinetic Monte Carlo simulations and the DFT calculations.

Papers not included in this section:

- V Budroni, M. A., Calabrese, I., Miele, Y., Rustici, M., Marchettini, N., and Rossi, F.
Control of chemical chaos through medium viscosity in a batch ferriin-catalysed Belousov-Zhabotinsky reaction
Phys. Chem. Chem. Phys (2017), 19, 32235-32241
- VI Intiso, A., Miele, Y., Marchettini, N., Proto, A., Sánchez-Domínguez and Rossi, F.
Enhanced solubility of trichloroethylene (TCE) by a poly-oxyethylene alcohol as green surfactant
Environ. Technol. Inno. (2018), 12, 72-79
- VII Miele, Y., Mingotaud, A-F., Caruso, E., Malacarne, M.C., Izzo, L., Lonetti, B., and Rossi, F.
Hybrid giant lipid vesicles incorporating a PMMA-based copolymer
Submitted to Biochimica et Biophysica Acta General Subjects.
- VIII Miele, Y., Mella, M., Izzo, L., and Rossi, F.
Composition and microstructure of biocompatible and pH-sensitive copolymers prepared by a free solvent ARGET ATRP
Submitted to Lecture notes in Bioengineering.
- IX Miele, Y., Fasulo, A., Bánsági, T. Jr., Taylor, A.F., and Rossi, F.
In preparation.

Papers published prior PhD:

- X Miele, Y., Bánsági, T. Jr., Taylor, A.F., Stano, P., and Rossi, F.
Engineering Enzyme - Driven Dynamic Behaviour in Lipid Vesicles
Communications in Computer and Information Science (2016), 587, 197-208

Paper I

Modelling Approach to Enzymatic pH Oscillators in Giant Lipid Vesicles

Ylenia Miele, Tamás Bánsági Jr., Annette F. Taylor
and Federico Rossi

Abstract The urease-catalyzed hydrolysis of urea can display feedback driven by base production (NH_3) resulting in a switch from acidic to basic pH under non-buffered conditions. Thus, this enzymatic reaction is a good candidate for investigation of chemical oscillations or bistability. In order to determine the best conditions for oscillations, a two-variable model was initially derived in which acid and urea were supplied at rates k_H and k_S from an external medium to an enzyme-containing compartment. Oscillations were theoretically observed providing the necessary condition that $k_H > k_S$ was met. To apply this model, we devised an experimental system able to ensure the fast transport of acid compared to that of urea. In particular, by means of the *droplet transfer method*, we encapsulated the enzyme, together with a proper pH probe, in 1-palmitoyl-2-oleoyl-sn-glycero-3-phosphatidylcholine (POPC) based liposomes, where differential diffusion of H^+ and urea is ensured by the different permeability (P_m) of the membrane to the two species. Here we present an improved theoretical model that accounts for the products transport and for the probe hydrolysis, to obtain a better guidance for the experiments.

Keywords Enzymatic oscillators · Urea-urease reaction · Lipid vesicles · pH oscillators

Y. Miele · F. Rossi (✉)

Department of Chemistry and Biology, University of Salerno, Via Giovanni Paolo II 132,
84084 Fisciano, SA, Italy
e-mail: frossi@unisa.it

T. Bánsági Jr. · A.F. Taylor

Department of Chemical and Biological Engineering, University of Sheffield, Mappin Street,
S1 3JD Sheffield, UK

1 Introduction

Oscillations can spontaneously arise in the concentration of some chemical reaction intermediates, provided that the system is sufficiently far from the state of the thermodynamic equilibrium [1]. The first examples of oscillating reactions can be traced back to the beginning of the 20th century, however it is only in the mid 1960's, after the discovery and characterization of the Belousov-Zhabotinsky (BZ) reaction that chemical oscillations begun to attract attention [2]: over the years the BZ system has been performed in a great variety of reaction environments such as gels [3], micelles [4–9], water in oil reverse microemulsions [10–13], lipid bilayers [14–18], organic and inorganic beads [19, 20] always looking for new spatio-temporal behaviours. Moreover, the number of chemical oscillators grew so much that it is now possible to list almost 200 variants ranging from the bromate family to the Mn-based to the most recent family of pH oscillators [2].

Oscillations in pH occur naturally in plants, during glycolysis in yeast cells and are also used by *C. elegans* for muscle contraction. In these systems the pH oscillations have small amplitude and are driven by other autocatalytic processes, rather than a direct feedback through acid/base interaction; on the contrary, in *synthetic* pH oscillators, the hydrogen ion plays the most important role in the reaction kinetics and the variation in pH can be as large as 6 pH-units [2]. So far several pH oscillators have been developed, however all of them require open (flow) reactors and harsh inorganic redox chemistry; in contrast to this, there is a need for increasing the range of closed autocatalytic reactions, in mild or physiological conditions, for biocompatible applications and pH oscillators driven by enzyme-catalyzed reactions seem to be a valid and promising alternative [21].

Among the several enzymatic reactions known to depend on the pH, one candidate, the urea-urease system has recently been revised by our group [21–23]. The hydrolysis of urea by the enzyme urease results in the production of a weak base, ammonia, and carbon dioxide, which hydrolyses to give bicarbonate. This reaction occurs in numerous cellular systems, for example it is used by bacteria *Helicobacter Pylori* in order to raise the local pH to protect himself from the harsh acidic environment of the stomach [24]. The urea-urease reaction follows Michaelis-Menten kinetics and has a bell-shaped rate-pH curve with maximum at pH 7. In non-buffered conditions, the rate-pH curve can be exploited to obtain feedback-driven behaviour, e.g. by delivering an acid or a base to the solution a reaction acceleration or inhibition can be obtained. The reaction has also the distinct advantages of high solubility and stability of substrate and enzyme in water making it suitable for experiments in vitro. Few nonlinear dynamical behaviors were obtained in different experimental conditions (bistability, front propagation, etc.) [21, 25], however oscillations were never observed.

In a recent work [23], we showed that for obtaining oscillations a fast transport of the acid with respect to that of urea must be ensured in the reaction medium; we then proposed to use 1-palmitoyl-2-oleoyl-sn-glycero-3-phosphatidylcholine (POPC)

liposomes to encapsulate the enzyme and profit of the different membrane permeability (P_m) of H^+ ($\sim 10^{-3}$ cm/s) and urea ($\sim 10^{-6}$ cm/s) [26, 27].

The encapsulation of the enzyme into liposomes could be attained by means of the droplet transfer method, introduced by the Weitz group [28], recently optimised by Luisi and collaborators [29] and successfully employed to confine the Belousov-Zhabotinsky chemical oscillator in a network of vesicles [30]. This innovative method first takes advantage of the facile compartmentalization of water-soluble solutes (enzyme in this case) in water-in-oil (w/o) droplets, and then convert the solute-filled w/o droplets into vesicles that can be dispersed in an acidic solution of urea. The pH changes in time can be monitored through the use of a pH probe, pyranine (8-hydroxy-1,3,6-pyrenetrisulfonate) whose emission intensity (at 510 nm) is strongly dependent upon the pH of the solution, over the range 6–10. Both the probe and the enzyme do not leak out of the vesicles once entrapped therein, while urea and proton can easily diffuse through the membrane at different rates (depending on the concentration gradient between the inside and the outside of the membrane).

The diffusion of urea (k_S) and proton (k_H) through the lipid bilayer has been investigated experimentally and the transport of acid was found to be faster than urea, thus confirming that the necessary condition for oscillation $k_H > k_S$ is met. Experimental investigations also showed that liposomes are indeed *open* compartments where both the reactants and the products can permeate the bilayer membranes by a passive diffusion mechanism; thus, the original two-variable model (see Eqs. (1) and (2) in the Results section) which did not account for the leakage of the products [23], had to be modified. In this work we present an improved model which accounts for the ammonia leakage and for the hydrolysis of the pH fluorescent probe used in the experiments; simulations show new phase diagrams where oscillations are still present but in a different part of the plane. Also other dynamical behaviours, such as low and high pH steady states, autocatalysis, clock regimes, etc. were predicted by the model for more realistic experimental conditions.

2 Results: Modelling

The two-variable model for describing the temporal dynamics of the urea-urease reaction in a confined environment, where a solution of urea (S) and acid (H^+) could be delivered into the system, had the form:

$$\frac{d[S]}{dt} = k_S([S]_0 - [S]) - R \quad (1)$$

$$\frac{d[H^+]}{dt} = \left(k_H \left([H^+]_0 - \frac{K_w}{[H^+]_0} - [H^+] + \frac{K_w}{[H^+]} \right) - 2R \right) \left(1 + \frac{K_w}{[H^+]^2} \right)^{-1} \quad (2)$$

where

$$R = \frac{k_E [E][S]}{(K_M + [S]) \left(1 + \frac{K_{ES2}}{[H^+]} + \frac{[H^+]}{K_{ES1}} \right)} \quad (3)$$

$k_E = 3.7 \times 10^{-6} \text{ ml Mu}^{-1}\text{s}^{-1}$, $K_m = 3 \times 10^{-3} \text{ M}$, $K_{ES1} = 5 \times 10^{-6} \text{ M}$, $K_{ES2} = 2 \times 10^{-9} \text{ M}$ are urease specific quantities and $K_w = 10^{-14} \text{ M}^2$ is the ion product of water.

The rate constants for the hydrolysis equilibria and for the enzymatic rate constants were taken from the literature, with values slightly adapted to match our experimental conditions [21]. The kinetic constants of the passive transport are expressed as $k_i = 6P_i/d$ where P_i denotes the permeability coefficients ($P_S = 2.45 \times 10^{-6} \text{ cm/s}$ and $P_H = 1.82 \times 10^{-3} \text{ cm/s}$ for bilayers made of lipids having a 16 carbon long hydrocarbon chain [27]) and $d = 10 \mu\text{m}$ is chosen as the diameter of the vesicle.

The model was scaled and simulations were carried out with XPPAUT [31] using CVODE as integration method; the diagrams reported in Fig. 1 were obtained by using the routine AUTO.

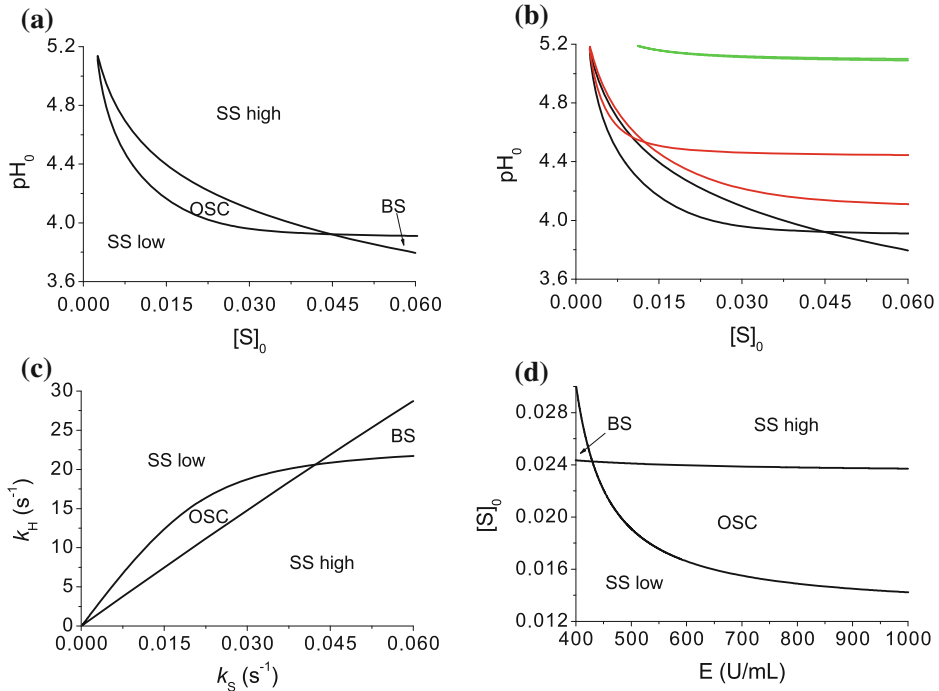


Fig. 1 **a** Phase diagram for $E = 1300 \text{ U/mL}$, $k_S = 0.0147 \text{ s}^{-1}$, $k_H = 10.9 \text{ s}^{-1}$. **b** Phase diagrams for $E = 1300$ (—), 130 (---), 13 (---), U/mL . **c** Phase diagram for $E = 1300 \text{ U/mL}$, $\text{pH}_0 = 4.1$, $[S]_0 = 0.02 \text{ M}$. **d** $k_S = 0.0147 \text{ s}^{-1}$, $k_H = 10.9 \text{ s}^{-1}$, $\text{pH}_0 = 4.2$

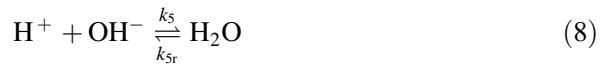
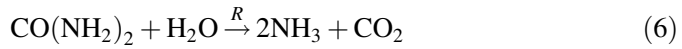
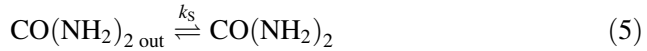
The cross-shaped phase diagrams reveal the presence of four possible states: two stable states (SS low and SS high) and two unstable (a bistability region and an oscillatory domain). The phase diagrams in Fig. 1a and b were obtained in the pH_0 versus $[\text{S}]_0$ parameter space and Fig. 1b shows the effect of the enzyme concentration on the shape of the diagram: decreasing the enzyme content the region of oscillations diminishes while the region of bistability increases; for very low concentrations (e.g. $E = 13 \text{ U/mL}$) the regions of bistability and oscillations become both very thin.

Figure 1c depicts the effect of the transport constants and, indirectly, the effect of the vesicle size (see the relationship between the permeability and the diameter) on the dynamical behaviour: for some droplet sizes the oscillations were suppressed, but a large region where oscillations exist is present.

Finally in Fig. 1d the phase diagram was obtained in the $[\text{S}]_0$ versus E parameter space once the value of pH_0 is fixed.

Despite the good results obtained with the two-variable model, we decided to add few more processes taking place in the vesicles to improve the confidence for the ability of the simulations to guide experiments.

As in the case of the two-variable model, here we take into account the main reactions occurring in the urea-urease system (without including the carbon dioxide equilibria) but we do not consider the steady state approximation for ammonia/ammonium equilibrium, we add the hydrolysis of the pH probe pyranine (pyrOH) and, most important, we consider that reaction products can leak out from the vesicles. The new model has, therefore, the form:



A cell-like compartment that reproduces our experimental conditions is schematically drawn in Fig. 2: the enzyme and the probe are encapsulated inside the vesicles, while the substrate and the acid are delivered as external solutions.

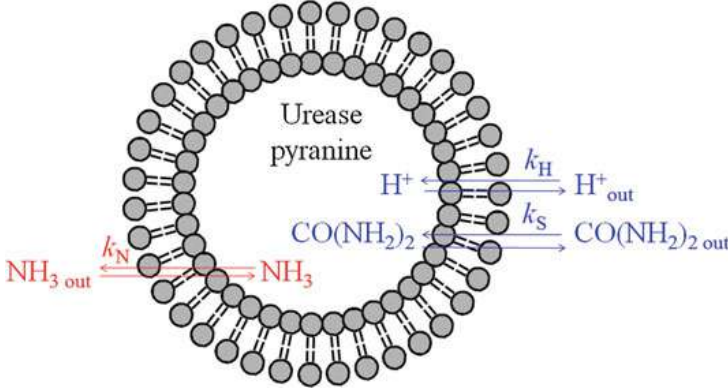


Fig. 2 Lipid vesicle containing the urea-urease reaction and the fluorescence probe: k_H = exchange rate of the acid, k_S = exchange rate of the urea, k_N = exchange rate of the product ammonia with the external solution of concentrations $[H^+]_o$, $[S]_o$ and $[NH_3]_o$

The exchange of matter between the urease-loaded compartment and its surrounding is modelled by the flow terms (4), (5) and (10). In Fig. 2 the substances added from the outside are shown in blue, while ammonia that is produced inside is shown in red.

The system of ODEs derived from reaction kinetics reads:

$$\frac{d[S]}{dt} = k_S([S]_o - [S]) - R \quad (11)$$

$$\frac{d[NH_3]}{dt} = 2R + k_{2r}[NH_4^+] - k_2[NH_3][H^+] + k_N([NH_3]_o - [NH_3]) \quad (12)$$

$$\begin{aligned} \frac{d[H^+]}{dt} = & k_{2r}[NH_4^+] - k_2[NH_3][H^+] + k_f[\text{pyrOH}] - k_r[\text{pyrO}^-][H^+] \\ & + k_H([H^+]_o - [H^+]) + k_{5r} - k_5[OH^-][H^+] \end{aligned} \quad (13)$$

$$\frac{d[OH^-]}{dt} = k_{5r} - k_5[OH^-][H^+] \quad (14)$$

$$\frac{d[\text{pyrOH}]}{dt} = -k_f[\text{pyrOH}] + k_r[\text{pyrO}^-][H^+] \quad (15)$$

$$\frac{d[\text{pyrO}^-]}{dt} = k_f[\text{pyrOH}] - k_r[\text{pyrO}^-][H^+] \quad (16)$$

$$\frac{d[NH_4^+]}{dt} = k_2[NH_3][H^+] - k_{2r}[NH_4^+] \quad (17)$$

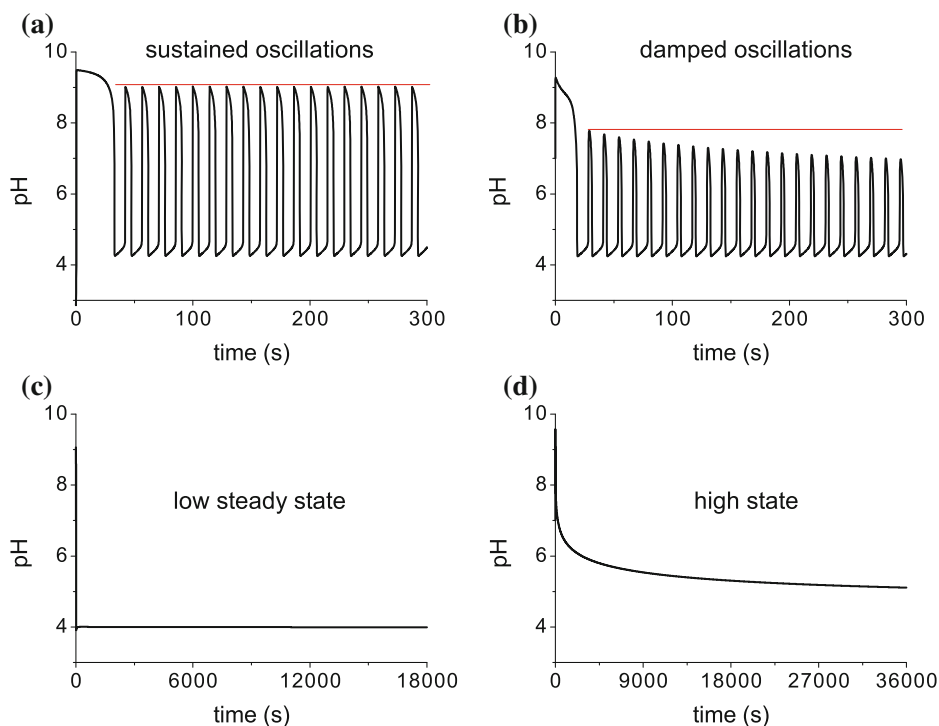


Fig. 3 pH-time plots for $E = 1300 \text{ U/mL}$, $k_S = 0.0147 \text{ s}^{-1}$, $k_H = 10.9 \text{ s}^{-1}$, $k_N = 1.08 \text{ s}^{-1}$, $[S]_0 = 0.015 \text{ M}$, $[\text{NH}_3]_0 = 0 \text{ M}$. **a** with the two-variable model and $\text{pH}_0 = 4.2$; **b** with the full model at $\text{pH}_0 = 4.2$; **c** with the full model and at $\text{pH}_0 = 3.9$; **d** with the full model at $\text{pH}_0 = 4.8$. The red line is intended to emphasise the difference between damped and sustained oscillations

The numerical simulations of the Eqs. (11)–(17) were performed using XPPAUT with the same integration method applied for the two-variable model.

Figure 3 shows the most common dynamical behaviours obtained from the integration of the two models; in contrast to the two-variable model which admits sustained oscillations (Fig. 3a), the full system shows damped oscillations (Fig. 3b), i.e. oscillations whose amplitude decreases over time until a steady state is attained. Figure 3c shows a typical low pH steady state, that can be easily found for several experimental parameters. High pH (basic) steady state are, on the contrary, difficult to obtain; this is probably due to the leakage of the NH_3 out of the vesicle. In fact, high pH transient states (*high state*) can be obtained for a limited amount of time, but the final attractor of the model is generally a low pH state (see Fig. 3d where the pH is still decreasing over a timescale of 10 h).

The phase diagrams reported in Fig. 4 were obtained by choosing a time interval of 10 h, the initial concentrations of the species inside the vesicle were in the range of those used for the experiments (e.g. $\text{pyrOH} = 50 \mu\text{M}$, $S = 0$ and $[\text{H}^+] = 10^{-7} \text{ M}$). The shape of the diagrams is similar to the two-variable model, however some differences can be pointed out: the region of bistability present in Fig. 1a disappears

in Fig. 4a and b, being replaced by the oscillatory domain; In Fig. 4c, where the ammonia permeability has been set to a lower value ($k_N = 1.08 \times 10^{-3} \text{ s}^{-1}$), the phase diagram E versus $[S]_0$ presents the same features of that obtained for the two-variable model (Fig. 1d), thus the higher the permeability of ammonia, the more the two models differ.

Panels a and b of Fig. 4 show the effect of k_N on the dynamics of the system: by increasing the ammonia permeability the region of damped oscillations becomes wider, but the number of oscillations decreases as reported in Table 1. Finally, Fig. 4d shows the k_S versus k_N parameter space once E, S_0 and pH_0 have been fixed. Here, when the permeability of ammonia is high, just a low steady state is possible and high pH values cannot be reached.

Despite kinetics (11)–(17) give a more realistic picture with respect to the two-variable model, some processes occurring in the experimental system were still neglected: for example the carbon dioxide equilibria and the leakage of the ammonium ion were not considered. As for the ammonium, we considered that the lipid membrane is only slightly permeable to cations different from protons [27], however, to better understand some of the dynamical behaviours found in simulations (damped oscillations and high states), we further included the permeability

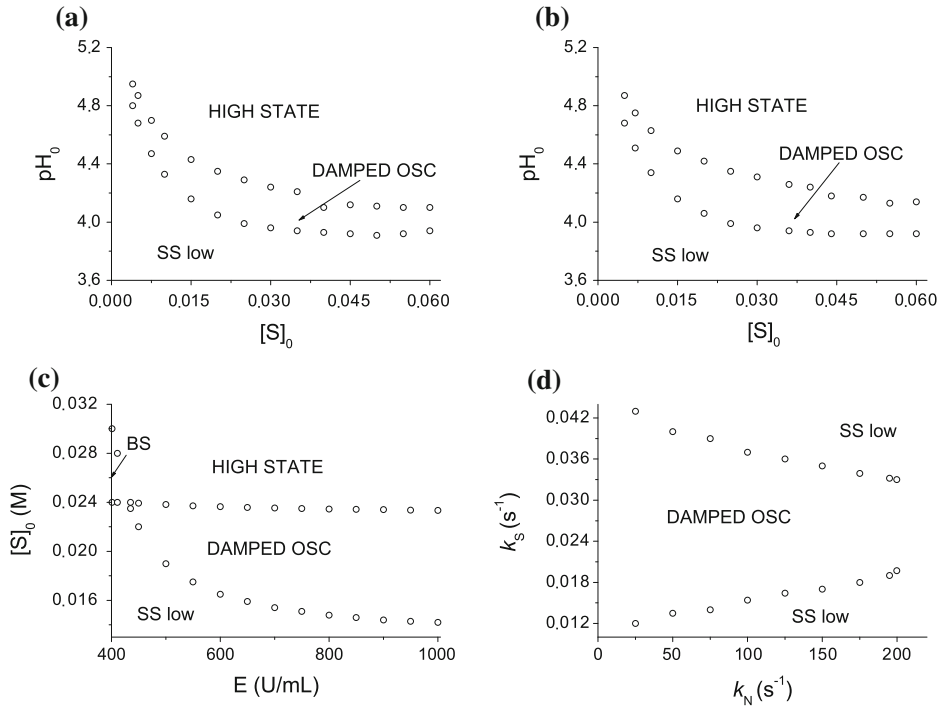
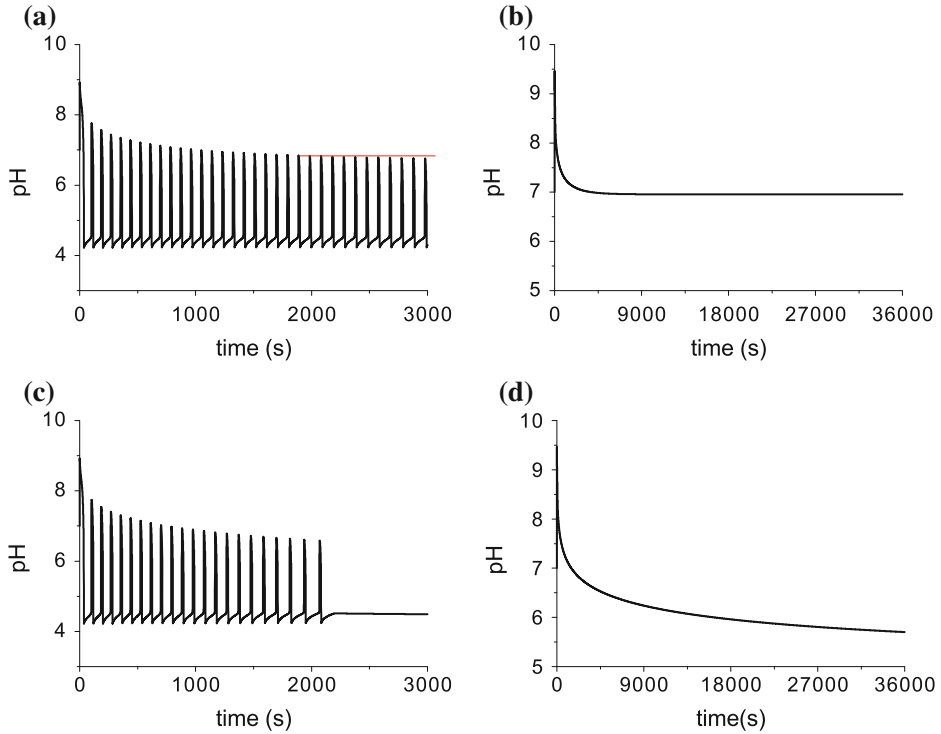


Fig. 4 Phase diagram for $E = 1300 \text{ U/mL}$, $k_S = 0.0147 \text{ s}^{-1}$, $k_H = 10.9 \text{ s}^{-1}$ **a** $k_N = 1.08 \text{ s}^{-1}$. **b** $k_N = 10.8 \text{ s}^{-1}$. **c** $\text{pH}_0 = 4.2$, $k_S = 0.0147 \text{ s}^{-1}$, $k_H = 10.9 \text{ s}^{-1}$, $k_N = 1.08 \times 10^{-3} \text{ s}^{-1}$. **d** $E = 600 \text{ U/mL}$, $[S]_0 = 0.02 \text{ M}$, $\text{pH}_0 = 4.2$, $k_H = 10.9 \text{ s}^{-1}$

Table 1 Total number of oscillations for the following conditions: $k_S = 0.0147 \text{ s}^{-1}$, $k_H = 10.9 \text{ s}^{-1}$, $[S]_0 = 0.02 \text{ M}$, $\text{pH}_0 = 4.2$, $E = 510 \text{ U/mL}$

Ammonia Permeability (k_N in s^{-1})	Total number of oscillations
0.8	34
1	27
2	13
5	5
7	3

**Fig. 5** Simulated time series for $[S]_0 = 0.024 \text{ M}$, $k_S = 0.0147 \text{ s}^{-1}$, $k_H = 10.9 \text{ s}^{-1}$, $k_N = 1.08 \text{ s}^{-1}$, **a** $k_{NH} = 6 \times 10^{-4} \text{ s}^{-1}$, $\text{pH}_0 = 4.18$, $E = 500 \text{ U/mL}$. **b** $k_{NH} = 6 \times 10^{-4} \text{ s}^{-1}$, $\text{pH}_0 = 4.2$, $E = 450 \text{ U/mL}$. **c** $k_{NH} = 6 \times 10^{-8} \text{ s}^{-1}$, $\text{pH}_0 = 4.18$, $E = 500 \text{ U/mL}$. **d** $k_{NH} = 6 \times 10^{-8} \text{ s}^{-1}$, $\text{pH}_0 = 4.2$, $E = 450 \text{ U/mL}$

of ammonium ion (k_{NH}). A relevant ammonium permeability can be physically possible when the membrane has structural defects and percolation takes place.

Thus, in this case, the following equilibrium must be added to the reactions (4)–(10).



and the ODE for the ammonium ion becomes:

$$\frac{d[\text{NH}_4^+]}{dt} = k_2[\text{NH}_3][\text{H}^+] - k_{2r}[\text{NH}_4^+] + k_{\text{NH}}([\text{NH}_4^+]_o - [\text{NH}_4^+]) \quad (19)$$

If the ammonium permeability (k_{NH}) has a value close or few orders of magnitude lower than the permeability of ammonia (k_{N}), the system shows the features typical of the two-variable model (possibility of sustained oscillations and high steady states, see Fig. 5a and b), while a low ammonium permeability (e.g. $6 \times 10^{-8} \text{ s}^{-1}$) gives the same results seen in the full model that didn't include the ammonium permeability (Fig. 5c and d show the same trends of Fig. 3b and d).

By properly balancing the permeabilities of ammonium and ammonia, the system behaves like an open reactor in which all the species can enter and exit; a low or zero ammonium permeability makes the system more similar to a semi-batch reactor in which the chemical species are continuously delivered in, but there is no outlet (in this case, the ammonia leaks out easily in contrast to its ionized counterpart, ammonium, that remains entrapped inside).

3 Conclusions

The pH dependence of the urea-urease reaction can be exploited to give base-catalyzed feedback. A simple model with two variables, the substrate and the acid as source of negative feedback, can capture the temporal dynamics of the urea-urease in CSTR but not in cell-like compartments. Indeed, while in a CSTR it is possible to set the flow rate of the reactants, in microcompartments like giant lipid vesicles the flow rate depends on the properties of the lipid boundary: the phospholipid bilayer is generally permeable to small neutral molecules but shows a low permeability for ions, with the exception of the proton which undergoes to a different exchange mechanism [32]. The transport rates of the products, completely neglected in the two-variable model, become relevant in the new model and, actually, they drive the whole dynamical behaviour. In fact, depending on the ratio between the ammonium and the ammonia permeability the model (11)–(17), (19) behaves in two different ways: at higher values of ammonium permeability sustained oscillations and both stable steady states can be possible, at lower values damped oscillations and only a low steady state are observed.

So far in our experiments, we verified the ability of urea, acid and ammonia to cross the lipid bilayer of giant vesicles, furthermore we successfully encapsulated the enzyme and the probe. The next step is to add a solution including both urea and acid to the GV and see if clock reactions, oscillations or bistability can be found. For this purpose, the simulations presented in this paper could help us in optimising the experimental conditions.

Acknowledgements Y.M. and F.R. were supported by the grants ORSA158121 and ORSA167988 funded by the University of Salerno (FARB ex 60%). The authors acknowledge the support through the COST Action CM1304 (Emergence and Evolution of Complex Chemical Systems).

References

1. Nicolis, G., Prigogine, I.: Self-organization in nonequilibrium systems. Wiley, New York (1977)
2. Orban, M., Kurin-Csorgei, K., Epstein, I.R.: pH-Regulated chemical oscillators. *Acc. Chem. Res.* **48**(3), 593–601 (2015)
3. Takeoka, Y., Watanabe, M., Yoshida, R.: Self-sustaining peristaltic motion on the surface of a porous gel. *J. Am. Chem. Soc.* **125**(44) (2003) 13320–13321 pH Oscillators in GVs 11
4. Paul, A.: Observations of the effect of anionic, cationic, neutral, and zwitterionic surfactants on the Belousov-Zhabotinsky reaction. *J. Phys.Chem. B* **109**(19), 9639–9644 (2005)
5. Rossi, F., Varsalona, R., Liveri, M.L.T.: New features in the dynamics of a ferroincatalyzed Belousov-Zhabotinsky reaction induced by a zwitterionic surfactant. *Chem. Phys. Lett.* **463** (4–6), 378–382 (2008)
6. Jahan, R.A., Suzuki, K., Mahara, H., Nishimura, S., Iwatsubo, T., Kaminaga, A., Yamamoto, Y., Yamaguchi, T.: Perturbation mechanism and phase transition of AOT aggregates in the Fe(II)[batho(SO₃)₂]₃—catalyzed aqueous Belousov-Zhabotinsky reaction. *Chem. Phys. Lett.* **485**(4–6), 304–308 (2010)
7. Rossi, F., Liveri, M.L.T.: Chemical self-organization in self-assembling biomimetic systems. *Ecol. Model.* **220**(16), 1857–1864 (2009)
8. Sciascia, L., Rossi, F., Sbriziolo, C., Liveri, M.L.T., Varsalona, R.: Oscillatory dynamics of the Belousov-Zhabotinsky system in the presence of a self-assembling nonionic polymer. Role of the reactants concentration. *Phys. Chem. Chem. Phys.* **12**(37), 11674–11682 (2010)
9. Rossi, F., Varsalona, R., Marchettini, N., Turco Liveri, M.L.: Control of spontaneous spiral formation in a zwitterionic micellar medium. *Soft Matter* **7**, 9498 (2011)
10. Vanag, V.K., Epstein, I.R.: Pattern formation in a tunable medium: The Belousov-Zhabotinsky reaction in an aerosol OT microemulsion. *Phys. Rev. Lett.* **87**(22), 228301–4 (2001)
11. Toiya, M., Vanag, V.K., Epstein, I.R.: Diffusively coupled chemical oscillators in a microfluidic assembly. *Angew. Chem. Int. Ed.* **47**(40), 7753–7755 (2008)
12. Rossi, F., Vanag, V.K., Epstein, I.R.: Pentanary cross-diffusion in water-in-oil microemulsions loaded with two components of the Belousov-Zhabotinsky reaction. *Chem. Eur. J.* **17** (7), 2138–2145 (2011)
13. Tompkins, N., Li, N., Girabawe, C., Heymann, M., Ermentrout, G.B., Epstein, I.R., Fraden, S.: Testing turing's theory of morphogenesis in chemical cells. *Proc. Natl. Acad. Sci.* **111**(12), 4397–4402 (2014)
14. Walde, P., Umakoshi, H., Stano, P., Mavelli, F.: Emergent properties arising from the assembly of amphiphiles. Artificial vesicle membranes as reaction promoters and regulators. *Chem. Commun.* **50**(71), 10177–10197 (2014)
15. Tomasi, R., Noel, J.M., Zenati, A., Ristori, S., Rossi, F., Cabuil, V., Kanoufi, F., Abou-Hassan, A.: Chemical communication between liposomes encapsulating a chemical oscillatory reaction. *Chem. Sci.* **5**(5), 1854–1859 (2014)
16. Rossi, F., Zenati, A., Ristori, S., Noel, J.M., Cabuil, V., Kanoufi, F., Abou-Hassan, A.: Activatory coupling among oscillating droplets produced in microfluidic based devices. *Int. J. Unconventional Comput.* **11**(1), 23–36 (2015)

17. Torbensen, K., Rossi, F., Pantani, O.L., Ristori, S., Abou-Hassan, A.: Interaction of the Belousov-Zhabotinsky reaction with phospholipid engineered membranes. *J. Phys. Chem. B* **119**(32), 10224–10230 (2015)
18. Stockmann, T.J., Noél, J.M., Ristori, S., Combellas, C., Abou-Hassan, A., Rossi, F., Kanoufi, F.: Scanning electrochemical microscopy of Belousov-Zhabotinsky reaction: how confined oscillations reveal short lived radicals and auto-catalytic species. *Anal. Chem.* **87**(19), 9621–9630 (2015)
19. Taylor, A.F., Tinsley, M.R., Wang, F., Huang, Z., Showalter, K.: Dynamical quorum sensing and synchronization in large populations of chemical oscillators. *Science* **323**(5914), 614–617 (2009)
20. Rossi, F., Ristori, S., Marchettini, N., Pantani, O.L.: Functionalized clay microparticles as catalysts for chemical oscillators. *J. Phys. Chem. C* **118**(42), 24389–24396 (2014)
21. Hu, G., Pojman, J.A., Scott, S.K., Wrobel, M.M., Taylor, A.F.: Base-catalyzed feedback in the urea-urease reaction. *J. Phys. Chem. B* **114**(44), 14059–14063 (2010)
22. Wrobel, M.M., Bánsági, T., Scott, S.K., Taylor, A.F., Bounds, C.O., Carranza, A., Pojman, J. A.: pH wave-front propagation in the urea-urease reaction. *Biophys. J.* **103**(3), 610–615 (2012)
23. Miele, Y., Bánsági, T., Taylor, A.F., Stano, P., Rossi, F.: Engineering enzyme-driven dynamic behaviour in lipid vesicles. In Rossi, F., Mavelli, F., Stano, P., Caivano, D. (eds.): *Advances in artificial life, evolutionary computation and systems chemistry*. Number 587 in communications in computer and information science, pp. 197–208. Springer International Publishing (2015)
24. Stingl, K., Altendorf, K., Bakker, E.P.: Acid survival of *Helicobacter pylori*: how does urease activity trigger cytoplasmic pH homeostasis? *Trends Microbiol.* **10**(2), 70–74 (2002)
25. Muzika, F., Banskagi, T., Schreiber, I., Schreiberová, L., Taylor, A.F.: A bistable switch in pH in urease-loaded alginate beads. *Chem. Commun. (Cambridge, England)* **50**(76), 11107–11109 (2014)
26. Lasic, D.D., Barenholz, Y.: *Handbook of nonmedical applications of liposomes: theory and basic sciences*, vol. 1. CRC Press (1996)
27. Paula, S., Volkov, A., Van Hoek, A., Haines, T., Deamer, D.W.: Permeation of protons, potassium ions, and small polar molecules through phospholipid bilayers as a function of membrane thickness. *Biophys. J.* **70**(1), 339 (1996)
28. Pautot, S., Frisken, B.J., Weitz, D.A.: Production of unilamellar vesicles using an inverted emulsion. *Langmuir* **19**(7), 2870–2879 (2003)
29. Carrara, P., Stano, P., Luisi, P.L.: Giant vesicles colonies: a model for primitive cell communities. *ChemBioChem* **13**(10), 1497–1502 (2012)
30. Stano, P., Wodlei, F., Carrara, P., Ristori, S., Marchettini, N., Rossi, F.: Approaches to molecular communication between synthetic compartments based on encapsulated chemical oscillators. In Pizzuti, C., Spezzano, G., (eds.): *Advances in Artificial Life and Evolutionary Computation*. Number 445 in Communications in Computer and Information Science, pp. 58–74. Springer International Publishing (2014)
31. Ermentrout, B.: *Simulating, analyzing, and animating dynamical systems: a guide to XPPAUT for researchers and students*, vol. 14. Siam (2002)
32. Mathai, J.C., Sprott, G.D., Zeidel, M.L.: molecular mechanisms of water and solute transport across archaeobacterial lipid membranes. *J. Biol. Chem.* **276**(29), 27266–27271 (2001)

Paper II



The Relevance of Inorganic Nonlinear Chemical Reactions for the Origin of Life Studies

Ylenia Miele¹ , Zsófia Medveczky², István Lagzi² , Marcello A. Budroni³ ,
and Federico Rossi⁴  

¹ Department of Chemistry and Biology, University of Salerno,
Via Giovanni Paolo II 132, 84084 Fisciano (SA), Italy

² Department of Physics, MTA-BME Condensed Matter Physics Research Group,
Budapest University of Technology and Economics,
H-1111 Budafoki ut 8, Budapest, Hungary

³ Department of Chemistry and Pharmacy, University of Sassari,
Via Vienna 2, 07100 Sassari, Italy

⁴ Department of Earth, Environmental and Physical Sciences - DEEP Sciences,
University of Siena, Pian dei Mantellini 44, 53100 Siena, Italy
`federico.rossi2@unisi.it`

Abstract. We discuss the fundamental role played by nonlinear inorganic chemical reactions to understand the minimal conditions for the origin of life. In particular, we propose a focus on the chemo-physical processes that modulate the interplay between self-organisation and self-assembly at the basis of important life-like functionalities. We present results about two proofs-of-concept that support this view. The first pertains the collective behaviours and patterns obtained from networks of autonomous inorganic oscillators confined in self-assembled structures and coupled *via* chemical communication. The second shows how a specific autocatalytic reaction can trigger conformational changes of self-assembled structures, giving rise to membrane self-division processes.

Keywords: Origin of life · Self-organisation · Self-assembly · Nonlinear chemistry · BZ oscillator · Compartmentalization · Replication

1 Introduction

The origin of life has always attracted attention for its important scientific, epistemological and social implications. The scientific investigation of this topic involves the interaction between different disciplines (chemistry, biology, physics, earth and planetary sciences), among which chemistry plays a prominent role [37]. Since the pioneering experiment of Miller and Urey of 1953 [22], it was demonstrated that, in proper conditions, organic molecules could originate from simple inorganic compounds similar to those found in Earth's early atmosphere.

From an experimental point of view, many efforts have been devoted to show possible prebiotic conditions for the formation of the building blocks of living systems, namely lipids, amino acids and nucleotides. About lipids, though Hargreaves et al. in 1977 [12] demonstrated that the synthesis of phosphatidic acid and other lipids could be achieved abiotically, it is considered improbable that fatty acids, glycerol, and phosphate could have been present together in high enough concentrations on the primordial Earth. For these reasons, it is generally assumed that the primordial membranes were mainly made of fatty acids with a chemical composition much simpler compared to the modern membranes. Fatty acids and fatty alcohols could have been produced through a sort of Fischer-Tropsch synthesis, in presence of metal surfaces and at high temperatures [10, 11, 24]. As for prebiotic amino acid syntheses, several plausible pathways have been reported. Here we name just two: (i) the Strecker reaction in which amino acids are obtained from carbonyl compounds, ammonia, and HCN [19]; (ii) the synthesis of α -amino acids and α -hydroxy acids under possible volcanic conditions by CO-dependent carbon fixation at temperatures between 80 °C and 120 °C, with nickel or nickel/iron precipitates as catalysts; carbonyl, cyano and methylthio derivatives as carbon sources; calcium or magnesium hydroxide as buffering species [13]. Comprehensive reviews on the main experimental and theoretical achievements in this research activity can be found in refs [9, 37].

In parallel, different approaches pointed at identifying inorganic processes and structures relying on “simple” molecules able to reproduce the minimal functionalities and traits of alive systems. The definition of an autopoietic system (from the Greek “self-production”), given by Maturana and co-workers [1, 52], well summarizes these essential traits: self-organised, complex, open, dissipative, self-referential, auto-catalytic, hierarchical, far from equilibrium and autonomous systems.

Self-organisation and related topics constitute the realm of nonlinear chemistry. This area has traditionally focused on the spontaneous formation and the dynamics of chemical self-organised structures in far-from-equilibrium conditions. According to the extended formulation of thermodynamics developed by Prigogine and co-workers [23], open systems fed by a constant flux of energy and/or matter can locally decrease their entropy to favour the emergence of ordered (so-called “dissipative”) structures [9, 30, 32]. In particular, systems governed by nonlinear kinetics can exhibit complex scenarios such as multistability, periodic and chaotic oscillations as well as stationary and dynamical spatio-temporal patterns in spatially extended systems, impossible to attain close to the equilibrium branch [5, 6, 8, 29]. From the theoretical viewpoint, nonlinear kinetic models have acquired great plaudits for the description of symmetry breaking phenomena (e.g. the emergence of homochirality), autocatalysis in prebiotic conditions and the origin of the RNA world [16, 18]. Autocatalytic cycles have been considered an essential feature in the origin of life as they exhibit the life-like property of exponential growth while being composed of relatively simple molecules. In this framework, inorganic oscillators and autocatalytic

reactions have been widely used as benchmark test-tube models to get insights on metabolic oscillations observed for instance in the Krebs reductive cycle and nonlinear behaviour characterising the RNA replication and enzymatic reactions.

Another essential feature for the development of life is compartmentalisation (hierarchical structures in Maturana's sense) [41–43], i.e. the physical or chemical confinement and accumulation of relevant molecules for life-type processes in sub-domains. Different plausible mechanisms have been proposed to fulfil this task, including natural convection induced by thermal gradients combined to thermophoresis [2, 4].

Nevertheless, *Self-assembly* appears the most convincing description of compartmentalisation as we observe in modern living systems. Differently from self-organisation, self-assembly is driven by the minimisation of free-energy in equilibrium conditions. This framework pertains the study of dispersed systems and addresses processes at the basis of formation and growth of thermodynamically stable structures such as emulsions, micelles and vesicles, reminiscent of those that typically characterise cellular environments.

While a rich literature exists on the study of self-organising and self-assembling systems alone, little has been done to understand the interplay between the two. Especially in the field of the origin of life, the innermost physico-chemical mechanisms ruling such a complex interplay have never been emphasised. In this work, we show how simple nonequilibrium and equilibrium systems can interact to produce emerging life-like properties in a prebiotic environment. In particular, by using relatively simple chemical systems allows one to focus on the crucial physico-chemical processes that govern the interplay between these two main levels of organisation, neglecting the role of *evolute* biological functionals.

Here we present two genuine examples of this promising perspective. The first focuses on the collective dynamics of ensembles of nano- and micro-inorganic oscillators, embedded in self-assembled supports (resin and clay micro-particles, emulsions, vesicles and double emulsions) that, thanks to different possible pathways for chemical communication, are capable to produce a variety of dynamical patterns. These dynamics are mediated by the nature of the supports, which can be tuned to selectively interact with the oscillating key intermediates and produce different global behaviours, especially synchronisation and quorum-sensing phenomena. Such systems may also provide simple models for communication in neural networks, logic implementation and possible memory architectures.

While in the first part we emphasise the influence of the self-assembled compartments on the self-organising properties of the protocells, in a second part we focus on the reverse case. In particular, based on two previous approaches, we propose a new idea where a nonlinear autocatalytic reaction is coupled to a stimuli-responsive membrane to trigger cell-like self-division phenomena, that is a key signature of living systems.

2 Self-organisation Phenomena Mediated by the Properties of the Compartments: Chemical Communication

In laboratory scale, protocells like lipid or fatty acid vesicles can be used to mimic the simplest features of living cells, while inorganic chemical oscillators and nonlinear (possibly autocatalytic) reactions are proofs-of-concept for reproducing the self-organised oscillatory dynamics typically occurring in cells during metabolic cycles or enzymatic processes.

The most familiar chemical oscillator studied in this field is the Belousov-Zhabotinsky reaction [40,45]. This reaction involves the oxidation of an organic species such as malonic acid by an acidified bromate solution in the presence of a metal ion catalyst. The BZ reaction represents a genuine inorganic analog of living-like systems (in Maturana's sense) as it develops self-organised and autonomous complex oscillatory behaviours (including spatio-temporal patterns such as chemical waves) in far from equilibrium conditions that can be maintained for a long period thanks to a slow depletion of the initial reactants. The system shows periodic oscillations between the oxidative state n and $n + 1$ of the metal and periodic changes in the concentration of other intermediates. Various redox metal catalysts can be employed, including ferroin (i.e. the redox couple red colored $[\text{Fe(II)phen}]^{2+}$ and blue coloured $[\text{Fe(III)(phen)}]^{3+}$), that allow following the oscillatory behaviour from chromatic changes of the reactive solution. The reaction mechanism is quite complicated, involving more than 18 reactions and the production of 21 species. However, according to the minimal FKN model [25,39], the complexity of the resulting dynamics can be reduced to the cyclic alternation of 3 processes: the first two steps involve the depletion of bromide ions (Br^-), the autocatalytic species HBrO_2 is produced and the catalyst oxidised; in a third step (the reset of the clock), the catalyst is brought back to the reduced form *via* a reaction with the oxidisable organic species (typically malonic acid) and, simultaneously, new Br^- ions are produced. The switching among the three steps is ruled by the concentration of bromides. High concentration of bromide precursor, Br_2 , corresponds to the dominance of the third process and low concentration of the autocatalytic species, and it thus identifies the inhibitor in the global mechanism.

The BZ reaction has been performed in a great variety of reaction environments and media such as surfactants [7], gels [44], micelles [26,34], water in oil reverse microemulsion [47], polymers [38], cation exchange particles [46] and clays [31]. In particular, the presence of zwitterionic surfactants dispersed in the BZ medium has been used to unveil possible breaks of symmetry in chemical patterns due to the mutual influence of self-organisation and self-assembly-induced processes [7].

When the reaction is encapsulated inside compartmentalized and self-assembled domains that are chemically coupled to build a network of micro-oscillators, different types of chemical communication can also be studied. Two characteristic behaviours are found depending on the chemical coupling:

in-phase synchronization occurs if the autocatalytic species HBrO_2 is the fast diffusing species and rules the communication among different compartments, and an *anti-phase* synchronization if Br_2 is the fast diffusing messenger species.

Figures 1 and 2 show respectively an array of cation exchange particles and an array of kaolinite microparticles. In both cases, the chemical communication is regulated by HBrO_2 giving rise to an *in-phase* synchronisation among the droplets (i.e. the phase difference between the different oscillatory droplets is $\Delta\phi \sim 0$).

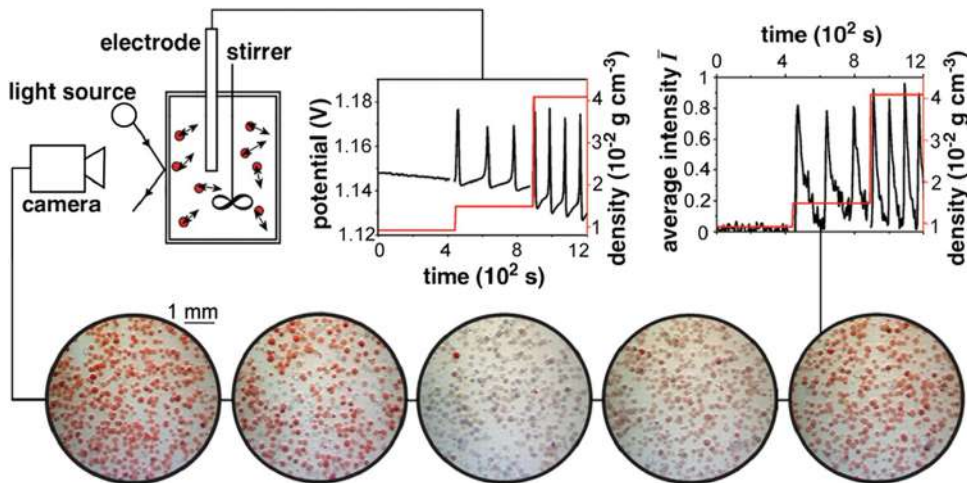


Fig. 1. Catalytic micro-particles are globally coupled by exchange of species with the surrounding catalyst-free BZ reaction medium. Electrochemical time series illustrate the change in oscillatory amplitude and period with increasing particle density (red line) for a stirring rate of 600 rpm. Reproduced with permission from [46] (Color figure online)

Figure 3 shows a network of water-in-oil droplets made of a fluorinated surfactant (PEG-PFPE amphiphilic block copolymer) separated by a fluorinated oil. In this case, the chemical oscillators confined in the droplets communicate through the exchange of the apolar bromine, giving rise to an *anti-phase* synchronization (i.e. the phase difference between confined oscillators is $\Delta\phi \sim \pi$).

In a more realistic biomimetic approach, our group proposes to substitute the synthetic surfactant introduced by Epstein and co-workers [47] with phospholipids. In this way, we can easily build an experimental model to study chemical communication in liposomes, double emulsions and emulsions made of 1,2-dimyristoyl-sn-glycero-3-phosphocholine (DMPC) [33, 35, 48–51]. In liposomes and double emulsions the communication among micro-oscillators is dominated by the activators (pulse transmission and *in-phase* oscillations). This is in contrast to what happens in simple emulsions where the communication between adjacent oscillatory droplets mainly exhibited an inhibitory character (*anti-phase*

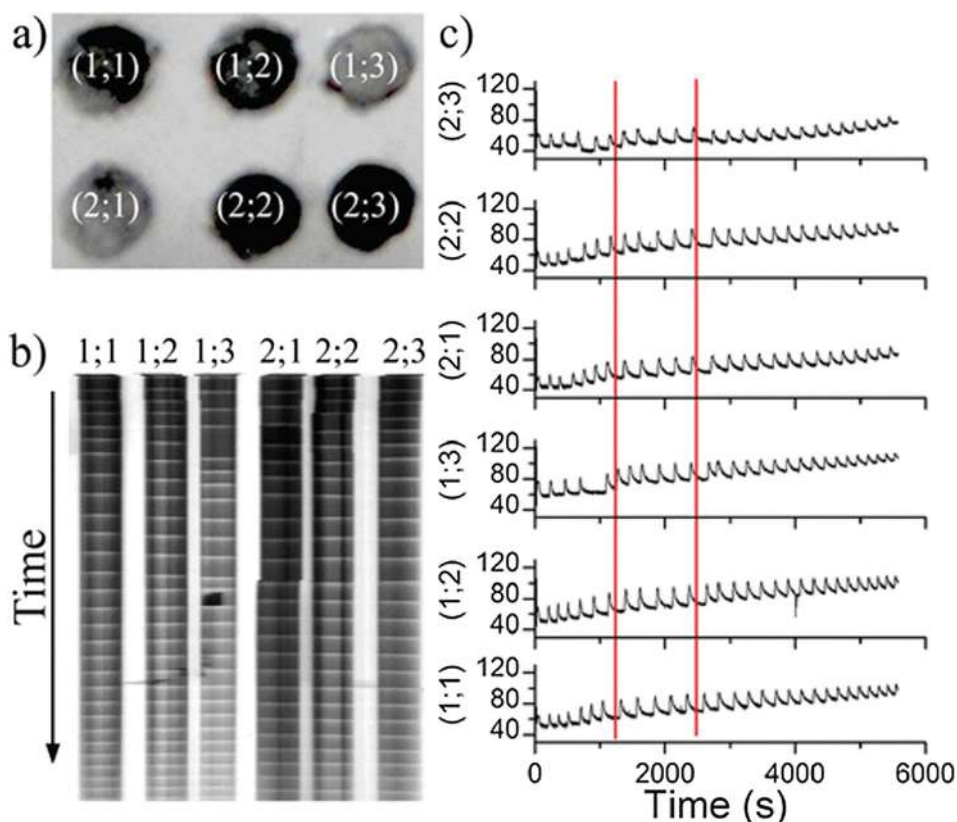


Fig. 2. Global behaviour of a 2×3 lattice where single ferriin-kaolinite oscillators are globally coupled through a BZ medium. (a) The 6 elements of the lattice ($i;j$) in different oxidation states: (1;3) and (2;1) are oxidized (bright color) while the remaining oscillators are in the reduced state (dark color). (b) ST plot of each element of the lattice. (c) Time series of the oscillatory dynamics of each element of the lattice, extracted from the ST plot. Reproduced with permission from [31]

oscillations), governed by the prominent role of Br_2 . In the presence of monolamellar membranes (lamellarity is controlled by using surfactants like Sodium Tetradecyl Sulphate, STS), in fact, molecular bromine has a higher permeability with respect to the activator HBrO_2 . This is also confirmed when bromine-blocking molecule (i.e. cholesterol) are intercalated in the membrane structure. In this case, the global dynamics results in a weakly coupled array with an erratic global behaviour (Fig. 4).

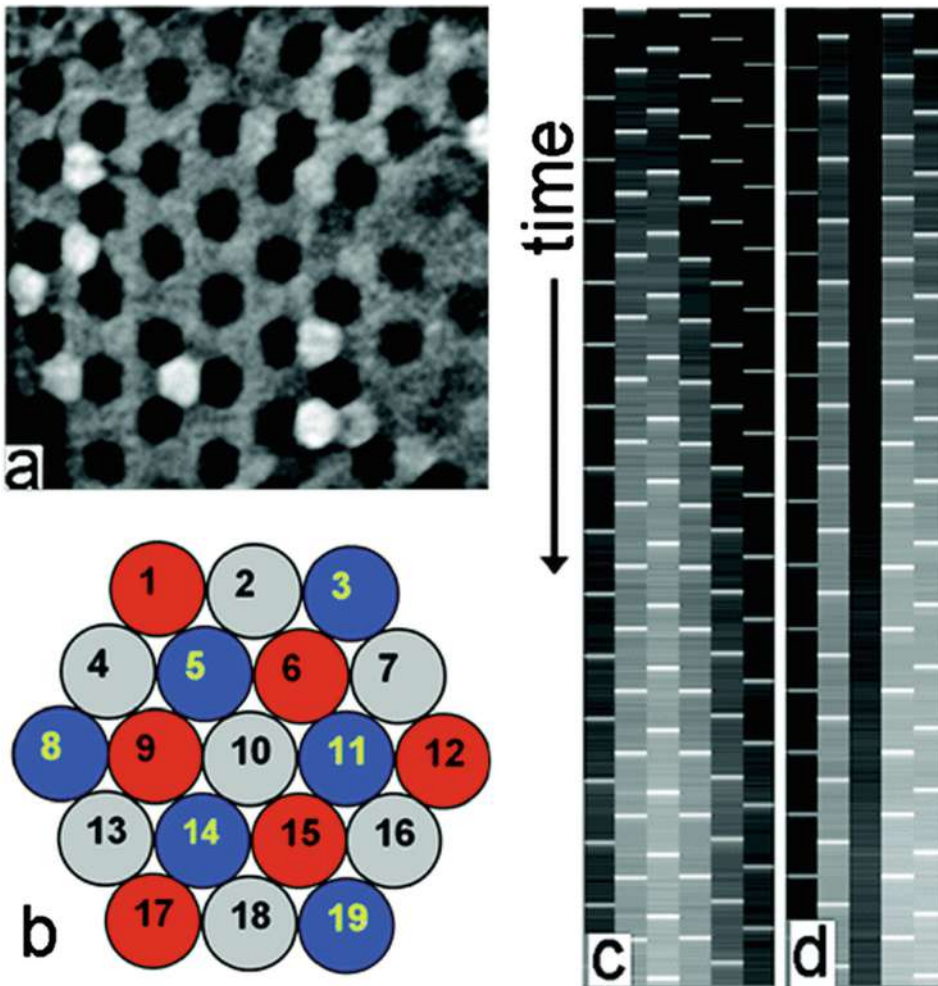


Fig. 3. Stationary and oscillatory BZ drops in 2D. (a) Hexagonally packed drops with BZ solution. The pattern arising from global chemical coupling form hexagons consisting of seven drops: each stationary drop (in black) is surrounded by six antiphase oscillatory drops. The imaged area is 0.7×0.7 mm. (b) Schematics of the pattern (stationary drops in grey). (c,d) ST plots (duration 2800 s) of drops 6, 11, 15, 14, 9, and 5 (c) and drops 1, 5, 10, 15, and 19 (d). Reproduced with permission from [47]

3 Influence of Autocatalysis on Stimuli-Responsive Compartments: Chemically-Driven Protocell Self-division

The reproduction in the laboratory of a self-division process could shed light on how the first protocells *learned* to divide and possibly to self-reproduce.

Following the pioneering work of Luisi [3] on the autopoietic behaviour of reverse micelles, the group of Szostak [53] conducted numerous studies to

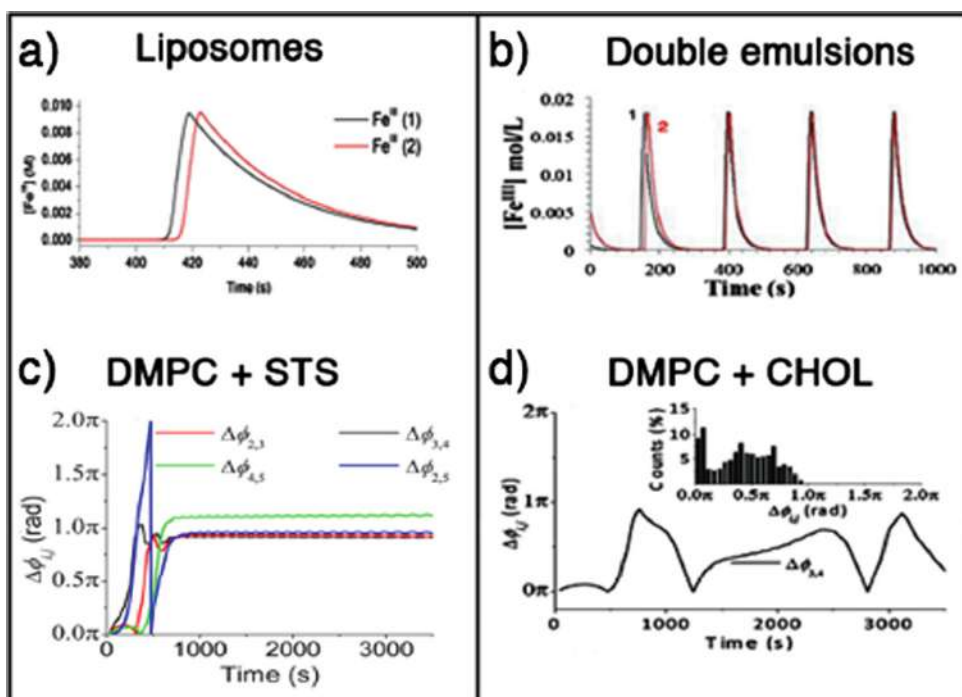


Fig. 4. (a) Signal transmission between two liposomes. At $t = 400$ s a signal is triggered in droplet 1 (black trace) and after 4 s the signal reaches droplet 2 and causes the oxidation of the catalyst (red trace); (b) Numerical simulations of the coupled dynamics of two BZ droplets in a double emulsion system. After a few cycles a perfect synchronisation is attained; (c) phase difference ($\Delta\phi_{ij} = \pi$) for the anti-phase droplets in an array of linearly coupled oscillating simple emulsions; (d) phase difference for droplets in the presence of a messenger-blocking molecule, showing uncorrelated phase behaviour over time [33]. (Color figure online)

examine how fatty acid vesicles may form, grow and divide. When fatty acid micelles are added to a solution of pre-formed vesicles, the vesicles grow rapidly. Vesicle growth is thought to occur first through the formation of a micelle shell around a vesicle. Individual fatty acids are transferred from the micelles to the outer leaflet of the vesicle membrane. Fatty acids may then flip from the outer leaflet to the inner leaflet, which allows the membrane bilayer to grow evenly. In case of multilamellar fatty acids vesicles fed with fatty acid micelles, the initially spherical vesicles turn into long thread-like vesicles, a process driven by the transient imbalance between surface area and volume growth.

Peterlin [27] also observed division in Giant Unilamellar Vesicles (GUV) of 1-palmitoyl-2-oleoyl-*sn*-glycero-3-phosphocholine (POPC) immersed in a solution of Large Unilamellar Vesicles of oleic acid/oleate (Fig. 5a). In the experiments of Szostak and Peterlin, the growth and the division of the vesicles are due to an imbalance between surface area and volume growth after the addition of fatty acids. More recently, Lagzi [17] managed to get the division of a fatty acid

emulsion (2-hexyldecanoic acid) in a solution of sodium hydroxide (Fig. 5b). The main routes to induce the division of a vesicle are thus external triggers: change of the surfactant concentration (addition of micelles to vesicles or hydrolysis of oleic anhydride) or change of the external pH.

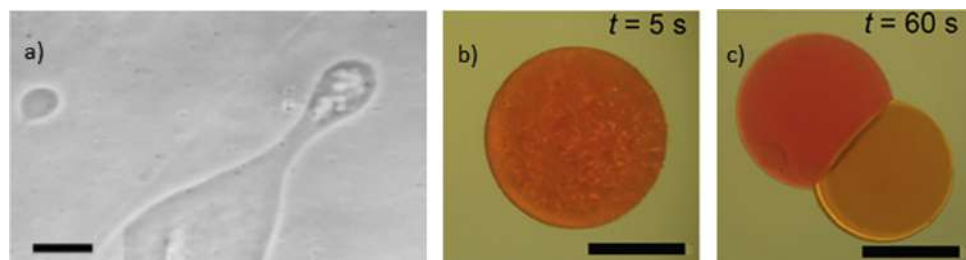


Fig. 5. (a) Image recorded upon the transfer of a POPC GUV into a 0.8 mM suspension of oleic acid in a 0.2 M sucrose/glucose solution buffered to pH 8.8. The bar represents 20 μm [27]; (b) and (c) Self-division of a mineral oil–fatty acid droplet in an alkaline solution of KOH (2 M, pH 14.3). The mineral oil droplet contains initially 30 v% 2-hexyldecanoic acid. The scale bar represents 1 mm. Reproduced with permission from [17]

In contrast to previous approaches, the challenge is to stimulate the protocell division with an internal chemical trigger. This approach would make the artificial cells more similar to the natural ones where the division is governed by internal complex biochemical reaction networks. The recent progresses in stimuli-responsive materials field [36] can help to develop a self-assembled system, possibly a vesicle-like compartment, compatible with a prebiotic environment and that is prone to self-divide by a simple chemical trigger. For example, one of the simplest chemical trigger that could likely take place in a prebiotic condition is a pH change; in this respect, mixed fatty acid/lipids compartments are reliable prebiotic model [15] that can respond to pH changes of the environment [14].

Nonlinear chemical reactions, such as the oscillating Belousov-Zhabotinsky, or *clock reactions*, which show an abrupt change of their parameters after a latency period, could be employed to control the division dynamics. The encapsulation of such reactions into pH-sensitive vesicles would refine the work of Lagzi to obtain a marked biomimetic character and possibly to reproduce the basic features of a self-dividing process.

The complex interplay between the Belousov-Zhabotinsky reaction and lipids forming archaeal plasma membrane (1,2-diphytanoyl-*sn*-glycero-3-phosphocholine, DPhPC), showed that the oscillating redox behaviour can induce important changes in the lamellarity of the lipid domains [28], however, the change of the redox state is not sufficient to prompt the conformational changes needed for fission and division processes of the membranes. Autocatalytic pH clock reactions, such as the formaldehyde-sulfite [20], seem to be a more suitable candidate for this purpose. In fact, such reactions can produce a

pH jump up to 5 units, a chemical shock that could drive pH-sensitive membranes out of equilibrium and ultimately to a conformational rearrangement compatible with a division dynamics.

Enzymatic clock reactions, though with a less prebiotic character, can also be employed as pH changing medium. In fact, it has been shown that the urease system can be successfully encapsulated in POPC vesicles and undergo a hydrolysis reaction (producing OH^- ions) following a trans-membrane input of urea [21]. A next obvious step would be the confinement of the urease system in mixed phospholipid/fatty acids compartments.

4 Conclusions

In this work we highlighted those characteristics of nonlinear chemical systems that can help to understand the transition from inanimate to animate matter and we presented few experimental systems able to reproduce in vitro, on a laboratory scale, complex biological processes. In particular, we showed how the oscillating Belousov-Zhabotinsky reaction, a model for biochemical autocatalytic cycles, can be employed in a confined environment to model trans-membrane communication by using simple periodic chemical signals. Such trafficking among individual self-organising chemical reactions generates biomimicking global behaviours; when many units are free to exchange activatory or inhibitory signals, in-phase and anti-phase oscillations or quorum sensing phenomena can be attained. Such dynamics are a genuine demonstration that simple abiotic chemical systems, when properly coupled with self-assembling confining membranes (or supports), can undergo bifurcations and symmetry-breaking dynamics, also at a population level.

We also proposed a simple experimental system to induce self-division in mixed fatty acids/phospholipids vesicles. Autocatalytic pH-changing clock reactions are thus employed to induce a chemical shock and drive out of equilibrium the vesicles membranes, that, on the basis of previous systems explored, should undergo a self-division process.

In conclusion, both population dynamics and self-division processes are distinctive traits of life that can be reproduced and explored by taking advantage of relatively simple nonlinear reactions coupled to self-assembled systems.

References

1. Amoroso, R.L., Amoroso, P.J.: The fundamental limit and origin of complexity in biological systems: a new model for the origin of life. In: AIP Conference Proceedings, vol. 718, pp. 144–159. AIP (2004)
2. Baaske, P., Weinert, F.M., Duhr, S., Lemke, K.H., Russell, M.J., Braun, D.: Extreme accumulation of nucleotides in simulated hydrothermal pore systems. *Proc. Natl. Acad. Sci.* **104**(22), 9346–9351 (2007)
3. Bachmann, P.A., Walde, P., Luisi, P.L., Lang, J.: Self-replicating reverse micelles and chemical autopoiesis. *J. Am. Chem. Soc.* **112**(22), 8200–8201 (1990)

- Braun, D., Libchaber, A.: Thermal force approach to molecular evolution. *Phys. Biol.* **1**(1), P1 (2004)
- Budroni, M.A., De Wit, A.: Dissipative structures: from reaction-diffusion to chemo-hydrodynamic patterns. *Chaos: Interdisc. J. Nonlinear Sci.* **27**(10), 104617 (2017)
- Budroni, M.A., Calabrese, I., Miele, Y., Rustici, M., Marchettini, N., Rossi, F.: Control of chemical chaos through medium viscosity in a batch ferrous-catalysed Belousov-Zhabotinsky reaction. *Phys. Chem. Chem. Phys.* **19**, 32235–32241 (2017)
- Budroni, M.A., Rossi, F.: A novel mechanism for in situ nucleation of spirals controlled by the interplay between phase fronts and reaction-diffusion waves in an oscillatory medium. *J. Phys. Chem. C* **119**(17), 9411–9417 (2015)
- Budroni, M.A., Masia, M., Rustici, M., Marchettini, N., Volpert, V.: Bifurcations in spiral tip dynamics induced by natural convection in the Belousov-Zhabotinsky reaction. *J. Chem. Phys.* **130**(2), 024902–8 (2009)
- Coveney, P.V., Swadling, J.B., Wattis, J.A., Greenwell, H.C.: Theory, modelling and simulation in origins of life studies. *Chem. Soc. Rev.* **41**(16), 5430–5446 (2012)
- Fiore, M.: The synthesis of Mono-Alkyl phosphates and their derivatives: an overview of their nature, preparation and use, including synthesis under plausible prebiotic conditions. *Org. Biomol. Chem.* **16**(17), 3068–3086 (2018)
- Fiore, M., Strazewski, P.: Prebiotic lipidic amphiphiles and condensing agents on the early Earth. *Life* **6**(2), 17 (2016)
- Hargreaves, W.R., Mulvihill, S.J., Deamer, D.W.: Synthesis of phospholipids and membranes in prebiotic conditions. *Nature* **266**(5597), 78 (1977)
- Huber, C., Eisenreich, W., Wächtershäuser, G.: Synthesis of α -amino and α -hydroxy acids under volcanic conditions: implications for the origin of life. *Tetrahedron Lett.* **51**(7), 1069–1071 (2010)
- Ikari, K., et al.: Dynamics of fatty acid vesicles in response to pH stimuli. *Soft Matter* **11**(31), 6327–6334 (2015). <http://pubs.rsc.org/en/Content/ArticleLanding/2015/SM/C5SM01248A>
- Jin, L., Kamat, N.P., Jena, S., Szostak, J.W.: Fatty acid/phospholipid blended membranes: a potential intermediate state in protocellular evolution. *Small* **14**(15), 1704077 (2018)
- Kitadai, N., Kameya, M., Fujishima, K.: Origin of the reductive tricarboxylic acid (rTCA) cycle-type CO₂ fixation: a perspective. *Life* **7**(4), 39 (2017)
- Lagzi, I.: Self-division of a mineral oil-fatty acid droplet. *Chem. Phys. Lett.* **640**, 1–4 (2015)
- Liu, Y., Sumpter, D.: Spontaneous emergence of self-replication in chemical reaction systems. arXiv preprint [arXiv:1801.05872](https://arxiv.org/abs/1801.05872) (2018)
- Martins, Z., Sephton, M., Hughes, A.B.: Aminoacids, Peptides and Proteins in Organic Chemistry - Origins and Synthesis of Amino Acids, vol. 1. Wiley, Weinheim (2009)
- McIlwaine, R., Kovacs, K., Scott, S.K., Taylor, A.F.: A novel route to pH oscillators. *Chem. Phys. Lett.* **417**(1), 39–42 (2006)
- Miele, Y., Bánsági, T., Taylor, A.F., Stano, P., Rossi, F.: Engineering enzyme-driven dynamic behaviour in lipid vesicles. In: Rossi, F., Mavelli, F., Stano, P., Caivano, D. (eds.) WIVACE 2015. CCIS, vol. 587, pp. 197–208. Springer, Cham (2016). https://doi.org/10.1007/978-3-319-32695-5_18
- Miller, S.L.: A production of aminoacids under possible primitive earth conditions. *Science, New Ser.* **117**(3046), 528–529 (1953). <http://www.jstor.org/stable/1680569>

23. Nicolis, G., Prigogine, I.: *Self-organization in Nonequilibrium Systems*. Wiley, New York (1977)
24. Nooner, D., Gibert, J., Gelpi, E., Oro', J.: Closed system fischer-tropsch synthesis over meteoritic iron, iron ore and nickel-iron alloy. *Geochimica Et Cosmochimica Acta* **40**(8), 915–924 (1976)
25. Noyes, R.M., Field, R., Koros, E.: Oscillations in chemical systems. I. Detailed mechanism in a system showing temporal oscillations. *J. Am. Chem. Soc.* **94**(4), 1394–1395 (1972)
26. Paul, A.: Observations of the effect of anionic, cationic, neutral, and zwitterionic surfactants on the Belousov-Zhabotinsky reaction. *J. Phys. Chem. B* **109**(19), 9639–9644 (2005)
27. Peterlin, P., Arrigler, V., Kogej, K., Svetina, S., Walde, P.: Growth and shape transformations of giant phospholipid vesicles upon interaction with an aqueous oleic acid suspension. *Chem. Phys. Lipids* **159**(2), 67–76 (2009)
28. Ristori, S., Rossi, F., Biosa, G., Marchettini, N., Rustici, M., Tiezzi, E.: Interplay between the Belousov-Zhabotinsky reaction-diffusion system and biomimetic matrices. *Chem. Phys. Lett.* **436**, 175–178 (2007)
29. Rossi, F., Budroni, M.A., Marchettini, N., Cutietta, L., Rustici, M., Turco Liveri, M.L.: Chaotic dynamics in an unstirred ferroin catalyzed Belousov-Zhabotinsky reaction. *Chem. Phys. Lett.* **480**(4–6), 322–326 (2009)
30. Rossi, F., Liveri, M.L.T.: Chemical self-organization in self-assembling biomimetic systems. *Ecol. Model.* **220**(16), 1857–1864 (2009)
31. Rossi, F., Ristori, S., Marchettini, N., Pantani, O.L.: Functionalized clay microparticles as catalysts for chemical oscillators. *J. Phys. Chem. C* **118**(42), 24389–24396 (2014)
32. Rossi, F., Ristori, S., Rustici, M., Marchettini, N., Tiezzi, E.: Dynamics of pattern formation in biomimetic systems. *J. Theor. Biol.* **255**(4), 404–412 (2008)
33. Rossi, F., Torbensen, K., Ristori, S., Abou-Hassan, A.: Signal transduction and communication through model membranes in networks of coupled chemical oscillators. In: Pelillo, M., Poli, I., Roli, A., Serra, R., Slanzi, D., Villani, M. (eds.) *WIVACE 2017*. CCIS, vol. 830, pp. 16–31. Springer, Cham (2018). https://doi.org/10.1007/978-3-319-78658-2_2
34. Rossi, F., Varsalona, R., Marchettini, N., Turco Liveri, M.L.: Control of spontaneous spiral formation in a zwitterionic micellar medium. *Soft Matter* **7**, 9498 (2011)
35. Rossi, F., et al.: Activatory coupling among oscillating droplets produced in microfluidic based devices. *Int. J. Unconventional Comput.* **11**(1), 23–36 (2015)
36. Roy, D., Cambre, J.N., Sumerlin, B.S.: Future perspectives and recent advances in stimuli-responsive materials. *Progr. Polym. Sci.* **35**(1), 278–301 (2010)
37. Ruiz-Mirazo, K., Briones, C., de la Escosura, A.: Prebiotic systems chemistry: new perspectives for the origins of life. *Chem. Rev.* **114**(1), 285–366 (2013)
38. Sciascia, L., Rossi, F., Sbriziolo, C., Liveri, M.L.T., Varsalona, R.: Oscillatory dynamics of the Belousov-Zhabotinsky system in the presence of a self-assembling nonionic polymer. Role of the reactants concentration. *Phys. Chem. Chem. Phys.* **12**(37), 11674–11682 (2010)
39. Scott, S.K.: *Chemical Chaos*. Oxford University Press, Oxford (1993)
40. Scott, S.K.: *Oscillations, Waves, and Chaos in Chemical Kinetics*. Oxford University Press, Oxford (1994)
41. Stano, P., D'Aguanno, E., Bolz, J., Fahr, A., Luisi, P.L.: A remarkable self-organization process as the origin of primitive functional cells. *Angewandte Chemie International Edition* **52**(50), 13397–13400 (2013)

42. Stano, P., Mavelli, F.: Protocells models in origin of life and synthetic biology. *Life* **5**(4), 1700–1702 (2015)
43. Szostak, J., Bartel, D., Luisi, P.: Synthesizing life. *Nature* **409**(6818), 387–390 (2001)
44. Takeoka, Y., Watanabe, M., Yoshida, R.: Self-sustaining peristaltic motion on the surface of a porous gel. *J. Am. Chem. Soc.* **125**(44), 13320–13321 (2003). <http://pubs.acs.org/doi/abs/10.1021/ja036904c>
45. Taylor, A.F.: Mechanism and phenomenology of an oscillating chemical reaction. *Progr. React. Kinet. Mech.* **27**(4), 247–325 (2002)
46. Taylor, A.F., Tinsley, M.R., Wang, F., Huang, Z., Showalter, K.: Dynamical quorum sensing and synchronization in large populations of chemical oscillators. *Science* **323**(5914), 614–617 (2009)
47. Toiya, M., González-Ochoa, H.O., Vanag, V.K., Fraden, S., Epstein, I.R.: Synchronization of chemical micro-oscillators. *J. Phys. Chem. Lett.* **1**(8), 1241–1246 (2010)
48. Tomasi, R., et al.: Chemical communication between liposomes encapsulating a chemical oscillatory reaction. *Chem. Sci.* **5**(5), 1854–1859 (2014)
49. Torbensen, K., Ristori, S., Rossi, F., Abou-Hassan, A.: Tuning the chemical communication of oscillating microdroplets by means of membrane composition. *J. Phys. Chem. C* **121**(24), 13256–13264 (2017)
50. Torbensen, K., Rossi, F., Pantani, O.L., Ristori, S., Abou-Hassan, A.: Interaction of the Belousov-Zhabotinsky reaction with phospholipid engineered membranes. *J. Phys. Chem. B* **119**(32), 10224–10230 (2015)
51. Torbensen, K., Rossi, F., Ristori, S., Abou-Hassan, A.: Chemical communication and dynamics of droplet emulsions in networks of Belousov-Zhabotinsky micro-oscillators produced by microfluidics. *Lab Chip* **17**(7), 1179–1189 (2017)
52. Varela, F.G., Maturana, H.R., Uribe, R.: Autopoiesis: the organization of living systems, its characterization and a model. *Biosystems* **5**(4), 187–196 (1974)
53. Zhu, T.F., Szostak, J.W.: Coupled growth and division of model protocell membranes. *J. Am. Chem. Soc.* **131**(15), 5705–5713 (2009)

Paper III



Self-Division of Giant Vesicles Driven by an Internal Enzymatic Reaction

Ylenia Miele,^a Zsófia Medveczky,^b Gábor Holló,^c Borbála Tegze,^d Imre Derényi,^e Zoltán Hórvölgyi,^d Emiliano Altamura,^f István Lagzi,^{b,c*} Federico Rossi^{a,g*}

Received 00th January 20xx,
Accepted 00th January 20xx

DOI: 10.1039/x0xx00000x

www.rsc.org/

Self-division is one of the most common phenomena in living systems and one of the important properties of life driven by internal mechanisms of the cells. Design and engineering of synthetic cells from abiotic components can recreate life-like function thus contributing to the understanding of the origin of life. Existing methods to induce the self-division of vesicles require external and non-autonomous triggers (temperature change, the addition of membrane precursors). Here we show that pH-responsive giant unilamellar vesicles in the micrometer scale can undergo self-division triggered by an internal autonomous chemical stimulus driven by an enzymatic (urea-urease) reaction coupled to a cross-membrane transport of the substrate, urea. The bilayer of the artificial cells is composed of a mixture of phospholipids (POPC, 1-palmitoyl-2-oleoyl-*sn*-glycero-3-phosphatidylcholine) and oleic acid molecules. The enzymatic reaction raises the pH in the lumen of the vesicles, which concomitantly changes the protonation state of the oleic acid in the inner leaflet of the bilayer causing the removal of the membrane building blocks into the lumen of the vesicles thus decreasing of the inner membrane area with respect to the outer one. This process coupled to the osmotic stress (responsible for the volume loss of the vesicles) leads to the division of a mother vesicle into two smaller daughter vesicles. These two processes must act in synergy, none of them alone can induce the division. Overall, our self-dividing system represents a step forward in the design and engineering of a complex non-autonomous model of synthetic cells.

Introduction

Synthetic Cells (SCs) or minimal cells can be defined as artificial cell-like systems constructed in the laboratory by introducing biological or synthetic molecules inside and on the surface of lipid vesicles (liposomes)^{1–4}. In a bottom-up approach to the construction of SCs, the emphasis is on mimicking the processes and the functions typical of living cells rather than reproducing their single biochemical components. In this context, the construction of entities with minimal complexity, yet being to reproduce biological processes, offers new perspectives and advantages in many fields, including medicine, material science and the origin of life studies.

Compartmentalization into separate domains is an essential characteristic of biological systems and this feature is universally

recognized as the basis on which SCs can be constructed^{1,5–8}. Giant Unilamellar Vesicles (GUVs) are water-in-water compartments stabilized by amphiphilic molecules (phospholipids for example) that self-assemble into bilayers and create membranes. GUVs range from 1 μm to more than 100 μm in size depending on the preparation method employed, and their popularity as artificial cell chassis increased because of a few distinctive advantages⁹: (i) they can be observed in real-time through optical microscopes; (ii) the membrane composition is tunable, which allows to control various bilayer properties such as curvature, stiffness or permeability; (iii) they are suitable for hosting chemical⁹ and biochemical¹⁰ reactions and biomimetic processes¹¹.

Synthetic GUVs are also very important in origin-of-life studies because they can be devised and constructed as models of primitive cells (protocells)¹². Szostak et al., for example, recently proposed fatty acid (oleic acid, HOA) – phospholipid (1-palmitoyl-2-oleoyl-*sn*-glycero-3-phosphocholine, POPC) mixture as plausible intermediates in protocellular evolution¹³; these mixed GUVs, in fact, combine the stability typical of POPC bilayers (for example they do not precipitate in the presence of divalent cations) with the plasticity and permeability of HOA structures¹⁴. Moreover, both components are present in living organisms (e.g., POPC is in the membrane of eukaryotic cells, HOA is a component of animal fats and vegetable oils)¹⁵.

Among the various cellular functions, vesicle “self-replication” and “self-division” attract distinguished attention of many research groups, because these features are essential prerequisites for life. Since the pioneering work of Luisi in the 1990s, most experimental works have focused on the division and replication of micelles, reverse micelles and vesicles made of fatty acids^{16–21}. Few

^a Department of Chemistry and Biology “A. Zambelli” University of Salerno, Via Giovanni Paolo II 132, 84084 – Fisciano (SA), Italy

^b Department of Physics, Budapest University of Technology and Economics H-1111, Budapest, Budafoki út 8, Hungary

^c MTA-BME Condensed Matter Research Group, Budapest University of Technology and Economics, H-1111, Budafoki út 8, Budapest, Hungary

^d Department of Physical Chemistry and Materials Science, Budapest University of Technology and Economics, H-1111 Budafoki út 8, Budapest, Hungary

^e Department of Biological Physics, Eötvös Loránd University, H-1117 Pázmány Péter sétány 1/A, Budapest, Hungary

^f Department of Chemistry, University of Bari, “Aldo Moro”, Via Orabona 4, I-70125 Bari, Italy

^g Department of Earth, Environmental and Physical Sciences – DEEP Sciences, University of Siena, Pian dei Mantellini 44, 53100 – Siena, Italy

† Electronic Supplementary Information (ESI) available: [Description of chemical model for the confined urea-urease enzymatic reaction. Descriptions of molecular dynamics simulations and film balance experiments. Description of videos (Videos S1–3). Supporting Tables S1 and S2, and Figures S1–S7.]. See DOI: 10.1039/x0xx00000x

experiments involving GUVs have also been reported^{22–32}, but in the origin-of-life perspective, they have been rarely considered, mainly because (i) the scarce biomimetic character of the membranes and (ii) the strong external control exerted on the systems to induce divisions^{12,33}. It is also to be pointed out that, in most of the systems explored, the trigger for the onset of the division process had a physical character (e.g., the addition of membrane precursors and temperature change) and acted externally on the outer surface of the protocell. In contrast, the cell division in living systems is a process governed by the biochemical reaction network of the cell, which is an internal and autonomous process, often induced by environmental inputs sensed by the cell through cross-membrane transport of chemical and biochemical information³⁴. One attempt has been made to internally drive GUVs shape transformation. A protein system (Min) has been encapsulated into the GUVs and used to reversible control the shape transformation of GUVs from pear shape to dumbbell shape, and to drive periodic budding and subsequent merging of the buds with the mother vesicles³⁵.

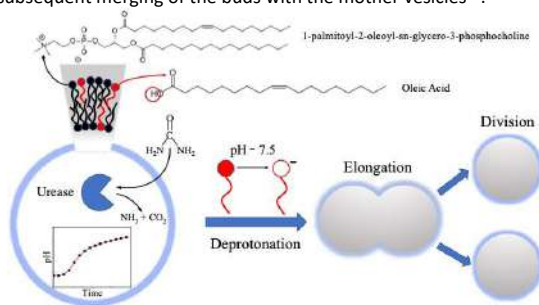


Figure 1. Schematic representation of GUVs self-division process. Mixed POPC/HOA ([POPC]/[HOA]=2.6 mM/2.4 mM) vesicles containing the enzyme urease were prepared by a phase transfer method. Urea was added to the external solution to trigger the reaction inside the lumen of the vesicles. Following the urea trans-membrane permeation the pH increase causes the deprotonation of the oleic acid in the inner leaflet of the bilayer, which, in turn, induces vesicle division.

In this work, we propose a model for protocell division based on a chemical trigger, activated by the transmembrane transport of a substrate, acting inside the lumen of the artificial cells. In particular, we employed mixed POPC/HOA vesicles and we exploited the characteristic sensitivity of HOA ($pK_a \sim 7.2 - 7.5$ in a phospholipid bilayer) to pH stimuli^{15,36} and the osmotic concentration gradient to induce the protocell division. As an internal chemical trigger, we used the urea-urease enzymatic reaction, i.e. the enzymatic hydrolysis of the urea catalyzed by the Ni-protein urease. This reaction produces ammonia and carbonic acid that, in unbuffered media, shift the pH towards alkaline range³⁷. The reaction rate, as a function of the pH, has a bell shape of the Michaelis-Menten type (see Supporting Information, S1, Figure S1a) that, in time, generates a pH profile typical of an autocatalytic process (Figure S1b)³⁸. In fact, when the initial pH is set to low values, the reaction products contribute to the rise of the pH, which leads to a rapid acceleration of the hydrolysis. After reaching a maximum in the proximity of neutrality ($pH = 7.4$), the reaction rate decreases with pH to finally attain a plateau generating a characteristic sigmoidal kinetic curve for the pH change.

Results and discussion

The sketch in Figure 1 summarizes the basic features of our experiments. A population of about 10,000 units of GUVs was prepared with a size between 5 and 50 μm , by using a phase transfer method^{39,40}. Following our previous works^{41,42}, we encapsulated the enzyme urease (0.5 U/mL) together with a pH-sensitive fluorescent dye (pyranine) (50 μM) into the lumen of the vesicles. Both the enzyme and the fluorescent dye are firmly confined into the GUVs⁴¹, however, the mixed bilayer allows the passage of small nonpolar molecules⁴³, such as urea, which is dispersed in the outer medium and can enter the lumen of the vesicles to trigger the reaction. Figure 2 shows a typical division process, taking place in about 1 minute after a solution containing urea (180 mM) is added to a dispersion of GUVs ($t = 0$, $[\text{urea}]_0 = 60 \text{ mM}$): starting from a spherical shape, the GUV elongates in a prolate form ($t \sim 12 \text{ s}$), assumes a pear shape ($t \sim 16 \text{ s}$) and eventually divides into two daughter vesicles ($t \sim 60 \text{ s}$) (Video S1).

We explored several membrane compositions by changing the ratio of concentrations $\alpha = [\text{POPC}]/[\text{HOA}]$ and keeping the total amount of amphiphiles constant $s = [\text{POPC}] + [\text{HOA}] = 5 \text{ mM}$. The ideal ratio to obtain the highest proportion of divisions in the population of vesicles was found to be $\alpha \sim 1$ (2.6 mM: 2.4 mM). Under these conditions in a population of GUVs, the pH triggered self-division process is a frequent event with a success rate of 25% irrespective of their size (400 GUVs analyzed in 3 experiments, Figure 3 and Figure S2). The rest of the GUVs elongated and changed shape, but did not complete the division process. Greater α provided stable, but non-pH responsive GUVs, while a lower α generated less stable GUVs in the course of the rise of the pH.

Complete separation of the daughter vesicles has not been observed. The vesicles always stay in close proximity and, therefore, are most probably remain connected by a narrow neck. This is in agreement with the widely accepted hypothesis that fission and fusion are activated processes with an energy barrier of at least 20 k_B ^{74,45}. In biology these processes rarely occur spontaneously, and are mediated by proteins⁴⁵. To check whether the lumens of the two daughter vesicles are contiguous, we carried out FRAP (fluorescence recovery after photobleaching) experiments. The fluorescence of one of the two daughter vesicles was bleached after the division process with a laser beam. This perturbation, however, resulted in a complete separation of the daughter vesicles, which then diffused away from each other, also preventing the fluorescence recovery of the bleached vesicle (Figure S3). This behavior is reminiscent of what was found by Zhu and Szostak in experiments with fatty-acid vesicles, where the kinetic energy of mildly agitated liquid water triggered the division and breaking up of thread-like aggregates.²⁶ In our case, the energy of the laser beam provides the trigger to complete the separation process. Based on our FRAP experiments, it can be concluded that after division the daughter vesicles remain connected by a common membrane neck, which can be broken by additional environmental triggers.

Epifluorescent imaging of the system confirmed that the stages of the division process correlate with the increase of the pH inside the vesicles (Figure 4a and Video S2). Based on these measurements, the pH inside the GUVs changes from $pH \sim 6$ to ~ 6.5 (Figure 4b and Figure S4), which, in our experimental conditions, can cause a change of up to 20% (considering $pK_a = 7.2$) in the protonation rate of the HOA molecules.

Interestingly, in almost all successful divisions, the mother vesicles divided into two daughter vesicles. Sometimes, especially when bigger GUVs divided ($R > 15 \mu\text{m}$), the GUVs budded off

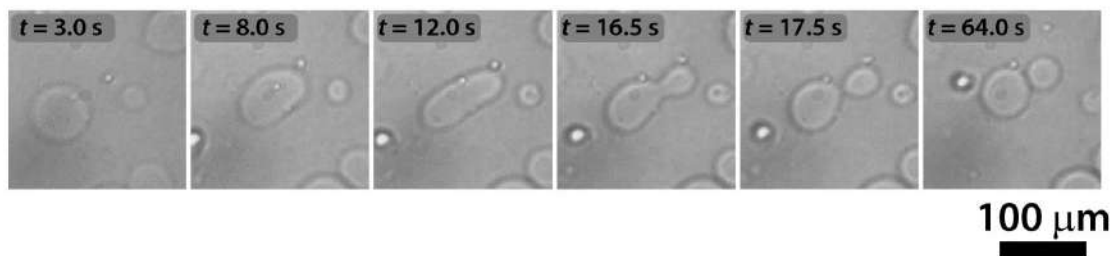


Figure 2. pH-triggered self-division of a GUV. Continuous shape transformation of a GUV, triggered by urea-urease enzymatic reaction, starting from a spherical shape through prolate and pear shapes into two daughter vesicles.

several smaller ones. During the transition from a sphere to a prolate spheroid, both the surface area and the volume decreased after the addition of the substrate (area and volume were estimated from the optical micrographs) and at the end of the division process, the volume of the vesicles was found to be decreased by about 25% on average (Figure 3b), while the average total surface area remained within the 10% of the mother vesicle (Figure 3c).

We carried out control experiments in a buffered medium (inside and outside of the GUVs) at pH = 6.4 adjusted by a phosphate buffer (0.14 M, K_2HPO_4 / KH_2PO_4) to check whether the pH change is indeed responsible for the self-division. In the case of buffered media, we did not observe any vesicle divisions, but only the elongation of a few GUVs (Video S3). This observation shows that pH change is an important ingredient of the division process. Additionally, we investigated the influence of an osmotic shock in the absence of a pH change by two types of control experiments. In a first approach, NaCl (0.1 – 0.3 M) was added to the external solution in the absence of the substrate urea; the ionic couple Na^+Cl^- cannot cross the bilayer and creates an outer hypertonic solution. As expected, a few vesicles deflated in time and some of them underwent small deformations, but divisions were never detected. A second check was performed by adding urea in the outer solution, but without encapsulating the enzyme into the lumen of the GUVs; in principle, urea is permeable towards the bilayer, and it should not cause a long term osmotic stress to the membrane. However, the permeability of urea is several orders of magnitude smaller than that of water and a temporary osmotic stress is present until the urea gradient is smoothed out. As in the NaCl case, vesicles became smaller and a few of them underwent deformation, but again, no division was observed. This finding indicates that the osmotic concentration gradient itself is not enough to cause division.

To explain the pH change (induction time and magnitude) and the osmotic concentration gradient inside and outside the GUVs driven by the urea-urease enzymatic reaction, we constructed a simple kinetic model that qualitatively describes the behavior observed in the experiments using the pH-sensitive fluorescent dye. The sketch in Figure S5 shows all chemical species responsible for the

pH changes inside the vesicles and in the outer environment. The enzyme (E) and the fluorescent dye (pyrOH) are confined into the lumen of the vesicles and cannot cross the membranes. The HOA molecules, which participate in the acid-base equilibrium, are considered homogeneously partitioned to the membranes, and both flip-flop movement from one leaflet to the other and the exchange of monomers with the water solution are neglected because of the slow timescales of these processes⁴⁶. The substrate, urea (S), delivered into the outer solution at time $t = 0$ in the kinetic simulations, the reaction products, CO_2 and NH_3 , produced inside the vesicles and the acetic acid (HA), added inside and outside the vesicle to lower the initial pH, are free to cross the membrane by passive diffusion. The concentration of each chemical species inside a vesicle changes due to chemical reaction and transport. The corresponding differential equation is the following (details in SI):

$$\frac{d[X]}{dt} = r([X]) + k_X([X]_o - [X]), \quad (1)$$

where $[X]$ denotes the concentration of the chemical species X , $r([X])$ represents the set of reaction rates involving X , and $[X]_o$ is the concentration of the chemical species in the outer phase. The transfer rate k_X (s^{-1}) is proportional to the surface-to-volume ratio of the vesicle and also the specific membrane permeability of the species: $k_X = 3P_X/R$, where P_X (dm/s) is the specific permeability and R (dm) is the vesicle's radius. The variation of $[X]_o$ in the outer solution depends on the number of vesicles where the enzymatic reaction takes place

$$\frac{d[X]_o}{dt} = r([X]_o) + d_f k_X([X] - [X]_o), \quad (2)$$

where the dilution factor d_f is proportional to the total number of vesicles N and also to the ratio between the inner volume of a vesicle V_i and the volume of the outer solution V_o , $d_f = NV_i/V_o$.

The osmotic concentrations (Π) inside and outside the vesicles were calculated as the sums of the concentrations of the ionic species that cannot cross the membrane due to electro-neutrality

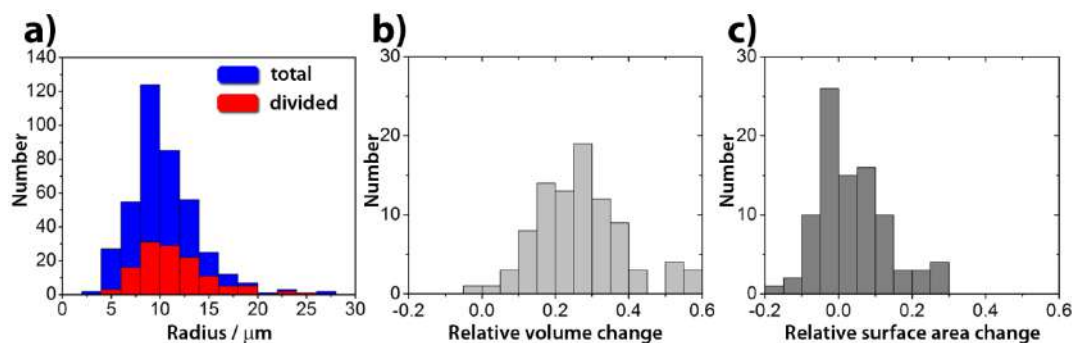


Figure 3. a) Size distribution of GUVs used in the experiments (blue) and the frequency histogram of the divisions (red). The success rate of a division is $\sim 25\%$, irrespective of the size of the GUVs. b) Relative volume change and c) relative surface area change in a population of GUVs. The relative change is defined as $(Y_{\text{mother}} - (Y_{\text{daughter1}} + Y_{\text{daughter2}})) / Y_{\text{mother}}$, where Y denotes either volume or surface area.

constrains (CH_3COO^- , NH_4^+ , CO_3^{2-} , HCO_3^-), the concentrations of bulky molecules initially encapsulated into the GUVs (urease, pyranine), and the concentration of urea. Here, we considered N identical vesicles having an average radius calculated from the size distribution in Figure 3a. The results of the numerical simulations (Figure 4c) are in accordance with the pH dynamics reconstructed from fluorescence time series in Figure 4b. In fact, the pH jump is about one unit, similarly to the experiments, and both the induction (inflection) time (i.e., when the pH increase rate has its maximum) and the plateau time are also consistent with the experiments

(Figure 4b and c). We performed simulations by varying those few parameters for which we had only rough estimates, namely the total number of vesicles in the sample ($10,000 < N < 50,000$) and the average radius of vesicles ($5 \mu\text{m} < R < 15 \mu\text{m}$), without revealing any significant deviation from what is reported in Figure 4c. Figure 4c also shows the simulated osmotic concentration difference ($\Delta\Pi$) between the vesicle lumen and the outer solution (volumes are assumed constant in the simulations) that explains the volume loss ($\sim 25\%$) observed during the division process. In fact, such a volume change is enough to smooth out the calculated osmotic

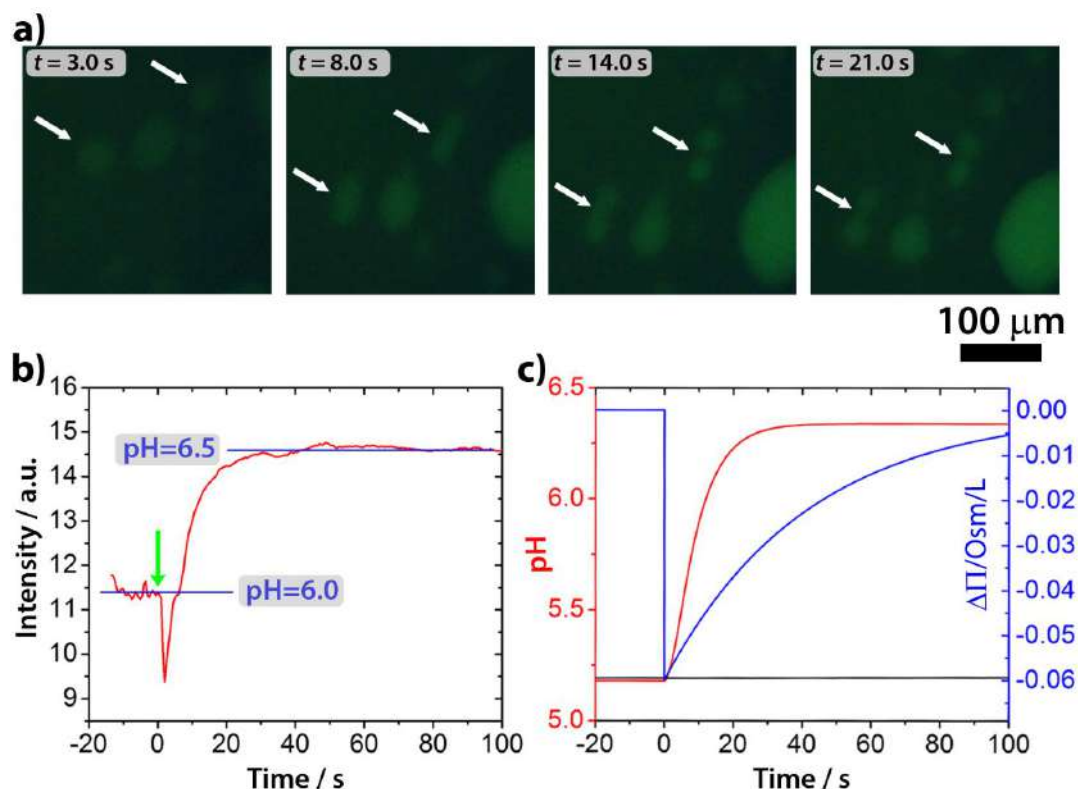


Figure 4. a) Fluorescence microscopy images of GUVs during the self-division process. An increase of the fluorescent signal by pH-sensitive fluorescent dye pyranine inside the GUVs indicates a pH change. b) Change of the fluorescent intensity in time inside the GUVs. c) Results of the numerical simulations of the pH change inside (solid red curve) and outside (solid black curve) of the vesicles. Urea is delivered into the outer solution at model time $t = 0$.

concentration gradient, mostly due to the addition of urea ($\Delta\Pi \approx 60\text{ mM}$). Figure 4c also shows that, in the first 20 s, pH increases faster than urea permeates the membrane by passive diffusion, therefore, the deprotonation of the OA must act in synergy with the osmotic stress.

To get some insight into how the change in the protonation rate of the HOA molecules at one side of bilayer affects the inner leaflet of the GUVs, we performed molecular dynamics (MD) simulations (NPT - isothermal-isobaric ensemble - simulations with a semi-isotropic pressure coupling). One of the two leaflets of the POPC/HOA bilayer was deprotonated step by step: in each step 10% of the HOA molecules were deprotonated, then the system was equilibrated for 10 ns, and the process was repeated until all HOA molecules became deprotonated. Figures S6 and S7 show the results of the MD simulations. Due to the electrostatic repulsion between

the negatively charged head groups of the leaflet being deprotonated, the average molecular surface area of this leaflet increased monotonically with the deprotonation ratio, resulting in both an increase in the total surface area of the bilayer and buckling of the membrane towards the deprotonated leaflet. (Figures S6 and S7). A similar effect due to a pH change was previously observed in a mixed bilayer of lysophosphatidylcholine and free fatty acids⁴⁷. The expansion of a POPC/HOA leaflet due to the electrostatic repulsion between the deprotonated HOA molecules was also confirmed by the Wilhelmy film balance experiments at different pHs in buffered media (Figure S8).

To understand the division mechanism, we have to bear in mind that both the bilayer-couple (BC)^{48–51} and the area-difference-elasticity (ADE)^{51,52} models of membranes, predict that any shape

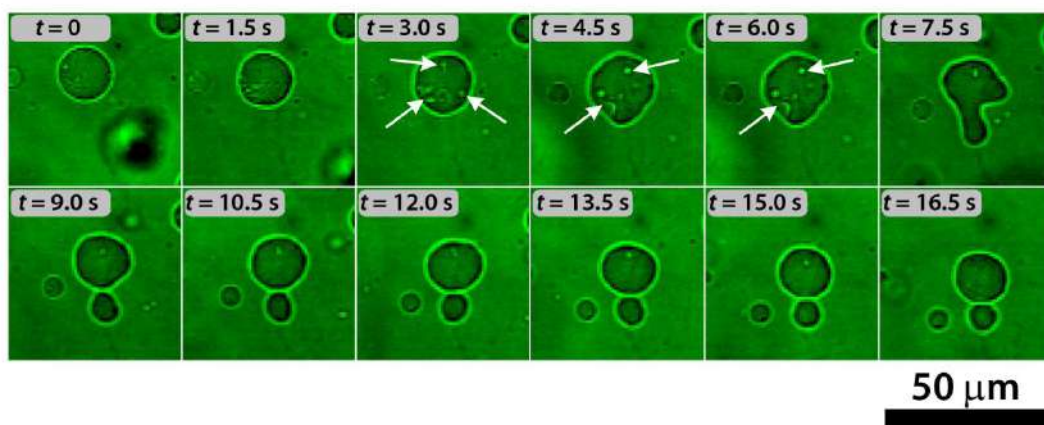


Figure 5. Self-division process in a GUV and the formation of protrusions inside the vesicles (indicated by the white arrows) observed by using confocal microscopy.

transformation of an initially spherical vesicle to a pear-shaped vesicle and, eventually, to two separate vesicles must be driven by two parallel processes: (i) the volume loss of vesicles and (ii) the decrease of the surface area of the inner leaflet relative to the outer one. The volume decrease can be explained by the transport of the water molecules through the bilayer from the vesicles induced by the initial osmotic concentration gradient. The decrease of the surface area is in an apparent contradiction with the results observed in both Wilhelmy film balance experiments and MD simulations. A possible mechanism behind this phenomenon is the formation of protrusions and micro aggregates (possibly vesicles) inside the lumen of the mother protocell (due to the preference of the deprotonated HOA molecules for curved and expanded surfaces) and the dissolution of deprotonated HOA molecules (prompted by their higher water solubility). Such a possibility is in line with both the surface area shrink measured during the division process and the ADE theory. The evidence for the formation of invaginated aggregates inside the lumen of vesicles can be seen in the confocal micrographs reported in Figure 5.

Note that the relative area difference between the inner and the outer leaflets of a spherical vesicle is $2w/R$, where w (a few nm) is the distance between the leaflets, and R is the radius of the vesicle. For our GUVs ($5 \mu\text{m} < R < 15 \mu\text{m}$) this relative area difference is very small, of the order of 10^{-3} . The shape transformation from a single sphere to two spheres requires only a similarly small amount of relative decrease of the inner leaflet.

Thus, in our interpretation, the initially added urea solution generates osmotic stress, urea penetrates into GUVs, however, concurrently, some water leaves vesicles to equilibrate the osmotic concentration difference. Since the permeability of water is several orders of magnitude greater than that of urea, the volume of the vesicles decreases. Parallel with this process, the urease-urea reaction starts in the GUVs and the pH of the inner compartment increases due to ammonia production. Any increase in pH (close to the pK_a of HOA) inside the vesicles involves an increase in the deprotonation rate of HOA, thus introduces negative charges in the inner leaflets of the GUVs. This charge accumulation affects the membrane stability and induces the formation of oleate aggregates inside the GUVs lumen, thereby decreasing the surface area of the inner leaflet with respect to that of the outer one. Both the volume loss and the surface area change between the inner and outer

leaflets drives the shape transformation of the GUVs and leads to their self-division.

To highlight the synergy between the action of the osmotic concentration gradient (inducing volume loss) and the pH change inside the vesicles (inducing the decrease of the inner surface area), we carried out two additional sets of experiments. In the first set, we avoided the initial osmotic gradient due the urea by adjusting the sugar concentration (required by the phase transfer method) in the outer solution. In this case, we observed no division, which means that pH change itself cannot produce a division of GUVs. Similarly, we observed no division if the induction time (clock time) of the enzymatic reaction was set to ~ 4 min by increasing the concentration of the acetic acid (1 mM) (reducing the initial pH) inside the vesicles even if the initial osmotic concentration gradient was present. From these observations, we can draw the conclusion that neither the osmotic concentration gradient (responsible for the volume loss) nor the pH change (responsible for the decrease of the inner surface area) alone can induce division. They must act in synergy, approximately at the same time scale.

Conclusions

We presented a simple autonomous internally triggered self-dividing system based on the fission of mixed giant unilamellar vesicles. Unlike previous approaches, the stimulus driving the division process is generated inside the lumen of the vesicles and triggered by cross-membrane transport. Also, the basic chemistry involved in our experiments and the type of membrane-forming amphiphiles render this system a plausible model for studying the self-division process of protocells under prebiotic conditions.

Experimental

Materials

For the enzymatic reaction, stock solutions were prepared of acetic acid (Carlo Erba), urea (Sigma), and urease (Sigma, Type III, from Jack Beans, typically 34310 units/g solid). Glucose and sucrose (Sigma) were used to adjust the density of the solutions for the vesicles preparation, pyranine was chosen for monitoring the pH changes. POPC (Lipoid) and oleic acid (HOA, Sigma) stock solutions were

prepared in mineral oil (Sigma M5904). All the reactants were used as received without any further purification. The solutions of urease, sucrose, glucose and oleic acid were freshly prepared daily.

Preparation of the vesicles.

Giant vesicles made of POPC and HOA were prepared using the “droplet (phase) transfer” method^{39–41}. An Eppendorf tube was filled with 500 μL of an aqueous phase, the so-called outer solution (O-solution) containing 200 mM of glucose and 10^{-3} mM of acetic acid and 300 μL of an interfacial phase ([POPC] = 2.6 mM and [HOA] = 2.4 mM in mineral oil). The interface was settled for 10–15 minutes.

A second Eppendorf tube was used to prepare a water/oil microemulsion. 20 μL of an aqueous solution, the so-called inner solution (I-solution): 200 mM of sucrose, urease 0.5 U/mL, 1×10^{-3} mM of acetic acid and 50 μM of pyranine solutions were mixed by pipetting up and down with 600 μL of an oil phase ([POPC] = 2.6 mM and [HOA] = 2.4 mM in mineral oil). This microemulsion was poured over the first Eppendorf tube. The formation of vesicles was facilitated by centrifuging the tube at 6000 rpm for 10 minutes at room temperature ($\sim 22^\circ\text{C}$).

After the centrifugation step a white pellet was visible at the bottom of the Eppendorf tube. The oil phase and the aqueous phase were carefully removed with a micropipette. The pellet was gently washed with 100 μL of O-solution to remove free solutes. 30 μL of pellet were finally resuspended in 60 μL of O-solution.

Observation of the vesicles and their self-division

20 μL of the final diluted solution were placed into a well of a multiwell plate letting the vesicles deposit on the support for few minutes. 10 μL of a solution containing 180 mM urea ($[\text{urea}]_0 = 60$ mM), 200 mM glucose and 1×10^{-3} mM acetic acid were added to trigger the division. The urea permeates through the lipid bilayer and it is converted into ammonia. After this addition we covered the multiwell plate with a lid in order to avoid the evaporation of the sample.

The number and the size of the vesicles was investigated by an epifluorescence microscope (ORMATEK TL-INV 100). Images were taken every 0.5 s by a CMOS camera (PIXELINK PL-D755CU) both in visible and in fluorescence ($\lambda_{\text{ex}} = 450$ nm and $\lambda_{\text{em}} = 510$ nm) mode. Fluorescence intensity was used to characterize the pH change inside the vesicles. Recorded images were analyzed by means of ImageJ software⁵³.

Calibration of the pH based on the fluorescence intensity. A calibration procedure was performed to relate the fluorescence intensity of pyranine, calculated as grey-scale level of the images, with the pH-values of the system. The calibration was performed by preparing a series of vesicles containing different buffers (using sodium phosphate monobasic dihydrate (Sigma-Aldrich) and sodium phosphate dibasic heptahydrate (Sigma-Aldrich)) in the range of pH 5.5 and 7.5 (Figure S4).

FRAP experiments

In FRAP experiments, the same experimental protocol was applied except that the pyranine was replaced with fluorescein because the latter fluorescent dye is more sensitive to photobleaching. Samples were characterized by confocal laser scanning microscopy with Leica SP8 X. Images were recorded with HC PL APO CS2 40x/1.30 OIL objective. Line 488 of an argon laser was used as excitation source while green fluorescence emission was recorded in the range 500–600 nm. Internal GUV photobleaching was obtained zooming in the target vesicle lumen and harvesting the sample until the

fluorescence disappeared. Then, images were recorded every 30 seconds with xyt scan mode.

Conflicts of interest

There are no conflicts to declare.

Acknowledgements

This study was supported by National Research, Development and Innovation Office of Hungary (NN125752 and K131425) and the BME-Nanotechnology FIKP grant of EMMI (BME FIKP-NAT). FR gratefully acknowledges the University of Salerno for supporting this work through the projects ORSA174250 and ORSA167988. FR and ZM gratefully acknowledge the COST action CM1304 “Emergence and Evolution of Complex Chemical Systems” for funding a Short Term Scientific Mission. Prof. Pasquale Stano is gratefully acknowledged for fruitful discussions.

Notes and references

- P. L. Luisi, *The Emergence of Life: From Chemical Origins to Synthetic Biology*, Cambridge University Press, Cambridge, U.K., 2006.
- P. Luisi, F. Ferri and P. Stano, *Naturwissenschaften*, 2006, **93**, 1–13.
- P. Stano and P. L. Luisi, *Chem. Commun.*, 2010, **46**, 3639–3653.
- P. Stano, G. Rampioni, F. D’Angelo, E. Altamura, F. Mavelli, R. Marangoni, F. Rossi and L. Damiano, in *Advances in Bionanomaterials*, Springer, Cham, 2018, pp. 141–154.
- J. W. Szostak, D. P. Bartel and P. L. Luisi, *Nature*, 2001, **409**, 387–390.
- D. Segre, D. Ben-Eli, D. W. Deamer and D. Lancet, *Origins Life Evol. B.*, 2001, **31**, 119–145.
- P. L. Urban, *New J. Chem.*, 2014, **38**, 5135–5141.
- K. Kurihara, Y. Okura, M. Matsuo, T. Toyota, K. Suzuki and T. Sugawara, *Nat. Commun.*, 2015, **6**, 8352.
- P. Walde, K. Cosentino, H. Engel and P. Stano, *ChemBioChem*, 2010, **11**, 848–865.
- A. Küchler, M. Yoshimoto, S. Luginbühl, F. Mavelli and P. Walde, *Nat. Nanotechnol.*, 2016, **11**, 409–420.
- E. Altamura, F. Milano, R. R. Tangorra, M. Trotta, O. H. Omar, P. Stano and F. Mavelli, *PNAS*, 2017, **114**, 3837–3842.
- K. Ruiz-Mirazo, C. Briones and A. de la Escosura, *Chem. Rev.*, 2014, **114**, 285–366.
- L. Jin, N. P. Kamat., S. Jena and J. W. Szostak, *Small*, 2018, **14**, 1704077.
- K. Morigaki and P. Walde, *Curr. Opin. Colloid Interface Sci.*, 2007, **12**, 75–80.
- P. L. Luisi and P. Walde, *Giant Vesicles*, Wiley-Interscience, Chichester, UK, 2000.
- P. L. Luisi and F. J. Varela, *Origins Life Evol. B.*, 1989, **19**, 633–643.
- P. A. Bachmann, P. Walde, P. L. Luisi and J. Lang, *J. Am. Chem. Soc.*, 1990, **112**, 8200–8201.
- P. A. Bachmann, P. L. Luisi and J. Lang, *Nature*, 1992, **357**, 57–59.
- P. Walde, R. Wick, M. Fresta, A. Mangano and P. L. Luisi, *J. Am. Chem. Soc.*, 1994, **116**, 11649–11654.
- N. Berclaz, M. Müller, P. Walde and P. L. Luisi, *J. Phys. Chem. B*, 2001, **105**, 1056–1064.

- 21 P. Stano, E. Wehrli and P. L. Luisi, *J. Phys.: Condens. Matter*, 2006, **18**, S2231–S2238.
- 22 J. Käs and E. Sackmann, *Biophys J*, 1991, **60**, 825–844.
- 23 K. Takakura, T. Toyota and T. Sugawara, *J. Am. Chem. Soc.*, 2003, **125**, 8134–8140.
- 24 T. Baumgart, S. T. Hess and W. W. Webb, *Nature*, 2003, **425**, 821–824.
- 25 T. Toyota, K. Takakura, Y. Kageyama, K. Kurihara, N. Maru, K. Ohnuma, K. Kaneko and T. Sugawara, *Langmuir*, 2008, **24**, 3037–3044.
- 26 T. F. Zhu and J. W. Szostak, *J. Am. Chem. Soc.*, 2009, **131**, 5705–5713.
- 27 P. Peterlin, V. Arrigler, K. Kogej, S. Svetina and P. Walde, *Chem. Phys. Lipids*, 2009, **159**, 67–76.
- 28 K. Kurihara, M. Tamura, K.-I. Shohda, T. Toyota, K. Suzuki and T. Sugawara, *Nat. Chem.*, 2011, **3**, 775–781.
- 29 Y. Sakuma and M. Imai, *Phys. Rev. Lett.*, 2011, **107**, 198101.
- 30 J. Dervaux, V. Noireaux and A. J. Libchaber, *Eur. Phys. J. Plus*, 2017, **132**, 284.
- 31 M. Fiore, O. Maniti, A. Girard-Egrot, P.-A. Monnard and P. Strazewski, *Angew. Chem. Int. Ed.*, 2018, **57**, 282–286.
- 32 M. Kurisu, H. Aoki, T. Jimbo, Y. Sakuma, M. Imai, S. Serrano-Luginbühl and P. Walde, *Commun. Chem.*, 2019, **2**, 117, 1–10.
- 33 J. M. Castro, H. Sugiyama and T. Toyota, *Sci. Rep.*, 2019, **9**, 165.
- 34 B. Novák and J. J. Tyson, *Nat. Rev. Mol. Cell Biol.*, 2008, **9**, 981–991.
- 35 T. Litschel, B. Ramm, R. Maas, M. Heymann and P. Schwille, *Angew. Chem. Int. Ed.*, 2018, **57**, 16286–16290.
- 36 K. Ikari, Y. Sakuma, T. Jimbo, A. Kodama, M. Imai, P.-A. Monnard and S. Rasmussen, *Soft Matter*, 2015, **11**, 6327–6334.
- 37 B. Krajewska, *J. Mol. Catal. B Enzym.*, 2009, **59**, 9–21.
- 38 G. Hu, J. A. Pojman, S. K. Scott, M. M. Wrobel and A. F. Taylor, *J. Phys. Chem. B*, 2010, **114**, 14059–14063.
- 39 S. Pautot, B. J. Frisken and D. A. Weitz, *Langmuir*, 2003, **19**, 2870–2879.
- 40 P. Stano, T. P. de Souza, P. Carrara, E. Altamura, E. D'Aguzzo, M. Caputo, P. L. Luisi and F. Mavelli, *Mech. Adv. Mater. Struct.*, 2015, **22**, 748–759.
- 41 Y. Miele, T. B. Jr, A. F. Taylor, P. Stano and F. Rossi, in *Advances in Artificial Life, Evolutionary Computation and Systems Chemistry*, eds. F. Rossi, F. Mavelli, P. Stano and D. Caivano, Springer International Publishing, 2016, pp. 197–208.
- 42 Y. Miele, T. Bánsági, A. F. Taylor and F. Rossi, in *Advances in Bionanomaterials*, eds. S. Piotto, F. Rossi, S. Concilio, E. Reverchon and G. Cattaneo, Springer International Publishing, Cham, 2018, pp. 63–74.
- 43 A. Walter and J. Gutknecht, *J. Membr. Biol.*, 1986, **90**, 207–217.
- 44 C. François-Martin, J. E. Rothman and F. Pincet, *PNAS*, 2017, **114**, 1238–1241.
- 45 S. Morlot, V. Galli, M. Klein, N. Chiaruttini, J. Manzi, F. Humbert, L. Dinis, M. Lenz, G. Cappello and A. Roux, *Cell*, 2012, **151**, 619–629.
- 46 F. Kamp and J. A. Hamilton, *PNAS*, 1992, **89**, 11367–11370.
- 47 K. Lähdesmäki, O. H. S. Ollila, A. Koivuniemi, P. T. Kovanen and M. T. Hyvönen, *BBA - Biomembranes*, 2010, **1798**, 938–946.
- 48 M. P. Sheetz and S. J. Singer, *PNAS*, 1974, **71**, 4457–4461.
- 49 S. Svetina and B. Žekš, *Eur. Biophys. J.*, 1989, **17**, 101–111.
- 50 U. Seifert, K. Berndl and R. Lipowsky, *Phys. Rev. A*, 1991, **44**, 1182–1202.
- 51 U. Seifert, *Adv. Phys.*, 1997, **46**, 13–137.
- 52 L. Miao, U. Seifert, M. Wortis and H.-G. Döbereiner, *Phys. Rev. E*, 1994, **49**, 5389–5407.
- 53 C. A. Schneider, W. S. Rasband and K. W. Eliceiri, *Nat. Methods*, 2012, **9**, 671–675.

Paper IV

On the Origin and Consequences of High DMAEMA Reactivity Ratio in ATRP Copolymerization with MMA: An Experimental and Theoretical Study[#]

Massimo Mella ¹, Mario Vincenzo La Rocca ¹, Ylenia Miele,² Lorella Izzo ^{2*}

¹Dipartimento di Scienza ed Alta Tecnologia, Università degli Studi dell'Insubria, via Valleggio 9, Como 22100, Italy

²Dipartimento di Chimica e Biologia, Università degli Studi di Salerno, Via Giovanni Paolo II, 132, 84084 Fisciano, Italy

Correspondence to: M. Mella (E-mails: massimo.mella@uninsubria.it or mellamax@gmail.com) or L. Izzo (E-mail: lorella.izzo@uninsubria.it)

Received 4 January 2018; accepted 16 March 2018; published online 00 Month 2018

DOI: 10.1002/pola.29017

ABSTRACT: Designing and tuning a copolymerization process to obtain specific material properties is still fundamentally empirical and requires the determination of apparent reactivity ratios r^s . To this end, PEG-(MMA-DMAEMA)_n copolymers obtained via ATRP of MMA and DMAEMA using a PEG-based initiator in toluene were analyzed to extract monomer relative reactivities; the impact of changing solvent on the latter was also tested. Differing from previous free radical and controlled radical copolymerizations (CRCoP), we found that DMAEMA is preferentially included ($r_{\text{MMA}}^s = 0.36(\pm 10\%)$ and $r_{\text{DMAEMA}}^s = 2.76(\pm 15\%)$) in toluene; increasing the solvent polarity decreased the gap between r^s . With these data, kMC simulations based on the copolymerization *terminal model* were used to investigate copolymer microstructure, which is not amenable to NMR investigation. kMC

simulations evidenced both a gradient-like nature of the copolymers and a somewhat unexpected qualitative change in the probability of finding MMA-rich triads along the chain depending on initial feed composition. An additional DFT analysis suggested the likely formation of a DMAEMA:CuBr:2-2'-bipyridine complex, which being involved in the regeneration of reactive radicals from dormant species, is expected to locally increase DMAEMA concentration favoring its addition to the growing chains. The formation of such complex is also supported by ¹H-NMR experiments. © 2018 Wiley Periodicals, Inc. *J. Polym. Sci., Part A: Polym. Chem.* **2018**, *00*, 000–000

KEYWORDS: ATRP; copolymer; DMAEMA; DFT; kinetic Monte Carlo; MMA; polyelectrolyte; reactivity ratio

INTRODUCTION Tailored polymers with controlled physical and chemical properties are attractive for a variety of applications in the fields of biotechnology and nanotechnology, so that the demand in macromolecular synthesis precision to obtain macromolecules with specific architecture, composition and functionality is continuously increasing. This applies especially to copolymerization processes, which, implying the simultaneous polymerization of different monomers, are the most used to obtain property-oriented engineered materials through techniques such as ionic, radical, and metathesis reactions. For these, however, improving the control over all aspects characterizing the monomer distributions along the

copolymer chain still remains a worthy goal, as this would allow one to impose specific physical properties to the final material with better precision. To exemplify the importance of the latter issue, at least for biomedical related applications, we recall that both macroscopic (e.g., amount and nature of hydrophobic pendants^{1,2}) and subtler (e.g., stereo-regularity³) features strongly affected the conformation of polymers in solution and consequently the solubility, transport, and protection of drugs that need to reach an intracellular target.

With this in mind, two of the Authors have recently provided quantitative indications on how varying a chain composition

*Present Address: Lorella Izzo, Dipartimento di Biotecnologie e Scienze della Vita, Università degli Studi dell'Insubria, via J.H. Dunant 3, 21100 Varese, Italy.

[#]L. I. and M. M. conceived and designed the experiments and modeling approach; L. I. and Y. M. performed the polymerization and NMR experiments, and M. M., M. V. L. R., and L. I. analyzed the data; L. I., M. V. L. R., and M. M. carried out the electronic structure calculations; M. M. analyzed the latter calculations; M. V. L. R. and M. M. wrote the Kinetic Monte Carlo (KMC) code, carried out the KMC simulations, and analyzed their results. L. I., M. V. L. R., and M. M. wrote the article.

Additional Supporting Information may be found in the online version of this article.

© 2018 Wiley Periodicals, Inc.

may impact on physico-chemical properties of copolymers specifically designed to act as antimicrobials at the nanoscale level^{4,5} and presenting a combined “block(b)-random(ran)” structure of the kind $A-b-(B\text{-}ran\text{-}C)_n$ (A = poly(ethylene glycol) monomethyl ether, mPEG; B = methylmethacrylate, MMA; C = alkyl aminoethyl methacrylate, AAEMA; n = 1, 2, or 4). These copolymers, obtained via a classic ATRP process using a catalyst based on Cu/bipyridine in toluene, demonstrated that small variations in chemical composition may be fundamental in defining the amount of surface charge responsible for their antimicrobial activity. Notably, it was suggested that the amount of AAEMA in plaques formed by the above reported copolymers influenced the probability of forming charged strong hydrogen bonds (C—H bonds) between protonated and unprotonated amino pendant-group. As C—H bond interactions are possible only between AAEMAs pendant groups that are first or second neighbors due to geometrical constraints, the plaque surface charge may also depend on the distribution of comonomers along the chains; this observation stresses the important role that may be played by the chain microstructure.

The latter issue may be of particular relevance for the short mPEG-*b*-(MMA-*ran*-dimethyl aminoethyl methacrylate (DMAEMA)) chains that were found to form polymersomes and, hence, studied as pH-sensitive drug delivery systems in solution due to their polyelectrolytic behavior. Indeed, it was found that the amount of DMAEMA in the copolymer backbone controlled the extent of polymersomers swelling induced by a decrease in solution pH^{6,7} and due to the protonation of the basic pendants. It can also impact on the stability of the swollen aggregates, reducing the amount of polyelectrolytes dispersed in the human body. Once again, controlling comonomers distribution may turn out to be key in tailoring properties.

Of direct relevance for the control that can be exerted on mPEG-*b*-(MMA-*ran*-AAEMA) copolymer microstructure, we recall that living anionic polymerization and controlled radical polymerization (CRP) techniques allowed the preparation of unprecedented microstructures such as multiblock copolymers or gradient copolymers.^{8–11} In these cases, attempts to produce tailor-made microstructures relied either on the controlled sequential addition of comonomers during the copolymerization process, or on the choice of comonomers with very different reactivity ratios, r_1 and r_2 , as in the case of styrene/butadiene copolymers obtained via living anion processes.^{12,13} Indeed, the latter scenario may even produce a copolymer with properties similar to the ones of a homopolymer at the beginning of the chain, which gradually includes more and more of the least reactive monomer. As far as our copolymers are concerned, this, however, did not seem to be the case, with previous literature on MMA/DMAEMA copolymers (*vide infra*^{14–17}) leading two of the Authors to believe that $r_{\text{MMA}} \simeq r_{\text{DMAEMA}} \sim 1$, and that copolymers should be expected to present a random comonomer distribution. Such idea was also supported by considerations on the similar electronic structure of the reactive functional groups and the lack of strong intermolecular forces between monomers.

At variance with such expectations, a strong preferential inclusion of DMAEMA with respect to MMA in the growing chain was instead found in the experimental conditions adopted, so that we were forced to employ high MMA/DMAEMA feed ratio to obtain a copolymer composition appropriate for the intended applications. A second, and we feel the most important, consequence springing from the difference in reactivity between MMA and DMAEMA is, of course, that the microstructure is likely to substantially deviate from the one of a random copolymer, the more rapidly polymerizing monomer possibly forming highly concentrated sequences of some length. Given the possible formation of C—H bonds between neighboring pendants along the chain, it would therefore be of interest to understand the dependence of the probability of finding a chosen monomer at a specific position along the chain, which correlates directly with its reaction probability (or rate) at a specific time during the polymerization, and the experimental conditions. Approaching this task from the experimental point of view was, however, made complicate by the inability of NMR to discriminate between different triads.

To reach a deeper understanding of the chemical behavior in ATRCopolymerization (ATRCop) of MMA and DMAEMA for the task of producing materials with better tailored features, in this paper we evaluate the reactivity ratios (r_{MMA} and r_{DMAEMA}) of the two monomers enlarging the set of available ATRP synthesized species obtained at different feed compositions. Apart from quantifying the relative monomer reactivity, these ratios allowed to stochastically simulate the copolymerization reactions within the framework of the “terminal model,”¹⁸ thus providing a complete representation of the chain microstructural details “in lieu” of the lacking NMR data. In the attempt of understanding the origin of the difference in behavior between the copolymerizations discussed in the literature and our results, we also employed density functional theory (DFT) electronic structures calculations to estimate reaction rates and the possible formation of dimers between monomers, growing radical chains, and catalysts. In the latter respect, we notice, however, that the chemical nature of the monomers does not suggest the presence of strong chemically specific interactions, so that only weak intermolecular or ligation forces should be expected to play a role, if any.

EXPERIMENTS, METHODS, AND MODELS

Polymers Synthesis

Materials

Poly(ethylene glycol) monomethylether (mPEG) (M_n = 2000 Da, M_w/M_n = 1.16), benzaldehyde dimethyl acetal, 2,2-Bis(hydroxymethyl)propionic acid, p-toluenesulfonic acid monohydrate (TsOH), acetone, *N,N'*-dicyclohexylcarbodiimide (DCC), 4-(dimethylamino)pyridine (DMAP), methanol, Pd/C 10%, 2-bromoisobutyryl bromide (BMPB), triethylamine (TEA), diethyl ether, ethanol, CuBr, 2,2'-bipyridine (bpy), chloroform and Al₂O₃ were purchased by Aldrich and used without any further purification.

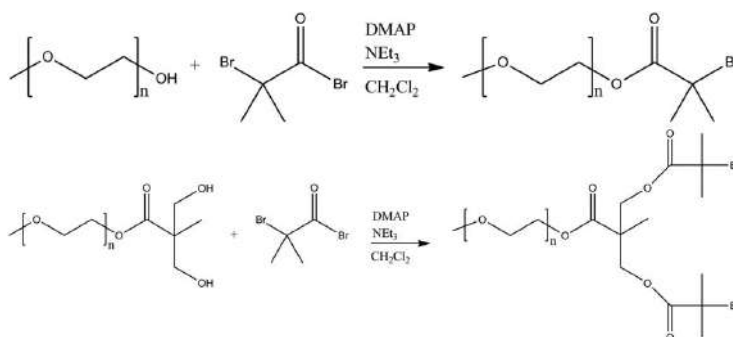


FIGURE 1 Chemical schemes for the synthesis of mPEG-Br linear (top) and mPEG-Br₂ (bottom) macro initiators.

All manipulations involving air-sensitive compounds were carried out under nitrogen atmosphere using Schlenk or dry-box techniques. Toluene (Aldrich) was dried over sodium and distilled before use. CH₂Cl₂ (Carlo Erba), methylmethacrylate (MMA) and 2-(dimethylamino)ethyl methacrylate (DMAEMA) (Aldrich) were dried over CaH₂ and then distilled, the latter under a reduced pressure of nitrogen.

Gel Permeation Chromatography (GPC)

The polydispersity index of copolymers has been evaluated by GPC.

GPC chromatograms were recorded on a system equipped with a Waters 1525 binary pump, a Waters 2414 RI detector and four styragel columns (range 10³–10⁶ Å). The measurements were carried out at 25 °C, using THF as eluent (1.0 mL min⁻¹) and narrow dispersity polystyrene standards as references.

NMR Analysis

Spectra were recorded on a Bruker Avance 400 MHz spectrometer at 25 °C with D1 = 3 s. The samples were prepared by introducing 20 mg of sample in 0.5 mL of CDCl₃ into a tube (0.5 mm outer diameter). TMS was used as internal reference.

Preparation of mPEG-Br Linear, mPEG-Br₂, and mPEG-Br₄ Branched Macroinitiators

mPEG-Br linear macroinitiator was synthesized according to the literature procedure starting from mPEG-OH (see Fig. 1 for the chemical schemes).¹⁹

For the preparation of mPEG-Br₂ and mPEG-Br₄ macroinitiators, first mPEG-OH₂ and mPEG-OH₄ were synthesized according to the literature procedure and characterized by ¹H NMR.¹⁹ In a typical procedure, mPEG-OH₂ (1.25 g, 0.59 mmol; 1 equiv) was dissolved, under nitrogen atmosphere, in 15 mL of dry CH₂Cl₂ into a 100 mL two neck round-bottom flask equipped with condenser, dropping funnel and magnetic stirrer. Then 0.22 g of DMAP (1.77 mmol) and 0.12 mL of TEA (0.88 mmol) were added and the reactor was thermostated at 0 °C. After cooling, 0.36 mL of BMPB

(2.95 mmol; 5 equiv) in 5 mL of dry CH₂Cl₂ were added dropwise during 1h. Subsequently the temperature was allowed to raise to room temperature and the reaction was continued under stirring for further 24 h. The solution was filtered and the product was precipitated in cold diethyl ether, filtered, washed with cold ethanol, and dried in vacuum.

mPEG-Br₂ (Yield : 66%). ¹H NMR(400 MHz, CDCl₃)
: δ1.91 (s, CO(CH₃)₂Br); 3.70–3.91 (bs, -CH₂-, mPEG);

mPEG-Br₄ (Yield : 63%). ¹H NMR(400 MHz, CDCl₃)
: δ1.91 (s, CO(CH₃)₂Br); 3.70–3.91 (bs, -CH₂-, mPEG).

Preparation of mPEG-*b*-(PMMA-Ran-PDMAEMA) Linear, mPEG-*b*-(PMMA-ran-PDMAEMA)₂ and mPEG-*b*-(PMMA-Ran-PDMAEMA)₄ Copolymers by ATRP

mPEG-*b*-(PMMA-ran-PDMAEMA) linear copolymer was synthesized in toluene at 90 °C (see Fig. 2 for the chemical schemes). The reaction was carried out in a 50 mL glass flask charged, under nitrogen atmosphere, with 0.1 g of mPEG-Br linear macroinitiator in 15 mL of dry toluene. After the dissolution of the macroinitiator, 0.013 g of CuBr, 0.03 g of bpy, 5 mL of MMA, and 0.5–3.5 mL of DMAEMA (depending on the initial feed ratio $q_0 = f_{\text{MMA}}/f_{\text{DMAEMA}}$, f being the molar fraction) were added. The mixture was thermostated at 90 °C and magnetically stirred. The reaction was stopped with *n*-hexane after 18 h. The copolymer was recovered, dissolved in the minimum amount of chloroform and passed over a column of activated Al₂O₃ to remove the catalyst. The solution was dried in vacuum, and the polymer was washed with cold methanol and then dried.

mPEG-(PMMA-ran-PDMAEMA)₂ and mPEG-(PMMA-ran-PDMAEMA)₄ copolymers were synthesized using a molar ratio mPEG-Br₂/CuBr/bpy = 1/4/8 and mPEG-Br₄/CuBr/bpy = 1/8/16, respectively. Notice that larger than stoichiometric amounts of CuBr and bpy were used to increase the copolymer yields, which were found low when employing the 1/1/2 ratio per initiation site. For copolymerizations carried out in acetonitrile, DMF and toluene, 2.0 mL of MMA and 1.2 mL of

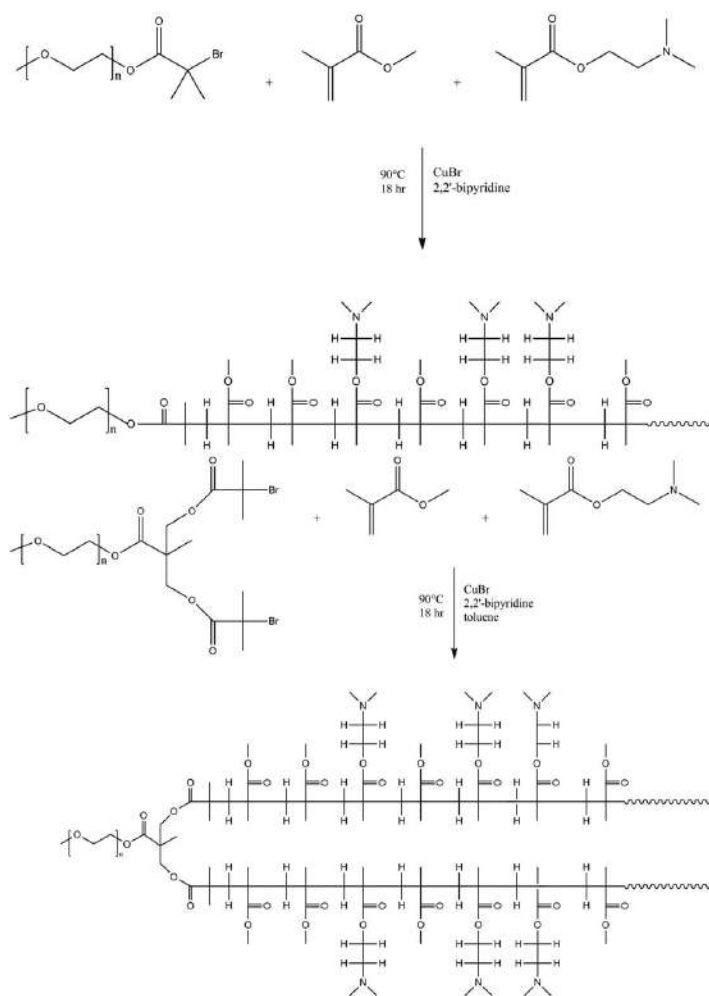


FIGURE 2 Chemical schemes for the synthesis of mPEG-*b*-(PMMA-*ran*-PDMAEMA) linear (top) and mPEG-*b*-(PMMA-*ran*-PDMAEMA)₂ (bottom) via ATRP.

DMAEMA were used. The reaction temperature was set at 60 °C and the polymerization stopped after 4 h.

¹H-NMR (400 MHz, CDCl₃): δ 0.87–1.03(CH₃ main chain), 1.83–1.91 (CH₂ main chain), 2.30 (–N(CH₃)₂), 2.58 (–O–CH₂–CH₂–N(CH₃)₂), 3.61 (–OCH₃), 3.61(–OCH₂CH₂–), 4.08 (–O–CH₂–CH₂–N(CH₃)₂). ¹³C-NMR (400 MHz, CDCl₃): δ 16.9–19.1 (CH₃ main chain), 44.9–45.3 (quaternary carbon in the main chain), 46.2 (–N(CH₃)₂), 52.2 (–OCH₃, MMA), 54.6 (CH₂ main chain), 57.6 (–O–CH₂–CH₂–N(CH₃)₂), 63.5 (–O–CH₂–CH₂–N(CH₃)₂), 70.9 (–OCH₂–CH₂–), 176.3–178.2 (–C=O).

Typical ¹H-NMR and ¹³C-NMR spectra for a linear species are shown in Figure 3 together with a chemical scheme indicating the assignment of each signal. Notice the partial

overlap between the ¹H-NMR signals of the methoxyl group (c) in MMA and the methylenic group (a) in mPEG. Occasionally, also an overlap between the methyl groups in the amino group (h) and the quaternary carbon atoms in the chain (d) appears in the ¹³C-NMR spectrum. Due to the overlaps just mentioned, we were forced to estimate the degrees of polymerization (*DP*'s) and *X*'s from the ¹³C-NMR spectrum, often using c and f signals. In this respect, the relative accuracy of the ¹³C-NMR derived results was tested against ¹H-NMR data obtained from (PMMA-*ran*-PDMAEMA) species (more details are provided in Supporting Information, Figs. 1 and 2), which are free of the overlaps between mPEG and MMA signals. In general, *X*_{MMA} estimates obtained from the H and C atoms differed by roughly 0.01.

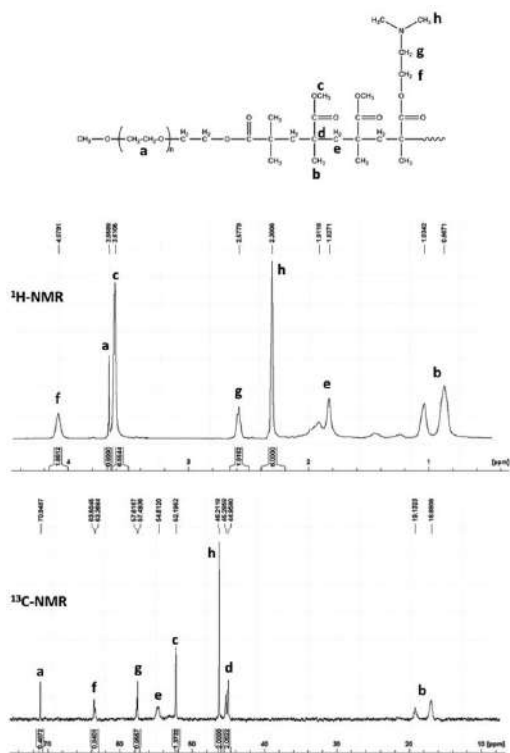


FIGURE 3 Chemical scheme for mPEG-*b*-(PMMA-*ran*-PDMAEMA) (top); ^1H -NMR (middle) and ^{13}C -NMR (bottom) spectra with signal assignments referring to labels in the top chemical scheme.

The molar mass of copolymers has been determined by the degree of polymerization (DP) as evaluated from ^{13}C -NMR, by the molar mass of monomers (MM) and by the signal intensities (I):

$$M_n = \text{DP}_{\text{mPEG}}(\text{MM}_{\text{EO}}) + \text{DP}_{\text{MMA}}(\text{MM}_{\text{MMA}}) + \text{DP}_{\text{DMAEMA}}(\text{MM}_{\text{DMAEMA}}) \quad (1)$$

where

$$\begin{aligned} \text{DP}_{\text{mPEG}} &= M_n(\text{mPEG})/44; \\ \text{DP}_{\text{MMA}} &= \text{DP}_{\text{mPEG}}(2I_{\text{MMA}}/I_{\text{mPEG}}); \\ \text{DP}_{\text{DMAEMA}} &= \text{DP}_{\text{mPEG}}(\alpha I_{\text{DMAEMA}}/I_{\text{mPEG}}) \end{aligned} \quad (2)$$

I_{mPEG} is the integration of the signal relative to mPEG units: $-\text{OCH}_2\text{CH}_2-$; I_{MMA} is the integration of the signal relative to MMA units: $-\text{OCH}_3$; I_{DMAEMA} is the integration of methyl group of the signal relative to DMAEMA units: if $-\text{N}(\text{CH}_3)_2$ signal is used, $\alpha = 1$; if $-\text{OCH}_2-\text{CH}_2-\text{N}$ is instead used, $\alpha = 2$.

Analogously, the monomers content of copolymers were calculated using the following equations:

$$X_{\text{mPEG}} \approx \frac{I_{\text{mPEG}}}{I_{\text{mPEG}} + 2I_{\text{MMA}} + \alpha I_{\text{DMAEMA}}} \quad (3)$$

$$X_{\text{MMA}} \approx \frac{2I_{\text{MMA}}}{I_{\text{mPEG}} + 2I_{\text{MMA}} + \alpha I_{\text{DMAEMA}}} \quad (4)$$

$$X_{\text{DMAEMA}} \approx \frac{\alpha I_{\text{DMAEMA}}}{I_{\text{mPEG}} + 2I_{\text{MMA}} + \alpha I_{\text{DMAEMA}}} \quad (5)$$

Modeling Approach and Electronic Structure Calculations

From the kinetic standpoint, describing the copolymerization of two monomers requires, at least, the knowledge of the kinetic rate constants for the reaction between two possible radical sites (one for each last entered monomer, MMA or DMAEMA) at the end of a growing chain and each of the two acrylic species. Indicating these quantities as k_{ij} (i being the monomer bearing the unpaired electron at the end of the chain and j the species that shall be added from the solution), it is customary to define reactivity ratios ($r_{\text{MMA}} = k_{\text{MMA,MMA}}/k_{\text{MMA,DMAEMA}}$, and $r_{\text{DMAEMA}} = k_{\text{DMAEMA,DMAEMA}}/k_{\text{DMAEMA,MMA}}$), from which details of the statistical microstructure and composition can be inferred. To do this, two independent transition probabilities can be defined from the reactivity ratios so that chain propagation is fully described by such quantities within the boundary imposed by the “terminal model,” that is

$$\begin{aligned} p_{\text{MMA,DMAEMA}} &= (1 + r_{\text{MMA}}q)^{-1} \text{ and } p_{\text{DMAEMA,MMA}} \\ &= \left(1 + \frac{r_{\text{DMAEMA}}}{q}\right)^{-1} \text{ with } q = \frac{[\text{MMA}]}{[\text{DMAEMA}]} \end{aligned} \quad (6)$$

thanks to the normalization conditions. Here, q is the instantaneous ratio between MMA and DMAEMA molar concentrations; where needed, we shall indicate the initial MMA/DMAEMA ratio as q_0 .

To exploit the definition of the two probabilities in eq 6 to investigate microstructural details of the copolymers, one thus needs to come up with an estimate for r_{MMA} and r_{DMAEMA} . To experimentally achieve this goal, it is enough to recall that copolymerization equation can be expressed in terms of the mole fraction (f_{MMA} and f_{DMAEMA}) of monomers MMA and DMAEMA in the feed, and mole fractions (F_{MMA} and F_{DMAEMA}) of monomers in the copolymer. Assuming a constant composition of the feed during the copolymerization (e.g., when copolymers are formed at very low conversion), the kinetic expressions can be combined to give

$$F_1 = \frac{r_1 f_1^2 + f_1 f_2}{r_1 f_1^2 + 2f_1 f_2 + r_2 f_2^2} \text{ or } \frac{F_1}{F_2} = \frac{f_1(r_1 f_1 + f_2)}{f_2(r_2 f_2 + f_1)} \quad (7)$$

($f_1 = f_{\text{MMA}}$ and $f_2 = f_{\text{DMAEMA}}$ for the sake of notation simplicity). Thus, with copolymer compositions obtained using different feed ratios, one may estimate the two reactivity ratios via nonlinear fitting of the parameters in eq 7. As for this, attention has to be paid in choosing the appropriate set of feed conditions,²⁰ and to the nonlinear fitting approach employed to avoid artifacts.²¹

If r_{MMA} and r_{DMAEMA} differ from one, or a monomer has a very low initial $f((f)_0)$, the comonomer feed changes in composition as one of the monomers preferentially enters the copolymer or quickly disappears due to its low initial quantity; thus, to determinate the instantaneous copolymer composition as a function of feed conversion, one must resort to an integrated form of the copolymerization equation. The final result of the mathematical analysis for such process relates the instantaneous comonomer feed composition to the degree of monomer conversion $\left(\frac{M}{M_0}\right)$ via:

$$1 - \frac{M}{M_0} = 1 - \left[\frac{f_1}{(f_1)_0} \right]^{\frac{r_2}{(1-r_2)}} \left[\frac{f_2}{(f_2)_0} \right]^{\frac{r_1}{(1-r_1)}} \left[\frac{(f_1)_0 - \frac{(1-r_2)}{(2-r_2-r_1)}}{f_1 - \frac{(1-r_2)}{(2-r_2-r_1)}} \right]^{\frac{(1-r_1)r_2}{(1-r_1)(1+r_2)}} \quad (8)$$

Noteworthy, it is the fact that fitting “feed composition versus conversion” data by selecting r_1 and r_2 to minimize the least square error between the latter and eq 8 may require sophisticated statistical approaches.²¹

Once the values for $p_{\text{MMA,DMAEMA}}$ and $p_{\text{DMAEMA,MMA}}$ become available, one may set up a stochastic simulation capable of describing all orders of correlations between monomers in the copolymer, as well as their time evolution while q changes. As using such an approach would also allow us to easily investigate composition fluctuations (our chains are relatively short) besides microstructural details (e.g., triads), we set as our task to implement an efficient kinetic Monte Carlo (kMC) code to obtain the needed results (*vide infra* Section 2.3).

Returning to the kinetic constants needed to define the reactivity ratios, these can, in principle, be obtained via electronic structure modeling assuming the validity of Transition State Theory²² (TST) in its harmonic oscillator approximation²³ (HTST). For convenience, we adopt the Eyring's style-approach,²⁴ which requires estimating TS Gibbs' energy barriers, ΔG^\ddagger . The latter are commonly computed as difference between G 's for the TS and asymptotic (i.e., at infinite distance) reactants. As for the latter, we modeled the terminal radical of the growing chains adding a methyl radical to MMA or DMAEMA so to generate a tertiary radical, which would then be made to react with both monomeric species. Notice that the tertiary radical is expected to be more stable than the alternative secondary counterparts, and hence more rapidly formed during chain propagation. With respect to this choice, we also mention that one could avoid study the very first chain propagation act, namely the reaction between the initiator and a monomer, within the framework of the *terminal model*. This possibility derives from the fact that only the very last enchainment monomer has an impact on the chain propagation, *de facto* forcing the whole process to “loose memory” of such first act.

In our case, energies and frequencies needed for estimating kinetics constants were obtained employing DFT at the B3LYP/6-31++g(d,p) level of theory; we also tested a few cases employing the B3LYP/6-311++G(2d,2p)/B3LYP/6-

31++g(d,p) level and found good agreement between ΔG^\ddagger values at the two levels. As polymerization experiments were carried out in solution, one may also wish to introduce solvent effects via self-consistent reaction field-type approaches;²⁵ these, however, are usually only able to adequately describe solvation effects due to polarization and charge displacements. Despite our monomers being polar, the impact of solvation on those interaction modalities in our case is unlikely to be more than weak, as the employed solvent is toluene ($\epsilon_r=2.38$); it was thus decided to neglect the use of continuous model solvents. We already provided evidences supporting this idea in a work were cationic metallocene complexes catalyzed olefin polymerization,^{26,27} and preliminary calculations on a few cases indicated this to be correct also for radical polymerizations in absence of chemically specific interactions such as normal or charged hydrogen bonds.^{4,5,28,29}

What may instead be more problematic in using continuous solvent models in the task we set to accomplish, it is their limited ability in correctly estimating the change in system entropy upon formation of the TSs from dissociated reactants. Such issue descends from the fact that reaction field models are not able to correctly describe the molecularity of the true solvent, which has to be displaced from the first solvation shell of each species for the reactive collision to take place. This necessity usually requires some reversible work to be carried out, whose numerical value is determined by excluded volume, intermolecular attraction, thermal excitations, and entropic effects (Is the system more disordered when two monomers are associated due to the increase in entropy of the solvent or when are unassociated?). With the last effect being potentially dependent on the solvent and solutes (e.g., the association of hydrocarbons in water increases the system entropy, as does the endothermic dissolution of ionic salts), it seems to us that it may be preferable to avoid the usage of implicit solvent models, accepting the fact that computed ΔG^\ddagger shall always be affected by some form of systematic error; at least, in the estimation of ΔS^\ddagger . This notwithstanding, we haste to notice that modeling copolymerization kinetics requires only ratios between kinetic constants (the r_{MMA} and r_{DMAEMA} previously discussed), so that one may reasonably hope to stumble upon some form of error cancellation when similar monomers are involved; we thus decided to avoid using model solvents altogether in our investigation.

When working with polar monomers as in our case, it is also important to remember that there may be some form of preferential monomer partitioning between the bulk solution and the growing radicalic end of the polymeric chain. This effect, a well-known form of which goes under the name of “bootstrap” effect (BSE),³⁰ is in principle capable to induce local enrichment of one of the comonomers compared to its nominal composition and thus to increase its reaction rate. Such an effect is usually modeled defining *partition coefficients* ($K_{\text{MMA}} = \frac{[\text{MMA}]_M [\text{DMAEMA}]_b}{[\text{MMA}]_b [\text{DMAEMA}]_M}$ and $K_{\text{DMAEMA}} = \frac{[\text{MMA}]_b [\text{DMAEMA}]_M}{[\text{MMA}]_M [\text{DMAEMA}]_b}$),³¹ so that $K_{\text{MMA}} \frac{[\text{MMA}]_b}{[\text{DMAEMA}]_b}$ and $K_{\text{DMAEMA}} \frac{[\text{MMA}]_M}{[\text{DMAEMA}]_M}$ give the effective concentration ratios between MMA and

DMAEMA in the vicinity of, respectively, the terminal MMA or DMAEMA radicals. In the previous formulae, $[MMA]_b$ represents the instantaneous nominal concentration of MMA in the bulk, so that $q_b = \frac{[MMA]_b}{[DMAEMA]_b}$ is the instantaneous nominal monomer feed; also, $[MMA]_M$ and $[DMAEMA]_M$ are the concentrations of MMA and DMAEMA close to the terminal MMA radical of the chain. Notice that, with the assumption of preferential partitioning, all the details (the monomer reactivity ratios) of the propagation mechanism could, again, be considered as solvent-independent.³²

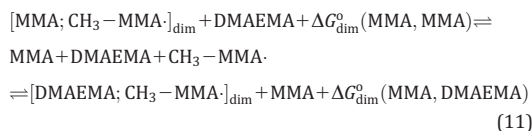
Taking into account the microphase difference compositions within the framework of the bootstrap model, the usually determined reactivity ratios must be considered apparent reactivity ratios

$$r_{MMA}^s = r_{MMA} K_{MMA} \text{ and } r_{DMAEMA}^s = r_{DMAEMA} / K_{DMAEMA} \quad (9)$$

where r_i ($i = \text{MMA, DMAEMA}$) are the true reactivity ratios and K_i are the coefficients defined above. The probabilities in the case of a radical copolymerization with BSE can be written in a way similar to eq 6:

$$p_{MMA,DMAEMA} = (1 + r_{MMA} K_{MMA} q_b)^{-1} \text{ and } p_{DMAEMA,MMA} = \left(1 + \frac{r_{DMAEMA}}{K_{DMAEMA} q_b}\right)^{-1} \quad (10)$$

In principle, the K s could be computed via equilibrium Monte Carlo (MC) or Molecular Dynamics (MD) simulations employing explicit solvent models and appropriately tuned force fields. With the assumption that only a single monomer molecule at the time can preferentially "sit" close to the radical center due to the difference in partitioning, the local relative concentration of MMA and DMAEMA at the chain end is, in fact, governed by the formation and break-up of dimers with the latter, for instance as in the following equilibria:



Here, $[X; Y]_{dim}$ is the dimer between monomer X and the radical-bearing last monomer of the chain, Y , and $\Delta G_{dim}^0(Y, X)$ is the change in Gibbs' energy associated with the formation of the latter dimer. From eq 11, it emerges that the change in Gibbs' energy the system has to sustain upon substituting with MMA the DMAEMA monomer in a dimer with the MMA radical amounts to

$$\Delta \Delta G_{dim}^0(MMA) = \Delta G_{dim}^0(MMA, MMA) - \Delta G_{dim}^0(MMA, DMAEMA); \quad (12)$$

the latter two quantities are the one that can be estimated via MC or MD.

As computing $\Delta G_{dim}^0(Y, X)$ is likely to require long and computationally expensive simulations involving extensive sampling

of many conformational isomers for the dimer and its isolated composing fragments in a viscous environment, we shall make the attempt of modeling monomer partition substituting it with the standard Gibbs' energy change upon formation of a van der Waals dimer between the terminal Y radical and the monomer X . Assuming for the moment that only a handful of isomers (or even a single one, how fairly often happens) for each of the involved species may be needed to appropriately describe their equilibrium statistical mechanics, the "harmonic superposition approximation" (HSA)³³ may be exploited to estimate the Gibbs' energy for model chain radicals, monomers and their dimers. Thus, instead of computing each $\Delta G_{dim}^0(MMA, X)$ via MC or MD to estimate $\Delta \Delta G_{dim}^0(MMA)$, one may simply optimize structural isomers with, for example, the DFT approach discussed above, select the minima with the lowest Gibbs' energy G and that, hopefully, are well separated by the remaining isomers, estimate the G for such a subset of species via HSA, and, eventually, $\Delta G_{dim}^0(MMA, X)$ or $\Delta \Delta G_{dim}^0(MMA)$. Notice that, in doing so, one exploits once again the possibility of error cancellation, as the contribution to the change in entropy related to the loss of translational and rotational freedom upon dimerization is largely cancelled out while computing $\Delta \Delta G_{dim}^0$. Similarly, one would hope that the differences between the solvent-accessible surface of, for example, MMA/MMA and MMA/DMAEMA dimers may be largely neglected, so that change in solvent entropy and enthalpy largely cancel. Obviously, such an approach has already been used (e.g., see Refs. 34–40) and shown to perform adequately even for carboxylic acid oligomers.³⁸

To conclude our methodological discussion, it is perhaps worth pointing out that even in absence of solute–solute interactions relatively stronger than solute–solvent ones, as between acid molecules in weakly polar solvents,^{34,35,38,40} the proposed approach could still be applied if our radical–monomer dimers in solution maintained, at least, the nature of local free energy minima. In that case, HSA should still be valid, as we would expect a Gibbs' energy barrier along the intrinsic dissociation coordinate due to the necessity for the solvent to reorganize as a consequence of the change in the distance between monomers and radicals. To substantiate this idea, we begin mentioning that even pure toluene shows a local maximum (roughly 0.4 kcal/mol above the leftmost minimum) in the potential of mean force (minimum in the pair distribution function) along the distance between the center of mass of two molecules.^{41–44} A similar, albeit more marked, feature is also seen in asphaltene solutions in toluene,^{45,46} with dissociation barriers varying in the range 2.6–12 kJ/mol.^{45–47} More importantly for our interests, polar (PEG- or vinyl alcohol-like) side branches of star-like polymers also show marked aggregation effects in toluene,⁴⁸ thus substantiating the claim that dimers of polar species would represent true minima over the Gibbs' energy surface of the monomers-growing chains solution.

Kinetic Monte Carlo Simulations and Code

As mentioned previously, we consider important to study chain growth by directly simulating subsequent monomer

additions exploiting the intrinsic stochastic nature of the “ultimate model” kinetic scheme via kMC, assuming that depolymerization cannot take place. Apart from average properties that may be obtained also with analytical methods, doing so would allow us to obtain all the relevant distributions and correlation functions that may help in better understanding how the copolymer properties depends on the length of the short chains that we synthesized. For instance, the position dependence of composition and the probability of finding a DMAEMA–DMAEMA diad along the chain may be quite useful. To this end, the kinetic Monte Carlo code receives as input the ΔG^\ddagger of the four possible propagation steps between MMA and DMAEMA (or experimental reactivity ratios), two partition coefficients, the initial MMA/DMAEMA feed ratio, the number of chains we wish to generate, the system temperature and the total (i.e., with respect to the total amount of monomers) percent conversion. After the calculation of reactivity ratios employing ΔG^\ddagger and TST, the core of simulation is articulated in few basic steps:

1. calculation of probabilities p_{12} and p_{21} (eq 6) with a feed modified by subtracting the amount of each monomer already reacted;
2. determining the new adding monomer basing on the nature (MMA or DMAEMA) of the radical-bearing chain by comparing a uniformly distributed random number with either p_{12} or p_{21} (respectively);
3. increase chain length by saving the new monomer in an array, recomputing feed composition and increasing counters to estimate diads, triads and n -monomer distributions;
4. calculate total conversion M/M_0 ; if the instantaneous conversion is lower than the maximal conversion allowed, go back to step 1 and continue the copolymerization.

This set of pseudo-instructions generates a single chain; it is nested inside another cycle that produce the desired number of chains. Exploiting the ensemble of chains thus generated, we compute the relative MMA/DMAEMA polymer composition, the triad distributions and the related standard deviations.

RESULTS AND DISCUSSION

Experimental Copolymerization Results

In the literature, we found that random DMAEMA/MMA copolymers have been synthesized using different approaches such as reversible addition-fragmentation chain transfer (RAFT),^{14,15} and radical polymerization in presence of AIBN¹⁶ or palladium acetylde¹⁷ as initiator species. The latter approach was suggested to present “some characteristics of atom transfer radical polymerization (ATRP)”.¹⁷ The reactivity ratios obtained showed an almost similar relative reactivity of the two monomers or, in few cases, a slightly higher reactivity of DMAEMA with respect to MMA despite the different experimental conditions (Table 1). In principle, this similarity can be taken to indicate the fundamentally

common radical nature of all processes, which was clearly supported for ATRP by the analysis of kinetic isotope effects via experimental and theoretical means.⁴⁹ The copolymers obtained were generally considered random copolymers in terms of the statistical distribution of the comonomers along the backbone.

Copolymers with specific biological behavior, as reported in the introduction of this work, were formed by block-random microstructure such as mPEG-*b*-(MMA-*ran*-DMAEMA)_{*n*} ($n = 1, 2,$ and 4) and were obtained via a classical ATRP of MMA and DMAEMA in toluene using an mPEG-based macro-initiator ($M_n = 2$ kDa, $M_w/M_n = 1.16$) and CuBr/bpy as catalyst. Considering the relative reactivity ratios reported in the literature and our intent of obtaining amphiphilic copolymers consisting of an MMA-based hydrophobic block having sporadic amino pendant groups into the back-bone, the three different structures (namely, one linear and two branched ones) were synthesized using feed ratios $q_0 = [MMA]_0/[DMAEMA]_0$ markedly higher than 1. Surprisingly, ¹³C-NMR characterization showed a greater tendency for DMAEMA to insert into the backbone with respect to MMA, independently of the copolymer structures. This result is clearly at variance with data published before, even when a reaction with some characteristic of the ATRP approach discussed in this work was used; we thus feel it is worth of further study.

To this end, we decided to extend our investigation synthesizing a variety of mPEG-*b*-(MMA-*ran*-DMAEMA)_{*n*} using q_0 in the range 2–17. The choice of synthesizing copolymers containing the mPEG block as macro initiator of the radical polymerization was made for two reasons. First, we wished to conserve exactly the same experimental conditions employed to obtain copolymers with biological activity to avoid introducing biases in the microstructure; second, the polymerization *versus* can be important to confer tailored properties for specific applications (e.g., forming pH-responsive vesicles), which would escape analysis without a well defining chain beginning although being investigable within the framework of the *terminal model*. The characterization of these copolymers in terms of chemical composition F , molecular weight, and polydispersity (M_w/M_n) is reported in Table 2. These new data confirmed the higher DMAEMA relative reactivity with respect to MMA; furthermore, they also indicated that copolymers architecture does not seem to have any influence on the monomers reactivity. With this in mind, we avoided to analyses separately results for each polymeric structure; such an effort would produce only results much less statistically robust than the ones we discuss in the following. Worth also a notice, it is the fact that the polydispersity index shown in Table 2 for the copolymeric species is in line with what previously published on ATRP-derived species;^{50–53} this is despite the homopolymeric nature of the chains described in the latter works.

With the new available polymers and their characterization increasing the data set at our disposal, we extracted experimental reactivity ratios from the composition data, and we

TABLE 1 Reactivity Ratios for Radical and CRP Polymerizations of MMA and DMAEMA. Also Indicated, There are Solvent and Numerical Approach to Estimate the r 's

Polymerization Method	Solvent	r_{MMA}	r_{DMAEMA}	Method	Reference
Radical copolym.	bulk	0.71($\pm 7\%$)	1.25($\pm 12\%$)	Kelen-Tudos	16
Radical copolym.	CHCl ₃	1.13	1.07	Extended Kelen-Tudos	17
RAFT	DMF	0.925(± 0.05)	0.854(± 0.04)	Extended Kelen-Tudos	15
RAFT	ethanol	0.9	0.8		14
ATRP	toluene	0.36($\pm 10\%$)	2.76($\pm 15\%$)	Eq. 8	This work
ATRP	toluene	0.48($\pm 8\%$)	1.60($\pm 26\%$)	Eq. 7	This work

did so by optimizing the parameters $r_1=r_{\text{MMA}}$ and $r_2=r_{\text{DMAEMA}}$ in eqs 7 and 8 fitting the behavior of the latter to the results. Worth a notice, it is the fact that the monomer conversion does not play any role when using eq 7 to model the results, as the latter implies a constant value for the feed composition q ; this assumption, however, does not represent accurately the experimental situations, as the DMAEMA monomer is present in smaller amount and should be consumed more rapidly than MMA.

The least square fitting of the parameters in both analytical forms was carried out employing the nonlinear least-squares (NLLS) Marquardt–Levenberg algorithm^{54,55} implemented in Gnuplot,⁵⁶ obtaining $r_{\text{MMA}}^s=0.36(\pm 10\%)$ and $r_{\text{DMAEMA}}^s=2.76(\pm 15\%)$ when using eq 8, or $r_{\text{MMA}}^s=0.483(\pm 8\%)$ and $r_{\text{DMAEMA}}^s=1.60(\pm 26\%)$ when employing eq 7. The variance of the residuals for the two cases was, respectively, 0.0038 and 0.0474, which indicates the markedly better performance of the model that takes into account the change in feed composition as expected basing on the experimental conditions despite containing the same amount of adjustable parameters. Moreover, the absolute r values obtained employing both models suggest the preferred insertion of DMAEMA whatever the ultimate unit is. In turn, this behavior should be expected to generate a DMAEMA-rich blocky structure at the beginning of the copolymerization (i.e., close to the linking group with mPEG), that turns into an MMA-rich blocky

one after a sufficiently high conversion of the most reactive monomer. *In absentia* of an NMR characterization of the chain triads, this aspect of the copolymerization would be discussed in Section 3.2 (*vide infra*) relying on kMC simulations exploiting the reactivity ratios just obtained.

While we also attempted an in-depth investigation of the possible origin of the marked difference between r_{MMA}^s and r_{DMAEMA}^s exploiting electronic structure calculations (see Section 3.3), a few hints on the relevance that reaction conditions may have on the polymer composition were sought synthesizing linear mPEG-*b*-(MMA-*ran*-DMAEMA) species in presence of three different solvents, namely acetonitrile, dimethylformamide, and toluene. The results of the three experiments, conducted well within the differential (low conversion) regime fulfilling the condition of validity for eq 7, are shown in Table 3.

At first sight, it appears evident that $\frac{F_{\text{MMA}}}{F_{\text{DMAEMA}}} < q_0$ for all three cases, which provides a clear indication of the higher reactivity of DMAEMA. This fact is, yet, at variance with the literature results in Table 1, as it can be made evident computing $\frac{F_{\text{MMA}}}{F_{\text{DMAEMA}}}$ with the reported reactivity ratios and our q_0 via eq 7. Following the order in Table 1, the theoretical copolymer composition ratios are: 1.94, 2.83, 2.59, and 2.58. In all cases, these are much (35–230%) higher than the ratios shown in Table 3. Of greater relevance for our intent, we

TABLE 2 Results for mPEG-*b*-(PMMA-*ran*-DMAEMA)_{*n*} (mPEG-*b*-(PM-*ran*-D)_{*n*}, $n=1-4$) Obtained by ATRP Conducted in Toluene at 90 °C

Polymer	Structure	q_0	$\frac{F_{\text{MMA}}}{F_{\text{DMAEMA}}}$	Conversion (MMA, %)	$M_n/10^3$ Da	M_w/M_n
1	mPEG- <i>b</i> -(PM- <i>ran</i> -D)	7.9	4.2	42	38	1.40
2	mPEG- <i>b</i> -(PM- <i>ran</i> -D)	3.8	2.0	30	70	1.28
3	mPEG- <i>b</i> -(PM- <i>ran</i> -D)	3.1	1.4	26	48	1.32
4	mPEG- <i>b</i> -(PM- <i>ran</i> -D)	2.3	1.2	34	76	1.50
5	mPEG- <i>b</i> -(PM- <i>ran</i> -D) ₂	17	11	57	61	1.52
6	mPEG- <i>b</i> -(PM- <i>ran</i> -D) ₂	7.7	3.6	54	58	1.51
7	mPEG- <i>b</i> -(PM- <i>ran</i> -D) ₂	3.1	1.7	34	62	1.44
8	mPEG- <i>b</i> -(PM- <i>ran</i> -D) ₂	2.6	1.2	42	87	1.61
9	mPEG- <i>b</i> -(PM- <i>ran</i> -D) ₄	7.7	3.8	55	75	1.48
10	mPEG- <i>b</i> -(PM- <i>ran</i> -D) ₄	5.3	3.1	45	80	1.51
11	mPEG- <i>b</i> -(PM- <i>ran</i> -D) ₄	3.8	2.2	47	90	1.51
12	mPEG- <i>b</i> -(PM- <i>ran</i> -D) ₄	3.1	1.7	45	93	1.60

TABLE 3 Results for mPEG-*b*-(PMMA-*ran*-DMAEMA) Obtained by ATRP Conducted in Different Solvent (60 °C). $q_0=2.63$

Solvent	Yield (g)	Conversion (MMA, %)	$\frac{F_{MMA}}{F_{DMAEMA}}$	M_n Da (NMR)	M_w/M_n
CH ₃ CN	0.1441	4	1.4	169,979	2.29
DMF	0.1968	5	1.4	98,663	1.70
Toluene	0.5682	9	0.85	51,689	1.80

also notice that $\frac{F_{MMA}}{F_{DMAEMA}}$ is much lower in presence of toluene as solvent than in the remaining two cases, suggesting that the polarity of the solvent may play a role in defining the effective relative reactivity of the comonomers. *De facto*, the higher polymer yield and MMA conversion obtained in toluene seem to suggest that also the absolute reactivity is indeed controlled by the solvent, the lower electric permittivity of toluene apparently being able, at least, to increase the concentration of both monomers close to the growing chain compared to the more polar acetonitrile and dimethylformamide.

Notice that, to internally compare polymerizations in toluene with lower boiling solvents, we were forced to run reactions at lower temperature than used to generate the species in Table 2. Thus, the above conclusion relies on the possibility of comparing ATRP results obtained in toluene at 60 and 90 °C and, to support such idea, we stress that the relative copolymer composition ($\frac{F_{MMA}}{F_{DMAEMA}}=0.85$) obtained in toluene at 60 °C is indeed quite similar with the one predicted by eq 7 employing $q_0=2.63$ and the reactivity ratios extracted via the nonlinear fitting of eq 8, which give $\frac{r_{MMA}^s}{r_{DMAEMA}^s}=0.95$.

As a last observation to conclude this analysis, we recall that, within the assumption of constant feed composition (or, at least, short polymerization time), eq 7 provides indication on how the copolymer composition (i.e., F_{MMA}/F_{DMAEMA}) varies with f_{MMA}/f_{DMAEMA} . From this, one can derive that $F_{MMA}/F_{DMAEMA} < f_{MMA}/f_{DMAEMA}$ whenever $q > (1-r_{DMAEMA}^s)/(1-r_{MMA}^s)$; as both experiments and theoretical results indicate that $r_{DMAEMA}^s > r_{MMA}^s$, the latter condition is always fulfilled during our copolymerization at least because $q_0 > 1$. This is clearly apparent from the plots of eq 7 versus q_0 in Figure 1.

Results from kMC Simulations

Before discussing the kMC results obtained simulating copolymerizations with the sets of reactive ratios discussed in the previous section, it is worth recalling that experimental polymerizations were interrupted after a chosen reaction time had elapsed. As a consequence, monomer conversion varies from case to case, depending on the relative amount of the two monomers and their relative reaction rates, and spans the range 20–60%. To facilitate comparison between experiments and theoretical data, we therefore stopped the simulations at conversions that matched the just mentioned interval extrema, thus generating composition “bands” that should represent all the synthesized species.

Apart from representing eq 7 with the sets of fitted r^s and the experimental polymer compositions, Figure 4 also shows

copolymer relative composition (F_{MMA}/F_{DMAEMA}) versus initial feed composition (q_0) as obtained from the kMC simulations. At a first glance, it immediately emerges that simulations employing the reactivity ratios obtained via eq 8 provide upper and lower bounds to the experimental results, thus substantiating the usage of such relationship for the description of our copolymerizations. It is also apparent that the experimental data can be appropriately fit via eq 7 (dashed blue line); however, the agreement worsen substantially if the r^s obtained via this fitting are employed in kMC simulations where the variation in q value is properly taken in consideration; these predict higher values for F_{MMA}/F_{DMAEMA} than obtained from eq 7, and this deviation increasing upon increasing the monomer conversion. Obviously, this descends from the preferential consumption of DMAEMA as the most reactive of the two monomers, and the consequent increase in q while the reaction takes place. It is also apparent that the behavior of F_{MMA}/F_{DMAEMA} versus q obtained via kMC at a chosen monomer conversion is substantially linear for $q > 1$ (i.e., the conditions in which the copolymerization took place). As for the latter, the slope of the straight line is clearly a function of the conversion degree, increasing toward a unit value upon increasing the conversion. Again, this effect is related to the initially faster consumption of DMAEMA.

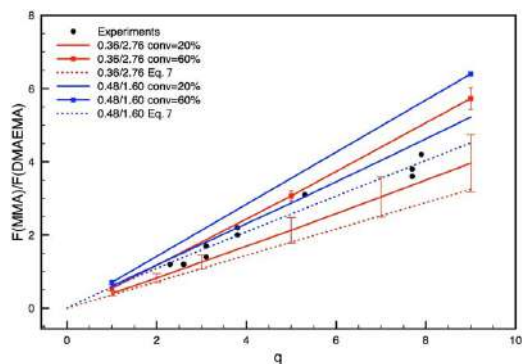


FIGURE 4 F_{MMA}/F_{DMAEMA} versus feed composition q_0 obtained experimentally (black circles), and via eq 7 (dashed lines) or kMC simulations with experimentally obtained r^s . The vertical error bars represent the standard deviation of the sampled copolymer composition values at each q_0 generated employing the reactivity ratios obtained via eq 8. [Color figure can be viewed at wileyonlinelibrary.com]

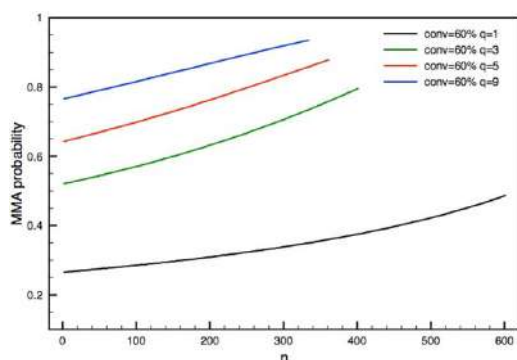


FIGURE 5 Probability of finding an MMA monomer enchain in position n along the chain versus feed composition q_0 , obtained using $r_{\text{MMA}}^s = 0.36(\pm 10\%)$, $r_{\text{DMAEMA}}^s = 2.76(\pm 15\%)$ and a 60% monomer conversion. [Color figure can be viewed at wileyonlinelibrary.com]

Given the somewhat limited copolymer lengths, one would expect that the $F_{\text{MMA}}/F_{\text{DMAEMA}}$ values were distributed over a fairly wide range of compositions; to investigate such aspect, we also computed the standard deviation of the copolymer composition, which is shown in Figure 4 as error bars for the kMC results obtained using the r^s obtained by fitting data in Table 2 with Equation 8. At first glance, it clearly appears that the distribution of composition values can be fairly wide (e.g., up to 30–35% of the average value), decreasing markedly upon increasing the monomer conversion. Interestingly, the amplitude of the fluctuation in composition shown by the kMC data seems of the same magnitude of the one shown by the experiment results, thus justifying the slight erratic behavior of the latter. In fact, we empirically found that all experimental results fall into the composition band defined by the fluctuation amplitudes obtained simulating with kMC copolymerization with $r_{\text{MMA}}^s = 0.36(\pm 10\%)$, $r_{\text{DMAEMA}}^s = 2.76(\pm 15\%)$ and a conversion of 40% (not shown in the figure).

Having somewhat verified the capability of the kMC simulations to reproduce composition data when employing fitted experimental results, the attention may now be directed toward understanding the impact on the microstructural details of the difference in monomer reactivity ratios. To this end, we begin discussing how the probability of enchaining a given monomer (e.g., MMA) in a specific position (n) along the chain may depend on the latter as a consequence of the variation in q during the copolymerization. Notice that we selected as origin of the chain the link between the mPEG macroinitiator and the copolymer. Thus, Figure 5 presents the average (over at least 10^6 generated chains) probability of finding a MMA monomer in the n th position along the chain at total monomer conversion of 60% and as a function of the feed ratio q_0 . Only data obtained with $r_{\text{MMA}}^s = 0.36(\pm 10\%)$, $r_{\text{DMAEMA}}^s = 2.76(\pm 15\%)$ are shown for sake of clarity and their relevance to experiments. Results for lower

conversions can be deduced from what shown in Figure 5 by, simply, selecting the chain length (i.e., the maximum value for n).

As expected, the probability of finding MMA along the chain increases with n , an effect, again, related to the decrease in DMAEMA content due to its relatively faster consumption. Notice that the relative change in MMA probability between the first and last enchain monomer remains substantial (20–80%) even at large q_0 values; some modulation of the probability is also due to the increase in chain length upon decreasing q_0 . Notice that the latter effect is not an artefact of our simulation approach, as also the experimental results indicate that, normalized to equal conversion, the molar mass of the copolymers increases upon decreasing the feed composition (Table 2). *De facto*, our choice to keep constant the number of initial MMA monomers in the simulations and to vary DMAEMA monomers in accord with the chosen q_0 closely follows the experimental approach (Section 3.1). Basing on the results in Figure 6, it thus seems correct to consider the copolymers discussed in Section 3.1 as proper members of the family of gradient copolymers.

Additional insights on the microstructure of the MMA–DMAEMA (M–D) copolymers emerge noticing that a local decrease in probability of finding the ionizable monomer along a chain, *de facto*, lowers the probability of finding two such monomers sufficiently close to form a charged hydrogen bond interaction,^{57,58} if one of them is protonated. To show that this is just the case, we have collected the probability of forming all possible triads as a function of the position of the first monomer in each triad. We opted to investigate triads instead of the simpler diads as the inherent flexibility of the ionizable pendants geometrically allows the formation of charged hydrogen bonds also between next neighbors, a situation present in the case of DMD. The data for two initial feeds ($q_0 = 1$ and 9) simulated with $r_{\text{DMAEMA}}^s = 2.76(\pm 15\%)$, $r_{\text{MMA}}^s = 0.36(\pm 10\%)$ and a 60% monomer conversion is shown in Figure 5. We have chosen these two specific cases to exemplify extremal behaviors that can be found during a copolymerization with a substantially different reactivity of the co-monomers.

From the data shown for the $q_0 = 1$ case, it emerges that the DMAEMA-richest triad DDD monotonically decreases along the chain due to the progressive consumption of this monomer while the polymerization progresses. Indeed, the decrease in DDD is quite marked, its probability dropping by roughly 50% while moving away from beginning of the chain. The other two DMAEMA-rich triads (DDM and DMD) do not follow a monotonic behavior, and are found to slightly increase at the beginning of the polymerization (by 3–4% maximum), and only subsequently to decrease due to the consumption of DMAEMA. Overall, the probability of finding two DMAEMA monomers sitting at least as next neighbors drops from roughly 0.82 to 0.52 upon going toward the chain end, a probability that nevertheless remains quite high and suggest the likelihood of charged hydrogen bonds

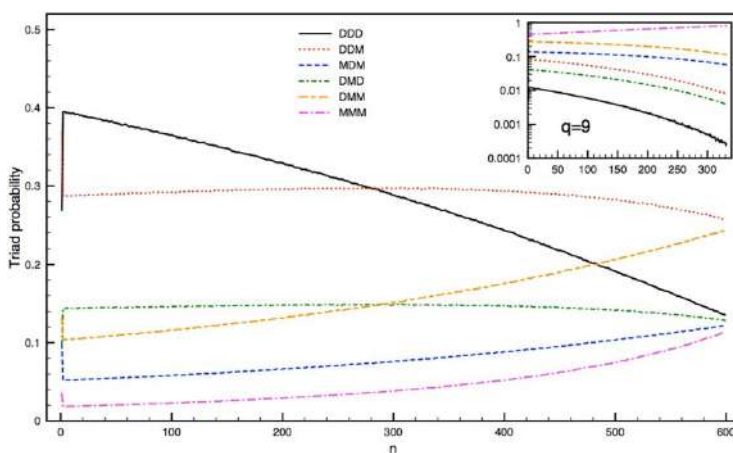


FIGURE 6 Probability of finding a specific triad with its first monomer sitting at position n along the chain when $q = 1$ and 9 (in the inset). D indicates DMAEMA, while M indicates MMA; the probabilities of DDM and MDD, as well as of MMD and DMM, are subsumed to preserve symmetry. Simulations were conducted with $r_{\text{MMA}}^s = 0.36 (\pm 10\%)$, $r_{\text{DMAEMA}}^s = 2.76 (\pm 15\%)$ and 60% monomer conversion. [Color figure can be viewed at wileyonlinelibrary.com]

formation. Obviously, one also notices the increase of MMA-rich triads (MMM, DMM, and MDM) parallel to the decrease in DMAEMA-rich triads. Perhaps also worth a mention, it is the very low probability of finding the MMM triad at the beginning of the chain, which suggests that only a very limited hydrophobic character should be displayed by the first part of the chain.

Turning to the $q_0 = 9$ case, we notice the substantial decrease in DMAEMA-rich triads, whose overall probability is only 0.14 at the beginning of the chain and rapidly drops to 0.01 upon going toward the chain terminus. Clearly, this finding correlates well with the substantial reduction of DMAEMA in the feed. Apart from the faster decrease just discussed, the $q_0 = 9$ case differs from the $q_0 = 1$ one also due to the fact that only the MMM triad is seen increasing while the reaction progresses, DMM and MDM both decreasing due to the decreasing DMAEMA content in the feed. Importantly, the difference in behavior between the $q_0 = 1$ and 9 cases is not an artefact of our simulation approach but an effect of the nonlinear relationship between the instantaneous probability of inserting, for example, an MDM triad and the feed composition, as discussed at length in Ref. 18.

Rationalization of the Experimental Results

Having explored the impact on the microstructural details of the $\text{mPEG-}b\text{-(MMA-}r\text{-ran-DMAEMA)}_n$ copolymers deriving by the difference in reactivity ratios and by the choice of q_0 , in this Section we present the results of our attempt of investigating the origin of the difference in r 's found experimentally. For the sake of conciseness, we limit our discussion on the copolymerization energy profiles to the minimum amount of information needed to appreciate the conclusions;

more details are provided to the interested Reader in the Supporting Information.

Figure 7 shows the lowest Gibbs' energy conformers optimized for the monomers and radicals involved in the copolymerization. Figure 8 shows, instead, the stationary geometry of the lowest Gibbs' energy TS's involved in the four propagation reactions generating the copolymer; the energy barriers reported in the figure are computed with the asymptotic reactants as zero of the scale. Of direct relevance for our purpose, we notice that all computed barriers appear of very similar height.

Assuming that only the most stable reactant and TS species are relevant for the propagation reactions, one can easily compute the two reactive ratios necessary to quantitatively describe the copolymerization as described in Section 2.2, and these are shown also in Figure 8. As we obtain $r_{\text{MMA}}^{\text{DFT}} = 1.040$ and $r_{\text{DMAEMA}}^{\text{DFT}} = 0.767$, one should obtain a copolymer more rich in MMA than in DMAEMA compared to the composition of the feed (i.e., $F_{\text{MMA}}/F_{\text{DMAEMA}} > f_{\text{MMA}}/f_{\text{DMAEMA}}$), which is clearly at variance with what shown in Tables 2 and 3. Instead, these results agree qualitatively with the reactivity listed in Refs. 14,15,17, where $r_{\text{MMA}} > r_{\text{DMAEMA}}$ are found even though only by limited amounts.

To proceed further with the approach introduced in Section Modelling, the lowest Gibbs' energy structure for all possible radical-monomer dimers are shown in Figure 9. This also presents values for the ΔG_{dim}^0 and $\Delta \Delta G_{\text{dim}}^0$ needed to compute the monomer partition coefficients and estimated as indicated in eq 12 from the lowest energy conformers of monomers and radicals. All $\Delta \Delta G_{\text{dim}}^0$ are positive, and from these one obtains $K_{\text{MMA}} = 2.51$ and $K_{\text{DMAEMA}} = 0.08$; these suggest that MMA preferentially partition closer to both radicals and thus the involved radical-monomer interactions do not

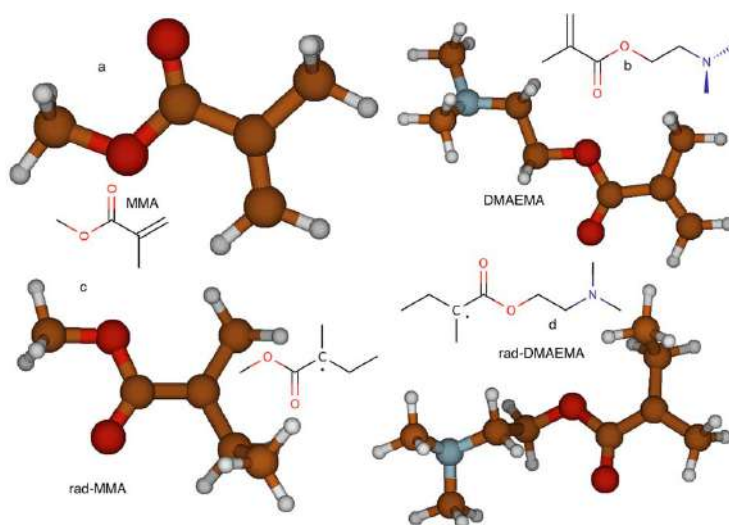


FIGURE 7 Lowest Gibbs' energy minima for (a) MMA, (b) DMAEMA, (c) CH₃-MMA· radical, and (d) CH₃-DMAEMA· radical. For the sake of clarity, CH₃-MMA· and CH₃-DMAEMA· are labeled in the figure as, respectively, rad-MMA and rad-DMAEMA. [Color figure can be viewed at wileyonlinelibrary.com]

provide a rationalization for the experimental results in Section Experimental results.

With the results on $\Delta\Delta G_{\text{dim}}^{\ddagger}$ suggesting a behavior opposite to what experimentally found in terms of reactivity ratios,

one may invoke the possibility that DMAEMA interacts with the CuBr/bpy complex needed to activate the alkyl-halogen bond during the polymerization to justify $r_{\text{MMA}} < r_{\text{DMAEMA}}$; the net effect of such interaction could be the preferential partitioning of DMAEMA closer to a just formed radical

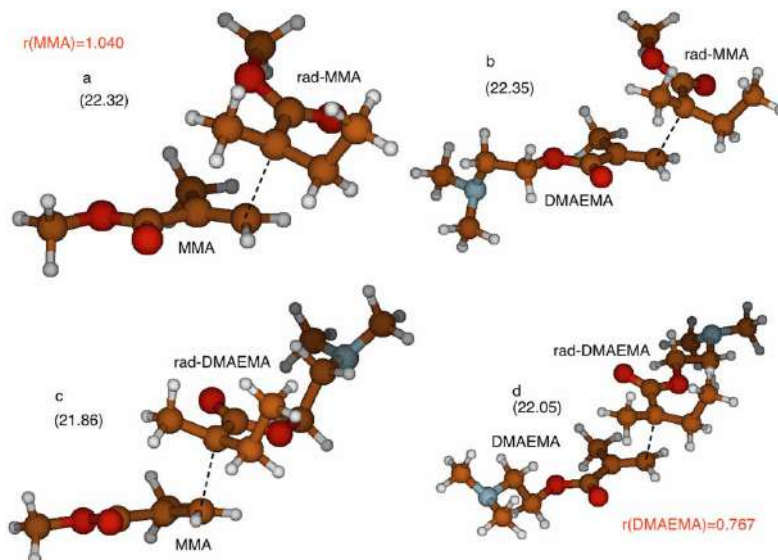


FIGURE 8 Lowest Gibbs' energy TS's for the reaction between (a) CH₃-MMA·/MMA, (b) CH₃-MMA·/DMAEMA, (c) CH₃-DMAEMA·/MMA radical, and (d) CH₃-DMAEMA·/DMAEMA radical. Also shown, there are the barrier heights from the asymptotic reactants (in black between brackets) and the corresponding reactivity ratio (in red). For the sake of clarity, CH₃-MMA· and CH₃-DMAEMA· are labeled in the figure as, respectively, rad-MMA and rad-DMAEMA. [Color figure can be viewed at wileyonlinelibrary.com]

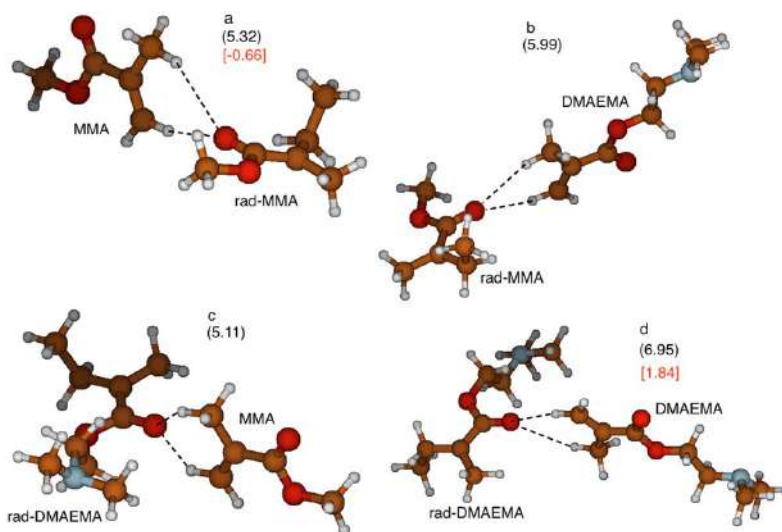


FIGURE 9 Lowest Gibbs' energy dimer for the reaction between (a) $\text{CH}_3\text{-MMA}/\text{MMA}$, (b) $\text{CH}_3\text{-MMA}/\text{DMAEMA}$, (c) $\text{CH}_3\text{-DMAEMA}/\text{MMA}$, and (d) $\text{CH}_3\text{-DMAEMA}/\text{DMAEMA}$. Dimerization Gibbs' energies (kcal/mol), $\Delta G_{\text{dim}}^{\circ}$, from the asymptotic reactants are shown (in black) between brackets; $\Delta G_{\text{dim}}^{\circ}$ computed assuming $\text{CH}_3\text{-MMA}/\text{MMA}$ and $\text{CH}_3\text{-DMAEMA}/\text{DMAEMA}$ as final state are shown (in red) between square brackets. For the sake of clarity, $\text{CH}_3\text{-MMA}\cdot$ and $\text{CH}_3\text{-DMAEMA}\cdot$ are labeled in the figure as, respectively, rad-MMA and rad-DMAEMA . [Color figure can be viewed at wileyonlinelibrary.com]

disregarding its nature compared to MMA. That this could be the case, up to the point of modifying the coordination environment of Cu(I), has been shown by Haddleton *et al.*⁵⁹ by directly treating the catalyst N-propyl 2-pyridylmethanimine/copper(I) with DMAEMA in an NMR tube. A less direct, even though still compelling, evidence is also provided by the requirement of using tri- or tetra-dentate amino ligands in the ATRP synthesis of polyDMAEMA to avoid the displacement of the ligand on the copper complex.⁶⁰ If this was the case, one would *de facto* have the transport of DMAEMA close to a forming radical by the very catalyst that helps in generating the latter.

To experimentally test the possible coordination of DMAEMA to Cu(I), we carried out ¹H-NMR experiments on various mixtures of the CuBr, bpy, and DMAEMA species. The results for two complementary regions of the proton chemical shifts are shown in Figure 10; from these, one can easily notice the change in proton chemical shifts of bpy due to the interaction with, first, CuBr, and successively DMAEMA. Similar shifts are also apparent for the hydrogen atoms on the sp^2 carbon of DMAEMA, thus suggesting that the complexation is indeed possible.

To quantitatively gauge the stability of the complex between DMAEMA and the catalyst used in this work, we optimized the CuBr/bpy and CuBr/bpy/DMAEMA complexes to compute the relative energetics. In Figure 11, we show the geometry of the two stationary points together with the change in enthalpy and Gibbs' energy upon coordination; as it can be seen, the former complex has a triangular

disposition of the coordinated atoms around Cu(I), while the additional coordination of DMAEMA distorts the geometry into a pyramid with a triangular base. As expected, the computed value of the coordination enthalpy ($\Delta H^{\circ} = -6.9$ kcal/mol) suggest the formation of the complex, the ΔG° value instead suffering for the inappropriate entropy reduction previously discussed.

Also interesting, there are the results on the CuBr₂/bpy/DMAEMA complex that may be formed upon extraction of the Br atoms from the dormant species. For this, we obtained a pyramidal minimum energy geometry with DMAEMA located at its vertex as fifth more weakly bound ligand, the two bromine atoms and bpy nitrogens nearly conserving the planar disposition (N-Br-N-Br dihedral angle $\approx 175^{\circ}$) of CuBr₂/bpy. Upon formation from DMAEMA and CuBr₂/bpy, also this species produces a negative enthalpy change, which suggests its likely presence in solution. The formed complex is however more labile than CuBr/bpy/DMAEMA, which is expected to favor the detachment of the copper complex from DMAEMA following the eventual addition to the growing chain.

As a last observation to conclude this theoretical analysis, we notice that the formation of a complex between DMAEMA and the copper(I) catalyst may also help to rationalize the reduction of $\frac{F_{\text{MMA}}}{F_{\text{DMAEMA}}}$ and yield upon going from toluene to the polar solvents acetonitrile and DMF. These are expected to make less negative the ΔH° associated to the ligation decreasing more the reactant enthalpy and Gibbs' energy, which ought to reduce the equilibrium constant and hence the concentration of the complex.

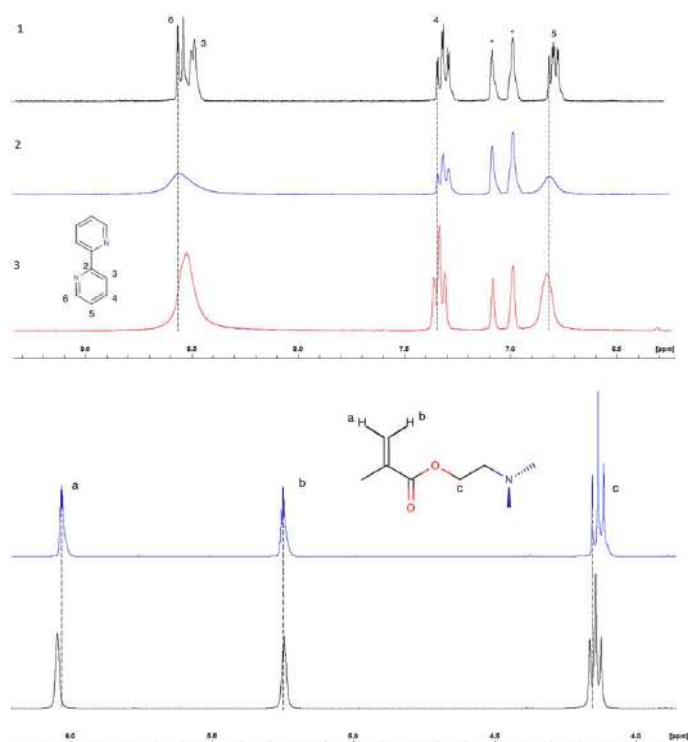


FIGURE 10 Top panel: $^1\text{H-NMR}$ in toluene at 90°C of bpy (1), CuBr/bpy 1:2 (2), and CuBr/bpy/DMAEMA 1:2:10 (3). * = toluene. Bottom panel: $^1\text{H-NMR}$ in toluene at 90°C of DMAEMA (top) and CuBr/bpy/DMAEMA 1:2:10 (bottom). [Color figure can be viewed at wileyonlinelibrary.com]

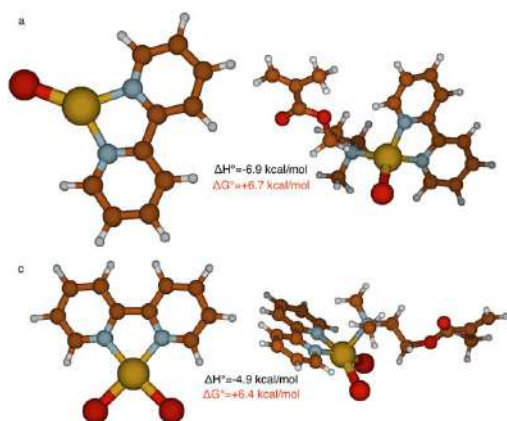


FIGURE 11 Minimum energy geometry of (a) CuBr/bpy, (b) CuBr/bpy/DMAEMA, (c) CuBr₂/bpy, (d) CuBr₂/bpy/DMAEMA, and standard enthalpy (black) and Gibbs' energy (red) changes occurring upon ligation of DMAEMA to the copper complexes. [Color figure can be viewed at wileyonlinelibrary.com]

GENERAL DISCUSSION AND CONCLUSIONS

Exploiting experimental results on the copolymerization of MMA and DMAEMA via ATRP in toluene, in this work we have provided evidences that unexpectedly marked reactivity effects can be induced even in absence of strong intermolecular forces such as hydrogen bonds^{61–63} and between copolymerization methods that are usually considered to provide similar results. Such conclusion emerges by comparing the mentioned results with both literature and ATRP data (the latter, again, by ourselves) obtained in different reaction environments (bulk, DMF, chloroform, acetonitrile, and dioxane). The large difference in the reactivity ratios ($r_{\text{MMA}}^s = 0.36$, $r_{\text{DMAEMA}}^s = 2.76$) extracted from our numerical analysis on the “feed versus polymer composition” data in toluene suggests that the copolymers obtained in the indicated conditions present gradient-like compositions, the initial part of the chains being always more rich in the ionizable monomer. In this respect, one should hasten to notice that the local properties (e.g., the behavior as weak polyelectrolyte) of the synthesized chains ought to depend on the position along the chain due to the composition change (for instance, see Ref. 64, where the behavior of the lower critical aggregation temperature was discussed).

Besides, r_{MMA}^s extracted from our analysis represent the lowest value found in the literature^{59,65–67} in an ATRP copolymerization with functional monomers such as DMAEMA, PEGMA, HEMA, or furfuryl methacrylate, a finding that we suggest to be due to the preferential coordination of the DMAEMA monomer to the copper catalyst. The latter is obviously modulated by the reaction solvent, as also shown by our data in Table 3.

Microstructural details related to the reactivity ratios have been investigated via KMC simulations closely mimicking the synthetic conditions. These indicated the presence of a higher DMAEMA concentration at the chain beginning (Fig. 5) compared to the average copolymer composition, a finding that has a direct relevance to both the theoretical foundations of the polymers designed for the discussed drug delivery applications^{6,7} and the analysis of the release kinetics from vesicles.^{28,29} Wishing to obtain copolymers of more uniform composition along a chain, a possible approach emerges from the modeling results in Section Rationalization, which suggest a difference between MMA and DMAEMA partition coefficients due to the complexation of the latter. Thus, one may favor (disfavor) even more the partition of MMA (DMAEMA) from the bulk to the regions surrounding the growing polymer by appropriately choosing the reaction solvent, which impacts on the stability of the complex between DMAEMA and CuBr.

In conclusion, we consider worth mentioning a few possible lines of investigation emerging from the current work. For instance, we notice that from the experimental standpoint, it would be interesting to investigate the impact of Cu(I) ligands on the DMAEMA reactivity ratios, which may allow fine tuning of the local relative amount of each monomer along the chain. Concerning possible theoretical work, an avenue of exploration may be represented by exploiting atomistic level simulations to investigate the eventuality of MMA and DMAEMA monomers partition close to a growing chain in the presence of explicit solvent molecules and coordinating catalysts.

ACKNOWLEDGMENTS

M.M. and M.V.L.R. thank Università degli Studi dell'Insubria for funding under the Fondo di Ateneo per la Ricerca (FAR 2016) scheme and for M.V.L.R.'s PhD studentship. L.I. and Y.M. thank Università degli Studi di Salerno for funding under the Fondo di Ateneo per la Ricerca di Base (FARB 2015 and 2016) scheme.

REFERENCES

- 1 M. Mella, L. Izzo, *Polymer* **2010**, *51*, 3582.
- 2 A. Paul, M. J. Vicent, R. Duncan, *Biomacromolecules* **2007**, *8*, 1573.
- 3 L. Izzo, P. C. Griffiths, R. Nilmini, S. M. King, K.-L. Wallom, E. L. Ferguson, R. Duncan, *Int. J. Pharma.* **2011**, *408*, 213.
- 4 G. Vigliotta, M. Mella, D. Rega, L. Izzo, *Biomacromolecules* **2012**, *13*, 833.
- 5 S. Matrella, C. Vitiello, M. Mella, G. Vigliotta, L. Izzo, *Macromol. Biosci.* **2015**, *15*, 927.
- 6 S. Villani, R. Adami, E. Reverchon, A. M. Ferretti, A. Ponti, M. Lepretti, I. Caputo, L. Izzo, *J. Drug Target.* **2017**, *25*, 899.
- 7 M. C. Barrella, A. D. Capua, R. Adami, E. Reverchon, M. Mella, L. Izzo, *Supramol. Chem.* **2017**, *29*, 796.
- 8 K. Matyjaszewski, *Progr. Polym. Sci.* **2005**, *30*, 858. plenary Lectures.
- 9 K. Matyjaszewski, M. J. Ziegler, S. V. Arehart, D. Greszta, T. Pakula, *J. Phys. Org. Chem.* **2000**, *13*, 775.
- 10 C. J. Hawker, A. W. Bosman, E. Harth, *Chem. Rev.* **2001**, *101*, 3661.
- 11 N. Hadjichristidis, H. Iatrou, M. Pitsikalis, J. Mays, *Progr. Polym. Sci.* **2006**, *31*, 1068–1050. years of living polymerization.
- 12 G. Kraus, C. W. Childers, J. T. Gruver, *J. Appl. Polym. Sci.* **1967**, *11*, 1581.
- 13 G. Kraus, K. W. Rollmann, *Die Angewandte Makromolekulare Chemie* **1971**, *16*, 271.
- 14 P. Cotanda, D. B. Wright, M. Tyler, R. K. O'Reilly, *J. Polym. Sci. Part A: Polym. Chem.* **2013**, *51*, 3333.
- 15 S. G. Roy, K. Bauri, S. Pal, A. Goswami, G. Madras, P. De, *Polym. Int.* **2013**, *62*, 463.
- 16 M. Camail, H. Essaoudi, A. Margaillan, J. Vernet, *Eur. Polym. J.* **1995**, *31*, 1119.
- 17 X. Pang, H. Sun, Q. Shen, *Polymer* **2004**, *45*, 4029.
- 18 G. Odian, *Principles of Copolymerization*, 3rd ed. Wiley & Sons: New York, **1991**.
- 19 G. Gorrasi, M. Stanzione, L. Izzo, *React. Funct. Polym.* **2011**, *71*, 23.
- 20 H. P. Plaumann, R. E. Branston, *J. Polym. Sci. Part A: Polym. Chem.* **1989**, *27*, 2819.
- 21 M. T. Hunley, K. L. Beers, *Macromolecules* **2013**, *46*, 1393.
- 22 E. Wigner, *Trans. Faraday Soc.* **1938**, *34*, 34.
- 23 G. H. Vineyard, *J. Phys. Chem. Solids* **1957**, *3*, 121.
- 24 H. Eyring, *J. Chem. Phys.* **1935**, *3*, 107.
- 25 R. E. Skyner, J. L. McDonagh, C. R. Groom, T. van Mourik, J. B. O. Mitchell, *Phys. Chem. Chem. Phys.* **2015**, *17*, 6174.
- 26 M. Mella, L. Izzo, *Organometallics* **2013**, *32*, 3192.
- 27 M. Mella, L. Izzo, C. Capacchione, *ACS Catal.* **2011**, *1*, 1460.
- 28 M. Mella, L. Mollica, L. Izzo, *J. Polym. Phys. Part B* **2015**, *53*, 650.
- 29 M. Mella, L. Izzo, *J. Polym. Phys. Part B* **2017**, *55*, 1088.
- 30 H. J. Harwood, *Macromol. Symp.* **1987**, *10–11*, 331.
- 31 B. Klumperman, K. F. O'Driscoll, *Polymer* **1993**, *34*, 1032.
- 32 L. K. Christov, G. S. Georgiev, *Macromol. Theory Simul.* **2000**, *9*, 715–724. p.
- 33 D. J. Wales, *Int. Rev. Phys. Chem.* **2006**, *25*, 237.
- 34 J. Chocholeuov, J. Vacek, P. Hobza, *J. Phys. Chem. A* **2003**, *107*, 3086.
- 35 D. Di Tommaso, *Cryst. Eng. Comm.* **2013**, *15*, 6564.
- 36 F. Ramondo, L. Bencivenni, R. Caminiti, A. Pieretti, L. Gontrani, *Phys. Chem. Chem. Phys.* **2007**, *9*, 2206.
- 37 R. F. Ribeiro, A. V. Marenich, C. J. Cramer, D. G. Truhlar, *Phys. Chem. Chem. Phys.* **2011**, *13*, 10908.
- 38 D. Di Tommaso, K. L. Watson, *J. Phys. Chem. A* **2014**, *118*, 11098.

- 39** H. Paali, A. J. A. Aquino, D. Tunega, G. Haberhauer, M. H. Gerzabek, H. C. Georg, T. F. Moraes, K. Coutinho, S. Canuto, H. Lischka, *J. Comput. Chem.* **2010**, *31*, 2046.
- 40** P. Friant-Michel, M. F. Ruiz Lpez, *Chem. Phys. Chem.* **2010**, *11*, 3499.
- 41** M. Fioroni, D. Vogt, *J. Phys. Chem. B* **2004**, *108*, 11774.
- 42** P. E. M. Lopes, G. Lamoureux, B. Roux, A. D. MacKerell, *J. Phys. Chem. B* **2007**, *111*, 2873.
- 43** C. M. Baker, G. H. Grant, *J. Chem. Theory Comput.* **2007**, *3*, 530.
- 44** C. Nieto-Draghi, P. Bonnaud, P. Ungerer, *J. Phys. Chem. C* **2007**, *111*, 15686.
- 45** T. Kuznicki, J. H. Masliyah, S. Bhattacharjee, *Energy Fuels* **2008**, *22*, 2379.
- 46** T. F. Headen, E. S. Boek, N. T. Skipper, *Energy Fuels* **2009**, *23*, 1220.
- 47** M. Sedghi, L. Goual, W. Welch, J. Kubelka, *J. Phys. Chem. B* **2013**, *117*, 5765.
- 48** A. Sharma, L. Liu, S. Parameswaran, S. M. Grayson, H. S. Ashbaugh, S. W. Rick, *J. Phys. Chem. B* **2016**, *120*, 10603.
- 49** D. A. Singleton, D. T. Nowlan, N. Jahed, K. Matyjaszewski, *Macromolecules* **2003**, *36*, 8609.
- 50** K. Matyjaszewski, J.-L. Wang, T. Grimaud, D. A. Shipp, *Macromolecules* **1998**, *31*, 1527.
- 51** X. Zhang, J. Xia, K. Matyjaszewski, *Macromolecules* **1998**, *31*, 5167.
- 52** X. Li, X. Zhu, Z. Cheng, W. Xu, G. Chen, *J. Appl. Polym. Sci.* **2004**, *92*, 2189.
- 53** E. Mastan, S. Zhu, *Macromolecules* **2015**, *48*, 6440.
- 54** K. Levenberg, *Quart. Appl. Math.* **1944**, *2*, 164.
- 55** D. W. Marquardt, *J. Soc. Ind. Appl. Math.* **1963**, *11*, 431.
- 56** T. Williams, C. Kelley, C. Bersch, H.-B. Bröker, J. Campbell, R. Cunningham, D. Denholm, G. Elber, R. Fearick, C. Grammes, L. Hart, L. Hecking, P. Juhász, T. Koenig, D. Kotz, E. Kubaitis, R. Lang, T. Lecomte, A. Lehmann, J. Lodewyck, A. Mai, B. Märkisch, E. A. Merritt, P. Mikulík, C. Steger, S. Takeno, T. Tkacik, J. Van der Woude, J. R. Van Zandt, A. Woo, J. Zellner, *Gnuplot 4.4: an interactive plotting program*, <http://gnuplot.sourceforge.net/> (**2010**).
- 57** A. Ponti, M. Mella, *J. Phys. Chem. A* **2003**, *107*, 7589.
- 58** M. Mella, A. Ponti, *ChemPhysChem* **2006**, *7*, 894.
- 59** J. Lad, S. Harrisson, G. Mantovani, D. M. Haddleton, *Dalton Trans.* **2003**, 4175–4180.
- 60** V. Coessens, T. Pintauer, K. Matyjaszewski, *Progr. Polym. Sci.* **2001**, *26*, 337.
- 61** G. Martinez, M. Sanchez-Chaves, E. Lopez Madruga, *J. Polym. Sci. Part A: Polym. Chem.* **2002**, *40*, 2427.
- 62** C. Fernández-Monreal, G. Martínez, M. Sánchez-Chaves, E. López Madruga, *J. Polym. Sci. Part A: Polym. Chem.* **2001**, *39*, 2043.
- 63** L. Martín-Gomis, R. Cuervo-Rodríguez, M. C. Fernández-Monreal, E. L. Madruga, M. Fernández-García, *J. Polym. Sci. Part A: Polym. Chem.* **2003**, *41*, 2659.
- 64** D. Fournier, R. Hoogenboom, H. M. L. Thijs, R. M. Paulus, U. S. Schubert, *Macromolecules* **2007**, *40*, 915.
- 65** A. A. Kavitha, N. K. Singha, *Macromol. Chem. Phys.* **2007**, *208*, 2569.
- 66** P. Maksym-Bębenek, T. Biela, D. Neugebauer, *React. Funct. Polym.* **2014**, *82*, 33.
- 67** I. Ydens, P. Dege, D. M. Haddleton, P. Dubois, *Eur. Polym. J.* **2005**, *41*, 2255.